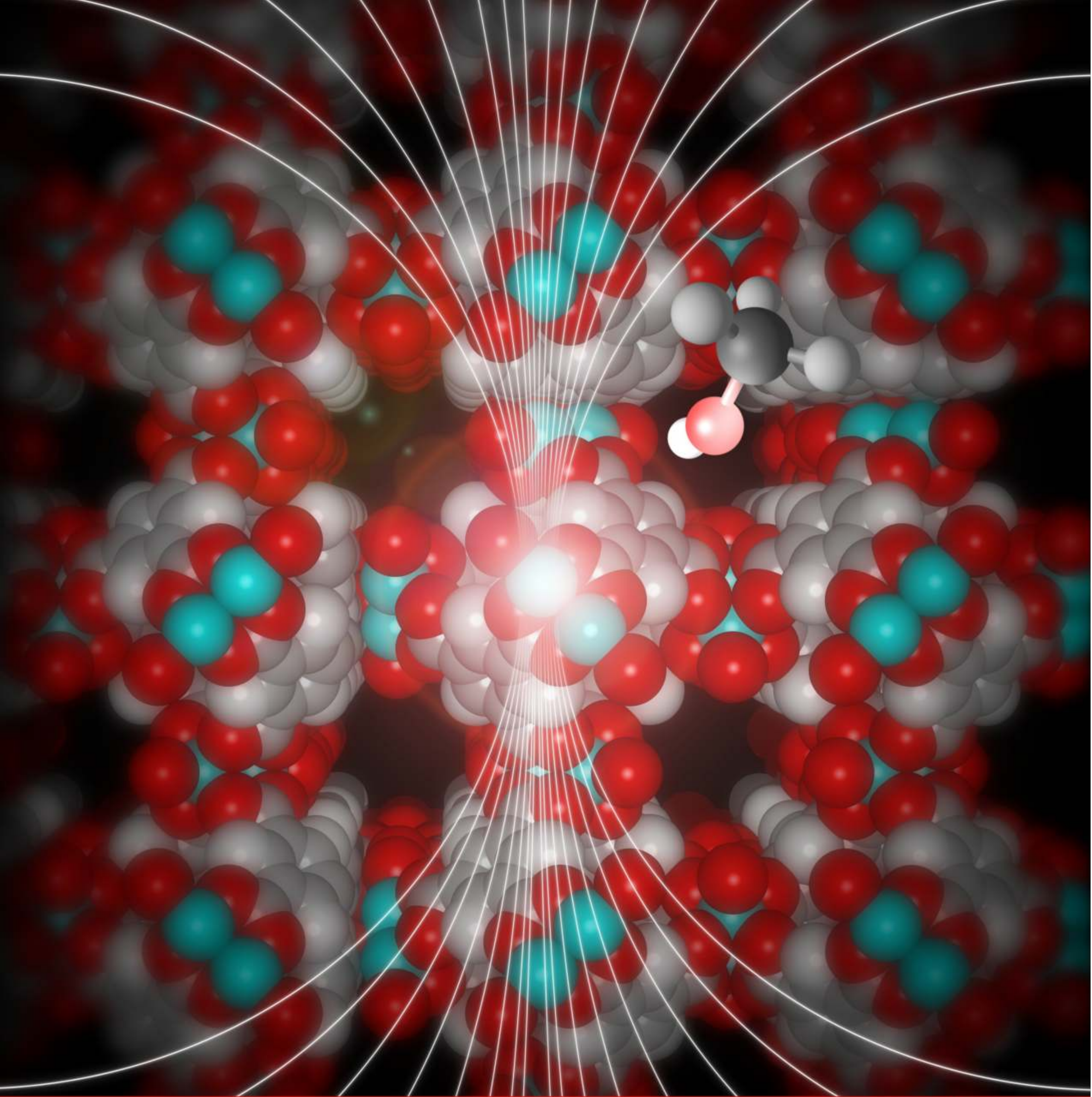

Stefan Friedländer

Increasing Sensitivity for Electron Paramagnetic Resonance Spectroscopy of Cupric Ions in Metal-Organic Framework Single Crystals and Thin Films

Increasing Sensitivity for Electron Paramagnetic Resonance Spectroscopy of Cupric Ions in Metal-Organic Framework Single Crystals and Thin Films

Von der Fakultät für Physik und Geowissenschaften
der Universität Leipzig
genehmigte
DISSERTATION
zur Erlangung des akademischen Grades

doctor rerum naturalium
(Dr. rer. nat.)

vorgelegt

von M.Sc. Stefan Friedländer
geboren am 13.05.1988 in Nordhausen

Gutachter: Prof. Dr. Andreas Pöppl
Prof. Dr. Klaus Köhler

Tag der Verleihung 10.07.2017

Bibliographische Angaben

Friedländer, Stefan
Increasing Sensitivity for Electron Paramagnetic Resonance Spectroscopy of Cupric Ions in Metal-Organic Framework Single Crystals and Thin Films
Universität Leipzig, Dissertation, 2017
139 S.[1], 224 Lit.[2], 13 Tab., 48 Abb., 2 Anlagen

Abstract

Metal-organic frameworks (MOFs) offer a large application potential in various areas such as adsorption, catalysis, and sensing. MOFs consist of metal ions connected by organic linker molecules and have gained interest in recent decades due to their large surface area and variety of functional specifications. MOFs exhibit interesting properties for gas storage and can be tailored to show ferromagnetism, even for such high porosities. While many of these materials contain paramagnetic ions as major framework constituents, electron paramagnetic resonance (EPR) investigations of MOF adsorption systems are often restricted to powder materials since single crystals are only available in sub-millimeter sizes. However, elucidation of the structure of those adsorption complexes requires knowledge about the orientation of the magnetic tensors which can only be deduced from single crystal experiments. This work shows that it is feasible to investigate small MOF crystallites by means of the widely used X-band EPR spectroscopy involving sensitivity enhancing techniques, which are applied to a MOF investigation series for the first time.

This thesis highlights different approaches for the sensitivity enhancement, which have currently reached an application level in EPR spectroscopy. First dielectric resonators (DRs) are employed in conventional EPR sample tubes. This combination is inserted into cavity resonators with continuous-flow cryostats in order to enhance the sensitivity of the EPR experiment significantly while still allowing for measurements at non-ambient conditions in commercial spectrometers. The DRs have been found to enhance the signal by up to a factor of 80. Second, the implementation of planar microresonators (PMRs) in commercial continuous wave (cw) and pulsed EPR spectrometer setups is evaluated, revealing signal enhancements of more than a factor of 51. These two methods are compared against other current developments in high sensitivity EPR, and the selection of DRs for the present MOF studies is discussed.

Furthermore, this thesis summarizes the findings of DR-aided EPR investigations of paramagnetic $\mathrm{Cu^{2+}}$ ions in various MOFs. First the nature of a mononuclear $\mathrm{Cu^{2+}}$ ion defect species in $^{3}_{\infty}[\mathrm{Cu^{I}_{2}Cu^{II}_{2}(H_2O)_2L_2Cl_2}]$ was discovered. The study identified defective copper paddle-wheel (PW) units with one missing $\mathrm{Cu^{2+}}$ ion for the first time in MOFs. Second, the interactions between the $\mathrm{Cu^{2+}}$ ions in $\mathrm{Cu_3(btc)_2}$ (HKUST-1) and $\mathrm{Cu_{2.965}Zn_{0.035}(btc)_2}$ with adsorbed gas molecules was elucidated, which allowed for the description of previously unknown structural data for the different adsorption states by identifying the magnetic tensor orientations with respect to the crystal axes for the first time in MOFs. Third, the magnetic properties of the SURMOF-2 thin film series were determined, revealing an unusual ferromagnetic phase. The thin film material is thus found to be representative of one of the novel functionalized MOFs, and can be studied effectively by the DR-aided cw EPR setup even for very small film thicknesses.

---

[1] . . . S. (Seitenzahl insgesamt)
[2] . . . Lit. (Anzahl der im Literaturverzeichnis ausgewiesenen Literaturangaben)

Referat

Metallorganische Gerüstverbindungen (engl. *metal-organic frameworks (MOFs)*) bieten vielfältige Anwendungsmöglichkeiten in unterschiedlichen Bereichen, darunter bei der Trennung von Gasen oder als Katalysator. Sie bestehen aus Metallionen, die über organische Moleküle verbrückt sind und konnten in den vergangenen zwei Jahrzehnten wachsende wissenschaftliche Aufmerksamkeit erregen. Dies ist darin begründet, dass sie eine große innere Oberfläche und variable Funktionalisierbarkeit, beispielsweise für Ferromagnetika, bieten. Da zudem MOF-Materialien bereits paramagnetische Ionen als maßgebliche Gerüstbestandteile aufweisen, bietet die Paramagnetische Elektronenspin-Resonanzspektroskopie (engl. *electron paramagnetic resonance (EPR)*) die Möglichkeit, MOF-Adsorptionssysteme effizient zu erforschen. Als problematisch erwies sich jedoch, dass solche Untersuchungen auf Pulvermaterialien beschränkt blieben, da einzelne Kristalle zu geringe Spindichten aufweisen. Die vorliegende Dissertation zeigt auf, wie mit neuen Bauteilen an üblichen Spektrometern mit hoher Empfindlichkeit erstmals MOF-Einkristalle gemessen werden können.

Die vorliegende Arbeit beleuchtet dazu diverse Ansätze. Zunächst werden Dielektrische Resonatoren (engl. *dielectric resonators (DRs)*) mit hoher Permittivität vorgestellt, welche in herkömmlichen EPR Röhrchen in kommerziellen Hohlraumresonatoren eingesetzt werden können. Weil dies die Verwendung von Standardkryostaten ermöglicht, wird die Empfindlichkeit signifikant erhöht, ohne auf tiefe Temperaturen und Drücke in kommerziellen EPR Spektrometern verzichten zu müssen. Die Empfindlichkeit kann um einem Faktor von bis zu 80 erhöht werden. Des Weiteren wurde die Einbindung von Planaren Mikroresonatoren (engl. *planar microresonators (PMRs)*) in EPR Spektrometer analysiert, wobei Verstärkungen um einen Faktor von mindestens 51 erzielt wurden. Beide Methoden vergleicht die vorliegende Arbeit mit anderen neuen und etablierten hochempfindlichen Messmethoden der EPR und diskutiert die Verwendung von DRs für vorgenommene MOF-Untersuchungen.

Schließlich fasst diese Dissertation die Untersuchungen zusammen, welche mithilfe der DR an paramagnetischen $\mathrm{Cu^{2+}}$ Ionen in diversen MOFs durchgeführt wurden. Hier konnten erstens die Eigenschaften einer mononukleären $\mathrm{Cu^{2+}}$ Defektspezies in ${}^{3}_{\infty}[\mathrm{Cu^{I}{}_{2}Cu^{II}{}_{2}(H_2O)_2L_2Cl_2}]$ charakterisiert werden, wobei defekte schaufelradförmige (engl. *paddle-wheel (PW)*) Einheiten identifiziert wurden. Zweitens wurde die Wirkung zwischen $\mathrm{Cu^{2+}}$ Ionen in $\mathrm{Cu_3(btc)_2}$ und $\mathrm{Cu_{2.965}Zn_{0.035}(btc)_2}$ mit adsorbierten Gasen untersucht. Dies erlaubte, zuvor unbekannte Strukturdaten unter Einfluss der verschiedenen Adsorbaten zu gewinnen, indem die magnetischen Tensororientierungen bezüglich des Kristallgitters erstmals in MOFs aufgelöst werden konnten. Diese Ergebnisse zeigen, dass konventionelle EPR Spektrometer trotz relativ niedriger X-Band Frequenzen durch die Ausrüstung mit DRs effizient für Einkristalluntersuchungen an MOFs benutzt werden können. Drittens werden Experimente vorgestellt, bei denen die Eigenschaften von SURMOF-2 Dünnfilmen erforscht wurde. Hier zeigte sich, dass eine ungewöhnliche Kopplung in quasi-eindimensionalen Ketten eine ferromagnetische Phase bei niedriger Temperatur und auch ohne externe Magnetfelder stabilisiert. Die charakteristische Curie-Temperatur des Phasenübergangs ist anomal hoch und kann zudem einfach durch die Wahl der organischen Verbindungsmoleküle beeinflusst werden. Dies identifiziert die SURMOF-2 Familie als Vertreter der neuartigen, funktionalisierten MOF-Materialien, welche ebenso durch die DR gestützte EPR selbst für sehr dünne Schichtdicken untersucht werden können.

Acknowledgements

This work has been accomplished under the supervision of Andreas Pöppl of the Spin Resonance Group of Jürgen Haase. Therefore, first I would like to thank them for the confidence they conferred upon me by offering this opportunity, the discussions and all the possibilities for additional learning that were presented to me at numerous conferences and a summer school. I have been provided with great insight into various aspects of scientific research in general, as well as magnetic resonance in particular. Maybe even more importantly, a little family has emerged around me in the past three years and I am especially thankful for my partner, who helped to ensure that we were able to balance my PhD and childcare. I am also thankful that my work group provided an extremely child-friendly working environment.

I would also like to thank all present and former scientific and technical coworkers, PhD fellows, students and trainees in our group for maintaining a pleasant working atmosphere and a spirit of cooperation. Firstly, of course, is Andreas Pöppl, for always being at my disposal in scientific, technical and administrative questions, and Rolf Böttcher, who was always available for valuable discussions about devices, samples and simulations, and who has introduced me to the great collection of vintage equipment in our group and the history of it. Secondly, Joachim Höntsch, for providing great support for technical issues with both old and new devices and all the discussions about CAD constructions, Horst Voigt for the help with microwave equipment and countless additional technical questions, and Gerd Klotzsche, for all I have learned about supporting techniques around the spectrometers.

I would like to thank Bettina Jee, whose experience helped me with everything from learning EPR in the first lab course to understanding the last sample measured, and who has introduced all modern spectrometers to me; Matthias Mendt, who shared his entire PhD time with me and was thus of great help in answering many questions; Mantas Šimėnas, for dielectric measurements and who was a great fellow both before and during the PhD, always contributing excellently in our discussions; Anastasia Kultaeva for all the shared experiences about samples and lab courses; Felix Bolling, for countless discussions about HKUST-1 and the little helping tools he developed during his Bachelors' and Masters' theses; our trainees Benno Krüger, Tilo Pilling, and Sascha Lettmann for their helping hands in many situations; our machinery shop with all their technical engineers and skilled staff, and the glass workers around Stephan Eckert for their consistently fast and excellent work.

Many special thanks must go out to our collaborators: Oleg Ovchar and Anatolii Belous from the National Academy of Sciences in Kiev, Ukraine, who provided our working horses – dielectric resonators – during a time of war at Europe's eastern boarders; Ryszard Narkowicz and Dieter Suter, Dortmund, and Edward Reijerse, Mühlheim, for sharing microresonators and experience about them; Michael Ziese and Marko Bertmer of Leipzig and Petko Petkov and others from Thomas Heine's Bremen and Leipzig groups for all joint studies and related discussions; Pierre Eckold and Merten Kobalz from Harald Krautscheid's group, Leipzig; Stefan Kaskel and Steffen Hausdorf, Dresden, Liu Jinxuan and Christof Wöll, Karlsruhe, and Winfried Böhlmann and Kathrin Koch of Leipzig for providing, modifying, characterizing and discussing the samples. Last but not least, I would like to thank the German Research Foundation (DFG) for the financial support provided to me.

Contents

List of Figures

List of Tables

Disclaimer Third Parties

All product and company names are trademarks™ or registered® trademarks of their respective holders. Use of them does not imply any affiliation with or endorsement by them.

Autodesk Inventor® is a registered trademark of the Autodesk Corporation, San Rafael, CA.

BRUKER® and respective spectrometer names are registered trademarks of the Bruker Corporation, Billerica, MA.

HP® refers to the former Hewlett-Packard Company, Palo Alto, CA. HP VEE® was a registered trademark of the former Hewlett-Packard Company, Palo Alto, CA. Today, the relevant trademarks are hold by Agilent Technologies, Santa Clara, CA.

LabVIEW® is a registered trademark by National Instruments, Austin, TX.

MATLAB® is a registered trademark by The MathWorks, Inc., Natick, MA.

Meilhaus® is a registered trademark by Meilhaus Electronic GmbH, Alling, Germany.

muRata® is a registered trademark by Murata Manufacturing Co., Ltd., Nagaokakyō, Japan.

OXFORD® refers to Oxford Instruments plc, Abingdon, England.

PYREX® is a registered trademark by Corning Inc., Corning, NY.

Rogers® refers to Rogers Corporation, Rogers, CT.

VARIAN® was a registered trademark by Varian Associates, Palo Alto, CA.

Other programs named in the text are cited upon first occurrence.

Glossary

cw	continuous wave
DFT	density-functional theory
DR	dielectric resonator
EPR	electron paramagnetic resonance
FMR	ferromagnetic resonance
HFS	hyperfine splitting
IC	integrated chip, ASIC application specific –
MOF	metal-organic framework
mw	microwave
PCB	physical circuit board
PMR	planar microresonator
PW	paddle-wheel
SNR	signal-to-noise ratio
SQUID	superconducting quantum interference device
XRD	X-ray diffraction
RF	radio frequency $f = 9\,\mathrm{kHz} \cdots \mathrm{THz}$ with mw $\subset$ RF, $f > 1\,\mathrm{GHz}$
R*n*	PMR setup release
T*n*	PMR series numbering scheme

List of Samples

sample	chemical formula	provided by
1	${}^{3}_{\infty}[\mathrm{Cu^{I}_{2}Cu^{II}_{2}(H_2O)_2L_2Cl_2}]$ as synthesized	Krautscheid et al., U Leipzig
$\mathbf{2}_{\mathrm{AS}}$	$\mathrm{Cu_3(btc)_2}$ as synthesized	Kaskel et al., TU Dresden
$\mathbf{2}_{\mathrm{act}}$	$\mathrm{Cu_3(btc)_2}$ activated	
$\mathbf{2}_{\mathrm{MeOH}}$	$\mathrm{Cu_3(btc)_2}$ w/ methanol ($\mathrm{^{13}CH_3OH}$) adsorbed	
$\mathbf{3}_{\mathrm{AS}}$	$\mathrm{Cu_{2.965}Zn_{0.035}(btc)_2}$ as synethesized	
$\mathbf{3}_{\mathrm{act}}$	$\mathrm{Cu_{2.965}Zn_{0.035}(btc)_2}$ activated	
$\mathbf{3}_{\mathrm{CO}}$	$\mathrm{Cu_{2.965}Zn_{0.035}(btc)_2}$ w/ carbon monoxide ($\mathrm{^{13}CO}$) adsorbed	
$\mathbf{3}_{\mathrm{CO_2}}$	$\mathrm{Cu_{2.965}Zn_{0.035}(btc)_2}$ w/ carbon dioxide ($\mathrm{^{14}CO}$) adsorbed	
$\mathbf{3}_{\mathrm{MeOH}}$	$\mathrm{Cu_{2.965}Zn_{0.035}(btc)_2}$ w/ methanol ($\mathrm{^{13}CH_3OH}$) adsorbed	
4	$\mathrm{Cu_2(bdc)_2(H_2O)_2 = (Cu,bdc)}$ SURMOF-2 as synthesized	Wöll et al., KIT Karlsruhe
5	$\mathrm{Cu_2(bpdc)_2(H_2O)_2 = (Cu,bpdc)}$ SURMOF-2 as synthesized	

Quantities and Constants

Frequently used variables

$\mathbf{A}$, A	HFS tensor	I_{DI}	double integral intensity
a	HFS constant or length	K_i	anisotropy constant
α	angle or initial quantum state	k	wave number
$\mathbf{B}_0$, B_0	external magnetic field	$\mathbf{L}$, L	total orbital angular momentum, length
ΔB_{pp}	peak-to-peak linewidth	λ	wavelength or spin-orbit coupling constant
$\mathbf{B}_1$, B_1	microwave magnetic field	M	magnetization
β	angle or final quantum state	m_I	nuclear magnetic spin number
C_i	conversion factor	m_S	magnetic spin quantum number
χ_{mag}	magnetic susceptibility M/B_0	$\boldsymbol{\mu}$, μ	total magnetic moment
χ''	absorption or $\mathrm{d}^2\chi_{\mathrm{mag}}/\mathrm{d}B_0^2$	N	number of particles nV
Δ_i	ligand field energy	ν_{mw}	microwave frequency
d, $\varnothing_{\mathrm{OD}}$	distance or diameter, outer diameter	ω	angular frequency $2\pi\nu_{\mathrm{mw}}$
E	electric field	P	power
η	filling factor	Q	quality factor
F	free energy	$\mathbf{S}$, S	electron spin
f, f_{GHz}	microwave frequency, in GHz	S_{ii}	scattering parameter
ϕ, φ	angle	T_1	spin-lattice relaxation time
Γ	linewidth FWHM/2	T, T_C	temperature, Curie temperature
$\mathbf{g}$, g	g tensor / factor	t	time
g_n	nuclear g factor	τ	pulse idle time
γ	gyromagnetic ratio	(V)SWR	(voltage) standing wave ratio
$\mathcal{H}$	Spin Hamiltonian	V	volume
$\mathbf{H}$, H	magnetic field strength B/μ	W	transition energy
$\mathbf{I}$, I	nuclear spin	Z	impedance

Constants

β_e	Bohr magneton	$\frac{\lvert e\rvert\hbar}{2m_e} = 9.274{,}009{,}49(80) \times 10^{-24}\ \mathrm{J/T}$
β_n	nuclear magneton	$\frac{\lvert e\rvert\hbar}{2m_p} = 5.050{,}783{,}43(43) \times 10^{-27}\ \mathrm{J/T}$
c	speed of light in vacuum	$299{,}792{,}458\ \mathrm{m/s}$
ε_r	vacuum (electric) permittivity	$8.854{,}187{,}817{,}6 \times 10^{-12}\ \mathrm{C/Vm}$
g_e	free electron g factor	$2.002{,}319{,}304{,}361{,}7(15)$
h	Planck constant	$2\pi\hbar = 6.626{,}070{,}040 \times 10^{-34}\ \mathrm{J\,s}$
k_B	Boltzmann constant	$1.380{,}649 \times 10^{-23}\ \mathrm{J/K}$
μ_0	vacuum (magnetic) permeability	$4\pi \times 10^{7}\ \mathrm{N/A^2} = 1.2566 \times 10^{-6}\ \mathrm{Vs/Am}$

Rounded or measured numbers and units are printed sans serif, mathematical integers in normal font.

Bold letters mark tensors and their *italic* equivalents denote isotropic or principal axis values.

1 New Frontiers in Sensitivity for EPR Spectroscopy

1.1 Electron Paramagnetic Resonance of Crystalline Samples

In 1944, E. Zavoisky conducted the first experiment on paramagnetic relaxation, later more generally denoted by electron paramagnetic resonance (EPR), in $\mathrm{CuCl_2 \cdot H_2O}$ in a magnetic field of $5.7\,\mathrm{mT}$ and detected by a radio frequency (RF) of $150(5)\,\mathrm{MHz}$, at Kazan University in Russia.[1] Successive inventions for microwave (mw) techniques such as radar helped to improve EPR spectroscopy significantly to nowadays spectrometers, which are currently capable of utilizing superconducting magnets with several Tesla of magnetic field strength and Terahertz radiation sources for excitation.[2] Despite the tremendous advancements that have been made in increasing spectral resolution by increasing the average magnetic field strength and mw frequency by four to six orders of magnitudes, compared to the experiment performed at Kazan more than 70 years ago, in principle, all EPR experiments still share that experiment's underlying physics. A clear majority of EPR spectroscopy even utilizes a similar instrumentation principle, the so-called continuous wave (cw) EPR, even though pulsed EPR experiments have become readily available.[3–5] In principle, the nature of split energy levels of matter is obtained by radiating a paramagnetic sample exposed to a known magnetic field with continuous or pulsed electromagnetic waves and observing the characteristic mw power affected by absorption, free induction decays or spin echoes. From the various responses to these advanced processes, a large amount of information on coordination, surrounding nuclei, and even dynamics of unpaired electrons like radicals,[6–8] transition metal complexes, rare earth ions or triplet states,[9,10] dopants in semiconductors,[11] defect species,[12] or in biological matter like proteins can be obtained.[13] Several other magnetic resonance techniques are closely linked to EPR, such as the older ferromagnetic resonance (FMR) or – a link to nuclear magnetic resonance (NMR) – electron nuclear double resonance (ENDOR).[14,15]

In addition to spectral resolution, advancements in spin sensitivity represent another important milestone for spectrometer development. Because sensitivity is a relevant issue for many applications, technical improvements have been aimed at tackling the problem ever since. While it is true that in general, higher frequencies increase the signal-to-noise ratio (SNR), the highest spin sensitivities are not only achieved by ultra-high frequency EPR spectrometers.[16] Considering reasonable cost efficiency, the peak of spin-sensitivity versus frequency is further shifted to lower ranges if the general applicability, affordability, and reproducibility for a wide range of laboratories is considered. One target for highly sensitive measurements is given by single crystals, and while EPR spectroscopy of sufficiently large crystals has been done like many other spectroscopies for decades,[17] the investigation of very small crystallites and thin films of porous, low-density materials presents some challenges. Silica, zeolites and metal-organic frameworks (MOFs), which frequently are investigated at relatively low mw frequencies of about 9 GHz at temperatures as low as 4.2 K,[18–20] are not available in sufficient sizes but are often the subject of even more challenging adsorption studies as powder materials.[21–23] This leaves a number of open questions: in principle, cw and pulsed EPR spectroscopy of paramagnetic centers in disordered materials allow for the measurement of the principal axis values of the magnetic interaction tensors and the relative principal axis orientations with respect to each other. Nevertheless, these measurements cannot give insight into the orientation of magnetic tensors with respect to the crystallographic axes themselves. Such information can only be obtained from single crystal experiments, and may reveal valuable details about the structure and dynamics of the paramagnetic adsorption complexes including, among others, distribution of complex geometries and motional effects of the adsorbed molecules, which are hardly accessible from powder experiments alone. This work will focus on this particular field of EPR and show how the SNR limits can be pushed to perform novel investigations on samples which previously have been inaccessible by EPR. It presents for the first time reliable methods for small single crystal EPR studies of paramagnetic adsorption complexes in porous, low-density materials at relatively low, but common, X-band frequencies to give new insight into the elucidated structures.

1.2 Project Description and Organization of Thesis

In many fields, porous materials are prime candidates for future applications. MOF compounds, with their large structural diversity, have great potential as tailored materials for specific tasks.[24–26] The high porosity of their structure often leads to the formation of small crystallites, which in the past have mostly been investigated in EPR as powders due to the low signal intensity. To date, only studies of MOF single crystals by methods such as single crystal X-ray diffraction (XRD) have been conducted.[27] Due to the information which can be learned from the smallest particles, more efforts must be carried out to increase the sensitivity in various fields. EPR has been regarded as a potential technique for improvements herein: the German Research Foundation's (German *Deutsche Forschungsgemeinschaft*, DFG) priority program "SPP 1601 – New Frontiers in Sensitivity for EPR Spectroscopy: From Biological Cells to Nano Materials" has therefore been devoted to developing methods for more sensitive measurements and the initiative of Leipzig's EPR group has in particular focused on the investigation of advanced techniques for regular X-band EPR spectrometers as a demonstration of the high potential of those investigations at low temperatures and non-ambient gas atmospheres.

From 2013 – 2016, different techniques have been developed through various collaborations and applied to a selection of porous materials which had previously been investigated by powder cw and pulsed EPR. However this left several questions, which now now can be addressed with the help of single crystals. In this regard, after the general introductions in EPR, instrumentation and sensitivity in Chapter Two, Section 2.1, it will be outlined, how cw EPR aided by dielectric resonators (DRs) described in Section 2.2 and planar microresonators (PMRs) introduced in Section 2.3 has been carried out to investigate different MOF samples which are presented in Section 2.4. The investigations performed on these different sensitivity-enhancing techniques are presented in Chapter Three, while a large part of this thesis is devoted to the novel insights gained on structural properties of the MOF compounds in Chapter Four. Finally, Chapter Five compares the two experimental methods, DRs and PMRs, in the context of other approaches and summarizes the MOF studies.

Several parts of this work have already been published and are cited throughout the manuscript (listed in chronological order):

(1) **Friedländer, S.**, Petkov, P., Bolling, F., Kultaeva, A., Böhlmann, W., Ovchar, O., Belous, A., Heine, T., Pöppl, A., 'Continuous Wave Single Crystal Electron Paramagnetic Resonance of Adsorption of Gases to Cupric Ions in the Zn(II) Doped Porous Coordination Polymer $Cu_{2.965}Zn_{0.035}(btc)_2$', *J. Phys. Chem. C* **2016**, *120*, 48, 27399

(2) **Friedländer, S.**, Liu, J.,[1] Addicoat, M., Petkov, P., Vankova, N., Rüger, R., Kuc, A., Guo, W., Zhou, W., Lukose, B., Wang, Z., Weidler, P. G., Pöppl, A., Ziese, M., Heine, T. and Wöll, C., 'Linear Chains of Magnetic Ions Stacked with Variable Distance: Ferromagnetic Ordering with a Curie Temperature above 20 K' *Angew. Chem., Int. Ed.* **2016**, *55*, 41, 12683

(3) **Friedländer, S.**, Šimėnas, M., Kobalz, M., Eckold, P., Ovchar, O., Belous, A. G., Banys, J., Krautscheid, H., Pöppl, A., 'Single Crystal Electron Paramagnetic Resonance with Dielectric Resonators of Mononuclear Cu^{2+} Ions in a Metal-Organic Framework Containing Cu_2 Paddle-Wheel Units' *J. Phys. Chem. C* **2015**, *119*, 33, 19171

(4) **Friedländer, S.**, Ovchar, O., Voigt, H., Böttcher, R., Belous, A., Pöppl, A., 'Dielectric Ceramic EPR Resonators for Low Temperature Spectroscopy at X-band Frequencies' *Appl. Magn. Reson.* **2015**, *46*, 1, 33

Additionally, the following publications have been coauthored but the results are not part of this thesis:

(5) Lorite, I., Kumar, Y., Esquinazi, P., **Friedländer, S.**, Pöppl, A., Michalsky, T., Meijer, J., Grundmann, M., Meyer, T., Estrela-Lopis, I., 'Photo-Enhanced Magnetization in Fe-Doped ZnO Nanowires' *Appl. Phys. Lett.* **2016**, *109*, 1, 012401

(6) Lorite, I., Zandalazini, C., Esquinazi, P., Spemann, D., **Friedländer, S.**, Pöppl, A., Michalsky, T., Grundmann, M., Vogt, J., Meijer, J., Heluani, S. P., Ohldag, H., Adeagbo, W. A., Nayak, S. K., Hergert, W., Ernst, A., Hoffmann, M., 'Study of the Negative Magneto-Resistance of Single Proton-Implanted Lithium-Doped ZnO Microwires' *J. Phys. Condens. Matter* **2015**, *27*, 25, 256002

(7) Böttcher, R., Pöppl, A., Lorenz, M., **Friedländer, S.**, Spemann, D., Grundmann, M., '^{55}Mn Pulsed ENDOR Spectroscopy of Mn^{2+} Ions in ZnO Thin Films and Single Crystal' *J. Magn. Reson.* **2014**, *245*, 0, 79

---

[1] First and second author contributed equally

(8) Lorenz, M., Böttcher, R., **Friedländer, S.**, Pöppl, A., Spemann, D., Grundmann, M., 'Local Lattice Distortions in Oxygen Deficient Mn-Doped ZnO Thin Films, Probed by Electron Paramagnetic Resonance' *J. Mater. Chem. C* **2014**, *2*, 25, 4947

In total, this thesis covers five chapters, cited in parts from publications (1 – 4) as listed above:

I Introduction (this chapter)

II Theory of EPR and how instrumental sensitivity can be enhanced

III Results and discussion of experimental methods from this project

  a) Efficiency of dielectric resonators for cw X-band EPR, published in (4)

  b) Ultra high sensitivity X-band EPR with planar microresonators, unpublished

IV Results and discussion of DR aided cw EPR MOF material studies in this project

  a) Postulation of a defect species in MOF single crystals of ${}^{3}_{\infty}[\mathrm{Cu^{I}_2Cu^{II}_2(H_2O)_2L_2Cl_2}]$, published in (3)

  b) Gas adsorption effects in MOF single crystals of $\mathrm{Cu_{2.965}Zn_{0.035}(btc)_2}$, published in (1)

  c) Discovery of ferromagnetism in (Cu,bdc) SURMOF-2, published in (2)

V Comparison of high sensitivity X-band EPR methods, conclusion and outlook

and an two appendices with

A Device details and respective experimental conditions

B Investigation procedures for relevant techniques of this work

2 Theory, Instrumentation and Sensitivity in Electron Paramagnetic Resonance

In the present chapter, Section 2.1 introduces the principles of the predominant technique used for the sensitivity enhancing spectroscopy methods. These methods are introduced in Section 2.2 – 2.3, and applied to various model samples, such as α,α'-diphenyl-β-picryl-hydrazyl (DPPH) and α,γ-bisdiphenylene-β-phenylallyl (BDPA) in this work,[28] as well as to characterize the real-world samples presented in Section 2.4.

2.1 Electron Paramagnetic Resonance Spectroscopy

EPR is a spectroscopic technique which probes energy levels related to the total spin of unpaired electrons of certain samples by mw radiation while usually exposed to an external magnetic field. Historically, EPR is founded on the early experiments of P. Zeeman,[29] O. Stern and W. Gerlach,[30] and subsequently, G. E. Uhlenbeck and S. A. Goudsmit,[31] who studied the effects of magnetic fields on electromagnetic radiation adsorption and discovered the quantum mechanical concept of electron spin.

Absorption spectra of various kinds have for a long time been the most powerful tools to investigate matter. Typically, a beam of light or different kind of electromagnetic wave enters or passes through a gas, liquid or thin, appropriately transparent piece of solid matter (or is reflected from it) and can interact with it. Suitably spectrally separated and collected, the transmission or reflection gives rise to a spectrum of spatially ordered and demodulated frequencies, interference points, lines or groups of lines (bands) which measure the energy separation of two corresponding energy levels or other interactions with the atomic constituents of solid matter.

For example, electromagnetic radiation from about $10^{9} \cdots 10^{11}$ Hz will interact with molecules which have a permanent electric dipole moment and probe molecular rotations. Higher frequencies of infrared light with $10^{12} \cdots 10^{14}$ Hz may interact with molecules with vibrational modes leading to the energy differences induced by dipole oscillations.[10] For even higher frequencies (about 10^{15} Hz), reactions to visible light occur and lead to the various spectroscopic methods known from optics. At very high frequencies of about 10^{18} Hz electromagnetic bremsstrahlung interacts with the electron shell of atoms and gives rise to XRD patterns. All of these interactions occur due to the interaction of the electric field component of the described waves with electric dipoles of molecules or with specific electrons in matter. Additionally, in the presence of an external magnetic field, the magnetic field component can interact with possible magnetic moments in the sample. Here, electromagnetic radiation of about $10^{7} \cdots 10^{9}$ Hz RF is the basis of probing nuclear magnetic energy levels in the very versatile NMR which is physically and technically closely linked to

EPR. Finally, microwaves from $10^9 \cdots 10^{12}$ Hz are used to induce and observe transitions of the energies of electron magnetic moments in resonance with the mw radiation in paramagnetic samples, from which the term electron paramagnetic resonance (EPR) is derived.

The physical concepts governing this latter effect will be described in Subsection 2.1.1, which is followed by Subsection 2.1.2, providing a closer look at the characteristics of the EPR line itself. The possible technical realization of EPR will be discussed in Subsection 2.1.3, while Section 2.1.4 shows how the theoretical and practical conditions lead to the sensitivity of EPR spectroscopy and how this can be tuned. Finally, Section 2.1.5 gives a short overview of related phenomena and techniques.

2.1.1 The Spin Hamiltonian of Paramagnetic Systems

The energy of an electron with electron spin S in an external magnetic field $\mathbf{B}_0$ can be written as Hamiltonian $\hat{\mathcal{H}}$:[10]

$$\hat{\mathcal{H}} = \underbrace{\beta_e \mathbf{B}_0 \mathbf{g}\hat{\mathbf{S}}}_{\hat{\mathcal{H}}_{\mathrm{EZ}}} + \underbrace{h\hat{\mathbf{S}}\mathbf{A}\hat{\mathbf{I}}}_{\hat{\mathcal{H}}_{\mathrm{HFS}}} + \underbrace{h\hat{\mathbf{S}}\mathbf{D}\hat{\mathbf{S}}}_{\hat{\mathcal{H}}_{\mathrm{FS}}} - \underbrace{J\hat{\mathbf{S}}_1\hat{\mathbf{S}}_2}_{\hat{\mathcal{H}}_{\mathrm{ex}}} - g_n\beta_n\mathbf{B}_0\hat{\mathbf{I}} + h\hat{\mathbf{I}}\mathbf{Q}\hat{\mathbf{I}} \tag{2.1}$$

The original theoretical formulation of Zavoisky's experiments was published in 1951 by A. Abragam and M.-H. L. Pryce.[32] Here, the two most important terms for this work are denoted by $\hat{\mathcal{H}}_{\mathrm{EZ}}$ for the Electron Zeeman interaction and $\hat{\mathcal{H}}_{\mathrm{HFS}}$ for the hyperfine splitting (HFS) interaction term. In general, a paramagnetic system can be composed of numerous constituents which contribute with further terms to the above Spin Hamiltonian and it is often feasible to form groups of equivalent terms by summing them up as for example

$$\hat{\mathcal{H}}_{\mathrm{EZ}} = \sum_i \beta_e \mathbf{B}_0 \mathbf{g}_i \hat{\mathbf{S}}_i \tag{2.2}$$

if several species with different Spin Hamiltonian parameters $\mathbf{g}$ and S are present. Likewise,

$$\hat{\mathcal{H}}_{\mathrm{HFS}} = h \sum_i \hat{\mathbf{S}}_i \mathbf{A}_i \hat{\mathbf{I}}_i \tag{2.3}$$

denotes the energies contributed by several systems with different HFS parameters. The stationary wave functions for eigenfunctions α and β of the electron spin $\mathbf{S}$ are[9]

$$\Psi_\alpha = \langle\alpha|\exp\left(-\omega_\alpha t\right), \quad \Psi_\beta = \langle\beta|\exp\left(-i\omega_\beta t\right) \tag{2.4}$$

with ω_α being the Larmor precession angular frequency defined later in Eqn. 2.10.[33] For completeness, the transition probability for a change between the two states of the two operators in Eqn. 2.4,

$$\Pi_{\beta\alpha} = \left|\langle\alpha|\hat{\mathcal{H}}|\beta\rangle\right|^2 \varrho\left(\omega\right) \tag{2.5}$$

with $\varrho\left(\omega\right)$ defining the frequency distribution of the mw radiation, shows the involvement of $\hat{\mathcal{H}}$ of Eqn. 2.1 for the further considerations. It remains to explain the various quantities: $\hat{\mathcal{H}}_{\mathrm{EZ}}$ refers to the Zeeman interaction of the electron with spin S (spin operator $\hat{\mathbf{S}}$) in the external magnetic field $\mathbf{B}_0$. β_e is the Bohr magneton, while the magnitude of the external magnetic field vector $\mathbf{B}_0$ is denoted by magnetic field strength $||\mathbf{B}_0|| = B_0$ but is usually only referred to as magnetic field B for convenience, omitting the digit-zero identifier. Other magnetic field vectors occurring in this thesis are never written without subscript.

The most important quantity in EPR, the **g** tensor, is defined as the proportionality factor between the total angular momentum $\boldsymbol{\mu}$ and the total magnetic moment $\mathbf{J}$, which in turn can be a sum of spin $\mathbf{S}$, total electronic orbital angular momentum $\mathbf{L}$, and rotational momentum $\mathbf{R}$. Typically, this is written as

$$\boldsymbol{\mu} \propto \mathbf{g} \cdot \mathbf{J}. \tag{2.6}$$

For a free electron, $S = \frac{1}{2}$ and the **g** tensor reduces to the isotropic value g_e.[1] Free radicals like DPPH and BDPA used in this work resemble this value almost, because $L = 0$. In general, for $S > 0$, $L > 0$, the value g_J applies for total angular momenta including first order perturbations.[9,34] In solids, usually in first order $L = 0$, but a part is restored, and $\mathbf{L}$ quenches $\mathbf{g}$ in second order from the spin orbit coupling between $\mathbf{S}$ and $\mathbf{L}$, such that it probes the local crystal field. This topic will be expanded further in Eqn. 2.19–2.21. **g** is usually diagonalizable and its diagonal components g_{xx}, g_{yy} and g_{zz} are important characteristics in cw EPR, since they often can be extracted from the spectra easily. The principal axis values g_{ii} in $i = x$-, y- and z-directions reflect the symmetry of the paramagnetic system. For simple and isotropic systems with $g_{xx} = g_{yy} = g_{zz}$ their magnitude is referred to as the g factor. For axial symmetry, $g_{xx} = g_{yy} \neq g_{zz}$ and the g factors are often grouped as $g_\perp$, $g_\parallel$. Systems with an orthorhombic **g** tensor exhibit three different principal axis values g_{xx}, g_{yy} and g_{zz}.

Resonance condition for $\hat{\mathcal{H}}_{\mathbf{EZ}}$ In a more classical interpretation of $\hat{\mathcal{H}}$, for a paramagnetic system with pure electron spin $S = \frac{1}{2}$ the component of the precessing magnetic moment $\boldsymbol{\mu}$ along the $\mathbf{B}_0$ field in the conventionally chosen z_L axis orientation in the laboratory frame, μ_z, is

$$\mu_z = -\beta_e g m_S, \tag{2.7}$$

where m_S is the magnetic spin quantum number attributed to the electron spin with possible values of $m_S = \pm\frac{1}{2}$. The negative sign in Eqn. 2.7 is due to the negative electron charge. The μ_x and μ_y components are averaged to 0 over the spin ensemble and time in equilibrium. Due to the quantized electron spin, the possible values of μ_z are discrete and quantized as well, which in turn leads to a quantized set of energies $W = -\mu_z B_0$ of the magnetic dipole in the external magnetic field $\mathbf{B}_0$:

$$W = \beta_e B_0 g m_S \tag{2.8}$$

Hence, for the latter electron spin S there are two possible values for W,

$$W = \pm\frac{1}{2}\beta_e B_0 g, \tag{2.9}$$

---

[1] All constants can be found on p. XII.

and the electron spin can be excited by a mw quantum with energy $\Delta E = h\nu_{\mathrm{mw}}$ to overcome the energy separation between the $\langle -\frac{1}{2}|$ and $\langle +\frac{1}{2}|$ energy eigenstates which is proportional to B_0. Here, h is the Planck constant and ν_{mw} the microwave frequency. This energy diagram is depicted in Fig. 2.1A for a $^{63}\mathrm{Cu}^{2+}$ ion. Cu^{2+} has an electronic configuration of $3d^9$ and therefore one unpaired electron in the $3d$-orbital with $S = \frac{1}{2}$, leading at first sight (left-hand m_S lines, $\hat{\mathcal{H}}_{\mathrm{EZ}}$) to a doubled of energy levels (multiplicity $(2S + 1) = 2$).

Eqn. 2.9 and the mw energy can be combined to the central resonance condition of EPR, sometimes called the Bohr frequency condition, and for $S = \frac{1}{2}$

$$\hbar\omega_{\mathrm{mw}} = h\nu_{\mathrm{mw}} = \beta_e B_0 g \tag{2.10}$$

with ω_{mw} being the Larmor frequency in the classical picture of a precessing magnetic moment $\boldsymbol{\mu}$.[9]

Hyperfine splitting $\hat{\mathcal{H}}_{\mathrm{HFS}}$ Since $^{63/65}\mathrm{Cu}^{2+}$ does not only possess an electron spin S but also a nuclear spin of $I = \frac{3}{2}$, Fig. 2.1A shows a further energy level splitting on the right-hand side for $\hat{\mathcal{H}}_{\mathrm{HFS}}$. This is represented by the second term in Eqn. 2.1 to describe the HFS interactions of an electron spin S with a nuclear spin $I \neq 0$ in its vicinity. With a multiplicity of $(2I + 1) = 4$ for $I = \frac{3}{2}$, instead of the doubled now four discrete energy levels are obtained: $m_I = -I, -I + 1, \cdots I$. This observation can be described by a local magnetic field B_{loc} induced by the nucleus, leading to an effective magnetic field B_{eff}. B_{loc} is proportional to the nuclear magnetic spin quantum number m_I and the hyperfine splitting constant a. Then, B_0 of Eqn. 2.10 is altered by B_{eff} to a new resonance field and for isotropic HFS

$$B_{\mathrm{eff}} = B_0 \mp \mu_0 \frac{a}{2} = B_0 - \mu_0 a m_I. \tag{2.11}$$

The nuclear HFS interaction splits each of the energy levels of $\hat{\mathcal{H}}_{\mathrm{EZ}}$ in Fig. 2.1A into four energy levels and the mw quantum of constant energy $h\nu_{\mathrm{mw}}$ excites four possible transitions. It is important to note that the mw cannot interact with the nuclear spin itself at EPR resonance fields $\mathbf{B}_0$, such that m_I must remain constant during an excitation while m_S is allowed to change. This behaviour is the simplest so-called selection rule, which in general prevents arbitrary transitions and allows only a few:

$$\Delta m_S = \pm 1, \ \Delta m_I = 0, \ \mathbf{B}_1 \perp \mathbf{B}_0 \tag{2.12}$$

The third condition is mentioned here for completeness ($\mathbf{B}_1$ is the mw magnetic field, cf. Section 2.1.3) and justified by the fact that the precession of the magnetic moment $\boldsymbol{\mu}$ around $\mathbf{B}_0$ (z component in Eqn. 2.7) must be perturbed along the instantaneous orientation in the μ_x, μ_y plane to maximize the EPR effect.

In general, the HFS depends on all local nuclear magnetic fields near an electron spin S and can thus vary with their orientation for non-isotropic systems. Then the HFS interaction is represented by the hyperfine coupling tensor $\mathbf{A}$ with principal axis values A_{xx}, A_{yy} and A_{zz}. Here, A_{ii} is the hyperfine coupling constant measured in frequency units:

$$A_{ii} = \beta_e g a_{ii}/h \tag{2.13}$$

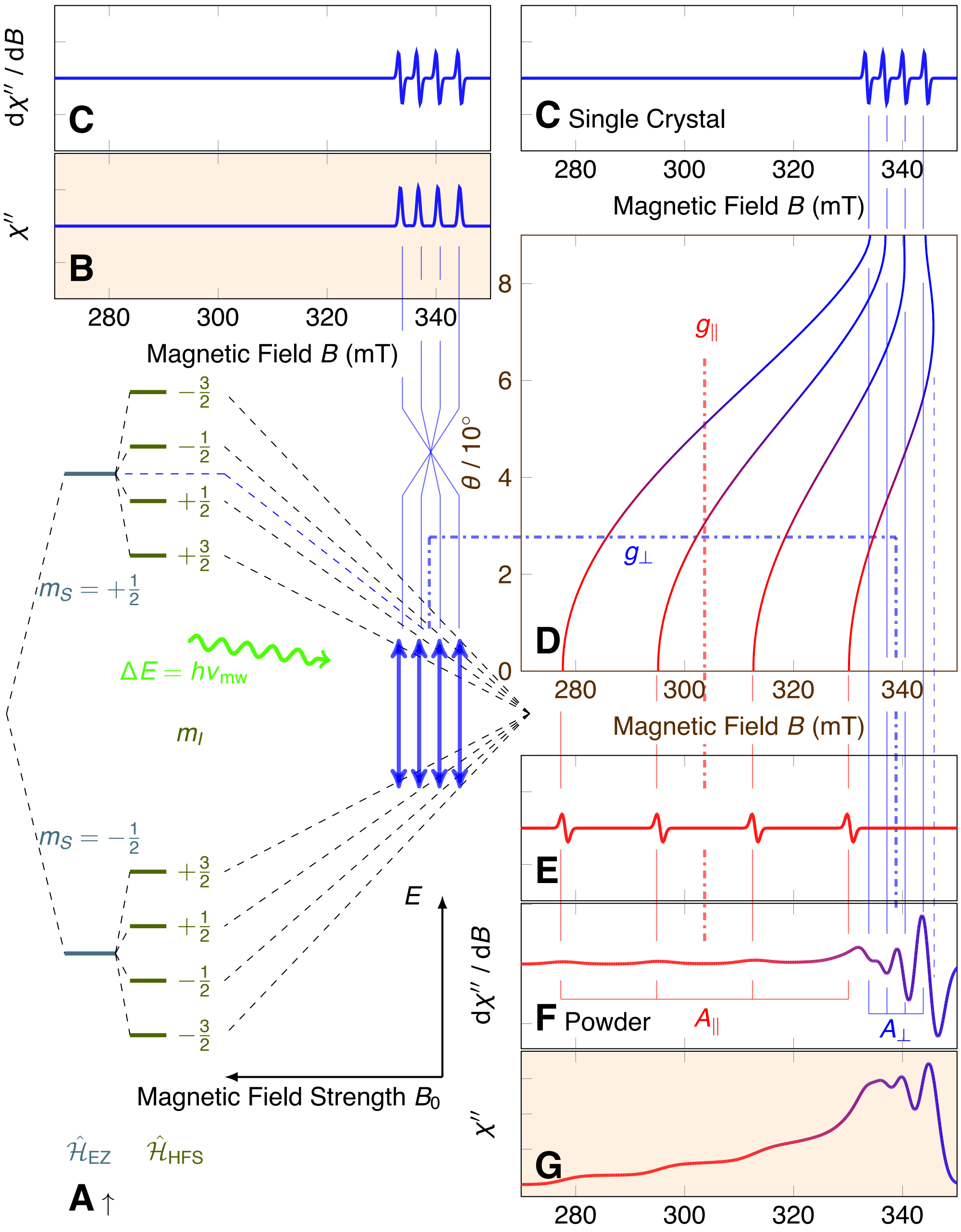

Fig. 2.1 Energy level splitting and cw EPR simulation: Single oriented spectrum and angular dependency summarized to powder signal. Dash dotted lines: w/o HFS, thin solid: w/ HFS, thick blue arrows: allowed EPR transitions.
(A) Energy diagram for ^{63}Cu^{2+} ions in $\hat{\mathcal{H}}_{\text{EZ}}$ and $\hat{\mathcal{H}}_{\text{HFS}}$. Note the inverse $\mathbf{B}_0$ axis.
(B) The four resulting cw EPR absorption lines, here a single ^{63}Cu^{2+} species with $\mathbf{g}/g \parallel \mathbf{A}/A$.
(C) First derivative EPR spectrum (blue: $\mathbf{B}_0 \perp z_M$, z_M: molecular frame $\mathbf{g}$ and $\mathbf{A}$ principal axis orientations).
(D) Angular dependency of ^{63}Cu^{2+} for rotation $\mathbf{B}_0 \perp z_M$ to $\mathbf{B}_0 \parallel z_M$ (red). Dashed blue line: extra-singularity.
(E) First derivative single crystal EPR spectrum of single ^{63}Cu^{2+} species with $\mathbf{B}_0 \parallel z_M$.
(F) Single isotope ^{63}Cu^{2+} powder EPR spectrum as 4π spherically integrated single crystal spectra.
(G) Powder EPR spectrum of the same isotope shown in mw absorption.

The right-hand side of Fig. 2.1A with dashed, gray lines depicts the dependence of ΔE on $\mathbf{B}_0$ (note the descending abscissa for convenience here). The direct proportionality of $\hat{\mathcal{H}}_{\mathrm{EZ}}$ on $\mathbf{B}_0$ results in increased fields in an increased mw excitation frequency for the same EPR transition, which can be directly deduced from the resonance condition Eqn. 2.10. Here it is also noteworthy that among others $\hat{\mathcal{H}}_{\mathrm{HFS}}$ does not depend on $\mathbf{B}_0$ which is the reason that measurements at different mw frequencies may be used to elucidate the Spin Hamiltonian parameters more reliably.

The four HFS energy level transitions indicated in Fig. 2.1A results in numerous absorbed mw energy quanta. The quantity of absorbed energy scales roughly with the number of spins in the sample and possible saturation effects, which depend on the excitation state lifetime versus mw irradiation power and will be discussed later in Section 2.1.2. For Fig. 2.1B-G one can assume enough spins at non-vanishing and finite lifetime to ensure a good signal intensity and narrow line shape as displayed here.

Magnetic susceptibility for cw EPR One can imagine a cw EPR excitation to be a continuous irradiation in a (long) time interval Δt with mw energy E_{mw} and power $P_{\mathrm{mw}} = E_{\mathrm{mw}}/\Delta t$.[28] If the reflected mw power was measured in a suitable system as described in Section 2.1.3 and the magnetic field $\mathbf{B}_0$ was increased during that time Δt, a fraction of E_{mw} would be absorbed by the sample at any allowed EPR resonance field magnitude one after another. In general, the electron spin is closely connected to the magnetic susceptibility, describing that in an external magnetic field H a field B is induced. While in vacuum $B = \mu_0 H$, in matter

$$B = (1 + \chi_m)\,\mu_0 H \tag{2.14}$$

with magnetic susceptibility $\chi_{\mathrm{mag}} > 0$ for paramagnetic samples. At a given resonance field $\mathbf{B}_0$, the magnetic susceptibility of the sample changes. χ_{mag} can be described as a complex number translating mw absorption and dispersion (shift in frequency), χ'' and χ', respectively:

$$\chi_{\mathrm{mag}} = \chi' - i\chi'' \tag{2.15}$$

In EPR, the power P_{mw} absorbed by the sample is measured and as shown later in Eqn. 2.32 it is proportional to χ''. Therefore, plots showing qualitative cw EPR spectra are often scaled in arbitrary units of χ'' (or its field derivative, as explained later) with relative intensities as ordinate. Hence, the four absorptions of $^{63}\mathrm{Cu}^{2+}$ in Fig. 2.1A would result in four absorption lines of χ'' as shown in Fig. 2.1B. The distinctively colored background of Fig. 2.1B and G may remind the reader of the fact, that those first integral spectra are not common in cw EPR for reasons explained in Section 2.1.3 but a spectrum such as that in Fig. 2.1C is more likely to depict a common measurement.

Phenomenological explanation of anisotropy The right-hand side plots of Fig. 2.1 show the tensor properties of $\mathbf{g}$ and $\mathbf{A}$ and their angular dependence with respect to $\mathbf{B}_0$. For Fig. 2.1C, a species in a sample with collinear $\mathbf{g}$ and $\mathbf{A}$ tensors of $^{63}\mathrm{Cu}^{2+}$ with axial symmetry is shown such that the principal axis orientations of $\mathbf{g}$ and $\mathbf{A}$ form a 90° angle with $\mathbf{B}_0$. Consequently, $g_\perp$ and $A_\perp$ are the parameters that define the center field and line spread of the four lines, respectively. Fig. 2.1D represents the rotation of that very species by

$\Delta\theta = -90°$ around an axis perpendicular to the principal axis orientations of $\mathbf{g}$ and $\mathbf{A}$ and the direction of $\mathbf{B}_0$ such that $\mathbf{B}_0$ and the tensor principal axis orientations form an angle of 0° at the bottom end of Fig. 2.1D. Phenomenologically, one finds that for axial symmetry, the g factor follows the general form

$$g = \sqrt{g_{\|}^2 \cos^2\theta + g_{\perp}^2 \sin^2\theta}, \tag{2.16}$$

where $g_{\|} = g_{zz}$ is the principal axis value along $\mathbf{B}_0/B_0$ and for Cu^{2+} it is the largest g factor. The values for $g_{\perp}$, $g_{\|}$ as well as $A_{\perp}$, $A_{\|}$ and the principal axis orientations of the respective tensors can be found experimentally from such an angular dependency. Fig. 2.1E shows the spectrum of the same $^{63}\mathrm{Cu}^{2+}$ species such that the principal axis orientations of $\mathbf{g}$ and $\mathbf{A}$ are collinear and in parallel to $\mathbf{B}_0$. Hence, $g_{\|}$ and $A_{\|}$ can be found by the center field and distance of the four lines. The situation described for Fig. 2.1C–E can be found in solids with a single, oriented Cu^{2+} species, for example in single crystals.

Fig. 2.1F and G show the cw EPR spectrum and its first integral representation of a disordered system of infinitely many spins of $^{63}\mathrm{Cu}^{2+}$ with their principal axis orientations distributed over a unit sphere. This is the case for many species orientations, for example many crystals in a powder. If finitely many vectors are pointing from the center to the surface of a sphere such that the interception points with the surface have a uniform distance from each other, at maximum only a single vector can point directly along a chosen axis, say the z-axis. On the other hand, a comparably large number of spins is perpendicular to that axis and is distributed on the equatorial plane of that sphere with respect to the z-axis. Therefore, powder EPR absorption spectra of such a Cu^{2+} species feature a singularity in the high B field, perpendicular part of the spectrum with high intensity. Towards the low B field, parallel oriented region, the intensity profile decreases. This situation can be observed in Fig. 2.1G as well. Again, for reasons explained in Section 2.1.3, Fig. 2.1F is the first derivative of Fig. 2.1G, and the parallel and perpendicular properties of the $\mathbf{g}$ and $\mathbf{A}$ tensors are manifested as peaks in the respective B field regions. As an extra property of Cu^{2+} EPR spectra the resonance line at highest B field does not originate from the perpendicular orientation, but an extra powder edge singularity occurs for intermediate orientations. It is indicated by the dotted, blue line.

Further energy perturbations For Fig. 2.1 it was enough to take the Electron Zeeman interaction $\hat{\mathcal{H}}_{\mathrm{EZ}}$ and the HFS interaction $\hat{\mathcal{H}}_{\mathrm{HFS}}$. Eqn. 2.1 describes several more possible interactions that occur frequently in paramagnetic samples. The third term takes into account the interactions between electron spins and spin-orbit coupling if more than one unpaired electron ($S \geq 1$) or certain high spin ions in non-cubic symmetries are present.[35] It is responsible for lifting the $(2S+1)$ fold energy level degeneracy of $\hat{\mathcal{H}}_{\mathrm{EZ}}$ at $\mathbf{B}_0 = 0$ and is therefore called the zero field splitting (ZFS) of the fine structure (FS). The FS tensors' principal axis values are $D_{zz} = 3/2D$ and $\left(D_{xx} - D_{yy}\right)/2 = E$, where D and E are the ZFS parameters but for the cubic symmetry of the samples **2** and **3** reported about in this work $D = E = 0$. The FS is among others relevant in EPR of semiconductors.[11,36,37]

The fourth term in Eqn. 2.1,

$$\hat{\mathcal{H}}_{\mathrm{ex}} = -J\hat{\mathbf{S}}_1\hat{\mathbf{S}}_2, \tag{2.17}$$

describes the exchange interaction effects occurring whenever two orbitals of neighboring atoms overlap.

Then the electrons can be exchanged between these atoms and various couplings can occur, which may have a significant influence on the EPR spectrum. This topic will be discussed briefly in Section 2.1.5 and may play a role for example for two antiferromagnetically coupled Cu^{2+} with $S = \frac{1}{2}$, such that the total spin can result from antiparallel or parallel alignment, leading to $S = 0$, 1, respectively. The exchange coupling constant J denotes the energy difference between this singlet state $S = 0$ and the triplet state, and if $J = 0$, the spins are ideally diluted and behave completely independently from each other. Eqn. 2.17 is called the Heisenberg Hamiltonian after W. Heisenberg.[38]

The fifth, listed term in Eqn. 2.1 describes the nuclear Zeeman interaction of nuclear spins $I > 0$. Here, β_n is the nuclear magneton and g_n the nuclear g factor, which will be elaborated a little further in Eqn. 2.25. The sixth term in Eqn. 2.1 involves nuclear quadrupole interactions of nuclear spins with $I > 1/2$ in formal analogy to the electron-electron interaction of the third term. The latter term is not of primary interest for the paramagnetic samples discussed in this thesis and therefore not described in this context.

For all systems involving host-ligand interactions additional terms of the next nearest neighbored ligand nuclei can explicitly be considered. In contrast to the weak influence from the ligand nuclei, the interactions to the central nucleus are much stronger. Therefore, the HFS of ligand molecules with low spin density usually cannot be evaluated directly with cw EPR but require pulsed EPR methods.[39] This has not been applied to the chemical systems investigated for this thesis in this work and was therefore not observed in the single crystals, but earlier EPR studies on powder materials have dealt with these questions.[40] Also, the internuclear interactions within the host system or with ligands have not been observed, since they are again much weaker than all other interactions. They will therefore not be described in further detail and Chapter 4 will concentrate on the evaluation of $\hat{\mathcal{H}}_{\mathrm{EZ}}$ and $\hat{\mathcal{H}}_{\mathrm{HFS}}$ of the host Cu^{2+} metal centers in different lattice site environments and under the influence of various ligands. As mentioned in the beginning of this Subsection, it is however very important to consider the effect of the ligand field to the host system itself.

Ligand field interaction The influence of the crystal or ligand field perturbs $\hat{\mathcal{H}}_{\mathrm{EZ}}$ in second order:[9]

$$\mathcal{H} = \beta_e \left(\mathbf{L} + g_e \mathbf{S}\right) \mathbf{B}_0 \tag{2.18}$$

Here, $\mathbf{L}$ defines the influence by a neighboring ion quenching the $\mathbf{g}$ tensor of the studied system. As an example, it shall be treated for a simple atomic model with an unpaired electron in a p orbital and four ligands in the equatorial plane with respect to the z-axis. In Eqn. 2.22, this model is expanded to the d orbitals involved in Cu^{2+} systems. For now, the ligand coordinates are $L_{1,3} = (\pm x, 0, 0)$, $L_{2,4} = (0, \pm y, 0)$ with $x < y$. Since there are three p orbitals in total, one might chose p_x along L_1 and L_3, p_y along L_2 and L_4 and the lone electron to be in p_z. Then the ligand field from L_1 and L_3 on the x axis interacts electronically with possible electrons in the p_x orbitals by the Coulomb-interaction and p_y is influenced, likewise.[41] Due to the stronger ligand potential at the shorter inter-atomic distance to L_1 and L_3, more energy is required to move the electron from p_z to p_x than to p_y for a field $\mathbf{B}_0$ pointing along x or y, respectively. One can thus denote these energies by Δ_1 and $\Delta_2 < \Delta_1$ and show that the eigenvalues of the Hamiltonian in the basis of

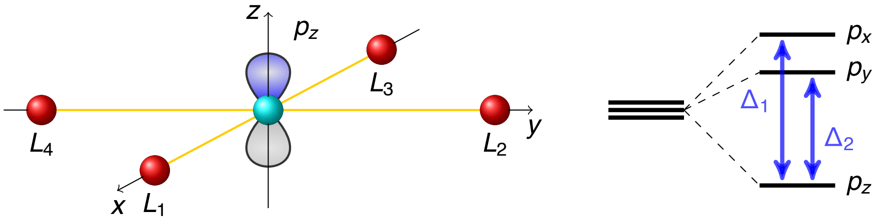

Fig. 2.2
Crystal field anisotropy: The crystal field from ligands $L_1 \cdots L_4$ shifts the energy levels for an unpaired electron in the p_z orbital of the central atom by Δ_1 and Δ_2.

the improved ground state wave functions result in energies[9]

$$W_x = \pm\frac{1}{2}\beta_e\left(g_e - \frac{\lambda}{\Delta_2}\right)B_0, \quad W_y = \pm\frac{1}{2}\beta_e\left(g_e - \frac{\lambda}{\Delta_1}\right)B_0, \tag{2.19}$$

with λ being the spin-orbit coupling constant. The situation is depicted in Fig. 2.2 and one can summarize the principal axis values of the **g** tensor from the energy difference ΔE_{ii} as

$$g_{xx} = g_e - \frac{\lambda}{\Delta_2}, \quad g_{yy} = g_e - \frac{\lambda}{\Delta_1}, \quad g_{zz} = g_e \tag{2.20}$$

for $\mathbf{B}_0$ along x, y and z. Clearly, the **g** tensor has thus become anisotropic, with the p_z orbital as ground state and the principal axis values are $g_{zz} > g_{yy} > g_{xx}$. Further it can be shown in general that for an arbitrary orientation of **g** along a unit vector (n_1, n_2, n_3) with respect to $\mathbf{B}_0$[9]

$$g\,(n_1, n_2, n_3) = \sqrt{n_1^2 g_{xx}^2 + n_2^2 g_{yy}^2 + n_3^2 g_{zz}^2}, \tag{2.21}$$

which has been introduced phenomenologically in Eqn. 2.16 and can be used to determine the influence of a ligand field on a paramagnetic center by its effective g value with respect to a reference value. This can be motivated as follows: when the field $\mathbf{B}_0$ points along x with the unpaired electron sitting mainly in p_z as initialized, the p_y and p_z orbitals are not degenerate. The spin-orbit coupling restores some orbital angular momentum into y by rotating the spin about x in the yz plane, with a strength depending on λ and Δ_2, implying that their ratio determines the deviation of g_{xx} from g_e. While a similar mechanism applies for $\mathbf{B}_0$ along y with Δ_1, only for $\mathbf{B}_0$ along z the rotation of the orbital does not transform it into one of the two other orbitals, leaving g_e unaltered.[9]

Finally, this theory can be expanded to the d orbitals involved in interactions with Cu^{2+}. This is done with great care in known textbooks like that from Atherton[9] and the result shall be given for the ^{63}Cu nucleus here,[9]

$$g_{xx} = g_{yy} = g_\perp = g_e + \frac{2\lambda}{\Delta_1}, \quad g_{zz} = g_e + \frac{8\lambda}{\Delta_2}. \tag{2.22}$$

The spin-orbit coupling constant λ for Cu^{2+} is 829/cm and the principal axis values of **g** are frequently found to yield values of $g_\perp = 2.045 \cdots 2.047$, $g_\parallel = 2.165 \cdots 2.349$ for Cu^{2+} in square-planar complexes and reaches up to $g_\perp = 2.13$, $g_\parallel = 2.44$ for strong tetragonal distortions.[9]

A last remark may concern the HFS interaction, because the principal axis orientations of the **A** tensor are dependent on the **g** tensor and the principal axis values can be calculated in a similar manner as for

Eqn. 2.22.[9] The energy differences for HFS transitions can be calculated as

$$\Delta W = g\beta_e B_0 + \sqrt{\frac{\mathbf{1gAAg1}}{\mathbf{1gg1}}} m_I \tag{2.23}$$

with $\mathbf{1} = \frac{\mathbf{B}_0}{B_0}$. From Eqn. 2.23 it can be deduced that information about the **A** tensor can only be obtained after learning the characteristics of the **g** tensor, which justifies the rule of determining **g** first to derive **A** for EPR. Now, for ^{63}Cu

$$A_\perp = T\left(\frac{2}{7} - \frac{11}{7}\frac{\lambda}{\Delta_2}\right), \quad A_\parallel = -T\left(\frac{4}{7} + 8\frac{\lambda}{\Delta_1} + \frac{6}{7}\frac{\lambda}{\Delta_2}\right), \tag{2.24}$$

$$T = \frac{\mu_0}{4\pi} 2\beta_e\beta_n g_n \left(^{63}\mathrm{Cu}\right) \langle r^{-3}\rangle \tag{2.25}$$

with $\langle r^{-3}\rangle = 8.455$ for ^{63}Cu as a distance measure of the effective nuclear charge and $g_n\left(^{63}\mathrm{Cu}\right) = 69.17$ is the g_n factor of the ^{63}Cu nucleus. The **g** value enters Eqn. 2.24 via the right-hand term inside the brackets.[9,42]

2.1.2 Temperature Dependence, Line Shapes and Line Broadenings

Ideally, EPR is performed in magnetically highly diluted paramagnetic spin systems to minimize mutual spin effects which otherwise can lead to non-deterministic spin behaviors and high linewidths because of the various dipole-dipole exchanges outlined in the following Section. A single mw absorption process such as the one described in the previous Section 2.1 however leads to a single EPR resonance line of non-existing width and diminutive intensity. Therefore, such infinitely diluted spins are not measurable and in practice rather large spin ensembles of approximately 10^{15}–10^{17} spins are measured frequently in current cw EPR spectrometers.[43] For these concentrations and given the imperfection which experimental conditions induce, various effects on the line shape and width are possible. Therefore, the observed cw EPR line is a statistical average over the ensemble of spins that fulfills a given resonance condition required by Eqn. 2.10 in a non-resolved field interval. This signal may emerge from the same kind of spins, which are in some way slightly differently excited, or from different spins, which either originate from different constituents of the same sample or which interact with their surroundings and therefore may find their individual environment altered slightly compared to other spins. Those interactions lead to a finite width of any cw EPR line and the effects responsible for the variations in excitation shall be introduced in the present Subsection to give an overview of the physics behind them.

The first mechanism to be explored is the spin-lattice relaxation time. An isolated magnetic dipole $\boldsymbol{\mu}$ with its component μ_z along $\mathbf{B}_0$ contributes as a vector summand to the net magnetization per unit volume $\mathbf{M}$ with M_z, respectively. The spin ensemble magnetization M_z follows a time dependence upon a sudden change of $\mathbf{B}_0$:[10]

$$M_z(t) = M_z^0\left(1 - \exp\frac{-t}{T_1}\right) \tag{2.26}$$

T_1 is the time required to raise M_z to a fraction of $\frac{1}{e}$ of its final magnetization value $M_z^0 = M_z(t \to \infty)$.

Despite denoting a time rather than a temperature here, the capital letter T is traditionally devoted to the original notation in F. Bloch's publication from 1946.[44] A change in M_z is connected to a change in m_S which must be either induced by the mw energy absorption of magnitude $h\nu$ or an interaction with the environment of the spin. T_1 characterizes this spin-lattice interaction and is hence called the spin-lattice relaxation time. It is also the inverse of the sum of those transition probabilities $P_{\alpha\beta}$ and $P_{\beta\alpha}$ which characterize the transition between the populations of the two energy levels given by $\hat{\mathcal{H}}_{\mathrm{EZ}}$ (Eqn. 2.9). These energy levels can be denoted by N_α and N_β for the upper and lower levels ($m_S\,(\alpha) = +\frac{1}{2}$, $m_S\,(\beta) = -\frac{1}{2}$). It is assumed that the spins are in some way coupled to the sample bulk or lattice. In a thermodynamic equilibrium of temperature T, the distribution among the two levels is given by Boltzmann distribution:[10]

$$\frac{N_\alpha}{N_\beta} = \exp\frac{-\left(W_\alpha - W_\beta\right)}{k_B T} = \exp\frac{-g\beta_e B_0}{k_B T} \tag{2.27}$$

From its defined nature as probability, T_1 is a distinctive parameter for the mean lifetime of a spin in the respective population level, and the Heisenberg uncertainty relation for energy and time,[45]

$$\Delta W \Delta t \geq \frac{h}{2\pi}, \tag{2.28}$$

leads to a first conclusion for the linewidth of an EPR line:[10] If T_1 is an estimate of Δt, T_1 scales inversely proportional to ΔW. In this regard, a small value of T_1 leads to a great variation in energy W and thus a broad, smeared-out EPR line. This mechanism applies especially for transition metal ions. In principle, linewidths in EPR may vary from a few μT to several hundreds of mT.

In this Subsection, the dash ($'$) will now denote a first field derivative instead of the real part of a complex number and the absorption χ'' will simply be denoted as χ, because the dispersion might be neglected in this Section. As stated previously in Section 2.1.1, the typical cw EPR line is presented in the form of a first derivative (now denoted by $\mathrm{d}\chi/\mathrm{d}B := \chi'$) of a full absorption curve, as with the four lines depicted in Fig. 2.1B (which will now be denoted by χ) for reasons explained in Section 2.1.3. It is often desired to know the relative intensities of EPR lines to estimate quantitative, yet relative, spin numbers. The most accurate procedure to do so involves a double integration of the latter first order derivative,[10]

$$I_{\mathrm{DI}} = \iint\limits_{B_1<B_{\mathrm{res}}}^{B_2>B_{\mathrm{res}}} \chi' \mathrm{d}B\mathrm{d}B = \int\limits_{B_1<B_{\mathrm{res}}}^{B_2>B_{\mathrm{res}}} \chi \mathrm{d}B \quad \text{for } B_2 - B_1 \gtrsim 10\Gamma, \tag{2.29}$$

where the desired integration interval 10Γ is normalized to a width property of the curve explained below and as shown in Fig. 2.3.

EPR lines can very often be described as Gauss or Lorentz functions. It is also possible to have a mixture of both, a Voigtian line. Fig. 2.3 shows the typical parameters of a cw EPR line of a simple $\hat{\mathcal{H}}_{\mathrm{EZ}}$ system with $S = \frac{1}{2}$ and Gaussian shape, listing its important characteristics such as the half width at half height (HWHH) 2Γ, peak-to-peak linewidth ΔB_{pp}, peak amplitude χ_{max} and first derivative peak amplitude χ'_{max}. A Gaussian curve ($\Delta B_{pp} = \sqrt{\frac{2}{\ln 2}}\Gamma$) occurs mostly for inhomogeneous line broadening effects and is much

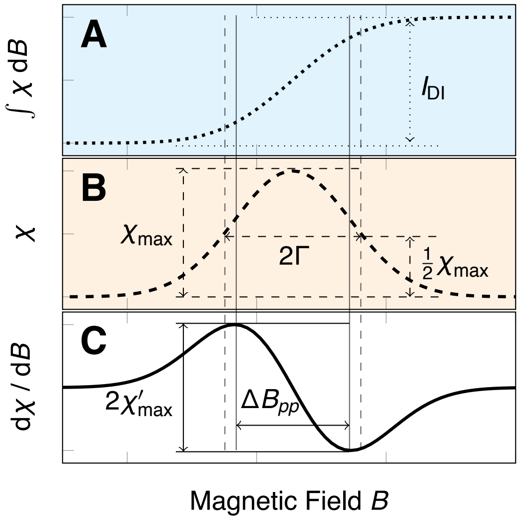

Fig. 2.3 EPR line shape and derivatives: $S = \frac{1}{2}$ cw EPR line, from top to bottom:
(A) integrated absorption line $\int \chi \mathrm{d}B$ for determination of double integrated first order derivative intensity I_{DI},
(B) full absorption curve (usually denoted by χ'') determining HWHH parameter Γ. Gaussian line shape shown here,
(C) first order derivative absorption curve $\mathrm{d}\chi/\mathrm{d}B = \chi'$ (usually $\mathrm{d}\chi''/\mathrm{d}B$) with indicated peak-to-peak linewidth ΔB_{pp} and peak-to-peak intensity $\chi'_{\max}$.

broader than the slim Lorentzian ($\Delta B_{pp} = \sqrt{\frac{4}{3}}\Gamma$), which occurs mostly for homogeneous line broadening effects.[10]

Inhomogeneous line broadenings occur if the unpaired electrons are subjected to slightly different magnetic fields and the sweeping field matches all resonance conditions for the spin packets slightly shifted with respect to each other. Then the resultant line is a superposition of many lines and results in a Gaussian distribution. This happens for inhomogeneous $\mathbf{B}_0$ fields, but also for randomly oriented systems in the solid state like the anisotropic $\mathbf{g}$ and HFS interactions presented in Section 2.1.1.[10] The physical origin for anisotropic broadenings is called a strain and describes a distribution in a Spin Hamiltonian parameter due to small structural variations among the paramagnetic centers in the sample.[42] In this way, a $\mathbf{g}$ strain describes a distribution of the principal axis values of the $\mathbf{g}$ tensor. Inhomogeneous broadening may also occur for unresolved HFS, where a multitude of lines merges into an observed envelope instead of resolved HFS lines.

For homogeneous line broadenings, the resultant line is Lorentzian, because the instantaneous magnetic field at each spin is not equivalent although the time average is, contrary to the inhomogeneous line broadening. Since the linewidth is greater than expected from T_1, an additional T_2 summarizes other relaxation effects such as the electron spin–electron spin dipolar, and exchange interactions. In all solids, undiluted spins interact by the magnetic field exerted by the precession of their magnetic moment to another spin in distance r inversely proportional to $1/r^3$. Other broadening effects may be found mainly in free radicals, such as the electron spin exchange, which is often dependent on the local concentration of spins.[10]

Chemical line broadenings can occur if the chemical environment of spins is altered. Further broadenings can give valuable information about molecular dynamics and tumbling in liquid EPR spectra. These experiment may influence the line shape as well: microwave power plays a role in the saturation of signals, which could lead to a suppression of resonance lines in cases of homogeneous or inhomogeneous saturation.[46]

2.1.3 Continuous Wave EPR Instrumentation

In the introduction, it was mentioned that magnetic resonance shares similarities to general absorption spectroscopy. This perspective, however, is limited to the basic principles of atomic physics and does not apply very much for the technical aspects. While primitive optical devices date back to our predecessors in the cradles of civilization, application in terms of modern physics occurred in the 17th century when, for example, the finding by W. van Roijen Snell allowed for a simple characterization of matter by its refractive index.[47] The basic technical tools for magnetic resonance spectroscopy, however, did not have their advent until the militarily-driven developments from the two world wars, alongside the theory on quantum physic which was established at about the same time. NMR and early implementations of EPR relied on RF electromagnetic radiation theoretically predicted by J. C. Maxwell in 1867 and realized and investigated first in 1887 by H. Hertz.[48,49]

Spin resonance spectroscopy has always benefited from developments in other fields such as radio communication, material sciences and of course magnetism. Practically, modern EPR has been made possible by the invention of non-visible electromagnetic wave emitting–vacuum tubes in 1937 by the American brothers R. and S. Varian,[50] which due to war times was needed for radar. For EPR, well known techniques have been employed since its discovery, yet sensitivity did not reach a sufficient level at first. The major technical difference between NMR and EPR is the usage of microwaves in EPR to access the different energy levels of electrons. Microwave technique was developed later, and faced several difficulties such as those concerning losses in materials (penetration depth) and the transmission abilities in wave guides and transmitters. Additionally, resonant circuits cannot generally be realized with discrete electronic devices such as capacitors and coils, as other types of resonators are needed. The benefits of EPR, however, include smaller, and thus cheaper, magnetic fields at a higher sensitivity per spin density at a given, experimental temperature. Additionally, the simpler cw method is still widely in use, while the pulse techniques made cw NMR obsolete decades ago.[28] Although microwave generation and detection devices as well as data recorders have changed during the past century, the principle techniques which were used by Zavoisky in 1946 can still be identified in contemporary spectrometers. In this Subsection, the special devices and operational principles of cw EPR spectrometers shall be presented.

Microwave generation Microwaves can be described mathematically by Maxwell's equations and classified by means of their propagation into so-called modes. An electromagnetic wave oscillates in free space with alternating electric ($\mathbf{E}_1$) and magnetic field magnitude ($\mathbf{B}_1$). Near a conducting wall, a reflected, standing wave polarized in x-direction can be expressed with the following, simple non-trivial form as complex quantity:[51]

$$E_x = -2iE \sin kz \mathrm{e}^{i\omega t}, \quad B_y = \mu_0 \frac{2E}{Z_0} \cos kz \mathrm{e}^{i\omega t}, \tag{2.30}$$

where $E(z) = 0$ is a boundary condition at the (conducting) wall and $Z_0 = \sqrt{\mu/\varepsilon}$ is the characteristic impedance of the medium. Here, the electromagnetic field has the form of a standing wave in front of the wall with respect to the z-direction and the form of a travelling wave in the x-direction. Hence, this propagation can be described with an oscillating propagation factor $e^{(i\omega t-kz)}$ with the wave number k. At every instance of time and in space each wave must fulfill all of Maxwell's equations. Two of these equations are

$$\nabla\times\mathbf{E}=-\frac{\partial\mathbf{B}}{\partial t},\quad \frac{1}{\mu_0}\nabla\times\mathbf{B}=\mathbf{J}+\varepsilon_0\frac{\partial\mathbf{E}}{\partial t} \tag{2.31}$$

with $\vec{J}=0$ in the interior of a microwave transmission line. Expressed in Cartesian components, the latter equations can be reduced to represent the three possible wave configurations inside a wave guide:[28] the transverse electromagnetic wave (TEM) with components $H_z=E_z=0$, the transverse electric wave (TE, $E_z=0$, $H_z\neq 0$) and the transverse magnetic wave (TM $H_z=0$, $E_z\neq 0$). A TEM mode is usually found in coaxial cables while hollow wave guides carry TE and TM modes. In this Subsection, the notion of these mw modes is employed in various descriptions of the devices used for this work.

The initial point of an mw network is a source for high frequency radiation. Especially in EPR, the mw source and detector are often limited to a very narrow band of emission and detection. Historically, microwave detectors did not allow a large frequency range detection and still do not in general as of today; high quality resonators implied an inflexible design and flexible microwave sources were hard to achieve.[46] Although later Fabry-Perót-interferometers could be used as highly tunable, high quality resonators[52] and quite universally sweepable microwave sources emerged,[53–56] the principle EPR set-up of many modern spectrometers still reflects that legacy. For economic reasons, the parts of the spectrometers dealing with the high frequent electromagnetic waves of the experiment are still operated from a small range of frequencies, although frequency variable devices were described by W. Urban in 1975.[57]

In practice, the choice of the mw frequency is limited by considerations of energy absorption and losses in the mw transmission network and the absorption minima of air define the preferred microwave frequencies for EPR spectrometers. From the origin of EPR technology, radar, these frequencies met the available mw sources' typical specifications and thus, powerful mw bridges could be used after optimizing them in terms of frequency stability and noise suppression. For this reason, in cw EPR X-band spectrometers are still among the most used in the applied spectroscopy and principally large powers can be generated given the radar history. The mw power, given by the Poynting vector,[28] $P_{\mathrm{mw}}=\frac{1}{2}\mathrm{Re}\left(\mathbf{E}_1\times\mathbf{B}_1^*\right)\propto B_1^2$ is delivered with an attenuation of the mw network to the sample, which absorbs it with the magnitude

$$P_{\mathrm{abs}}=\pi\mu_0^2\nu_{\mathrm{mw}}B_1^2\chi, \tag{2.32}$$

where χ is again the magnetic susceptibility from Eqn. 2.15. However, as saturation effects and sample heating issues often limit the B_1 field magnitudes, P_{mw} is limited to only a fraction of what could be produced by the radar mw sources they were derived from.

For EPR, the most frequently used mw sources were klystrons, which nowadays have been replaced by microwave diodes. The latter use the same principle as the klystron or the even more basic drift tubes (also denoted as space-charge-wave or velocity-modulated tube due to their operating mode): charge carriers (electrons or holes) traverse a certain distance within a time with their drift velocity, here inside a semiconductor. Two major types are of importance: impact ionization by avalanche effects and transit time (IMPATT-diode) and diodes using the Gunn effect.[58,59] IMPATT-diodes may be used for very large output powers but provide a broad spectrum due to the avalanche effect. The Gunn effect was first observed in GaAs semiconductors. Under certain conditions of large external electric fields the drift velocity of electrons can me modified such that charge carriers bunch. The bunching domain drifts through the diode and is converted at the electrodes to a current and field pulse. As in a space-charge-wave tube or the reflector-gap-combination of the klystron the runtime of these bunched regions sets the frequency of the emerging wave. In semiconductors, the drift area can be very small by proper spatially doping such that much higher frequencies than in conventional tubes can be achieved.

Power induced signal saturation Typically, cw EPR experiments are operated with powers from nW to 200 mW. Pulse experiments may be performed with very high powers ($\approx$ 1 kW). The mw power has a crucial effect on the SNR, as the magnitude of the mw $\mathbf{B}_1$ increases the signal linearly and leads to an SNR increase by the square root of the mw power. To achieve comparable results in a quantitative EPR measurement avoiding changes in the line shape the excitation must be performed with the same incident mw power at the sample, leading to ideally comparable signals proportional to the susceptibility given in Eqn. 2.32. Generally, it is not desirable to expose the sample to very high microwave powers under continuous irradiation due to heating and saturation effects.

Paramagnetic samples experiencing identical local magnetic field domains of $\mathbf{B}_0$ are assumed to be in a thermal equilibrium with the incident mw power. This means the spin polarization spreads over all spins fast enough and the line shape of the cw EPR signal is Lorentzian. A measure for the description of the perturbation of the thermal equilibrium is the time T_t which describes the time that the spins need to spread the energy until $1 - \frac{1}{e}$ of the spins are excited. If σ is a parameter which relates the relaxation time T_1 from Eqn. 2.26 to T_t by

$$\sigma = \frac{T_1}{T_t}, \tag{2.33}$$

then for $\sigma > 1$ the higher energy levels are not populated fast enough and the system is out of the Boltzmann equilibrium (Eqn. 2.27), while the latter holds for $\sigma \ll 1$ and[46]

$$\sigma \propto \frac{1}{4} B_1^2 T_1 T_2, \tag{2.34}$$

such that σ is dependent on the two relaxation times and the mw magnetic field. The intensity of the absorption signal is proportional to

$$I \propto \frac{B_1 T_2}{1 + \sigma\left(B_1\right)}. \tag{2.35}$$

This is the saturation dependence of a homogeneously broadened resonance line. For them, a maximum signal intensity is reached for $\sigma\left(B_1\right) \equiv 1$, however in practice measurements are not conducted at the largest possible mw field B_1 as the linewidth depending on $\Delta f = \frac{1}{T_2}\sqrt{1 + \sigma\left(B_1\right)}$ has increased by a factor of $\sqrt{2}$ there already. For even larger mw powers the intensity drops again.[46,60] This maximum of a specific, homogeneously saturating specimen can be used to identify the conversion factor of a certain microwave network whenever mw power is delivered to an EPR measurement. The practical application of this principle is outlined in Section B.2 in the Appendix.

Waveguides, microwave $\mathbf{B}_1$ fields in resonators and signal detection An actual microwave network further consists of the mw waveguides and in EPR different types can be found: first, conventional, mostly rectangular, waveguides are traditionally used to guide microwaves. These waveguides are typically not flexible but cheap to manufacture and can withstand both strong mechanical as well as mw power related influences. Their dimensions also resemble the transmittable frequencies to some extent as shown later for cavity resonators in Eqn. 2.37, such that a given waveguide cross section gives rise to a high-pass, cutoff frequency ν_c and only waves with $\nu_\mathrm{mw} \geq \nu_\mathrm{c}$ can propagate.[28] Second, dielectric waveguides are used widely today as well, such as coaxial waveguides and strip line structures. They mostly differ by the transmitted wave mode and in application area. All types of waveguides can be optimized for certain mw frequencies and characteristic damping profiles.[28] The efficient delivery of microwaves through the various waveguides in a mw network used to transport, compare and convert mw power is ensured by impedance matched waveguide converters.

In magnetic resonance the electromagnetic mw field is guided in such a way towards the sample, that the latter is mostly irradiated by $\mathbf{B}_1$ instead of losing energy to electric dipoles in the sample via the $\mathbf{E}_1$ field. With a few exceptions, most of the EPR spectrometers employ a resonator of some kind to join mw energy and sample and collect and enhance the emerging signal,[61,62] which helps to decrease noise by reducing mw dissipation and unwanted external excitation of the sample and avoid stray fields. For RF frequencies, resonant circuits are known to consist of coils and capacitors, which are nowadays used in NMR to house the sample and tune the resonator system with respect to the RF network, respectively. For microwaves, this lumped element model does not translate directly into reality as screening length and power issues usually prevent microwaves from being able to travel through wires and electronic devices. Instead, the previously mentioned waveguides are used and hence, modified waveguides are promising candidates for mw resonators.

Cavity resonators represent the simplest, classical resonator type. Like a piece of a waveguide, cavity resonators can hold TEmnp and TMmnp-modes, where m, n and p denote the number of half wavelengths fitting into the space spanned by the resonators walls. Hence, the cavity has a dimension in x-direction of $a = m/2$ in units of the wavelengths. Then the wave number in x-direction

$$k_x = \frac{m\pi}{a} \tag{2.36}$$

and in general, with the resonance frequency $\nu_\mathrm{mw,0} = \frac{\omega_0}{2\pi}$ the wave vector k of a mode with mnp half-wavelengths is given by[28]

$$k = \omega_0\sqrt{\mu\varepsilon} = \frac{2\pi\nu_\mathrm{mw}}{c} = \pi\sqrt{\frac{m^2}{a^2} + \frac{n^2}{b^2} + \frac{p^2}{d^2}} \tag{2.37}$$

with c being the velocity of light. From Maxwell's Eqn. 2.30 in combination with Eqn. 2.36–2.37 one can find the field distributions inside a cavity and calculate the resonant frequency for each possible mode. In

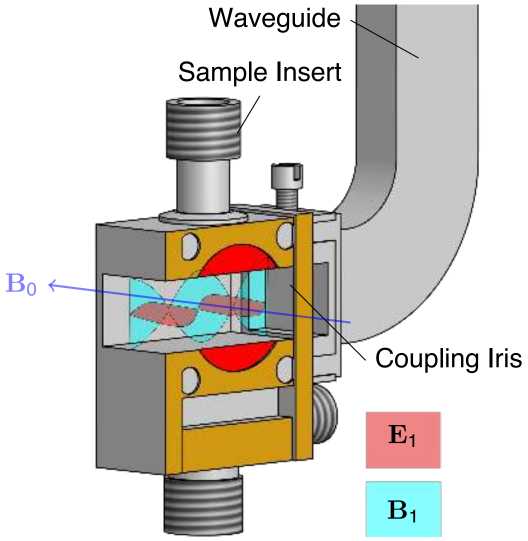

Fig. 2.4 Cavity resonator, mw field distribution: A typical rectangular TE102 cavity resonator with sketched normal magnetic $\mathbf{B}_1 \perp \mathbf{B}_0$ and electric $\mathbf{E}_1$ mw field planes.

practice one can find dimensions for hollow waveguides and cavity resonators, that separate adjacent modes in the desired frequency range maximally such that the energy exciting a cavity can be focused maximally to a small bandwidth. In rectangular waveguides, the TE102 mode is the most dominant one, giving rise to a maximum in the magnetic field in the center of the cavity and ideally to no electric field there, which is shown in Fig. 2.4. There, a typical, rectangular cavity resonator is depicted, but other cavity resonators, such as cylindrical cavities exist as well. In Sections 2.2 and 2.3, other types of resonators will be introduced, which are closely related to the other, dielectric type of waveguides mentioned above. They all share the principal condition to align $\mathbf{B}_1 \perp \mathbf{B}_0$ (Eqn. 2.12), unless forbidden transitions shall be excited on purpose.

A resonator is designed to store and dissipate energy but does not guide the wave. The dimensions of a resonator are chosen such that a standing wave is enhanced in the resonator and its most outstanding characteristic is its ability to continuously reflect the mw power at its walls. The quality factor Q is the characteristic parameter for a resonator system with confinement walls fulfilling Maxwell's Eqn. 2.30. It gives a measure of the mw energy dissipation per cycle:

$$Q := \frac{2\pi \cdot \text{Stored Energy}}{\text{Energy Dissipation per Cycle}} \tag{2.38}$$

Additionally, the entire mw system can have ohmic losses, a (dielectric) sample holder and a paramagnetic sample in it. Then the loaded Q_L can be computed from the reciprocal sums of the individual qualities:

$$\frac{1}{Q_L} = \frac{1}{Q_{\text{walls}}} + \frac{1}{Q_{\text{dielectric}}} + \dots \tag{2.39}$$

By $Q_{\text{dielectric}}$ the quality of the medium inside the resonator walls is denoted. In resonance, per Eqn. 2.10 the magnetic susceptibility of the sample changes and it absorbs a fraction of the stored energy of the resonator with the rate as described in Eqn. 2.32. This change in the overall Q is the primarily detected quantity in cw

EPR.

The reflected signal is detected, which has been the task of diodes since the 1960's. Previously and for some special applications today, the heating effect of microwave was used in bolometers, calorimeters and thermistors.[46] First, Schottky diodes (metal pins pointing onto a silicon semiconductor surface) were employed, while later the tunnel effect (backward-diodes) and so-called hot-carrier diodes were used. In principle, signal detection works based on the fact that a diode barrier with a certain barrier capacity and resistance absorbs microwave power which changes a current through the diode. This current can be measured and because voltage across the barrier mostly depends on the incident mw power but not on the frequency which might change upon dispersion at resonance, the effective detector voltage depends on the mw frequency ν_{mw}. Hence, the mw power absorbed by the barrier can be deduced.[46]

As introduced in the beginning of this Subsection, klystrons and most modern diodes can be modified in frequency only by a few percentage points with the help of additional resonators and different excitation RF fields which allow for modern spectrometers to cover about 1 GHz of frequency range and to adapt to different resonators with fixed frequency and different dielectric insets (such as samples and cryostats). Since cw EPR is most cost-effectively performed with fixed-frequency resonators, it is the static $\mathbf{B}_0$ field which is swept most often to scan through the resonance condition Eqn. 2.10.

External static $\mathbf{B}_0$ field and modulation For the most commonly used mw frequencies between 2 GHz (S-band) and 35 GHz (Q-band), the static magnetic fields are reasonably low and can be reached by conventional resistive magnets with sufficient sweeping abilities and field resolution as well as reasonable power and cooling agent consumption compared to superconducting magnets applied from W-band frequencies onward. Most higher frequencies can be accessed with superconducting magnets well known from NMR, although resistive magnets are better suited for cw techniques with fixed mw frequency than superconducting magnets, which cannot be altered in their magnetic field strength as quickly and easily.

The absolute signal changes of the absorbed mw power are very small compared to the mw output power. Hence, a DC-based detection would have to be very sensitive. For this reason, all modern homodyne cw EPR spectrometers are equipped with modulation coils, which manipulate the static magnetic field in time and produce an AC outcome.[28]

This method combines both a higher detection sensitivity and high stability of the measurement. While a DC detector would have to cover a large range of absolute power levels with equal accuracy, lock-in modulated measurements are only sensitive to changes of the absorption signal. This allows the detector to be narrow-banded and suppress all other signals besides those from the desired frequency. Fig. 2.5 illustrates the working principle behind the modulation of the static magnetic field. A time dependent modulation field $B_{\mathrm{mod}}\,(t)$ interferes with quasi-static $\mathbf{B}_0$, such that the total field at the macroscopic sample position becomes within an infinite time step[46]

$$B_{\mathrm{sample}} = B_0 + \frac{1}{2} B_{\mathrm{mod}} \cdot \cos\left(\omega_{\mathrm{mod}} t\right), \tag{2.40}$$

neglecting field inhomogeneities from the resonator and local field distortion effects inside the sample.

The modulation coils are placed either outside the resonator with the possible cryostat right next to the main

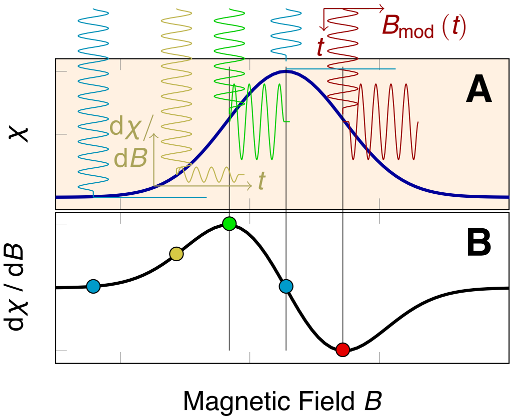

Fig. 2.5 Magnetic field modulation: Illustration of the modulation principle on EPR absorption spectra:
(A) B_0 is altered in time by $B_{\mathrm{mod}}\,(t)$, thus the DC microwave absorption signal χ is detected as AC signal $\mathrm{d}\chi/\mathrm{d}B\,(t)$.
(B) The resulting signal is the phase sensitive amplitude $\propto \frac{\mathrm{d}\chi}{\mathrm{d}B}$ and has under ideal circumstances the shape of the first field derivative of the EPR absorption signal as is commonly referred to.

Helmholtz-coils or directly around the resonator. The coils are powered by a modulation generator supplying a constant but arbitrary RF current with frequencies of about 10 ⋯ 100 kHz and detected by a narrow-band mw diode. The diode's signal is amplified and lock-in coupled to a rectifier, such that the modulation phase can be changed relative to the incident RF phase. This is important as the field derivative must be detected with the correct sign to distinguish the indicated third (green) and last (red) point in Fig. 2.5. Calibrations of the modulation magnitude are required to produce reliable and reproducible spectra. The mathematical formulation shows the significant disadvantage of this method by expressing the time dependent AC signal $\frac{\mathrm{d}\chi}{\mathrm{d}B} := A\,(t)$ at an instantaneous, modulated field (Eqn. 2.40) as Taylor series

$$\begin{aligned}\frac{\mathrm{d}\chi}{\mathrm{d}B} := A(B_0,t) = &\left[A(B_0) + \frac{1}{4}A''(B_0)\cdot B_{\mathrm{mod}}^2 + \ldots\right] + \\ &+\left[A'(B_0)B_{\mathrm{mod}} + \frac{1}{8}A'''(B_0)\cdot B_{\mathrm{mod}}^3 + \ldots\right]\cdot\cos\left(\omega_{\mathrm{mod}}t\right) + \\ &+\left[\frac{1}{4}A''(B_0)B_{\mathrm{mod}}^2 + \frac{1}{96}A^{(4)}(B_0)\cdot B_{\mathrm{mod}}^4 + \ldots\right]\cdot\cos\left(2\omega_{\mathrm{mod}}t\right) + \ldots,\end{aligned} \tag{2.41}$$

in which the first terms are Taylor series in B_0 themselves giving rise to the respective notation of the EPR absorption signal emphasized repeatedly in the previous Subsection. As long as the modulation magnitude B_{mod} is small, $A(t)$ is proportional to the n-th derivative of the DC signal $A\,(B_0)$. Indeed, it can be useful to record higher derivatives as it increases the resolution but decreases sensitivity. If now B_{mod} increases, higher derivatives become part of the detected signal and very high modulation magnitudes will cause the signal to decrease. Therefore, the modulation magnitude must be chosen depending on the sample according to the goal of maximizing the AC signal without distorting or smoothening it too much. This process is practically an empirical one, but in good approximation the following estimation holds:[46]

$$B_{\mathrm{mod}} = \frac{\Delta B}{2}\cdots 2\Delta B, \tag{2.42}$$

where ΔB is the linewidth of the smallest signal which shall be recorded. In this work, modulation coils have been customized regarding the latter guideline.

2.1.4 Sensitivity in EPR

An important task in the development of spectroscopic methods has always been the improvement of sensitivity. It is of general scientific interest to investigate very small or thin samples or specimen, which contain the actual probe particles in a very small concentration and still get a sufficient signal with respect to other contributions to the spectrum. Also, magnetic resonance techniques have addressed this issue ever since their development. While NMR is one of the least sensitive spectroscopies, as the population difference of nuclear energy levels is in its nature very small, it has recently made remarkable advances even for the challenging measurement conditions of high pressures.[63] In contrast to NMR, EPR can take advantage of the significantly better spin population and its considerably lower typical magnetic fields, turning it into an assistant for nuclear polarization in the dynamic nuclear polarization (DNP) spectroscopy.[64] Eventually, the parameter estimating the sensitivity is the signal-to-noise ratio (SNR),

$$\mathrm{SNR} = \frac{I_{\mathrm{signal}}}{I_{\mathrm{noise}}} = \frac{\langle P_{\mathrm{signal}} \rangle}{\langle P_{\mathrm{noise}} \rangle}, \tag{2.43}$$

relating the signal intensity, I (cf. Eqn. 2.29, expressed by the signal power ideally proportional to the susceptibility χ, Eqn. 2.32), to the signal generated by noise. Here, the so called white noise of special interest, which will be described in the following as indeterminable signal channel oscillations around zero which do not originate from other, competing species, gives rise to signals with equal resonance conditions. In practice, the SNR can be measured to rate the efficiency of a new spectroscopic technique or evaluated by finite-element simulations.[65,66] In this work, comparative measurements will be used to elucidate the efficiency of the later employed spectroscopic techniques.

Without taking losses into account, the absorbed power P given in Eqn. 2.32 is proportional to the amount of energy, that is dissipated in the resonator due to the sample in magnetic resonance. Regarding this power in Eqn. 2.43 two principal possibilities are given to increase the SNR. Either, the signal is enhanced without increasing the noise or the noise is decreased without limiting the signal. Noise that originates from the microwave bridge and noise from the detector and the amplifiers must be regarded as given in the context of this thesis as conventional spectrometers are employed as a basis for all measurements. Overall, the noise can be estimated as loss power by

$$P_L = k_B T \Delta\nu, \tag{2.44}$$

where $\Delta\nu$ is related to the bandwidth of acquisition.

Consequently, it is worth it to investigate the possibilities of increasing the signal intensity. Here, the following points are of interest: the magnetic field $\mathbf{B}_0$ and mw frequency ν_{mw} joined in the resonance condition Eqn. 2.10 correspond on the one hand directly to the spectral resolution as shown above. The most thrilling developments here have been achieved for high-frequency EPR, such as W-band spectroscopy or even beyond as of today.[61,67] Apart from increasing strain effects in high fields, the aim of this work is the promotion of sensitivity increasing techniques for X-band EPR spectroscopy such that high frequencies are not competitive within this study. Furthermore, the mw power leading to major improvements in pulse EPR techniques and generally increasing the signal intensity as seen in Eqn. 2.32 shall be left out, as the relevant information about the investigated samples has been acquired by cw EPR. Whenever temperature can be modified without harming the sample, the pure temperature induced spin polarization as given in Eqn. 2.27 increases the signal as it can reach almost unity for sufficiently low temperatures, which are feasible in solid state EPR. Cooling the sample might also lead to a cooling of the resonator and thus may change the mw properties as discussed in Section 2.2 or coupling and matching abilities to the microwave network relevant for some recent developments as shown in Section 2.3. Also, an increase of the signals from impurities in the resonator or cryostat may play a significant role, which disqualifies the temperature from being a promising parameter for increasing the signal intensity unconventionally. Lastly, the already treated modulation frequency and amplitude are ruled out as optimizers for their line shape disturbing properties. The only easy method to improve the SNR is to increase the number n of accumulations then, which increases the SNR by a factor of $\sqrt{n}$. Finally, there are two parameters which can be tremendously influenced by the type of resonators employed without changing the spectrometer basis significantly. Tuning those resonator properties is a way out of the above dilemma:

Filling factor As described before in Section 2.1.3, in EPR a sample is placed in a resonator to detect changes in the absorbed mw power. The mw energy density w and with it the mw power (B_1^2) needs to be high near the sample and it is obvious that parts of the microwave that do not penetrate the sample cannot contribute to the signal. Consequently, one can define a filling factor η as

$$\eta = \int_{\text{sample}} B^2_{\text{mw},\perp} \mathrm{d}V \Big/ \int_{\text{cavity}} B^2_{\text{mw}} \mathrm{d}V = \frac{V_s \langle B^2_{\text{mw}} \rangle_s}{V_c \langle B^2_{\text{mw}} \rangle_c}, \tag{2.45}$$

where the last step is valid provided the cavity is placed such that $\mathbf{B}_1 \perp \mathbf{B}_0$. It is useful to express the filling factor, that enters the SNR linearly for some special cases of interest. The integration for a point sample in the middle of a rectangular cavity works straightforwardly by analyzing the sinusoidal field distribution in the cavity and is given in large detail in standard textbooks,[28] next to a powder of these crystals in a filled EPR tube with radius r in the same cavity yielding

$$\eta_{\text{point}} = 2\frac{V_{\text{sample}}}{V_{\text{cavity}}}, \quad \eta_{\text{tube}} = \frac{V_{\text{sample}}}{V_{\text{cavity}}}. \tag{2.46}$$

Considering that a small volume point-like probe is much smaller than an entirely filled sample tube, the factor 2 due to the better mw field coverage between η_{point} and η_{tube} does not play a role and such a signal may give rise to several orders of magnitudes lower absorbed mw power. Therefore, it makes sense to increase the filling factor dramatically by shrinking the cavity size and reducing the resonator basically to the size of the sample. Two possible approaches for this consideration are given in Section 2.2 and Section 2.3.

Quality factor The second important parameter is the previously defined quality factor Q from Eqn. 2.38. To relate η and Q to the SNR Eqn. 2.32 can be used, showing that it is possible to define the signal to be a change in this power, ΔP. This difference with respect to the total detected power P can be phenomenologically explained with a change in Q, which in turn means the resonator dissipates a different amount of power per cycle. This fraction is approximately[28]

$$\frac{\Delta P}{P} \approx \frac{\Delta Q}{Q} = 4\pi\chi\eta Q \tag{2.47}$$

and using Eqn. 2.44 the SNR can finally be concluded as

$$\mathrm{SNR} \approx \frac{\Delta P}{P_L} \propto \frac{\eta Q \chi \sqrt{P}}{8\sqrt{k_B T \Delta \nu}}, \tag{2.48}$$

which is a linear expression in B_1, meaning it is proportional to the square root of the incident mw power.

Finally, the minimal number of detectable spins may well serve as a definition for the overall spin sensitivity.[68] This quantity is dependent on the linewidth ΔB_{pp} of the detected cw EPR resonance line and the frequency bandwidth Δf of the detection system and recorded for a standardized time constant of 1 s,

$$\min\left(\frac{N}{B}\right) = \frac{nV}{\mathrm{SNR}\sqrt{\Delta f}\Delta B_{pp}}, \tag{2.49}$$

where the number of spins $N = nV$ refers to the sample used in the experiment with the respective observation of its cw EPR signal with a certain SNR.

2.1.5 Beyond Paramagnetism – Antiferromagnetism and Ferromagnetism

This last Subsection of the basic introduction in the theoretical and technical background of EPR spectroscopy shall be devoted to the magnetic susceptibility, which is revisited to broaden the view on the occurring physical phenomena in magnetic resonance. In Eqn. 2.14 no special assumptions about the magnetic susceptibility χ_{mag} (or later χ) have been made apart from it being strictly larger than zero. At this point, some more precise options shall be presented. In general, substances with χ can be called

$$\text{diamagnetic} \iff \chi_{\mathrm{dia}} < 0, \quad \text{paramagnetic} \iff \chi_{\mathrm{par}} > 0$$

with $|\chi_{\mathrm{dia}}| < \left|\chi_{\mathrm{par}}\right|$ in general.[69] In this Section, the magnetization M will play a very important role. In general, it denotes the magnetic moment per unit volume of a body immersed in an external field linked via the susceptibility χ as proportionality constant to the magnetic field $\mathbf{B}_0$:[9]

$$M = \chi B_0 \tag{2.50}$$

The magnetization M of a system of N magnetically diluted, non-interacting paramagnetic spins is derived as the statistical average of all single spins S with magnetizations m,[9]

$$\langle M\rangle = -N\frac{\sum_{m=-S}^{S} g\beta_e m \exp\left(-\frac{mg\beta_e B_0}{k_B T}\right)}{\sum_{m=-S}^{S} \exp\left(-\frac{mg\beta_e B_0}{k_B T}\right)} \tag{2.51}$$

$$= Ng\beta_e S B_S(x), \quad x = \frac{gS\beta_e B_0}{k_B T}, \tag{2.52}$$

where $B_S(x)$ is the Brillouin function,[70]

$$B_S(x) = \frac{2S+1}{2S}\cdot\coth\left(\frac{2S+1}{2S}\,x\right) - \frac{1}{2S}\cdot\coth\left(\frac{1}{2S}\,x\right). \tag{2.53}$$

In the high temperature approximation ($h\nu \ll k_B T$), Eqn. 2.52 can be expanded as Taylor series and M or χ (Eqn. 2.50) follows an inverse-temperature behavior,[9]

$$\chi_{\text{par}} = \frac{N}{3}\frac{\beta_e^2 g^2 S\,(S+1)}{k_B T}, \tag{2.54}$$

which is called Curie's law.[71] Paramagnetic samples are pulled into an inhomogeneous magnetic field, while a diamagnetic sample is forced out of it. Diamagnetism is present in almost every substance, originating from most atomic nuclei. Therefore, diamagnetic samples with nuclear spin can be observed with NMR, while paramagnetism can among others be studied with EPR as presented above. For the basic interactions in $\hat{\mathcal{H}}_{\text{EZ}}$ and $\hat{\mathcal{H}}_{\text{HFS}}$, it was assumed that the individual paramagnetic spins do not interact with each other (Section 2.1.1), while weak interactions usually lead to line broadenings (Section 2.1.2).

However, it is also possible for the spins to couple strongly and align with respect to each other, also without the presence of an external magnetic field $\mathbf{B}_0$. This interaction may lead to an antiparallel spin alignment, which is called antiferromagnetism. Additionally, the spins may align parallel, a phenomenon which is called ferromagnetism. The following model partly completes the abbreviated description of the omitted terms in the Spin Hamiltonian, Eqn. 2.17 of Section 2.1.1. Here, ferromagnetism shows coupling constants $J > 0$, while antiferromagnetism can be interpreted as two ferromagnetically coupled sublattices with $J < 0$. The ordered spin states also remain in the presence of $\mathbf{B}_0$ or may even be induced only upon such an influence. Typically, they persist at very low temperatures and transform into a paramagnetic phase above the Néel temperature T_N or Curie temperature T_C.[70,72] The dependence of the magnetization $\mathbf{M}\,(\mathbf{B}_0)$ of an antiferromagnet is more characteristic of a paramagnet, although it originates from different effects. For antiferromagnets, the susceptibility χ_{af} is a useful parameter for the description, and antiferromagnetically coupling spins can be detected and described in terms of EPR with spin-spin interactions below T_N. In contrast, below T_C χ_{fer} is no longer a useful parameter, since it is both field- and history-dependent. Although it is possible to show these long-range phenomena both with and without external $\mathbf{B}_0$, a typical property of such ferromagnetically coupled spins is their ordering dependence on the direction of $\mathbf{B}_0$, such that the susceptibility takes significantly different values for $\chi_{\parallel}$ and $\chi_{\perp}$ and a strong temperature dependence of those two values can be observed.[70] In this regard, the saturation magnetization $\mathbf{M}_S$ is regarded as an important intrinsic property.[73] These magnetization properties are commonly measured in a superconducting quantum interference device (SQUID). Nevertheless, also ferromagnetism can also be recorded in an EPR spectrometer, allowing for the study of important properties no competing spectroscopy can reveal. This special application of EPR instruments for ferromagnetic samples was observed well before Zavoisky's experiments by W. Arkadiew in 1911,[74] due to the much more intense signal. Relevant theoretical descriptions were also given earlier in 1931 by L. Landau and E. Lifschitz,[75] and later by C. Kittel.[76–79] The principles of this magnetic resonance are introduced below.

Theory of magnetic anisotropy Magnetic anisotropy describes the different total energies of the ground state of ferromagnetic matter depending on the magnetization $\mathbf{M}_S$, which is itself dependent on the direction of the external magnetic field $\mathbf{B}_0$. The magnetic anisotropy energy ΔE_{MAE} is defined as the work needed to turn $\mathbf{M}_S$ from the direction it points along without external fields towards the direction $\mathbf{B}_0/B_0$. If the directional change of $\mathbf{M}_S$ happens at a constant temperature, this difference corresponds to the differences in the free energy, F. F is minimal for a magnetic easy axis and largest for a magnetic hard axis. Magnetic anisotropy occurs due to both boundary conditions from the external shape as well as intrinsic lattice properties. For example, a magnetic easy axis of thin films will always be in the film plane.[80,81]

Microscopically, two reasons are considered for the intrinsic, magnetocrystalline anisotropy: dipole-dipole as well as spin-lattice interactions. In general, a magnetic dipole $\boldsymbol{\mu}$ induces a magnetic field $\mathbf{B}_\mu$ in distance $\mathbf{r}_\mu$,

$$\mathbf{B}_\mu\left(\mathbf{r}_\mu\right) = \frac{\mu_0}{4\pi}\left(\frac{3\left(\mathbf{r}_\mu \cdot \boldsymbol{\mu}\right)\cdot \mathbf{r}_\mu}{r_\mu^5} - \frac{\boldsymbol{\mu}}{r_\mu^3}\right) \tag{2.55}$$

and another dipole $\boldsymbol{\xi}$ in distance $\mathbf{r}_\mu$ has the corresponding energy $E_\xi = \boldsymbol{\xi} \cdot \mathbf{B}_\mu$. Due to the lattice pinning of the dipoles and the possibly different lattice constants a magnetic anisotropy might occur. The total free energy in a lattice is then the sum of all dipolar interaction energies. Without many further comments on the theory behind this summation, it is natural to assume without loss of generality that for a crystal with volume V this summation can be transformed into an integral, allowing for the identification of the boundary conditions as the origin of the external, shape anisotropy:

$$F = \sum_{i=\xi,\ldots} E_i \Rightarrow F = \frac{1}{V}\int_V \mathbf{M}_S \cdot \mathbf{B}_\mu \mathrm{d}V \tag{2.56}$$

Hence, the free energy of a system can be deduced from its symmetry and approximate outer shape. For the uniaxial geometry of the thin film samples studied in this work, a magnetocrystalline anisotropy energy containing uniaxial second and fourth order anisotropy terms with anisotropy constants $K_{2\perp}$ and $K_{4\perp}$ is required. The free energy density is then given by[82]

$$F = -\mu_0 \mathbf{M}_S \cdot \mathbf{H} + \left(\frac{1}{2}\mu_0 M_S^2 + K_{2\perp}\right)\cos^2\theta + K_{4\perp}\cos^4\theta, \tag{2.57}$$

where θ denotes the angle between the magnetization vector and the film normal. It can be assumed that both $\mathbf{M}_S$ and $\mathbf{H} = \mathbf{B}_0/\mu_0$ are in a similar plane, which the film normal spans with the two of them, and because they do not align collinearly, θ_H shall denote the angle between $\mathbf{B}_0$ and the film normal, such that $\mathbf{M}_S \cdot \mathbf{H} = M_S H \cos(\theta - \theta_H)$. In general, F is a function of the temperature T. Therefore, all anisotropy fields described in the following are assumed to be saturated at low temperatures.

Ferromagnetic resonance (FMR) The actual FMR spectrometer does not differ from a cw EPR spectrometer as described in Section 2.1.3. The resonance condition Eqn. 2.10 adapts to the new resonance field:

$$B^{\mathrm{eff}} = \mu_0 (H_0 + M_S) = \mu_0 H^{\mathrm{eff}}_{\mathrm{res}}, \quad h\nu_{\mathrm{mw}} = g_J \beta_e B^{\mathrm{eff}} \tag{2.58}$$

$$\Rightarrow \omega = \gamma B^{\mathrm{eff}}, \quad \gamma = \frac{2\pi g_J \beta_e}{h} \tag{2.59}$$

In any measurement, only $\mu_0 H_0$ is known, as the internal fields define the actual resonance field B^{eff} incident on the observed spins.

In contrast to the quasi isolated spins focused so far, strong interactions must be considered as leading to strong internal fields. Additionally, anisotropy fields as discussed above perturb this field, which are all collected in the effective field B^{eff}. The gyromagnetic ratio γ is more frequently used in FMR than the g factor, which is now affected by the strong spin couplings. The time derivative of the torque by the total moment of inertia $\boldsymbol{\mu_n}$ induced by $\mathbf{J}$ in B^{eff} can with the help of γ be expressed by

$$\frac{1}{\gamma}\frac{\mathrm{d}\boldsymbol{\mu}}{\mathrm{d}t} = \boldsymbol{\mu} \times \mathbf{B}^{\mathrm{eff}}, \tag{2.60}$$

which is integrated over a volume V to the total magnetization time derivative of thin ferromagnetic films possessing usually aligned magnetic momenta:

$$\frac{\mathrm{d}\mathbf{M}_S}{\mathrm{d}t} = \gamma \left(\mathbf{M}_S \times \mathbf{B}^{\mathrm{eff}}\right) \tag{2.61}$$

This equation is the Landau-Lifschitz equation, reobtained later via quantum mechanics by J. H. van Vleck and used in the following.[75,83] The solution of the Landau-Lifschitz equation is the key to connect the anisotropy fields with the resonance fields found for an FMR signal, allowing to resolve the angular distribution of the magnetic easy and hard axes and the respective anisotropy constants. An approach to this solution is given by J. Smit and H. G. Beljers.[84] It is based on the picture of the precessing magnetic moment describing a cone around $\mathbf{B}^{\mathrm{eff}}$ (cf. Eqn. 2.7). Eqn. 2.61 can herein be expanded in its equations of motion based on the earlier described angle θ and an additional, azimuthal precession angle φ with the assumption that $M_S = \text{const.}$:

$$\frac{\mathrm{d}\theta}{\mathrm{d}t} = \gamma \frac{\partial \mathrm{B}^{\mathrm{eff}}}{\partial \varphi} =: \gamma \mathrm{B}^{\mathrm{eff}}_{\varphi}, \quad \frac{\mathrm{d}\varphi}{\mathrm{d}t} \sin\theta = -\gamma \frac{\partial \mathrm{B}^{\mathrm{eff}}}{\partial \theta} =: -\gamma \mathrm{B}^{\mathrm{eff}}_{\theta} \tag{2.62}$$

In a thermodynamic equilibrium $\mathbf{M}_S$ and $\mathbf{B}^{\mathrm{eff}}$ might be assumed to align for a moment and the equilibrium orientation of $\mathbf{M}_S$ in terms of θ and φ can be found in the minima of F:

$$F_\theta = \left.\frac{\partial F}{\partial \theta}\right|_{\theta_0} \overset{!}{=} 0, \quad F_\varphi = \left.\frac{\partial F}{\partial \varphi}\right|_{\varphi_0} \overset{!}{=} 0 \tag{2.63}$$

However, since the alignment of $\mathbf{M}_S$ and $\mathbf{B}^{\text{eff}}$ is not an initial requirement, small deviations are allowed and can be expanded in a Taylor series involving second order derivatives of the equilibrium:

$$F_\theta = F_{\theta\theta}\delta\theta + F_{\theta\varphi}\delta\varphi, \quad F_\varphi = F_{\varphi\theta}\delta\theta + F_{\varphi\varphi}\delta\varphi \tag{2.64}$$

From a Lagrangian equation of motion approach a combination of Eqn. 2.56 and Eqn. 2.62 can be used to replace the left-hand sides of Eqn. 2.64 and obtain a set of linear differential equations,[81]

$$-\frac{M_S}{\gamma}\sin\theta\frac{\partial\left(\delta\theta\right)}{\partial t} = F_{\theta\theta}\delta\theta + F_{\theta\varphi}\delta\varphi, \quad \frac{M_S}{\gamma}\sin\theta\frac{\partial\left(\delta\varphi\right)}{\partial t} = F_{\varphi\theta}\delta\theta + F_{\varphi\varphi}\delta\varphi \tag{2.65}$$

and a solution of Eqn. 2.65 is the resonance equation by Smit and Beljers, solved for the resonance field:[84]

$$\mu_0 H_0 = \frac{\omega}{\gamma} = \frac{1}{M\sin\theta}\sqrt{F_{\theta\theta}F_{\varphi\varphi} - F_{\theta\varphi}^2} \tag{2.66}$$

The latter equation lacks a solution for the case $\theta = 0$, therefore an equivalent solution by Baselgia et al.[85] can considered instead:

$$\frac{\omega}{\gamma} = \frac{1}{M}\sqrt{F_{\theta\theta}\left(\frac{F_{\varphi\varphi}}{\sin^2\theta} + \frac{\cos\theta}{\sin\theta}F_\theta\right) - \left(\frac{F_{\theta\varphi}}{\sin\theta} - \frac{\cos\theta}{\sin^2\theta}F_\varphi\right)^2} \tag{2.67}$$

Finally, it is necessary to expand the specific free energy for the sample of this work given in Eqn. 2.57 in the formalism of Eqn. 2.67:

$$\begin{aligned} \mu_0 H_0 = {} & \frac{\left(M_{\text{eff}} + \frac{H_4}{2}\right)\cos 2\theta + \frac{H_4}{2}\cos^2 4\theta + H_4\cos^4\theta}{2\cos\left(\theta - \theta_H\right)} + \\ & + \frac{\left(M_{\text{eff}} + \frac{H_4}{2}\right)\cos 2\theta + \frac{H_4}{2}\cos 4\theta - M_{\text{eff}}\cos^2\theta + H_4\cos^4\theta}{2\cos\left(\theta - \theta_H\right)} \end{aligned} \tag{2.68}$$

$$\theta_H = \theta - \arcsin\left(\frac{2M_{\text{eff}} + H_4}{H_0}\sin 2\theta + \frac{H_4}{8H_0}\sin 4\theta\right) \tag{2.69}$$

with $M_{\text{eff}} = \frac{2K_{2\perp}}{M_S} - 4\pi M_S$ being the effective anisotropy field and $H_4 = \frac{K_{4\perp}}{M_S}$. For $M_{\text{eff}} < 0$, the magnetic easy axis is either perpendicular to the film plane or embedded in the plane. The mutual dependency of Eqn. 2.68-2.69 can be fitted numerically. For the special case of $\mathbf{B}_0$ along an easy axis (either intentional or due to large field strengths) and $\mathbf{B}_0$ and $\mathbf{M}_S$ in the thin film plane ($\theta_H = \theta = 90°$) neglecting the H_4 terms

Eqn. 2.69 reduces to

$$(\mu_0 H_0)^2 = B_{0\parallel}\left(B_{0\parallel} - M_{\mathrm{eff}}\right) \tag{2.70}$$

and for $\mathbf{B}_0$ and $\mathbf{M}_S$ normal to the film plane ($\theta_H = \theta = 0°$), it becomes

$$\mu_0 H_0 = B_{0\perp} + M_{\mathrm{eff}}. \tag{2.71}$$

The FMR linewidth and T_C Eqn. 2.67 can be expanded to predict the full line shape.[86] In principle, the FMR line is like a Lorentzian, homogeneously broadened EPR signal as outlined in Section 2.1.2. Hereby, $\Delta B_{pp} = \mu_0 \omega \frac{G}{\gamma^2 M_S}$ is proportional to the Gilbert damping term G introduced by T. L. Gilbert in 1955 (however unpublished at the time).[87] At this point, it is not relevant to determine which microscopic process leads to the signal broadening, but it is clear, that a dynamic motion of the spins would physically lead to a broadened FMR line as in the case of EPR signals described in Section 2.1.2. The linewidth also depends on the orientation, and it has been shown that[88]

$$\Delta B_{pp} \approx \frac{2\mu_0}{\sqrt{3}} \frac{G}{\gamma^2 M} \frac{\omega}{\cos\left(\theta_0 - \theta_H\right)}. \tag{2.72}$$

Hence, the linewidth is small whenever $\mathbf{M}_S$ and $\mathbf{B}_0$ are parallel, for example in a magnetic easy axes. If they are not parallel, ΔB_{pp} increases depending on the equilibrium angle θ_0.

A further dependency of the line shape and linewidth is observed upon changes of the temperature. With decreasing temperature, the resonance fields shift both for the magnetic hard and easy axis to lower external fields $\mathbf{B}_0$, as the internal anisotropy fields typically increase. Ideally, the linewidth decreases linearly with temperature until it saturates. Since the linewidth of the FMR signal is related to fluctuations of the magnetization, T_C can be determined from the linewidth as the onset of its decrease.[89] This is demonstrated in Section 4.3.1 of this work.

2.2 High Sensitivity EPR with Dielectric Resonators

Dielectric resonators (DRs) are a well-established technology in mw techniques and like many oscillators, they are primarily used for frequency selection in filters, frequency stabilization in oscillators, and short-term energy storage. A DR consists of a disk or ring of dielectric, non-conductive and non-magnetic material with high quality factors, therefore opening up potential applications in cw EPR as well. In the following Subsection, the requirements for this application will be elucidated in order to highlight the necessity of the novel dielectric resonators employed in this work.

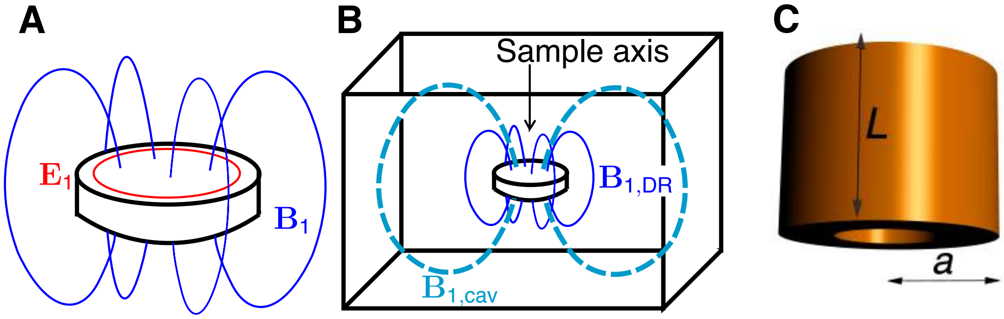

Fig. 2.6 Dielectric resonator modes:
(A) The $TE_{01\delta}$ of a DR with concentric $\mathbf{E}_1$ and parallel $\mathbf{B}_1$ fields with respect to the disk normal. $\mathbf{E}_1$ is concentrated mostly in the outer ring sections, $\mathbf{B}_1$ has highest η in the center of the disk.
(B) DR coupled to TE102 of cavity resonator.
(C) Schematic drawing of applied dielectric resonator with 1.2 mm hole.

2.2.1 Dielectric Resonators for Microwave Applications

The principles of DRs have been known since 1939,[90] and dedicated theory has been under development since 1960.[91] Soon after, they were tested also for EPR,[92] however a broad application has been prevented by the lack of materials with a sufficiently high dielectric constant, $\varepsilon_r \approx 20 \ldots 100$, which appeared about 10 years later. Then, numerous applications were found for DRs and the benefiting properties like their high Q (Eqn. 2.38) and high η (Eqn. 2.45) could also be employed for magnetic spectroscopy. This is possible because the DR can easy be driven to oscillate in a suitable mode for application in EPR.

As seen in Section 2.1.3 about EPR cavity resonators, an important condition for regular cw EPR is the orthonormality of $\mathbf{B}_0$ and $\mathbf{B}_1$ while having $E_1 = 0$ at the same point for every instance of time. A commonly used mw mode with DRs is the $TE_{01\delta}$ mode. This mode is depicted in Fig. 2.6A. In principle, it is not very different from the TE102 mode. The $TE_{01\delta}$ mode was introduced by Cohn[93] and from a distance it looks like a magnetic dipole. On the one hand, it has the advantage, that about 60 % of the magnetic field energy is concentrated in the center of the DR already at $\varepsilon_r \approx 40$, which leads to the conclusion that a hole in the center of the DR is a good choice for placing the sample.[94] One the other hand the similarities in the modes' field lines allow for a simple coupling mechanism which was applied in this work and is depicted in Fig. 2.6B. The electric field lines form concentric circles in the DR material and thus do not interfere with the sample, if it is placed in a hole as shown in in Fig. 2.6C and in Fig. B.7 on page 104 in the Appendix in more detail.

The oscillation occurs due to energy transfer between electric and magnetic fields, reflected in the DR's boundaries and the surrounding air. In this way, a standing wave is formed and energy which is not concentrated in the hole dissipates in the air around the DR with rapidly decreasing field magnitudes. Despite the relatively simple shape of the depicted DR, the exact field distribution must be calculated with finite element methods,[94] which have not been part of this work. Instead, a modest estimation achieved from such finite element simulations can be used to estimate the resonance frequency from such DRs. Kajfez and Guillon[94] give a first approximation of the frequency for the $TE_{01\delta}$-mode if the ratio a/L of cylindrically shaped DRs and their permittivity meet the reproduced requirements:

$$f_{\mathrm{GHz}} = \frac{34}{a\sqrt{\varepsilon_r}}\left(\frac{a}{L} + 3.45\right), \quad 0.5 < \frac{a}{L} < 2 \text{ and } 30 < \varepsilon_r < 50, \tag{2.73}$$

where the radius of the DR is denoted by a and its height by L, both measured in units of mm. A more accurate empirical formula was derived later from simulations by Kishk and Antar[95]:

$$f_{\mathrm{GHz}} = \frac{2.921c\varepsilon_r^{-0.465}}{2\pi a \cdot 10^6} \cdot \left[0.691 + 0.319\frac{a}{L} - 0.035\left(\frac{a}{L}\right)^2\right], \tag{2.74}$$

where c is the speed of light in vacuum. Kishk and Antar[95] showed that for arbitrary ε_r individual simulations would be necessary and if the ratio of a/L is out of the range as specified in Eqn. 2.73, other modes may be enhanced while undesired modes can be suppressed.[95]

DRs consist of dielectric ceramics,[97] or ferroelectric materials with low loss tangents tan δ and preferably high temperature stability $\tau_\varepsilon = \frac{1}{\varepsilon}\frac{\partial\varepsilon}{\partial T}$.[98,99] After higher ε_r ceramics were developed, the main limitation, besides non-optimal temperature stability, preventing a universal use in EPR spectroscopy was the presence of large amounts of paramagnetic impurities in the ceramics, giving rise to rich, temperature dependent EPR baseline perturbations which limited the accessible temperature and spectral region. Recently, more attempts have been carried out to overcome these limitations. Belous et al.[100] have found dielectric ceramics belonging to the wide family of barium lanthanide titanates (BLTss) with the structure of tetragonal tungsten bronze (TTB) oxide ceramics depicted in Fig. 2.7. The DR materials with composition $\mathrm{Ba}_{6-x}\mathrm{Ln}_{8+2x/3}\mathrm{Ti}_{18}\mathrm{O}_{54}$ (Ln = Sm, Nd) have been slightly modified by means of partial iso- and aliovalent substitution in their crystalline lattices to suppress mw dielectric losses and improve the temperature stability of ε_r.[100] The latter parameter is crucial in terms of suppressing the temperature changes of the resonant frequency of a

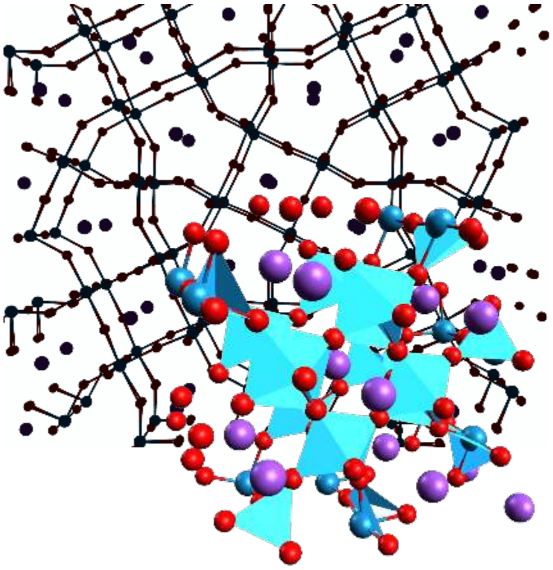

Fig. 2.7 Tetragonal tungsten bronze structure: Structural representation of tetragonal tungsten bronze (TTB) as a group of nonstoichiometric compounds (space group $P4/mbm$) viewed along [0 0 1] axis (top) and [1 1 0] axis (bottom). Tetragons indicate oxygen octahedra containing the cations in variable concentration which represents a metal with a large variety of species, among them the family of barium lanthanide titanates (BLTss) used for the DRs.[96]

DR. In this regard, the DRs' materials generally also contain slight amounts (up to 1 . . . 5 % wt.) of calcium, strontium, and magnesium oxides. The ceramics were made by solid-state synthesis at a sintering temperature of 1350 °C for 6 – 8 h. A cylindrical compression mold of the required diameter was used.[100] Therefore, the DRs demonstrated low dielectric losses in the desired mw range ($\tan\delta$ below 10×10^{-3} at 10 GHz), and good temperature stability of dielectric constant ($\tau_\varepsilon = \pm 5\,\mathrm{ppm/K}$). Golovina et al.[101] were able to show that with these DRs at temperatures of 77 K, stable mw properties and acceptable background signal around $g = 2$ could be achieved. The materials had a dielectric constant of $\varepsilon_r \approx 35$ by this time.

2.2.2 Implementation of Dielectric Resonators in EPR

Actual implementation of DRs for EPR requires an efficient coupling of the DR to the mw network. In principle, a DR can be coupled via antennae like it was done in the discovery of microwaves by Hertz[49] and for loop-gap resonators invented by Froncisz and Hyde[102], which have become a standard in pulse EPR.[103] This has also been applied to DRs before,[104] as well as experimentally in this work as seen in Fig. B.1 on page 96 in the Appendix, but there exists an easier method which does not require alteration of the EPR setup significantly. This is the insertion of the DR into cavity resonators.[105,106] Due to the relatively collinear $\mathbf{B}_1$ field distributions of DRs and cavity resonators as depicted in Fig. 2.6B, the $\mathrm{TE}_{01\delta}$ mode can be excited in rectangular and cylindrical cavity resonators.[95] The frequency of a free DR in standalone configuration f_{GHz} (Eqn. 2.74) that is usually considered as optimal when employed in cavity resonating systems should be close to the frequency of that very metal cavity resonator.[101]

Today's availability of DRs with high dielectric constants of $\varepsilon_r \approx 80$ allow for usage with coupling provided via cavity resonators even in commercial flow cryostats, which have a relatively narrow inner diameter that the DR must fit in. This limits the reachable frequency range (Eqn. 2.74) but is just enough for X-band frequencies.[101] This easy-to-use setup would offer the opportunity to measure small single crystals and thin film samples at non-ambient atmospheres and a wide temperature range of $4.2\,\mathrm{K} \leq T \leq 300\,\mathrm{K}$, provided the DR does not have paramagnetic impurities detectable at those low temperatures. At room temperature, DRs proved versatility for various solid state experiments[105] and aqueous samples in stopped flow experiments.[107,108] Although numerous different shapes and designs for various applications have been studied,[97,109–112] so far all easily applicable measurements in commercial spectrometers with standard cryostats have been limited to relative high temperatures, due to either dimensions that were too large for a common cryostat,[2] high impurity contents,[113] or substantial temperature dependencies on the stability of ε_r, τ_ε and of $\tan\delta$.[114]

As outlined above, very sophisticated ways of predicting the mw field distribution are available by finite element simulation or novel improvements of coupled mode theory (CMT).[115–117] These theoretical investigations found that the $\mathrm{TE}_{01\delta}$ mode is able to couple in a parallel (symmetric, in phase) and antiparallel (antisymmetric, out of phase) configuration with respect to the TE_{102} or TM_{110} modes of the rectangular or cylindrical cavities, respectively.[101,111,115–117] The parallel field superposition results in lower resonance frequencies, and the antiparallel field shows the opposite behavior with higher coupled mw resonance

---

[2] Popular DRs were supplied by muRata Manufacturing Inc., Japan, and coupled in highly advanced, customized setups,[104,106,108] but their outer diameters usually exceeded those given in Section A.1 in the Appendix.

frequencies. Higher frequencies yield lower signal enhancements, while lower frequencies are the preferred ones with even higher SNR gains. The low-frequency parallel mode was experimentally excited for DRs with lower $\varepsilon_r \approx 35$, whereas the high frequency antiparallel mode is reported to be the dominating one for DRs with higher ε_r.[101] Mett et al.[115] state that with an iris coupling of electrically coupled cavity-DR systems, only one of the modes can be excited at the same time, and the coupled resonance frequencies with $f_{\text{antiparallel}} > f_{\text{empty cav.}} > f_{\text{parallel}}$ never cross.

The goal of this work was to show that DRs provide an easy-to-use setup for commercial spectrometers, where the DR is placed in a typical EPR sample tube together with the studied sample, as shown in Fig. 2.6C, to perform experiments under non-ambient gas atmospheres, such as in vacuum or under gas loading at temperatures below the 77 K reported so far. To achieve this, an optimal material which is sufficiently clean from paramagnetic impurities, enhances the filling factor η reasonably, and enhances the B_1 field reasonably had to be found. While the first two points are self-explanatory, the third one is caused by the fact that all experiments which compare the SNR must be carried out at the same measurement conditions. This, however, results in the situation that the augmented mw B_1 field magnitude must also be considered as it enters the SNR (Eqn. 2.48) directly proportional via the mw power P. Since in cw EPR power is practically unlimited (Section 2.1.3), at first sight increasing B_1 by using a DR does not assist the EPR measurement. Moreover, for every coupled DR this factor must be known in order to correct the achieved SNR gain for it. On the other hand, the increased B_1 does only affect the studied sample in the vicinity of the DR. If, therefore, the DR can help to reduce the incident power on impurities which are outside the DRs high η, one can no longer reject the benefits of the B_1 field magnitude increase. A proportionality constant C for the incident mw power to B_1-field conversion which is referred to as probe's efficiency parameter 2Λ, can be given as[115,116]

$$B_{1,i} = C_i\sqrt{P} = 2\Lambda\sqrt{P}. \tag{2.75}$$

In this work, C will be evaluated for the various DRs tested in Section 3.1.

2.3 Very High Sensitivity EPR with Planar Microresonators

Another recent method for ultra-sensitive cw and pulsed EPR methods was adapted from the development of planar or spatially distributed miniaturized mw structures, which are applied widely in physics and engineering.[118] For EPR, planar microresonators (PMRs) are a sophisticated approach for new resonators. The following Section shall give an overview of the wide field which has been made possible by this technology.

2.3.1 Electronic Strip Line Architecture in High Frequency Techniques

Like many other technologies, it is desirable for mw processing to happen in miniaturized design layouts on physical circuit boards (PCB) to provide easy, reliable, and cheap production and handling. In the 1950's, microwaves were processed on circuit boards that were designed similarly to coaxial wave guides. Later, with further implementation of integrated circuit (IC)-technology and electronic circuitry, microstrips

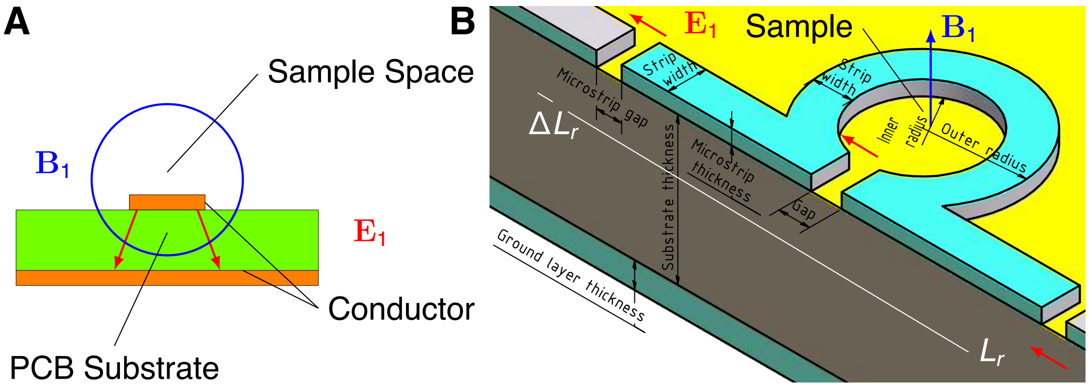

Fig. 2.8 Microstrip TEM mode, planar microresonator: Magnetic field lines (blue) are concentrated around the sample, while electric field lines (red) do not penetrate the sample.
(A) Cross section of dual-layer PCB strip line and sketched TEM mode with concentric $\mathbf{B}_1$ field which has highest η close to the conductor.
(B) PMR coupled to strip line, the sample must be placed in the loop of the Ω structure with highest η of $\mathbf{B}_1$.

were used instead. This type of waveguide provides the cheapest way to guide microwaves but struggles with higher powers, stray fields, and cross talking interferences. Also, the limitation of appropriate PCB materials proving high, constant ε_r and rigid mechanical properties in a large temperature range prevents the technology from becoming as popular in microwave engineering as in other electronics. For EPR, the paramagnetic impurities in the PCB materials set another limit. It is only recently that high ε_r PCB materials partly overcoming these limitations have been introduced for example by Rogers Corp.,[3] or single crystals like sapphire with more challenging mechanical properties and known as DR material already were used as wafer substrate.[97,120]

Classically, as explained above in Section 2.1.3, microwaves are guided along cavity structures and tend to oscillate within resonators with dimensions of integer multiples and fractions of the mw wavelength λ, which for X-band frequencies implies structures of several cm in size. From microstrip waveguides, another type of mw resonator can be deduced, and this was already applied for EPR in 1974 by Johansson et al.[121] based on the working principle of miniaturized lumped element structures, which can be sub-wavelength in dimension. Inside individual parts of these structures there are no longer standing microwaves, but they may nevertheless serve for EPR usage as shown already and outlined below.[102] Fig. 2.8A shows the principal layout of the parent microstrip waveguide principle. Nowadays, the complete implementation of the EPR experiment (apart from the external magnetic field) on a circuit board or ICs can lead to new possible areas of application.[122,123]

---

[3] See Fig. B.2 on page 98 for a Rogers Ro3010 EPR spectrum.[119]

2.3.2 Implementation of Planar Microresonators in EPR

So far the EPR resonators which have been presented here have had a dimension of mnp half wavelengths, optimized for standing waves in cavities or strip lines with low losses and high quality factors. Their advantage is the high sensitivity to changes in Q which in most cases can compete with the low filling factors η. The design of the resonators allows for an easy substitution of samples within the resonator and of the resonators at the spectrometer. Also, microwave losses between the resonator and the rest of the microwave network are low, because the resonators are build to match characteristic impedances. Another approach for EPR resonators is to increase the filling factor η by decreasing the resonator size below common integer fractions of the wavelength, often in expense of the quality factor and impedance matching. This can only be of use if the sample size cannot be increased arbitrarily without harming the integrity of the sample properties like crystallographic unity, purity or homogeneity. Morita and Ohno[124] and Mahdjour et al.[62] proposed the use of non-resonant coils or microcoils adopted from NMR for the detection of low amounts of liquids. The most simple microstrip resonator is a microstrip with impedance Z and half-wavelength $\lambda_{\mathrm{mw}}/2$ strip line length. It is separated from the waveguide strip line by a certain gap as shown for the straight strip line part in Fig. 2.8B. Accurate predictions of the microstrip resonator dimensions and properties are the subject of theoretical treatments by dedicated finite-element simulations.[125,126] Wallace and Silsbee[127] constructed resonators and by decreasing the wafer and strip size they could increase the filling factor to almost unity. By using this approach, a thin film could be investigated, however the sample size still needs to be in the range of the wavelength.

A novel method of miniaturization is provided by Narkowicz et al.[128], proposing lumped-element layouts inspired by macroscopic loop-gap resonators coupled to microstrips acting as antennae or integrated in the conductor of a microstrip, resulting in the characteristic shape of a planar, capital Greek letter Ω. These are then referred to as planar microresonators (PMRs). Fig. 2.8B shows the typical layout and dimensions of the Ω-shaped PMRs. For X-band frequencies, two differently shaped microresonators had initially been proposed,[128,129] and they were intended to confine the B_1-field to a very limited space and address very small domains or small samples. Later, the principle was also applied to planar loop-gap resonators and other array structures.[130] Via the small volume with high filling factors η of the lumped elements, a high mw power is achieved (Eqn. 2.48), leading as with the DRs to strong mw B_1 fields. The resonance frequency for the PMRs can be estimated by the following formula:

$$(L_r + \Delta L_r) = \frac{c}{2 f_0 \sqrt{\varepsilon_{\mathrm{eff}}}} \tag{2.76}$$

Here, ΔL_r is the heuristic length of the microstrip gaps at the outer ends of the PMR. This additional length influences both the resonance frequency f_0 and the capacitance of the resonator, which is important considering the requirement of the impedance matching. To evaluate the optimal structure for a matched microstrip with a characteristic impedance of 50 Ω and the desired field distribution, Narkowicz et al.[128] optimized the properties by finite element simulations,[125] and found the inverse proportionality,[129]

$$2\Lambda \propto d^{-1}, \tag{2.77}$$

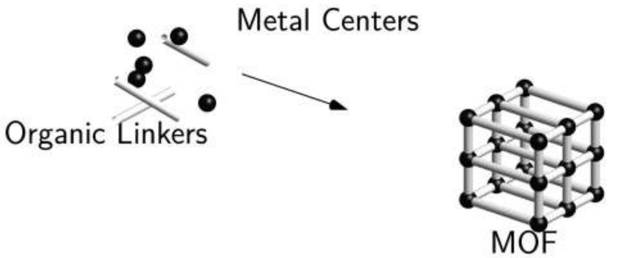

Fig. 2.9 General metal- organic framework scheme: Schematic representation of a metal-organic framework structure showing the metal center and linker building blocks forming a regular network.

where d denotes the PMR loop diameter and 2Λ is used as in Eqn. 2.75 for the DRs. Furthermore, with the mw efficiency of high $\mathbf{B}_1$ fields inside the structure the detection sensitivity of the PMR in pulsed EPR applications increases as its size gets smaller. As sketched in Fig. 2.8B, the PMR design is considered as very advantageous due to its lack in $\mathbf{E}_1$ and $\mathbf{B}_1$ field overlap, which is a benefit for achieving higher quality factors Q. However, the overall Q is still very low, making them also generally suitable for pulse EPR experiments. The PMRs designed by the Suter group, TU Dortmund, are manufactured with PCB lithography technology at TU Ilmenau. The easy layout simplifies production and reduces the resonator cost. However, the planar structure requires very customized couplings, positioning in an optional cryostat and orientation of the sample. Small samples are placed on the substrate inside the loop structure or a capillary is used to hold a liquid sample in a drilled hole inside the loop. Due to the small dimensions, this positioning must be very precise and it is difficult to manipulate the sample orientation other than under an optical microscope.

As outlined above, it is preferable to produce small PMRs. Sensitivity tests with DPPH samples resulted in the remarkable sensitivity value according to Eqn. 2.49 of $2.3 \times 10^9\,\mathrm{spins/(G \cdot Hz^{1/2})}$ at $300\,\mathrm{K}$.[128] The PMRs also have been applied to ultra small single nanomagnets with volumes of $(100\,\mathrm{nm})^3$ for FMR measurements (Section 2.1.5).[131] In this work, the implementation of a PMR for an actual, low temperature EPR investigation of a small, single crystal has been attempted.

2.4 Porous Metal-Organic Frameworks Investigated by EPR

Over the last couple of decades, an interest in MOFs as a discrete class of porous solids has emerged.[132] MOFs, which are formed of metal centers and organic linkers as depicted in Fig. 2.9, are dedicated for gas separation and storage[21] and reveal interesting properties for catalytic application.[133,134] A growing part of research is dedicated to the magnetic properties of MOFs,[25,135] such as the recently observed ferromagnetism in dinuclear Cu^{2+} based MOFs with $Cu_2(COO)_4$ paddle-wheels (PWs).[136] As many of them already contain paramagnetic ions, or can be doped by paramagnetic ion sensors, EPR spectroscopy, among other characterization methods, has been used to elucidate the nature of paramagnetic probes,[137] including their interaction with diamagnetic and paramagnetic adsorbates in MOFs as well as structural deformation processes upon gas adsorption.[22,23] EPR can be used together with theoretical models like those obtained from density-functional theory (DFT), allowing for the analysis of important aspects of MOF structures, as the large variety of studies on MOFs shows.[25,138,139]

The presented MOFs in this work have partly been analyzed previously as powder materials by other methods, including cw and pulsed EPR. Due to the information deficit for the elucidation of complex structures regarding specific magnetic **g** and **A** tensor principal axis orientations with respect to crystallographic axes obtained by powder studies, single crystal EPR of MOF crystals is needed to obtain get further insight into the structures. Moreover, adsorption complexes formed with paramagnetic ions in porous materials such as MOFs and also zeolites, AlPOs and SAPOs have been investigated widely, yet in powders only.[140–143] For single crystals, so far EPR has often not been feasible, since the low-density materials typically form small crystallites of sub-millimeter size which themselves feature relatively few atoms due to the high porosity. Therefore, single crystal EPR has been restricted to a few studies of framework substitutions in high-field EPR experiments.[144] For this work, three examples of MOFs have been selected to show the opportunities given by the new, sensitive methods introduced in Section 2.2 and 2.3.

2.4.1 A New Approach for Structure Determination in a Robust MOF

One of the most studied MOFs is the well-known HKUST-1 presented in Section 2.4.2.[145] The high porosity found for HKUST-1 in numerous studies set benchmarks for adsorption capabilities of MOFs and the effectiveness of the separation of $\mathrm{CO_2}$ and $\mathrm{CH_4}$.[146] Despite the benefiting properties, a number of difficulties arise in large scale handling, among them instability against humid environments and low thermal resilience,[147] which make it worthwhile to synthesize and investigate novel compounds. For this reason, a MOF material with the chemical formula $^{3}_{\infty}[\mathrm{Cu^I{}_2Cu^{II}{}_2(H_2O)_2L_2Cl_2}]$ (denoted in short as **1** throughout this thesis) was prepared with solvothermal synthesis by P. Eckold.[148,149]. Here, L is a short form of 3,3'-(5,5'-(thiophene-2,5-diyl)bis(3-methyl-4H-1,2,4-triazole-5,4-diyl))dibenzoate, such that the extended formula reads $^{3}_{\infty}[\mathrm{Cu^I{}_2Cu^{II}{}_2(H_2O)_2\{(Me-trz-}m\mathrm{ba)_2thio)\}_2Cl_2}]$.

The structure of this more durable MOF was characterized by single crystal XRD analysis and discussed by Šimėnas et al.[149] A presentation of the network with space group I 2_1 2_1 2_1 is shown in Fig. 2.10A. The three-dimensional network contains both $\mathrm{Cu^+}$ and $\mathrm{Cu^{2+}}$ ions. The $\mathrm{Cu^{2+}}$ ions build PW units coordinated by four carboxylate groups of the ligand L and two water molecules on the apical positions. The $\mathrm{Cu^+}$ ions are coordinated by four nitrogen atoms of four bridging triazole rings resulting in a tetrahedral coordination environment. Synthesis, crystal structure, and powder cw EPR spectroscopy data of the MOF have been described and analyzed before this work.[149] A single crystal of that material with approximate dimensions of $200 \times 50 \times 50\ \mu\mathrm{m}^3$ (see Fig. B.5 on page 102 and Section B.3 in the Appendix) contains about 10^{14} unit cells.

It was found that the $\mathrm{Cu^{2+}}$ ions in Cu / Cu PW units are coupled antiferromagnetically and have an excited $S = 1$ electron spin state and an EPR silent $S = 0$ ground state.[150] The observed coupling is a direct consequence of the super exchange of two unpaired electrons residing in a single Cu / Cu PW unit. Moreover, a pronounced interdinuclear exchange of the excited spin triplets between neighboring Cu / Cu PW units in the dehydrated MOF has been reported.[149] In addition, the cw EPR experiments revealed a mononuclear $\mathrm{Cu^{2+}}$ ion species of unknown origin. The elucidation of the origin of such mononuclear $\mathrm{Cu^{2+}}$ ions in MOFs containing Cu / Cu PW units seems to be a general problem, since minor mononuclear $\mathrm{Cu^{2+}}$ species have also been observed in the formerly mentioned HKUST-1,[22,150], $[\mathrm{Zn_{1-x}Cu_x(bdc)(dabco)_{0.5}}]_n$[151] and STAM-I

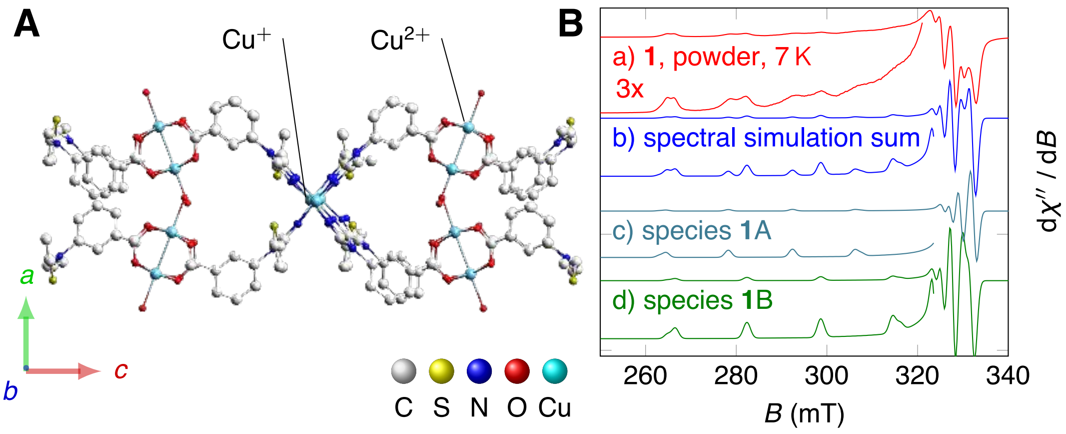

Fig. 2.10 $_{\infty}^{3}[\mathrm{Cu^{I}_2Cu^{II}_2(H_2O)_2L_2Cl_2}]$ with cw powder EPR spectrum:

(A) Structural ball-and-stick representation of $_{\infty}^{3}[\mathrm{Cu^{I}_2Cu^{II}_2(H_2O)_2L_2Cl_2}]$ with indicated $\mathrm{Cu^{+}}$ and $\mathrm{Cu^{2+}}$ in the Cu / Cu PW units (for an isolated PW see Fig. 2.11A).

(B) (a) Experimental powder EPR spectrum at 7 K, (b) sum of the simulated spectra of the two mononuclear species, (c) species **1**A, (d) species **1**B. The lower line reproductions of the $g_{\|}$ part are magnified.

MOFs.[152] and have so far been attributed to extra framework impurities in high local concentrations from untransformed reactants. However, in many cases, direct proof about the origin of these cupric ion defect species has not been provided. Preliminary tests of powder materials of the mononuclear $\mathrm{Cu^{2+}}$ ion species in the as-synthesized crystals **1** were used to estimate the percentage of $\mathrm{Cu^{2+}}$ ions with respect to other framework constituents and their origin.[153] These will be shown below before the results of the single crystal analysis of **1** are presented in Section 4.1.

X-Ray Diffraction During refinement of the crystal structure of **1** based on single crystal XRD data a peculiarity concerning the $\mathrm{Cu^{2+}}$ ions was observed.[153] In contrast to the $\mathrm{Cu^{+}}$ ions, the anisotropic displacement factors for the $\mathrm{Cu^{2+}}$ ion were slightly increased. To investigate the origin of this deviation the site occupancy factors (sof) of $\mathrm{Cu^{+}}$ and $\mathrm{Cu^{2+}}$ ions were refined. Whereas the sof of the $\mathrm{Cu^{+}}$ ions were found to be 0.49 and 0.50, respectively (the positions of $\mathrm{Cu^{+}}$ ions are located on twofold axes, so the expected sof is 0.50), the sof for the $\mathrm{Cu^{2+}}$ ion was refined to 0.933(4). A possible explanation for this observation is the presence of defective PW units, in which only one $\mathrm{Cu^{2+}}$ position is occupied. Based on the XRD data, about 13 % of all PWs would be defective.

Mononuclear $\mathrm{Cu^{2+}}$ Concentration X- and Q-band powder EPR measurements of $_{\infty}^{3}[\mathrm{Cu^{I}_2Cu^{II}_2(H_2O)_2L_2Cl_2}]$ have been repeated for this work as a preliminary test for the single crystal measurements presented in Chapter 4.[149,153] Fig. 2.10B shows the powder spectrum of **1** measured at X-band frequency and 7 K around values of $g = 2$. The experimental spectrum of **1** Fig. 2.10B(a) (upper two lines, red) shows the well-known anisotropic EPR powder pattern of mononuclear $\mathrm{Cu^{2+}}$ ions with $S = \frac{1}{2}$ electron spin interacting with the nuclear magnetic moments of the $^{63}\mathrm{Cu}$ and $^{65}\mathrm{Cu}$ isotopes with nuclear spin $I = \frac{3}{2}$ each. The excited $S = 1$

Tab. 2.1 $^{3}_{\infty}[Cu^{I}_2Cu^{II}_2(H_2O)_2L_2Cl_2]$ simulation parameters: Axial **g** and **A** tensors' principal axis values of mononuclear Cu^{2+} species **1**A and **1**B.

Parameter	Species **1**A	Species **1**B
$g_{\|}, g_{\perp}$	2.317(2), 2.055(5)	2.359(2), 2.044(5)
$A_{\|}, A_{\perp}$ / 10^{-4}/cm	173(1), 18(2)	153(1), 18(2)

spin state EPR resonance lines of the antiferromagnetically coupled Cu^{2+} pair in the Cu / Cu PW units are not present in the spectrum due to the low temperature of 7 K. In the spectrum two different patterns assigned to two axially symmetric Cu^{2+} species **1**A and **1**B can be identified in accordance to an earlier report.[149] Both species show well resolved HFS signals in the $g_{\|}$ part of their powder pattern, indicating only moderate strain effects. At 7 K, the spectrum of each species can be simulated using Eqn. 2.2 and 2.3 from Eqn. 2.1 with two terms each for species **1**A and **1**B. The principal axis values of the axially symmetric **g** and **A** tensors of species **1**A and **1**B are given in Tab. 2.1. Though strain effects are moderate, the increasing line widths of the HFS signals in the $g_{\|}$ part with increasing field for both Cu^{2+} species are typical for correlated **g** and **A** strain distributions.[154] Consequently, a correlated and Gaussian weighted distribution of the principal axis values has been considered in the simulation of the EPR powder patterns of the Cu^{2+} species **1**A and **1**B. For the simulation of **1** a Gaussian distribution of the $g_{\|}$ components with a center given in Tab. 2.1 and a width of $\Delta g_{\|} = 0.015$ has been assumed heuristically, taking the two species **1**A and **1**B as limits. The HFS parameters $A_{\|}$ are in first approximation assumed to be correlated with the Gaussian distributed values $g_{\|}$ by

$$A_{\|} = -m \cdot g_{\|} + k, \tag{2.78}$$

where m and k are determined by a linear fit to the two $g_{\|}$ and $A_{\|}$ parameters of species **1**A and **1**B, such that $m = 476.2 \times 10^{-4}$/cm and $k = 1276.4 \times 10^{-4}$/cm. The simulations revealed almost equal intensities for both species with axially symmetric and collinear **g** and **A** tensors as seen in Fig. 2.10B(b–d).

In addition to the mononuclear Cu^{2+} ion signal, the fine structure pattern of Cu / Cu PW units ($S = 1$) appears at temperatures above 50 K allowing for the determination determination of the ratio between the number of mononuclear Cu^{2+} species and Cu / Cu PW units.[149] This can be done as per Eqn. 2.48, where $\eta Q\sqrt{P}/\left(8\sqrt{k_B T \Delta\nu}\right)$ is assumed to be equal for the mononuclear and dinuclear Cu^{2+} centers.[155] However, the temperature dependence of χ of these two species differs significantly. The susceptibility of mononuclear Cu^{2+} centers at relatively high temperatures obeys the Currie law (Eqn. 2.54). In contrast, in the case of Cu / Cu PW units it is governed by the Bleaney-Bowers equation[22,152,156–158] and Šimėnas et al.[149] have estimated the exchange coupling constant J (cf. $\hat{\mathcal{H}}_J$ in Eqn. 2.17) to be −278/cm. From this, the ratio N_M/N_{PW} has been determined from a room temperature Q-band spectrum,[153] allowing for the complete fine structure pattern of the $S = 1$ state of the Cu / Cu PW units to be obtained. The intensities were determined by double integration of the cw EPR spectra (Eqn. 2.29) and yielded the ratio $N_M/N_{PW} = 0.11(2)$. From this, a net spin number of 10^{13} mononuclear Cu^{2+} EPR spins in the single crystals of **1** was estimated,[153] which has also been found to be in excellent agreement with an improved analysis of magnetic susceptibility

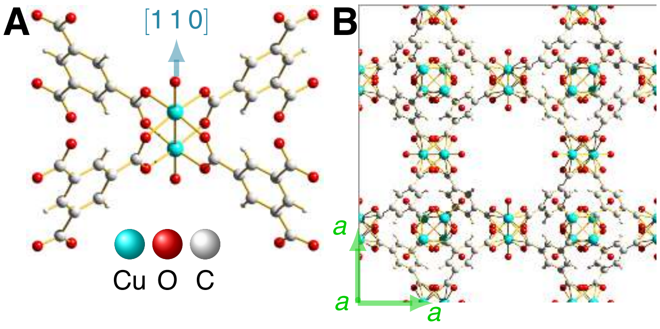

Fig. 2.11 PW structure and HKUST-1 unit cell: **(A)** Structural ball-and-stick presentation of a hydrated Cu / Cu PW unit in **2**. **(B)** Unit cell of hydrated $\mathbf{2}_{H_2O}$ with large cages and pores.

measurements of **1**.[153] The principal aim in the scope of this work has thus been to elucidate these unknown Cu^{2+} species and the results of this analysis will be presented in Section 4.1.

2.4.2 The Classical MOF HKUST-1 Revisited

One of the most well studied MOFs is $Cu_3(btc)_2$ (btc = benzene-1,3,5-tricarboxylate), also known as HKUST-1 in honor of its invention at Hong Kong University, and it is shown in Fig. 2.11.[135,145] It will be denoted as sample **2** and indices shall indicate the adsorption state. HKUST-1 is based on PW secondary building units with two Cu^{2+} ions (Fig. 2.11A) and forms a regular three-dimensional (3D) network with defined channels and cages (Fig. 2.11B). This MOF was among the first commercially available representatives of these hybrid materials with outstanding properties, as outlined before in Section 2.4.1.[146] Besides MOF-5,[159] HKUST-1 is also one of the best-studied MOF materials. The structure of HKUST-1 belongs to the cubic space group $Fm3m$ and it contains antiferromagnetically coupled Cu^{2+} ions which are coordinated in a square by carboxylate groups whereas ligand molecules weakly bind to the residual axial binding site of the Cu^{2+} ions after synthesis ($\mathbf{2}_{AS}$).[135,145] They can be easily removed from the Cu^{2+} ions by a moderate heat treatment in vacuum to form structurally well-defined accessible Lewis acid copper sites for catalytic applications.[134] The Cu^{2+} pairs are connected by btc linker molecules to form a 3D porous network with interconnected cages having two different pores ($d_1 \approx 0.9$ nm and $d_2 \approx 0.7$ nm measured between the oxygen atoms of the carboxylate groups). The cubic unit cell has a lattice constant of $a = 26.3$ Å.

Powder EPR Studies Within the wide variety of applications of MOFs, it is crucial to tune their chemical and physical properties without altering the underlying structural features. It has been shown, that this can be achieved by either manipulating the organic linker molecule[160] or by modifying the inorganic building unit. An example of the latter is the partial substitution of the metal species to introduce local probes or special adsorption sites.[161] It is possible to synthesize partially Zn^{2+} substituted HKUST-1 to form binuclear Cu / Zn PW building blocks (denoted as **3** here).[40] The Zn substitution offers the opportunity to explore Cu^{2+} adsorbate interactions and determine the structure of adsorption complexes. This is possible by the separation of the binuclear, antiferromagnetically coupled Cu / Cu PW to Cu / Zn PW units, such that the excited $S = 1$ electron spin state and an EPR silent $S = 0$ ground state are replaced by a mononuclear Cu^{2+} ion with $S = \frac{1}{2}$ ground state which is accessible by EPR spectroscopy at low temperatures with high polarizability.[150] The verification of such an isomorphous framework substitution has been shown by powder EPR spectroscopy for low Zn^{2+} concentrations and upon different gas adsorptions.[40,149,151,162] Despite the limitations set for studies of small, porous crystals discussed earlier, it is important to elucidate the structural changes upon gas adsorption in terms of the magnetic **g** and **A** tensor principal axis orientations by single crystal EPR. Hereby, it had to be considered that a single crystal of **2** or **3** with approximate dimensions of $200 \times 100 \times 100\ \mu m^3$ contains about 10^{14} unit cells, and therefore **3** contains almost equally many $S = \frac{1}{2}$ Cu / Zn PW with single Cu^{2+} spins, given that 3.5 % Zn^{2+} equals roughly one substitution per unit cell.[163] Given this content, effective single crystal EPR is not feasible with conventional cavity resonators at X-band frequencies, if different adsorption states and numerous crystals shall be measured angular-dependently with high angular resolution. This has been addressed for the first time in this work by DR-aided single crystal cw EPR as shown in Section 4.2.

Density-Functional Theory Calculations DFT was used to evaluate the **g** and HFS tensor principal axis values and principal axis orientations (Section 4.2.3).[163] In contrast to earlier results from powder EPR of purely axially symmetric tensors, the values found by DFT suggested a slightly rhombic deformation,[163,164] yet close enough to the powder EPR experiments published earlier.[40,149,151,162] Motivated by recent experimental findings from single crystal EPR,[163] DFT was used to optimize the structure of **3** to estimate the possible effects of the isomorphous framework substitution and gas adsorption on the ideal structure.

2.4.3 The New Thin Film Class SURMOF-2

Dimeric copper was also widely investigated in molecular magnetism[165] long before it became interesting in the MOF context. In numerous compounds, the spin-singlet state of dinuclear Cu^{2+} dimers was found to be the ground state with the triplet state becoming thermally populated at higher temperatures, leading to a characteristic broad susceptibility maximum.[166–169] Beyond this characteristic behavior, spin canting and ferromagnetic order in Kagomé lattices was reported.[170–172] While dinuclear Cu^{2+} complexes in MOFs typically show the characteristic Bleaney-Bowers behavior as outlined in Section 2.4.1, recently Shen et al.[136] observed ferromagnetism in several dinuclear Cu / Cu unit-based MOFs. The occurrence of this state depended on the nature of the non-magnetic molecular linkers, and it seemed that with extended π-electron systems these linkers were most effective in mediating ferromagnetism. In view of recent developments in the field of defect-induced ferromagnetism in semiconductors and graphene, a model for the ferromagnetic order based on localized spins generated by Cu vacancies was proposed by Shen et al.[136]

The Cu / Cu units of recently developed MOFs can be arranged in a zip-fastener fashion, allowing for the production of a quasi linear, 1D chain of copper ions.[139,173,174] This arrangement is of special interest for both application in spintronic and data storage,[175], and as model system for the theoretical description of magnetism in confined geometries. The first theoretical treatment of linear magnet arrangements was reported by Ising[176] and revealed that in a single, isolated 1D chain, no magnetic ordering is possible in the ground state. In contrast, in many 2D and 3D spin lattices, theory predicts well-defined phase transitions to a ferromagnetic state with a T_C depending on the magnetic coupling between the individual magnets. The

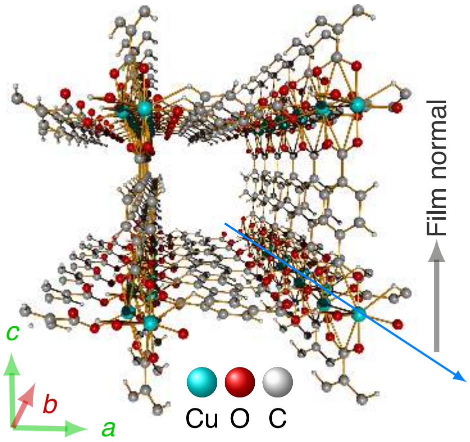

Fig. 2.12 Stacked thin film 2D layers and quasi 1D chain in structural representation of 4: Six stacked 2D-layers with 2×2 unit cells, each. In every unit cell, a Cu / Cu PW unit is accompanied by four half bdc linker molecules. The Cu^{2+} ion chain (blue arrow) is in-plane of the thin film, but normal to the 2D-layers. The quasi 1D Cu^{2+} chain are arranged in zipper-like fashion.

Ising-model is now one of the best-studied models in physics, and more recent work has revealed that 1D systems can also show ferromagnetism if the linear (or quasi-linear) chains are embedded in a host matrix providing very small, albeit finite, magnetic interactions.[177–180] However, a crystalline material which clearly exhibits 1D ferromagnetism at low temperatures in the absence of strong external fields and for which the T_C can be determined in a straightforward fashion has not yet been reported. Fe-MOF 74 is one example with anti-ferromagnetic ordering in its ground state but showing ferromagnetic behavior when exposed to high magnetic fields above 2 T with a very low transition temperature of $T_C \approx 13$ K.[181]

Shekhah et al.[173] introduced an easy-to-fabricate material class which is prospectively suited for application and carried out a more detailed magnetic-property investigation of the isoreticular series SURMOF-2.[174] The SURMOF-2 series can be fabricated in a straightforward fashion using a quasi-epitaxial liquid-phase process and has already led to six different members characterized by DFT and XRD.[174,182] In the next step, it is also required to investigate the magnetic properties of the SURMOF-2 class further. For this purpose, two different SURMOF-2 members with various thin film thicknesses have been synthesized. (Cu,bdc) SURMOF-2 (**4**) with the chemical formula $Cu_2(bdc)_2(H_2O)_2$ (bdc = benzdicarboxylic acid) was grown on a COOH-terminated Au substrate in a layer-by-layer fashion,[183,184] resulting in the characteristic Cu / Cu PW unit layer network shown in Fig. 2.12. The bdc linker can also be exchanged with other molecules, giving rise to different stacking distances of the Cu^{2+} chains. As the second member of the SURMOF-2 class, (Cu,bpdc) SURMOF-2 (**5**) with chemical formula $Cu_2(bpdc)_2(H_2O)_2$) has been investigated in this work. The bpdc-linker denoting biphenyl-dicarboxylic acid results in longer separation distances of 15.28 Å of the Cu^{2+} chains in each direction compared to those in (Cu,bdc) SURMOF-2 (10.71 Å).

In Fig. 2.12, (Cu,bdc) SURMOF-2 is shown with six layers weakly bound by antiferromagnetic coupling. The 2D-layers are fixed at one edge to the substrate and can be grown along the crystallographic [0 0 1] axis direction with a tetragonal unit cell of $P4$ symmetry with lattice constants $a = c = 1.071$ nm and $b = 0.58$ nm (b-axis in-plane) to several μm film thickness.[174] Perpendicular to these 2D-layers, a quasi 1D-chain of Cu^{2+} ions is formed. The refined structure shown here was derived from DFT calculations[139] following surprising observations obtained by EPR measurements on (Cu,bdc) SURMOF-2 (Section 4.3). A concluded ferromagnetic phase transition gave rise to the model outlined in Section 4.3.3.

3 Evaluation of Current Experimental Methods for High-Sensitivity X-Band EPR

3.1 Efficiency of Dielectric Resonators for CW X-Band EPR

3.1.1 Customization of Dielectric Resonators

To match the frequencies of the available spectrometer mw source (Section A.1 in the Appendix), the DRs must be suited for X-band frequencies between $9.1 \cdots 9.9\,\mathrm{GHz}$. The ESR 900 flow cryostat intended for the low temperature measurements (Section A.1 in the Appendix) supports cylindrical sample tubes of up to $5\,\mathrm{mm}$ outer diameter.[185] For a safe operation the DRs' outer diameter was fabricated with $\varnothing_{\mathrm{OD}} \leq 4\,\mathrm{mm}$ which enables the employment of quartz glass sample tubes with up to $500\,\mu\mathrm{m}$ wall thicknesses to accommodate the DR together with the sample in the test tube at non-ambient atmospheres. According to Eqn. 2.74 this geometry requires relative permittivities of the DRs of 70 or more to serve for X-band frequencies.

Two sets of DRs having $\varepsilon_r = 80$ and $\varepsilon_r = 85$ labelled K80-H and K85-H, respectively, have been selected for application in EPR spectroscopy. They are shown in Fig. 3.1A. The preparation and customization is described in Section B.1.2 in the Appendix. The mw properties of the coupled DRs are given in Tab. 3.1 and Tab. B.1 in the Appendix. Here, the typical DR K80-H is compared to a thin DR named K80-H' and the DRs without hole, K-80 and K-85 for comparison. It can be seen that the DRs in general maintain their mw properties also at low temperatures which makes them especially suited for these kind of experiments, provided they do not show unwanted paramagnetic impurities below $77\,\mathrm{K}$. The standing wave ratios allowing to estimate the cw coupling to the mw network (cf. Section B.1.1 in the Appendix) are excellent at room temperatures and drop towards lower temperatures. However, the DRs always stay closely coupled and will allow a sufficient mw signal being transmitted.[186]

Fig. 3.1B shows the lowest-frequency modes obtained in a boxed, antenna coupling for a closely shielded DR as depicted and explained in Fig. B.1A in the Appendix. Hereby, the DRs of types K80-H and K85-H revealed three modes in the frequency range from $8.5 \cdots 14.0\,\mathrm{GHz}$ and depending on the cylinder height L these frequencies could be tracked as shown in Fig. 3.1C(2, 5, 8). While Eqn. 2.73 shows no closer matching to these obtained values, Eqn. 2.74 from Kishk and Antar[95] shows good agreements to the $\mathrm{TE}_{10\delta}$ (3), $\mathrm{HE}_{10\delta}$ (6) and $\mathrm{TM}_{10\delta}$ (7) modes, which therefore could be assigned to the three modes observed in Fig. 3.1B. A special remark shall be given to Fig. 3.1C(1 and 4). The constant (1) sets a lower limit for the frequencies obtained for a DR in the cavity resonator (4), and because it is closest to the points (2) and approaches the fit (3) in the low height region, the obtained frequencies (4) have been attributed to the antiparallel coupled

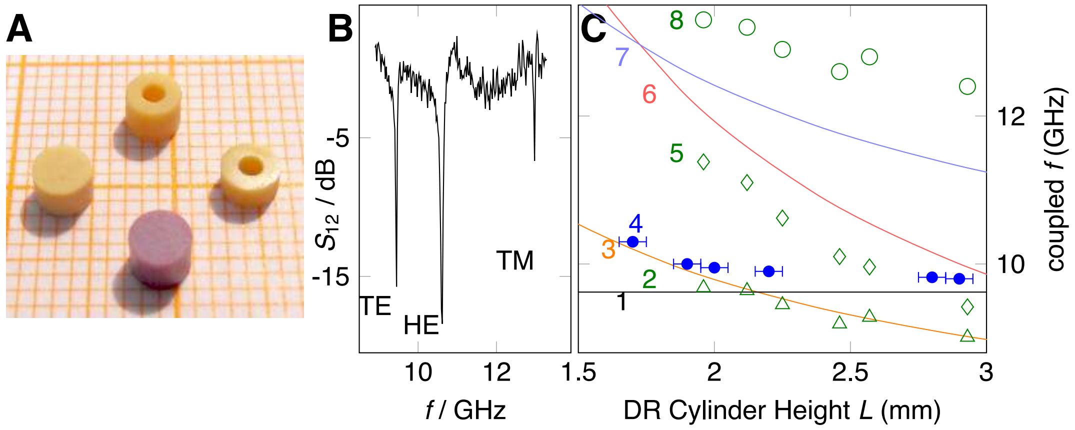

Fig. 3.1 Dielectric resonator microwave adjustments:

(A) Excerpt of tested DRs, clockwise from left to bottom: K-80, K80-H, K80-H’, K-85.

(B) S_{12} transmission measurement of mw modes of a K80-H showing the three modes with lowest frequencies assigned to $\mathrm{TE}_{10\delta}$, $\mathrm{HE}_{10\delta}$ and $\mathrm{TM}_{10\delta}$ modes according to the closer mapping given in

(C) The obtained frequencies versus DR heights in comparison to Eqn. 2.74: 1 empty cavity resonator, 2 boxed DR first mode, 3 $\mathrm{TE}_{10\delta}$ (Kishk and Antar[95]), 4 K80-H in cavity resonator, 5 boxed DR second mode, 6 $\mathrm{HE}_{10\delta}$ (Kishk and Antar[95]), 7 $\mathrm{TM}_{10\delta}$ (Kishk and Antar[95]), 8 boxed DR third mode . The term ’boxed’ refers to the experiment given in Fig. B.1A in the Appendix.

Tab. 3.1 Microwave parameters of dielectric resonators: DRs coupled to cavity resonator as explained in Section B.1.1 and Section B.3.2 in the Appendix. Errors $\Delta L = 0.05$ mm, $\Delta f = 5$ MHz.

resonant system	T [K]	ε_r	$2a$ [mm]	L [mm]	f_{boxed} [GHz]	f_{coupled} [GHz]	coupled Q	VSWR
empty cavity resonator	300					9.62	3400±50	1.005
	8						3400±50	1.03
K80	300	80	3.6	2.9	9.05	9.73	2300±50	1.025
	8						2400±100	1.060
K80-H	300			2.8	9.12	9.75	2500±100	1.095
	8						2500±100	1.160
K80-H’	300			2.0	9.74	9.89	1500±100	1.61
	8						2100±100	1.27
K85	300	85	3.4	2.8	9.14	9.86	2300±100	1.025

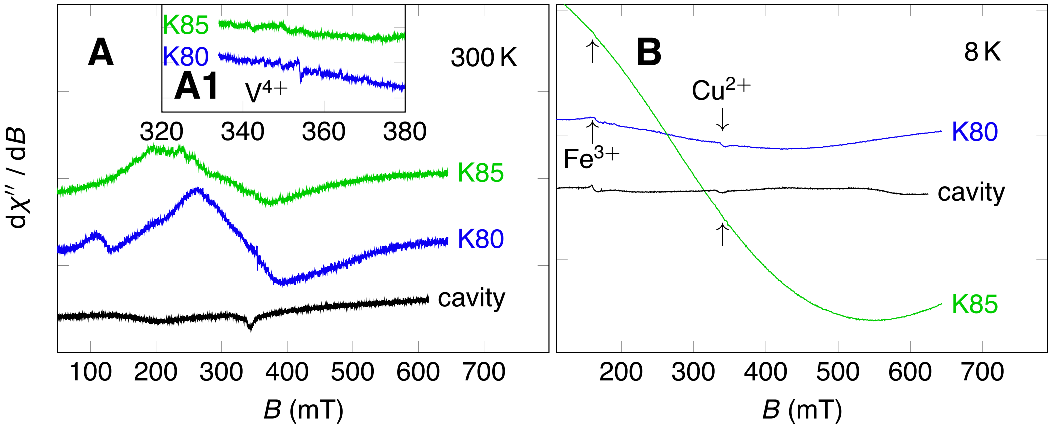

Fig. 3.2 Dielectric resonators materials' EPR spectra:
(A) X-band EPR spectra of K80 and K85 DRs as seen in the plots for room temperature (10 scans) including an inset showing more details around $g = 2$ and
(B) at 8 K sample temperature. The arrows in Fig. 3.2B indicate impurity signals from the resonator-cryostat combination and are therefore regarded as reference signals.

$TE_{10\delta}$ mode.[186] This matches the theoretical prediction by Golovina et al.[101] that with an iris coupling only one of the split modes can be excited. For more images of the actual DR employed in an EPR experiment refer to Fig. B.7 in the Appendix. In general, from the mw properties alone all tested DRs can be rated as excellently suited for EPR experiments and it remained to verify their EPR background signal at low temperatures.

3.1.2 The Background Signal

To obtain the desired mw characteristics the ceramics for DRs is doped by several transition metal ions and rare earth elements and some of them may give rise to paramagnetic impurities. EPR spectra of those impurities should be inexistent or, if this is not possible, must at least not interfere with the studied EPR signals in a broad temperature range. Therefore, EPR characterization of the used DR materials is inevitable and has been carried out incrementally.[187] Spectra for the final materials originating from a typically sized DR are given in Fig. 3.2.[186] At room temperature, the material with $\varepsilon_r = 85$ (K85) reveals almost no paramagnetic signals (Fig. 3.2A). A weak signal with a large peak-to-peak line width of $\Delta B_{pp} = 200$ mT of unknown origin can be subtracted from spectra as baseline correction. As seen from the inset in Fig. 3.2A some very weak remaining signals around $g \approx 2$ with a SNR of 1 or less are visible after 10 scans which cannot be attributed to any impurity directly. Furthermore, a small signal at $g = 2.92$ is visible; its intensity is comparable to that of the impurities in the cryostat and cavity resonator and therefore acceptable. However, at 8 K K85 has a very strong signal with $B_{\mathrm{pp}} = 480$ mT which is much more pronounced.

In contrast to K85, at room temperature the DR material with $\varepsilon_r \approx 80$ (K80) has some more of the broad signals and they are more intense than those of K85, among them the largest at $g = 2.4$ with $\Delta B_{pp} = 170$ mT.

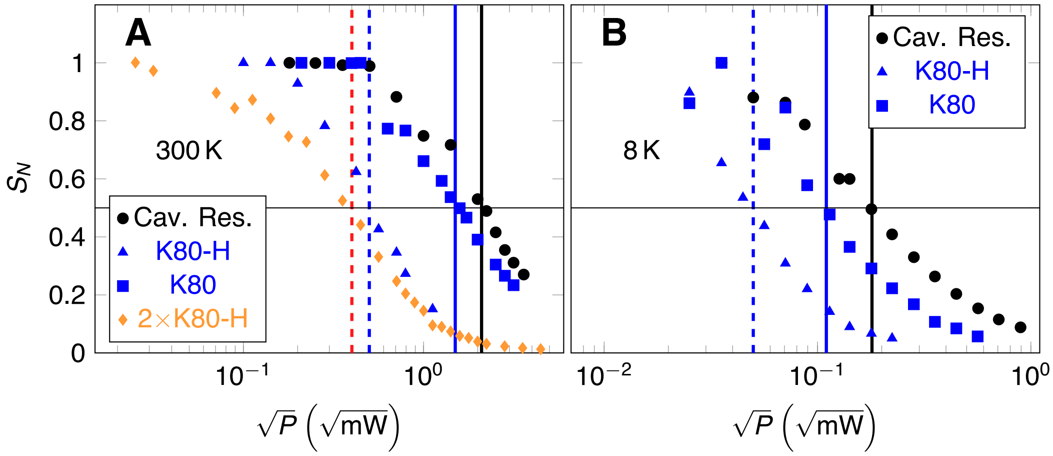

Fig. 3.3 Dielectric resonator rollover saturation curves: Rollover saturation curve of BDPA at **(A)** 300 K and **(B)** 8 K of the cavity-coupled DRs K80, K80-H, dual-DR combination (two K80-H) and the resonator-cryostat combination alone. $\sqrt{P}$ denotes the root of the incident mw power and $S_N = (S(P)/\sqrt{P})/(S(P')/\sqrt{P'})$ with a reference value $S(P')$ from a non-saturating low power P'.[189]

In addition, a weak signal at $g = 1.995$ could be attributed to V^{4+} as seen from the 8-line hyperfine pattern due to the $I = \frac{7}{2}$ nuclear spin of ^{57}V ($3d^1$, $S = \frac{1}{2}$)[188] with the approximate SNR of 1 after 10 scans (inset in Fig. 3.2A). At 8 K the spectra of K80 reveals a weak and broad signal of unknown origin with a g-value of 3.1 and a peak-to-peak line width of $B_{pp} = 330$ mT. Overall, the signal intensity of the signal in K80 is comparable to that from the Fe^{3+}-impurity in the cryostat as seen in Fig. 3.2B. The impurity signals at room temperature from K80 may possibly interfere with EPR spectra of interest at room temperature and hence K85 was better suited for room temperature measurements, whereas K80 DRs were selected for sensitivity enhancement investigations at low temperatures.[186]

3.1.3 Microwave Field Conversion

Relative mw conversion factors C_i/C_{ref} of the coupled DR systems in comparison to the resonator-cryostat combination have been determined by saturation experiments as proposed by Nesmelov et al.[189] Fig. 3.3 shows the rollover saturation curves of the DRs K80 and K80-H coupled with the cavity resonator,[186] and moreover, two DRs in an optimized relative distance which maximizes the magnitude of B_1. In Fig. 3.3 the normalized saturation powers per square root of the incident mw power of a BDPA sample are plotted versus the square root of the incident mw power. The DRs convert the mw power into stronger B_1 fields than the cavity resonator alone. The BDPA sample saturates at about 1.4 times smaller mw powers if placed on top of the DR K80 and at approximately 3.6 times smaller powers in K80-H (4.0 for two K80-H and close to that, but not shown, 4.2 for K80-H') than for the cavity resonator without DR. The C_i/C_{ref} are obtained by comparing the half saturation drop square root power values indicated by the vertical lines.[189] They are given in the second column of Tab. 3.2 in the next Section 3.1.4. A similar behavior is found for low

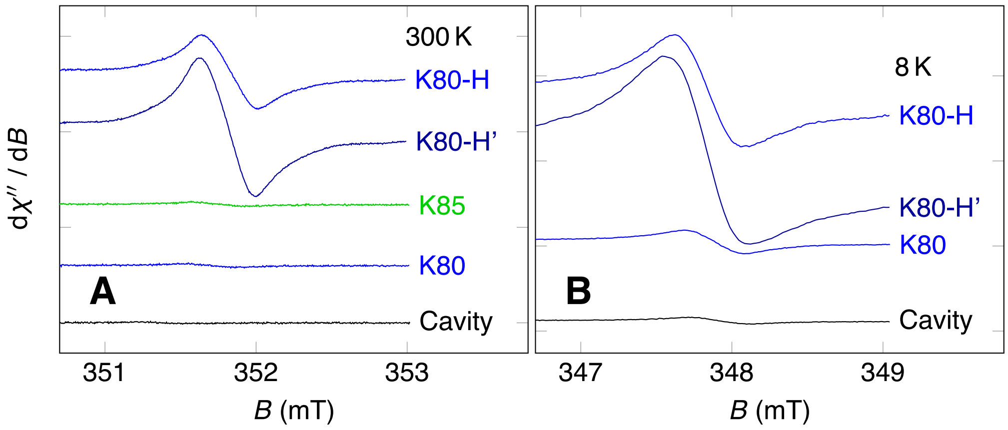

Fig. 3.4 Dielectric resonator enhanced EPR spectra of MgO :Cr^{3+}: EPR spectra of MgO :Cr^{3+} at 60 nW mw power at
(A) room temperature and
(B) 8 K sample temperature. The bottom spectrum in each plot represents the sample in the cavity resonator alone, above them in combination with the different DRs to scale within one temperature. All values are given in Tab. 3.2.

temperatures.[186]

In general, the DR behavior is similar at all temperatures, that means the order of B_1 field enhancement is the same within the assumed errors.[186] Among all tested DRs, K80-H' was the DR which enhances the B_1 field most (4.8 for K80-H' at 8 K). Smaller L lead to higher frequencies as expected from Eqn. 2.73 and higher C_i/C_{ref}. Those with higher ε_r and comparable geometry enhance the field slightly more, while a hole enhances the field significantly more because of the more suitable position of the sample.[111] The relative stability of the C_i/C_{ref} as well as f_{coupled} and Q at all measured temperatures (Tab. 3.1) supports the small temperature dependencies of the dielectric constant and loss tangents reported for the DR material.[100] In the following, this conversion factor is taken into account in all discussions, although the figures for the SNR enhancements are not normalized with respect to C_i/C_{ref} on purpose.

3.1.4 EPR Performance of DRs at Room and Low Temperatures

As seen above, ring DRs with a hole in their middle can be used to achieve a much stronger B_1 field,[111,186] and even two DRs can be employed to maximize B_1 if desired. This feature helps to suppress signals from impurities outside the DR; furthermore, a ring can be fixed and mounted very easily as seen in Fig. B.7 in the Appendix. In contrast to disks, rings suppress higher modes, while the $TE_{10\delta}$ is mainly unaffected.[95] With these apparent advantages of ring shaped DRs it was predicable that this type would rule out the disk DR, which has been checked experimentally.[186]

The performance of the coupled DRs in the cavity resonator equipped with cryostat was tested with a MgO :Cr^{3+} sample with a moderate number of 10^{14} spins at room temperature, 77 K and 8 K.[186] The signal enhancement for a selection of the investigated DRs at room temperature is depicted in Fig. 3.4A and the

Tab. 3.2 Conversion factors and SNR gain of dielectric resonators: C_i/C_ref, absolute and normalized SNR gains of the different DRs and different cavity resonators at two selected temperatures. All DRs tested in combination with rectangular cavity resonator.

Resonator	C_i/C_ref	SNR Gain **300 K**	Norm. Gain	C_i/C_ref	SNR Gain **8 K**	Norm. Gain
ER 4102ST	1	1	1	1	1	1
ER 4119HS	2.2	4.8	2.2	5	8	1.6
ER 4122SHQ	2.5	6.6	2.6			
K80	1.4±0.2	2.2±0.4	1.6±0.4	1.6±0.3	1.8±0.2	1.1±0.3
K85	1.5±0.2	2.8±0.5	1.9±0.5			
K80-H	3.6±0.4	40 ±3	12 ±2	4.2±0.5	36 ±2	8.5±2
K80-H'	4.2±0.5	80 ±3	19 ±3	4.8±0.6	74 ±3	15±2

SNR enhancements achieved in these EPR measurements are summarized in Tab. 3.2.[186] As expected, K80 performs worst and has an absolute enhancement of 2.2, normalized by C_i/C_ref this corresponds to a normalized gain in the SNR of only 1.6. The DRs with higher ε_r (K85) have only a slightly higher gain in SNR which is not significant regarding the errors. Still, due to the lower background signal at room temperature, the K85 series was considered as better suited for room temperature measurements. It must be assumed that the actual SNR gain for larger samples can be less if their size extends from the center of the disk shaped DRs such as thin films. The ring DRs K80-H and K80-H' perform significantly better, if the sample is placed well centered inside the hole. This observation has been stated by several authors before.[94,97,105] The absolute SNR enhancement for the highest gain of K80-H' corresponds to a factor of 80 compared to the cavity resonator without additional DR and is the highest achieved factor at room temperature as well as the relative SNR enhancement of 19 which is the highest increase that was achieved with the DRs at room temperature. The DRs K80 and K80-H/ K80-H' were also investigated at low temperatures with the $\mathrm{MgO{:}Cr^{3+}}$ powder sample while K85 is not suited for these measurements due to the background signal at low temperatures. For multiple DRs no increased normalized SNR has been found. At 8 K the observed signals shown in Fig. 3.4B are, partly more pronounced than at room temperature in accordance to the slightly enhanced Q-values in Tab. 3.1. Again, the DRs with smaller L perform somewhat better in general and the highest SNR gains are likewise obtained for K80-H' as in the room temperature experiments and experiments at 77 K (not shown).[186] Overall, room and low temperature experiments lead to comparable and very constant results.

It has been confirmed experimentally that our DRs enhance the SNR without affecting the noise in a wide temperature range.[186] They perform best if they are shaped like a ring and the sample is positioned in the middle of its symmetry axis as it has been theoretically derived with CMT.[117] Hence, DRs are most useful for the applications involving samples with small volume such as small single crystals as proposed by Golovina et al.[101] and Nesmelov et al.[189] but may also be helpful for thin films to some extent. In accordance to Nesmelov et al.[189] and del Monaco et al.[110] we find an increase of C_i/C_ref of about 4 to 5 for the ring shaped DRs, meaning an enhanced B_1 field at constant incident mw power compared to the cavity resonator alone. The B_1 field can further be enhanced by using multiple DRs as the usage of two K80-H has shown (Fig. 3.3), however no further increase in normalized SNR is observed for this combination. Thinner DRs results in higher B_1 field gains. As the study has shown, our DRs are suited for a large magnetic field and temperature range regarding residual impurities and SNR enhancements with a gain of more than 75 at all temperatures of which a normalized gain of more than 15 is not due to a higher ratio of C_i/C_ref but presumably a higher filling factor.[186] At temperatures below 77 K it was found that the DRs show slightly less SNR enhancements which might be due to increasing $\tan\delta$ as seen from Tab. 3.1 with the VSWR which shows worse couplings at lower temperatures. Otherwise, from 300 to 8 K the ratio C_i/C_ref is constant within the order of errors supporting the high stability on temperature τ_ε reported for the material.[100]

In all studied cases a significant shift of f_coupled matched with the cavity resonator towards higher resonance frequencies in comparison to the cavity alone was found.[186] This effect agrees well with the observation of Golovina et al.[101] and points towards a $\mathrm{TE}_{10\delta}$ mode coupling antiparallel with the cavity mode. With the DRs coupled in cavity resonators, no further modes within a reasonable range of 1 GHz is observed, which represents a benefiting situation for the suppression of unwanted mw power distribution into different modes for narrow band cw EPR measurements. Additionally, from experiments with non-centered DRs and larger DR diameters from other DR prototypes not presented here it has been confirmed that the VSWR coupling can be improved by larger DRs, suggesting that it is the electric field component not present in the center of a cavity resonator that leads to an excitation for these DRs. Obviously, because of the relatively small diameter of the K80-H DRs and the small field overlap with a cavity mode the coupling therefore is a compromise devoted to the required dimensions. The full potential of ring DRs is exploited for very small samples not only because of the immanent signal enhancement. Another advantage is the fact, that the higher C_i/C_ref only leads to stronger mw fields near the sample which has been calculated with CMT also.[115,116] Therefore, the actual SNR increase in comparison with unwanted impurity signals from the cavity or cryostat may be even higher than the normalized numbers we give in Tab. 3.2. In fact, as shown in Fig. 3.5, the DRs K80-H may save several hundreds of accumulations for very small samples. Here, the Cu^{2+} EPR spectrum of the single crystals of ${}^3_\infty[\mathrm{Cu^I}_2\mathrm{Cu^{II}}_2(\mathrm{H_2O})_2\mathrm{L}_2\mathrm{Cl}_2]$ (**1**) presented in Section 2.4.1 is shown to illustrate this effect. It was recorded under correction for C_i/C_ref, such that significantly less signals from the Cu^{2+} impurities in the cryostat contributed to the spectrum. Nevertheless, the ${}^3_\infty[\mathrm{Cu^I}_2\mathrm{Cu^{II}}_2(\mathrm{H_2O})_2\mathrm{L}_2\mathrm{Cl}_2]$ signal becomes clearly visible already after only some, few accumulations, facilitating the efficient angular dependent spectrum recordings presented later in Chapter 4. Above of that, it has been found that the optimal position of the DR in a cavity resonator can very easily be found by inserting the DR into the cavity (which increases the joint frequency) just to the point when the coupled frequency reaches a maximum. Then the DR is exactly in the middle of the cavity resonator, which ensures automatically that the tiny sample is at an ideal position for the $\mathbf{B}_0$ field modulation (Section 2.1.3) and additionally, the sample is automatically at an ideal position of maximum $\mathbf{B}_1$ (if it was placed there within the DR initially). These features may ensure a successful measurement of very tiny samples with low spin densities also for non-experienced experimentalists. Note that this advantage and the easy handling is lost upon the usage of several DRs within one experiment, such as two K80-H as shown above in Fig. 3.3. Here, the second DR is found to act mainly as a frequency tuner and to achieve significantly higher SNR the first DR housing the sample is not necessarily in a corresponding position to the modulation coils,[111] which is why these combinations have not been studied further. Finally,

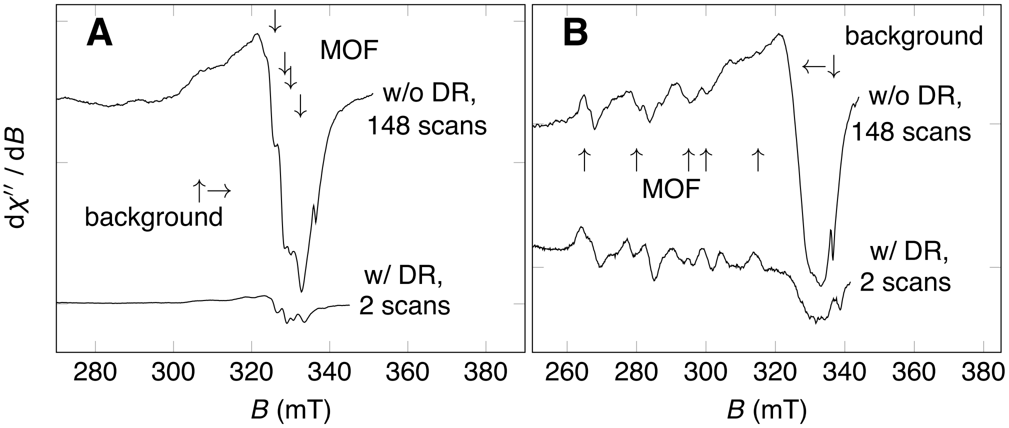

Fig. 3.5 Dielectric resonator background noise suppression: EPR spectra of single crystal of **1**
(A) with $\mathbf{B}_0$ in ac plane, aligned with the c axis,
(B) $\mathbf{B}_0$ aligned with a axis, measured without DR (upper spectra) and with DR (lower spectra), both including all background noise. The signals are normalized to the Cu^{2+} HFS lines of the crystal and adjusted to correct for the frequency offset. Note that the DR does not add noticeable background noise, while the lowered mw power (62 μW versus 1.1 mW) reduces the Cu^{2+} powder spectrum from the cryostat impurities, which are not to be confused with the signal of interest.

the samples can be kept in thin quartz capillaries for EPR measurements under non-ambient atmospheres in a wide temperature range and an easy transfer to investigations with other methods such as XRD analyses is still possible. Therefore, the application of DRs in cw EPR measurements is extremely useful for efficient studies of small samples with low spin concentrations under non-ambient atmospheres and variable temperatures even at X-band frequencies.[186]

3.2 Implementation of Planar Microresonators in X-Band EPR

3.2.1 The X-Band EPR Probe Head in the Microwave Network

Planar Microresonators Setup Evolution To implement the PMR into an EPR spectrometer setup a scaffold as resonator holder connected to a helium-tight head for cryostats of the OXFORD CF-Series (Section A.2) has been constructed. It is shown in Fig. 3.6A and has been used for the entire measurement series with adoptions (Fig. 3.6B) for the various PMRs (Fig. 3.6C). The framework is also supposed to guide all necessary mw and RF wiring and keep the modulation coils and possible matching mechanics at the right position with respect to the PMR. The general design approach differs from the setup of a fixed resonator, in which the sample usually can be rotated in its EPR sample tube to acquire angular dependent spectra as it will be shown in Section 4.1 and 4.2 for the spectra received with the help of the DRs presented in the previous Section 3.1. In contrast, now the sample attached to the PMR has been supposed to remain in a fixed position due to the reasons explained in Section 2.3.2.

The construction constraints have been eased as the external magnets generating $\mathbf{B}_0$ available in this work

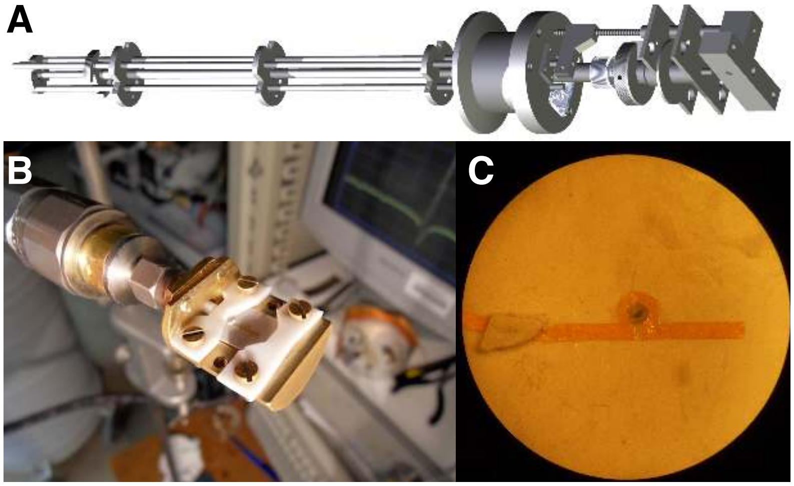

Fig. 3.6
First general planar microresonator setup: Release R1 with PMR T1.
(A) Exploded view of cryostat inset for flow cryostats of OXFORD CF-Series used for all PMR coupling setup releases R1 – R2.1.
(B) PMR coupling R1 with PMR type T1.
(C) PMR T1 (A41) with DPPH sample incorporated in Ω-loop and tuning cover sheet to the left.

are revolvable themselves around the cylindrical CF cryostats and may therefore compensate for the issue of the fixed sample in the PMR. However, to realize cw EPR, also the modulation coils close to the PMR are required to follow the orientation of $\mathbf{B}_0$ and additionally, they must be designed such that the sample can be easily manipulated in the PMR or the whole PMR can be replaced quickly in the entire setup. For that

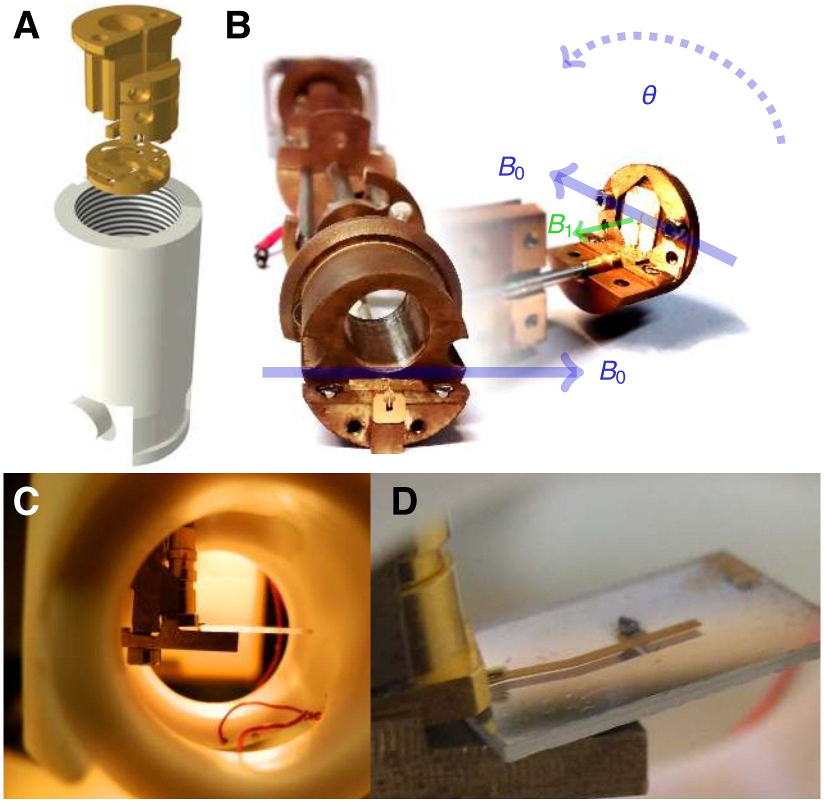

Fig. 3.7
Later releases of planar microresonator setups: Releases R2 and R2.1 with PMR T1 and T2, resp.
(A) Exploded view of mount for PMR coupling to waveguide R2 with PMR of type T1: brass parts fixing semi rigid wave guide, mSMP coupler and PMR (yellow), revolvable modulation coil holder (white).
(B) The new setup allows for a 90° turn by mSMP couplers facilitating modulation coils which can turn by θ around the PMR's $\mathbf{B}_1$. Note the permanently perpendicular external $\mathbf{B}_0$ field.
(C) Coupling R2.1 with new PMR T2 (5A26) with sapphire substrate seen though new modulation coils.
(D) Setup R2.1 with PMR T2 seen in iso top view with large DPPH crystal in Ω-loop.

purpose, the modulation coils are separated from the PMR holder itself and mounted on a cylindrical shell as shown in white in Fig. 3.7A, which is in some limits revolvable around the inner construction. The idea is to leave the coupling of the PMR constant by not moving or turning it itself with respect to the sample but turning the modulation coils inside the cryostat and the external magnets outside the cryostat. The inner scaffold (brass color in Fig. 3.7A, photo composition in Fig. 3.7B) holds the PMR with sample, the mw guide and a matching mechanism.

The first setup shown in Fig. 3.6B involved a massive brass body, keeping the SMA bulkhead jack and PMR in place and in direction of the semi rigid waveguide. This setup release R1 with the first stage PMR T1 by D. Suter et al. (see Appendix, Section B.6) followed the recommended design guides given so far,[128,129] but did not allow for angular dependent measurements with respect to $\mathbf{B}_0$ due to the smaller footprint of the used cryostat and the special requirements of a fixed sample with respect to the PMR. To keep $\mathbf{B}_1$ perpendicular to $\mathbf{B}_0$, only one possible orientation of the setup in the cryostat was allowed.

To overcome this limitation, a second setup R2 depicted in Fig. 3.7B replaced the SMA jack with a Mini SMP (mSMP) PCB straight plug with significantly smaller footprint resulting in a 90° turning of the mw propagation. With this, $\mathbf{B}_1$ can point in the same direction as the semi rigid mw cable, along the cryostat. Then $\mathbf{B}_0$ can be rotated around this axis without violating a central selection rule of EPR, Eqn. 2.12: $\mathbf{B}_1 \perp \mathbf{B}_0$. This construction principle has been maintained in a revised setup R2.1 depicted in Fig. 3.7C-D, which will be explained in more detail below.

Microwave Properties of the Setups As a benefit of the improvements to R2, a better coupling was achieved with mSMP plugs instead of the previously used SMA plugs. Fig. 3.8A shows a comparison of the old coupling with a SMA plug versus the new one, involving mSMP plugs at room temperature and compares these S_{11} reflection parameters to the actual setups with all mw wiring necessary to work at the spectrometer, R1 and R2, respectively. It can be seen, that the actual implementations in the spectrometer lead to various mw reflections in the cables and plugs, imitating high-quality resonant structures. At this point, however, it can be stated already that tuning the spectrometer on such a peak does not enhance the sensitivity of the cw EPR measurement. Instead, the SNR is governed by the underlying Q of the PMR. This is shown in Tab. B.3 in the Appendix, comparing the SNR of various, narrow S_{11} reflections around the actual mode frequency. As it can be seen, the SNR is not correlated to the quasi-quality factors of the reflections, but instead resembles the inherit S_{11} curve of the PMR. It is further important to note in Fig. 3.8A that the better S_{11} reflection parameter of the new, mSMP coupling compared to the old, SMA coupling does not result in a narrower frequency dip at a half-power drop, $-3\,\mathrm{dB}$ reflection level, i.e. the characteristic width of the curve remains constant and with it Q. It can be seen, that sharp quasi-resonances in R1 and R2 are not leading to higher SNR gains but are just apparent reflections on top of the low quality ($Q = 24$) PMR S_{11} response. In fact, they do not even necessarily match the resonance frequency of the PMR itself. From here it could be concluded that the measurements should to be performed close to the actual frequency with a tolerance of about $\pm 50\,\mathrm{MHz}$. Due to the low Q of the PMR all achieved SNR values within a tolerable range with respect to the best value can be regarded as acceptable.

During the experiments with setup R1, the PMRs of series T1 decreased significantly in quality, such that

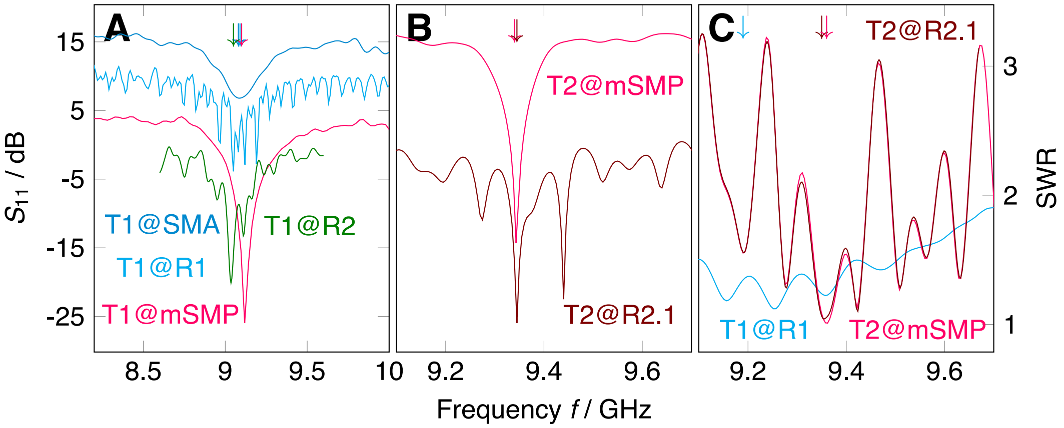

Fig. 3.8 Microwave characteristic improvements of PMR setups: Releases R1 through R2.1 with PMR T1 and T2, resp. The arrows ↓ mark the PMR resonance frequencies.
(A) From top to bottom: S_{11} coupling (blue) of the PMR T1 to a SMA-microstrip waveguide transducer measured directly, (cyan) as seen through actual wiring in setup R1, (red) with mSMP-coupler directly, (green) PMR T1 in actual wiring of setup R2.
(B) S_{11} of (red) empty PMR T2 (5A26) coupled via mSMP and short wiring to network analyzer versus (brown) implementation of T2 in improved setup R2.1 with small DPPH sample in Ω-loop as seen by the spectrometer through all microwave wiring of the probehead.
(C) Standing wave ratio (SWR) of (red) empty PMR T2 and (brown) PMR T2 with small DPPH sample via R2.1 at the spectrometer versus (cyan) T1 in setup R1.

even the improved setup R2 involving the new designed mSMP coupling was not able to improve the cw EPR results, as it will be shown below. During the fabrication time of improved PMRs on a sapphire substrate, labeled T2 here, also the modulation coils have been improved, as recorded spectra have shown that the line width of a DPPH sample could not be improved above 0.12 mT. The results from setups R1 – R2 lead to an improved probehead R2.1 as seen in Fig. 3.7C-D, which could be employed with new PMRs of type T2. Fig. 3.8B shows the S_{11} mw reflection of the new PMR at mSMP plug. The coupling could be repeatedly optimized to achieve S_{11} curves in the complete probehead R2.1 almost identical to the bare mSMP coupling. Note however, that the underlying Q of the PMR cannot differ between the direct coupling (T2@mSMP) and the implementation of T2 in the probehead R2.1 either but the plot resembles most likely reflections in the cable, imitating a high apparent Q value with no additional SNR gain on its own.

A significant difference in the interplay of PMR T2 with the improved setups versus PMR T1 with probehead R1 can be seen in Fig. 3.8C. The SWR of R1 was significantly worse (around 1.2), while T2 in combination with mSMP-jacks is almost ideally close to 1 with and without wiring in setup R2.1. The mode at 9.345 GHz shows an excellent absorption of $S_{11} = -28$ dB and $Q \approx 60$. This mode can be found safely in a typical EPR spectrometers tuning procedure. It is still wide enough to avoid dispersion observations even without the usage of an AFC. Together with improvements of the modulation coils PMR T2 in setup R2.1 was therefore more likely to receive valuable SNR gains compared to other, leading sensitivity enhancing X-band cw EPR techniques and the current publications on PMRs.[128,129]

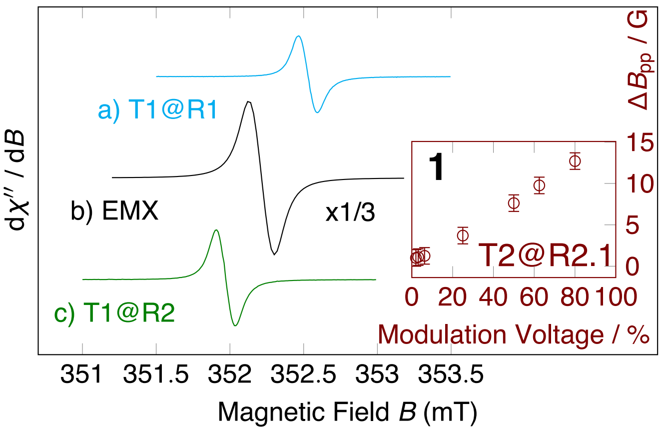

Fig. 3.9 First cw EPR tests and improvements: (a) Release R1 with PMR T1 versus (b) BRUKER high sensitivity cavity and (c) setup R2 with PMR T1 lacking competitive SNR gains.
(1) The inset shows the improvements made for the $\mathbf{B}_0$ modulation field in setup R2.1 which is now linearly increasable to 1.5 mT.

3.2.2 Planar Microresonators for CW X-Band EPR at Room Temperature

Successive improvements of the coupling lead to significantly increased S_{11} parameters and much more ideal standing wave ratios. While the first setup with a flat pin coupling to the microstrip lacked a decent mechanical connection, later probe head setups failed due to the decreasing qualities of the first batch PMRs over time. Now, the latest setup R2.1 joined by the latest PMRs of type T2 is delivering an overwhelming S_{11} reflection suitable for cw EPR. The first actual cw EPR measurements with PMRs of type T1 are depicted in Fig. 3.9(a) versus an experiment with the same DPPH sample of about 10^{16} spins in a BRUKER high sensitivity cylindrical cavity at an EMX spectrometer in Fig. 3.9(b). The recorded spectrum (a) shows the typical first derivative cw EPR line shape of the $S = \frac{1}{2}$ radical sample but did neither resemble the same line width, nor could it compete with the SNR of the cavity resonator.

The new setup R2 with the same PMRs T1 presented in Fig. 3.9(c) did not result in a better SNR either for the DPPH spectrum. Also, the modulation field strength was limited to the same small value of about 0.1 mT for reasons outlined above. In the measurements with PMR T1 in setup R2 the influence of the incident microwave power, the modulation field amplitude and the SNR were tested in more detail. The DPPH sample shown in the Ω-loop of Fig. 3.6C with about 10^{16} spins shows saturation above 2.5 mW at 9.038 GHz. In the cylinder resonator BRUKER ER 4119HS this happens at 80 mW which can give a rough estimate of the power conversion factor of the PMR T1 as factor of 30. The power conversion factor for the final setup has been determined with higher precession and will be presented below. The new mSMP coupling improved the line shape symmetry compared to the previous probehead R1. The SNR is increased slightly to about 1270. The line width of 1.280 G corresponds to a 0.1 mT modulation in a calibrated BRUKER cavity resonator at an EMX spectrometer. There, the SNR is 2510 with the same modulation and mw power at the same sample. After all, the observed spectrum of the DPPH sample in PMR T1 at setup R2 is of acceptable SNR compared to a current high sensitivity cavity resonator but does not enhance this value. Also, the high power conversion does not point to an efficient SNR gain and makes it in contrary difficult to measure strongly saturating samples such as BDPA.

During the development of R2.1, the modulation coils have been enlarged and narrowed such that tests with the line width of a smaller DPPH sample with about 10^{15} spins lead to improvements with the measured line

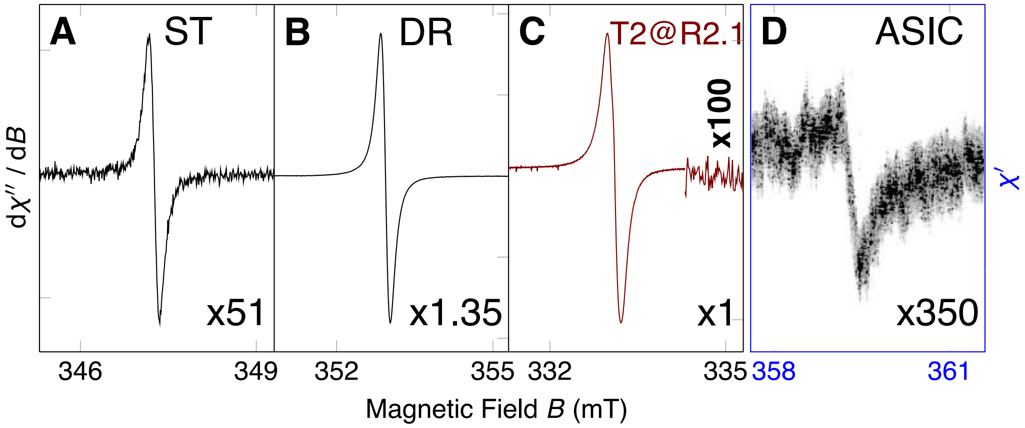

Fig. 3.10 Final cw EPR SNR comparison: Releases R2.1 with PMR T2 versus other high sensitivity techniques with highest absolute SNR gain per single scan without $\mathbf{B}_1$ field correction.
(A) Regular cavity resonator BRUKER ER 4102st with EMX spectrometer.
(B) DR K80-H in latter cavity resonator at same EMX spectrometer.
(C) PMR setup R2.1 at VARIAN spectrometer.
(D) Application specific integrated circuit (ASIC) cw EPR spectrometer in directly detected dispersion without modulation. It is shown in Fig. B.3C in the Appendix.

width ΔB_{pp}, which was compared to the simulated line width.[42] The result is shown in the inset of Fig. 3.9 and Fig. A.1 on page 93 in the Appendix. With the new setup R2.1 and the improved modulation coils the second PMR batch T2 could benefit from the experience gained with the first PMRs. Fig. 3.10A shows the cw EPR spectrum of a small DPPH radical sample with about 10^{15} spins recorded with a single scan in a rectangular BRUKER standard cavity resonator at an EMX spectrometer. For comparison, Fig. 3.10B shows the same sample encapsulated by the DR K80-H presented in the previous Section 3.1. As expected, the SNR was about 38 times higher as there was no correction for the incident mw power in this experiment. Ultimately, the PMR setup R2.1 with recent sapphire PMRs T2 could record a signal from the same small DPPH sample. The spectrum shown in Fig. 3.10C shows this single scan spectrum with a SNR gain of 51 compared to the rectangular standard cavity. Again, this spectrum was recorded with the same mw power with no correction for the conversion factor but adjusted modulation field strength to obtain the same line width. For comparison, in the high $\mathbf{B}_0$ field region of Fig. 3.10C the noise level of a spectral region away from the signal recorded with 100 times higher receiver gain ins shown to justify the noisy trace of the main graph. This is necessary, as all spectra are compared with the help of the same noise level but recorded with differently accurate analog-digital-converters as outlined in Section A.1 in the Appendix.

Fig. 3.10D gives another current approach for high sensitivity EPR. The device is shown in Fig. B.3C in the Appendix and the spectrum here displays the same sample recorded with an on-chip EPR spectrometer by J. Anders et al. used in its simplest working principle without lock-in modulation as direct detection of the frequency dispersion χ'.[123] The dispersion has been acquired at constant frequency of 10,068.48 GHz in a magnetic field sweep and due to the missing modulation and detection of χ' instead of absorption χ''

is differs significantly from a regular EPR spectrometer. However, it is remarkable that the detection of the small DPPH sample is possible although the missing lock-in modulation in this work leaves the on-chip spectrometer lagging significantly behind its potential.

With the recorded spectra from R2.1 and the spin number of 10^{15} spins one can estimate a spin sensitivity according to Eqn. 2.49 with the DPPH line width of $0.19\,\mathrm{mT}$ to be about $10^{9}\,\mathrm{spins}/(\mathrm{G}\times\mathrm{Hz}^{1/2})$. [28] This matches with the reported spin sensitivity of Narkowicz et al. [128] of a smaller Ω-loop PMR of batch T1. Most importantly, the new setup R2.1 with new PMRs T2 is significantly better suited for cw EPR measurements than what was previously realized in this work. Furthermore, the quality of the PMRs allows for a stable, over and over identifiable PMR mode even after multiple sample exchanges in the setup. From the saturation power P_{sat} measured for the small DPPH sample one can estimate that the $\mathbf{B}_1$ field is approximately 40 times larger in the PMR than in the rectangular cavity resonator. Various tests with differently shaped DPPH samples have confirmed the inhomogeneous $\mathbf{B}_0$ field distribution in the Ω-loop of the PMR. Larger samples filling the loop were observed to produce inhomogeneously broadened lines due to this field inhomogeneity. Therefore, the SNR gain of 51 presented above has not to be regarded as a maximum. Even smaller, planar samples with diameters below $50\,\mu\mathrm{m}$ (one tenth of the loop diameter) were observed to enhance the SNR – depending on the position in the loop – by up to three times more than reported above and it is likely, that the EPR signals from even smaller samples can be enhanced even more in comparison with conventional cavity resonators. Then it is also likely, that after a correction for the power conversion an efficient usage is possible for cw EPR. In the Appendix in Section A.2 an additionally tested sample is documented.

3.2.3 Planar Microresonators for Pulsed X-Band EPR at Room Temperature

The low quality factor of PMRs suggests a primary application in pulsed EPR instead of cw operational modes. [128,129] While in the scope of this thesis no pulsed EPR measurements have been conducted for the investigation of those samples presented in the next chapter, Section 4.1 – 4.3, the typical pulsed methods were aimed to be included in the PMR implementation research. The preliminary probehead releases R1 and R2 in connection with a PMR of the first batch, T1, was tested without success for a signal reception. Even worse, the narrow quasi-resonances observed for the unmodified setups R1 through R2 shown in Fig. 3.8A and especially in R2.1 (Fig. 3.8B) prevented the effective usage as pulse setup, giving rise to drastic ringing during echo detections. It can be assumed that the ringing is caused by reflections at badly matched cable junctions and plugs rather than high quality resonant structures, nevertheless it was obvious that more efforts would be needed to improve the mw wiring.

The first success was achieved with a setup combining the new PMR T2 with a modified R1 probehead involving high quality mw cables and the SMA-flat pin coupling leading essentially to a S_{11} reflection as that of T1 with SMA coupling (top curve in Fig. 3.8A). The setup is shown in Fig. A.2 on page 94 in the Appendix. This is possible as no modulation coils are needed for pulse EPR, restricting the space left for the PMR probehead otherwise. With this setup and a Q of 60 for PMR of type T2, no ringing was observed for any incident, pulsed mw power at all. Fig. 3.11 shows the echo detected two-pulse field sweep absorption spectra of a micro crystalline diamond single crystal sample with implanted substitutional nitrogen (P1 defects) in

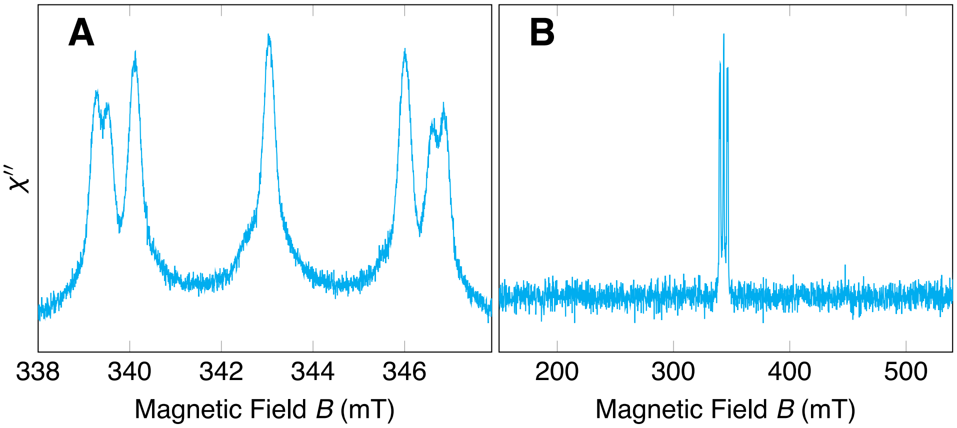

Fig. 3.11 Pulsed field sweep with PMRs: Modified release R1 with PMR T2 via high quality 3.5 mm mw wiring.
(A) Echo detected 2-pulse 2-phase cycling field sweep electron spin echo (FS ESE) spectrum of the nitrogen P1 defect in a single micro crystalline diamond crystal sample shown in Fig. A.2 on page 94 in the Appendix.
(B) The larger scan range shows the EPR silent substrate of PMRs T2. The measurement conditions are given in Section A.3 in the Appendix.

a wide and more narrow field range spectrum, displaying the three ^{14}N ($I = 1$) HFS lines of the $S = \frac{1}{2}$ defect center incorporated at four magnetically inequivalent lattice sites.[190–192] There are no signals visible except from the micro crystal which is depicted in Fig. A.2 on page 94 in the Appendix. The measurement conditions and pulse sequence specifications are given in Section A.3.

Fig. 3.12 shows the time traces of two-pulse and three-pulse electron spin echo envelope decay experiments of the latter diamond crystal. The plots reveal the typical exponential decay of the real part of the acquired data.

Tab. 3.3 shows the pulse EPR travelling wave tube amplifier (TWT) attenuation in logarithmic units of the PMR setup versus the standard BRUKER pulse resonator type. The high attenuation even at shortest pulse lengths shows the high $\mathbf{B}_1$ power conversion leading to high bandwidth and large power reserves. In particular, comparing the TWT attenuations at a 30 ns $p_{\frac{\pi}{2}}$ pulse one obtains a power ratio of

$$\frac{P_{\mathrm{PMR}}}{P_{\mathrm{MD5}}} = \frac{34\,\mathrm{dB}}{6\,\mathrm{dB}} \approx \frac{2500}{4} = 625, \tag{3.1}$$

which means that the PMR saves almost three orders of magnitude in power amplification. The conversion factor for the $\mathbf{B}_1$ field is according to Eqn. 2.32 about 25 times higher than with the BRUKER standard MD5 resonator.

The presented electron spin echo (ESE) experiments with the applied amplifier attenuations in Tab. 3.3 show the principle applicability of the PMR setups for pulsed EPR and confirm the high potential for this field from the excellent power conversion factors, high filling factors and low Q factors predicted by Narkowicz et al.[128]. An evaluation of the PMR measurements in comparison to other, high sensitivity measurement methods will be given in Chapter 5.

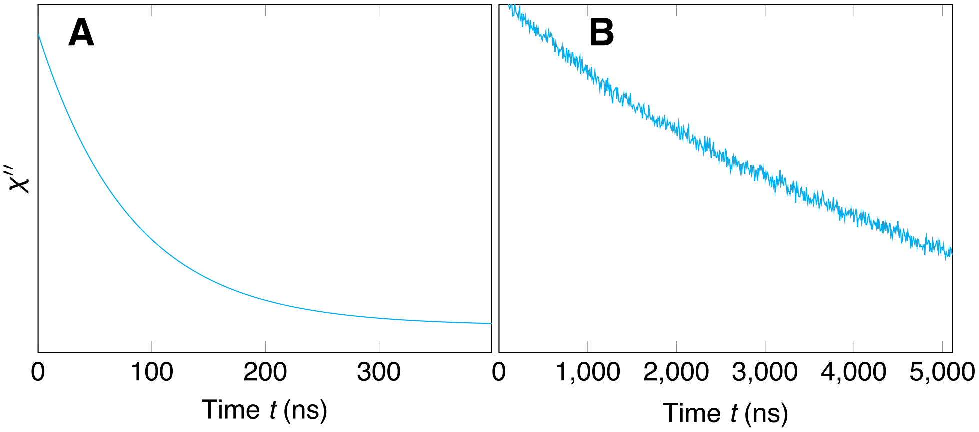

Fig. 3.12 Pulsed ESEEM with PMRs: Modified release R1 with PMR T2 via short SMA mw wiring.

(A) 2-pulse 2-phase cycling electron spin echo decay of a micro crystalline diamond single crystal sample with three N-centers.

(B) 3-pulse 4-phase cycling electron spin echo decay. The measurement conditions are given in Section A.3 in the Appendix.

Tab. 3.3 PMR $p_{\frac{\pi}{2}}$ pulse TWT attenuation: Pulse duration versus mw power shows ultra high bandwidth and power reserve of PMR setups.

Resonator	$p_{\frac{\pi}{2}}$ / ns	TWT attenuation / dB
MD5	30	6
PMR R1/T2	4	22
	8	28
	16	31
	20	32
	30	34
	40	36

4 Experimental Results and Discussion of Single Crystal and Thin Film EPR

4.1 Determination of Structural Parameters of $^3_\infty[\mathrm{Cu^I{}_2Cu^{II}{}_2(H_2O)_2L_2Cl_2}]$

4.1.1 Single Crystal EPR of $^3_\infty[\mathrm{Cu^I{}_2Cu^{II}{}_2(H_2O)_2L_2Cl_2}]$

As outlined in Section 2.4.1, a $\mathrm{Cu^{2+}}$ species of unknown origin has been found in $^3_\infty[\mathrm{Cu^I{}_2Cu^{II}{}_2(H_2O)_2L_2Cl_2}]$. The aim of this work was to study its origin with the help of single crystal cw EPR experiments. Fig. 4.1A shows the experimental single crystal spectrum with 40 accumulations and the $\mathbf{B}_0$ field vector in the *ac* plane with ±5° uncertainty for this experiment. Further information about the sample preparation and orientation is given in Fig. B.5 on page 102 and in Section B.3.2 in the Appendix. Other experimental conditions are outlined in Section A.1 in the Appendix. The crystal is oriented such that its *a* axis and the direction of $\mathbf{B}_0$ form an angle of 20°.[153] The singe crystal spectra display several distinct, angular-dependent $\mathrm{Cu^{2+}}$ EPR signals of varying width and resolution. These signals can be fitted using the Spin Hamiltonian terms for the electron Zeeman and hyperfine interactions, as detailed in Eqn. 2.2 and 2.3 which are excerpts from Eqn. 2.1 as described for the powder simulations in Section 2.4.1. The poor spectral resolution and the low SNR in this experiment is the result of the low spin number of 10^{13} spins in the single crystals of **1** and the line broadening effects among others caused by correlated **g** and **A** strains, as in the powder EPR spectra (cf. Fig. 2.10 and Section B.5 in the Appendix). In this way, the EPR lines in the high field region are broader compared to those in the low field region, and are consequently of a lower resolution. The simulated spectra in Fig. 4.1A(b–f) will be explained in more detail below.

An example of complete angular dependence of the single crystal of **1** with $\mathbf{B}_0$ rotated in the *ac* plane determined with an accuracy of ±5° is shown in Fig. 4.1B. The spectra were taken about every 5°, and a 90° excerpt is presented in this figure. The resonance fields vary from $B = 290\,\mathrm{mT}$, which corresponds to the parallel part of the powder spectrum of **1**, to $B = 340\,\mathrm{mT}$, representing the perpendicular part of the corresponding powder spectrum. The angular dependence shown here resembles a two-fold symmetry for the rotation in the *ac* plane about the angle φ in regards to the respective crystallographic axes. Experimental EPR spectra for rotations in the other, *ab* and *bc* planes are published in Friedländer et al.[153] Overall, four angular-dependent sets of the four $S = \frac{1}{2}$, $I = \frac{3}{2}$ single crystal copper HFS resonance field lines can be identified. Two sets of resonance lines, denoted by A and B of **1**, each follow the same angular dependence (α or $beta$), but with slightly different resonance positions and hyperfine splittings, and reach their maximum respective copper HFS and effective g values under an angle of $\varphi = \pm 20(5)°$ with the *a* axis. These two

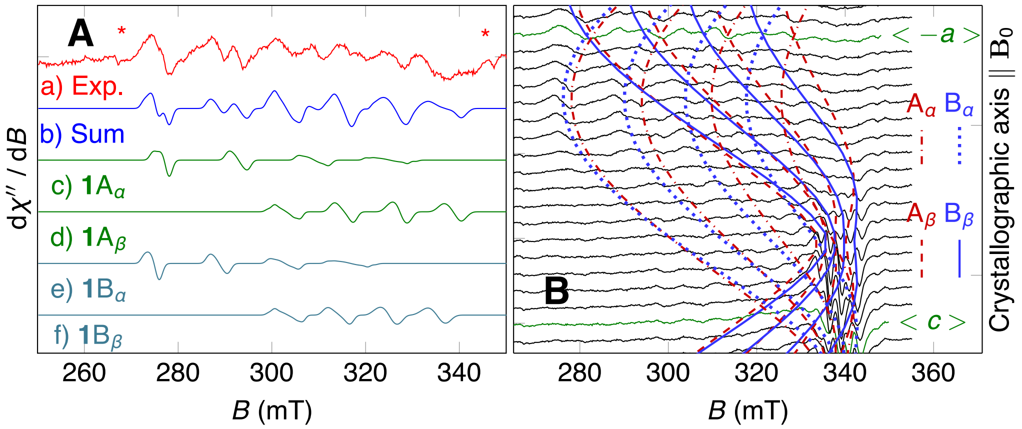

Fig. 4.1 Single crystal EPR spectra of $^{3}_{\infty}$[Cu$^{I}_{2}$Cu$^{II}_{2}$(H$_2$O)$_2$L$_2$Cl$_2$]: Single crystal EPR spectra of **1**.
(A) (a) Experimental spectrum at 7 K, $\mathbf{B}_0$ in ac plane, the angle of $\mathbf{B}_0$ with the a axis is 20(5)°, the asterisks mark artifacts from background subtraction, (b) sum of simulated spectra and individually for (c-f) **1**A$_\alpha$, **1**A$_\beta$, **1**B$_\alpha$ and **1**B$_\beta$.
(B) Angular dependent EPR spectra every 5° of the single crystal of **1** for a rotation of the magnetic field vector $\mathbf{B}_0$ in the ac plane with ±5° accuracy for all angles. The colored and differently dashed lines mark the four sets of simulated resonance fields of the two species A and B of **1**, each for the two tensor orientations α and β.

distinct sets of resonance lines have been assigned to the two mononuclear Cu^{2+} species A and B of **1** observed in the EPR powder spectra of $^{3}_{\infty}$[Cu$^{I}_{2}$Cu$^{II}_{2}$(H$_2$O)$_2$L$_2$Cl$_2$].[153] Consequently, the species (**1**A$_\alpha$, **1**A$_\beta$, **1**B$_\alpha$ and **1**B$_\beta$) with distinct angular dependencies are assigned to two orientations – α and β of their **g** and **A** tensors – representing two magnetically non-equivalent, symmetry-related incorporation sites of the mononuclear Cu^{2+} species of **1**A and **1**B. The rotations in the other two crystallographic planes provide only one set of copper HFS lines for each species of **1**A and **1**B,[153] indicating that the projections of the tensor orientations α and β onto the ab and bc plane are equivalent.

The complete angular dependent resonance fields as measured in three orthogonal planes are summarized in Fig. 4.2. The two species of **1**A and **1**B are fitted simultaneously for these three single crystal angular dependencies. The fit yields similar principal axis values of the **g** and **A** tensors as found in the respective powder spectrum (Tab. 2.1) and specific angles $\theta^{\alpha,\beta}_{a,b,c}$ of the z principal axis directions of the **g** and **A** tensors of the species **1**A$_\alpha$, **1**A$_\beta$, **1**B$_\alpha$ and **1**B$_\beta$, with respect to the crystal axes a, b and c of the orthorhombic unit cell. Here, the z axes correspond to the symmetry axis of the two magnetic tensors. The angles $\theta^{\alpha,\beta}_{a} = \pm 20(5)°$, $\theta^{\alpha,\beta}_{b} = 90(5)°$ and $\theta^{\alpha,\beta}_{c} = \mp 70(5)°$ of the two tensor orientations assigned to the two magnetically non-equivalent incorporation sites of both species in **1**A and **1**B have been determined. Fig. 4.1 and 4.2 shows that for all three planes, the experimentally-obtained resonance fields fit well to the computed angular dependencies (red and blue lines) using the obtained angles $\theta^{\alpha,\beta}_{a,b,c}$ and the principal values from Tab. 2.1.

Discrepancies between the experimentally-obtained and computed resonance fields in the angular dependencies are caused by different error contributions. First, in this experiment one must assume a systematic

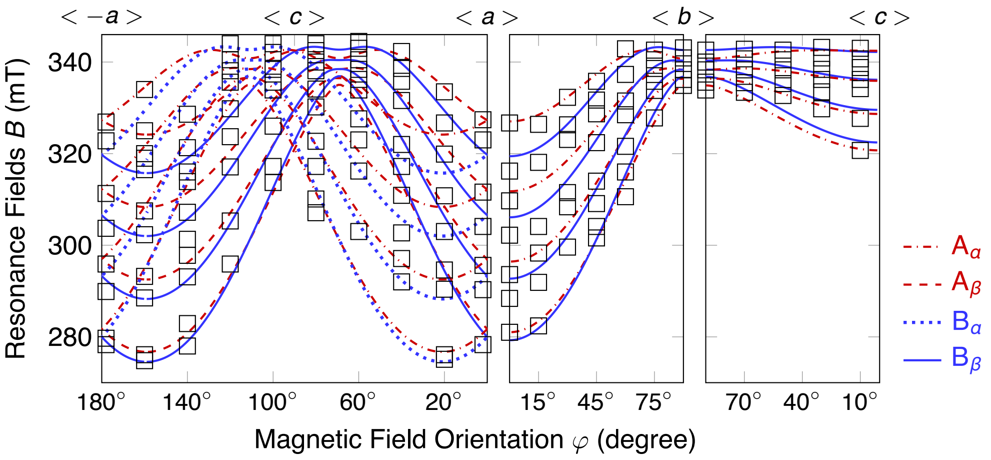

Fig. 4.2 Resonance field positions of ${}^3_\infty$[Cu$^{I}_2$Cu$^{II}_2$(H$_2$O)$_2$L$_2$Cl$_2$]: Angular dependent EPR resonance field positions of the mononuclear Cu^{2+} species measured in three orthogonal planes (the size of the black open squares resembles error limits) and the simulated angular dependencies of the single crystal of **1** (red, blue lines).

uncertainty of about 5° for all orientations with respect to the indicated angles. Second, a line broadening effect by correlated g and A strains was observed in the powder EPR spectra (see Fig. 2.10). Therefore, in the single crystal spectra, the resonance field lines in the high field region are broader, as compared to those in the low fields. Consequently, resonance fields of the low field signals must be considered more reliable for analysis of the angular dependency. Finally, the asymmetric experimental line shape, which is due to insufficient background subtraction, line broadening effects, and the general low SNR, as seen in the detailed background subtracted single crystal spectrum previously shown in Fig. 4.1A, introduce an appreciable uncertainty of up to 1.5 mT in the determination of the resonance field positions. Even when taking into account these error contributions, the simulated resonance field positions reproduce the experimental observations with acceptable accuracy.

Using the principal values of the **g** and **A** tensors of the two Cu^{2+} species of **1** A and B (Tab. 2.1) and the above determined angles $\theta^{\alpha,\beta}_{a,b,c}$ of the z principal axis directions with the crystallographic axes, it is now possible to simulate the single crystal spectrum in Fig. 4.1A(b) with $\mathbf{B}_0$ in the ac plane. This spectrum is composed of a superposition of the EPR spectra of the four species $\mathbf{1}$A$_\alpha$, $\mathbf{1}$A$_\beta$, $\mathbf{1}$B$_\alpha$ and $\mathbf{1}$B$_\beta$ which correspond to the two magnetically non-equivalent sites of species A and B of **1** with tensor orientations α and β. A correlated g and A strain line broadening model using the same parameters as the simulation of the powder pattern was also employed in the simulation of the single crystal spectra. This line broadening model may also account for the increasing line widths of the copper HFS signals in the single crystals spectrum, which range from lower to higher magnetic fields. However, one also observes that the low field HFS line of the species $\mathbf{1}$A$_\beta$ and $\mathbf{1}$B$_\beta$ are broadened more than those of $\mathbf{1}$A$_\alpha$ and $\mathbf{1}$B$_\alpha$, indicating the presence of an additional line broadening mechanism. For the given orientation, the magnetic field $\mathbf{B}_0$ is approximately parallel to the symmetry axis of the **g** and **A** tensors for the tensor orientation α (species

1A_α, **1**B_α), whereas it forms an angle of 40° for the tensor orientation β. As the latter orientation is more affected by this second line broadening effect, a Gaussian distribution of the angles $\theta_a^{\alpha,\beta}$ and $\theta_c^{\alpha,\beta}$ with a small distribution width $\Delta\theta \approx 2.4°$ has been proposed.[153] Indeed, by considering both line broadening mechanisms, one can simulate the single crystal spectrum in Fig. 4.1A(a) by a superposition of the EPR signals of all four species in Fig. 4.1A(c–f), namely **1**A_α, **1**A_β, **1**B_α and **1**B_β, with satisfying agreement. In this simulation, identical intensities were assumed for species A and B, although in general, the intensity ratio of species A and B of **1** may vary to a certain extent among different crystals. In the low field region of Fig. 4.1A(a), it is relatively easy to identify the resonance fields, while at higher fields (300 mT – 340 mT), the resonance lines are broader, less resolved and rather asymmetric. This also explains why the degree of accuracy in determining the resonance fields in the range 300 mT – 340 mT is limited and leads to some discrepancies between experimental and computed angular dependencies of the resonance fields in that field range (Fig. 4.2).[153]

Furthermore, in this work, two approximately equally-populated, axially-symmetric Cu^{2+} species A and B of **1** that are incorporated into the framework at two magnetically non-equivalent, symmetry-related sites (tensor orientations α, β) have been identified.[153]

4.1.2 Geometry of Paramagnetic Local Probes

The single crystal cw X-band EPR data reveal the presence of two distinct mononuclear Cu^{2+} species A and B in **1**. EPR measurements on single crystals provided clear twofold angular dependencies of their corresponding resonance fields. This can be linked to the crystal structure of **1** with space group I 2_1 2_1 2_1 with perpendicular screw axes along the three crystallographic axes leading to two magnetically non-equivalent, symmetry related sites. Hence, the obtained angular dependency mirrors the crystal structure of **1**. Therefore, one may conclude that species **1**A_α, **1**A_β, **1**B_α and **1**B_β are located at well-defined sites within the MOF crystallites of **1** and are not formed in a minor amorphous impurity phase.[153] Moreover, the well-resolved EPR powder patterns of A and B in **1** with only minor correlated g and A strain effects suggest an incorporation of the mononuclear cupric ion species at well-defined lattice sites, as it is for instance known for Cu^{2+} ions in the Cu / Zn PW units of a partial Zn^{2+} substituted HKUST-1 MOF, which exhibit similar EPR powder patterns of superior resolution without very pronounced strain effects.[40] This particular issue will be inspected further in Section 4.2. Otherwise, extra framework Cu^{2+} species usually give rise to poorly resolved powder spectra due to very substantial g and A strains or high local concentrations.[150]

There are three distinct metal ion sites in the framework of **1**, two Cu^{+} (Cu(I)) sites each with a distorted tetrahedral coordination to four nitrogen atoms and the third Cu^{2+} (Cu(II)) site in the Cu / Cu PW units, which have a local C_4 symmetry axis along the Cu-Cu direction. In these Cu / Cu PW units the cupric ions are coordinated by four basal oxygen atoms of bridging carboxylate groups of the ligands and an apical oxygen atom of the axially coordinating solvent water molecule in a square pyramidal coordination symmetry (Fig. 2.10). The two magnetically non-equivalent, symmetry related PW orientations are formed by the screw axes in a, b, and c direction of space group I 2_1 2_1 2_1.[153]

Although it is usually not possible to deduce the exact metal ion coordination geometry from the principal

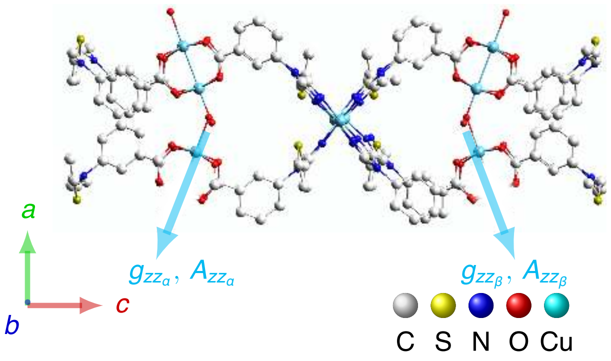

Fig. 4.3 Defect paddle-wheel model of 1: Projection of **1** with two magnetically non-equivalent, intact Cu / Cu PW units and two defective PW units. The vectors indicate the two possible orientations α and β of the z principal axis directions of the tensors $\mathbf{g}$ and $\mathbf{A}$.

values of the Cu^{2+} $\mathbf{g}$ and $\mathbf{A}$ tensors, the g_{zz} and A_{zz} parameters of the cupric ion species provide a rough guide to the overall coordination geometry of the metal ion site. Based on a number of studies of Cu^{2+} ions in an oxygen coordination environment,[193,194] A_{zz} increases from ~ 0.007 cm^{-1} for tetrahedral symmetry, through elongated distorted, octahedral symmetry (~ 0.0130 cm^{-1}), square pyramidal and trigonal pyramidal to square planar symmetry (~ 0.0190 cm^{-1}), whereas g_{zz} decreases from 2.516 to 2.245 for this sequence of coordination symmetries. So the values of $g_{zz} \sim 2.42$ and $A_{zz} \sim 0.0130$/cm indicate a distorted octahedral coordination of the Cu^{2+} ions to six oxygen atoms,[195] but $g_{zz} \sim 2.279$ and $A_{zz} \sim 0.0190$/cm suggest rather a square planar coordination.[40] In case of a coordination of the cupric ion to four nitrogen atoms, a transformation from a tetrahedral to a planar coordination symmetry is accompanied by change from $g_{zz} \sim 2.32$ and $A_{zz} \sim 0.0080$/cm to $g_{zz} \sim 2.18$ and $A_{zz} \sim 0.0200$/cm.[196] The obtained parameters g_{zz} and A_{zz} of two distinct mononuclear Cu^{2+} species A and B of **1** in Tab. 2.1 indicate a square pyramidal oxygen environment. Alongside, comparable Cu^{2+} Spin Hamiltonian parameters have been reported for cupric ions with axially-coordinating water or methanol molecules in Cu / Zn PW units of a partially zinc substituted HKUST-1 MOF as shown in Section 4.2. Furthermore, both tensors $\mathbf{g}$ and $\mathbf{A}$ are axially symmetric within the bounds of the experimental accuracy levels in accordance with a square pyramidal coordination of the Cu^{2+} ions.[40] Therefore, for chemical aspects of improbable bond formations, one may rule out that the two Cu^{2+} species A and B in **1** are formed by oxidation of Cu^{+} with their distorted tetrahedral nitrogen coordination. One can rather assume the formation of defective PW units with one missing cupric ion as illustrated in Fig. 4.3.

4.1.3 Discussion of the Defect Model

If the above defect model would describe the framework correctly, the z principal axes of the $\mathbf{g}$ and $\mathbf{A}$ tensors of the metal ion should be directed along the local C_4 symmetry axis of the former Cu / Cu PW unit. The angular dependent EPR measurements on the small single crystals of **1** confirm this assignment. The C_2 symmetry in the angular dependent spectra can be explained fully with the two magnetically non-equivalent sites for the Cu / Cu PW units related via the 2_1 screw axes in the crystal structure of **1** with space group I 2_1 2_1 2_1 as illustrated in Fig. 4.3. For both sites the local C_4 symmetry axis of the Cu / Cu PW units is oriented parallel to the crystallographic ac plane and form an angle with the a lattice axis of about ±21°.

Tab. 4.1 compares the found angles θ_a, θ_b and θ_c, which describe the direction of the C_4 symmetry axes of the Cu / Cu PW units with respect to the crystallographic axes with those angles, the z principal axis directions of the **g** and **A** tensors of the two Cu^{2+} species A and B in **1** form with those axes for the two tensor orientations α and β. Both sets of angles are in accordance considering the experimental errors of the determined angles of the z principal axis directions of the two tensors. The direction of the z principal axis directions of the tensors **g** and **A** deviates only by $\angle(z, \mathbf{r}) \leq 1°$ from the C_4 symmetry axis **r** of the Cu / Cu PW units, neglecting the 5° uncertainty given for all measurements. Moreover, EPR angular dependencies and the obtained two orientations α and β of the **g** and **A** tensors are in accordance with the two magnetically non-equivalent sites of the PW units (Fig. 4.3) and reflect the crystal symmetry of **1**.

This suggested defect model for the mononuclear Cu^{2+} species A and B in **1** of a defective PW unit with one missing cupric ion is supported by the results of XRD measurements and relative EPR intensity measurements.[153] The XRD refinement of the crystal structure of **1** gave a site occupancy factor of 0.933(4) for cupric ions in PW units. Consequently, approximately 13 % of the PW units are defective with one missing cupric ion. The analysis of the relative intensities in the EPR powder spectra of **1** provide a ratio between the mononuclear Cu^{2+} species, in that case the defective PW units, and the intact Cu / Cu PW units. This ratio of 0.11 corresponding to about 10 % defective PWs with respect to all PW units is in good accordance with the XRD sof-analysis. The approximately 10 % of defective PWs must be compared to 0.01 % of the PWs located at the surface of a single crystal with these dimensions, which rejects surface-related effects as the source.

The proposed defective PW unit model helps to explain the associated EPR results of both powder and single crystal studies of **1**, as well as the XRD refinement of the crystal structure. However, an explanation for the occurrence of two mononuclear Cu^{2+} species A and B in **1** with identical orientations of the z principal axis frames of their **g** and **A** tensors but with distinct principal values can only be attempted. The differences in the g and HFS values indicate slightly different coordination environments of the two cupric ion species, presumably caused by some minor but well-defined deformations of the defective PW units. One possible explanation might be that a defective PW unit with one missing Cu^{2+} ion carries a twofold negative charge that must be compensated, for instance, by the protonation of the non-bonding oxygen atoms of the carboxylate groups. The required two protons may either bind to two adjacent or two opposite lying oxygen atoms leading to two slightly different coordination environments of the Cu^{2+} ion in the defective PW unit. Otherwise, a removal of the axial water ligand to the cupric ions in the PW units or its substitution by another polar solvent molecule may lead to a modification of the axial ligand field at the metal ion and consequently likewise to a small change in the g_{zz} and A_{zz} principal values of the tensors **g** and **A**.[164] In both scenarios, the changes to the coordination symmetry of the cupric ion are assumed to be small so that the axial symmetry of the **g** and **A** tensors and its orientation is conserved within the experimental accuracy. It must be noted that the **g** and **A** parameters of the two species in the compound MOF are very sensitive to minor structural changes of the framework induced for example by different activation procedures as tested by Šimėnas et al.[149] This shows the sensitivity of both tensors with respect to small changes in the coordination environment of the Cu^{2+} ions in the defective PW units.[153]

Tab. 4.1 Local ${}^3_\infty[\mathrm{Cu^I{}_2Cu^{II}{}_2(H_2O)_2L_2Cl_2}]$ structure compared: EPR tensors and XRD results compared. $\theta^{\alpha,\beta}_{a,b,c}$ of z principal axis directions of $\mathbf{g}$ and $\mathbf{A}$ tensors of mononuclear $\mathrm{Cu^{2+}}$ ions with respect to crystallographic axes a, b and c and directions of the local C_4 symmetry axis $\mathbf{r}$ of the Cu / Cu PW units as defined by the vector pointing from one to the other $\mathrm{Cu^{2+}}$ ion in the PW unit.

Angle	$\theta^{\alpha,\beta}_a$	$\theta^{\alpha,\beta}_b$	$\theta^{\alpha,\beta}_c$
$\mathbf{r}$	±20.88°	90°	∓69.12°
z	±20(5)°	90(5)°	∓70(5)°

4.1.4 Conclusions for ${}^3_\infty[\mathrm{Cu^I{}_2Cu^{II}{}_2(H_2O)_2L_2Cl_2}]$

Relatively identifiable, distinct, angular dependent EPR spectra of mononuclear $\mathrm{Cu^{2+}}$ ion species have been found in single crystals of the framework ${}^3_\infty[\mathrm{Cu^I{}_2Cu^{II}{}_2(H_2O)_2L_2Cl_2}]$ and lead to the assignment of these signals to a crystalline phase incorporated in the framework.[153] It has been verified that this angular dependency at three different rotations of $\mathbf{B}_0$ in the crystallographic ab, bc and ac plane as shown in the published material.[153] The recorded spectra are sufficient to identify two species A and B in **1** of the mononuclear $\mathrm{Cu^{2+}}$ in two magnetically non-equivalent sites each. The angular dependencies can be fitted by the principal values of the $\mathbf{g}$ and $\mathbf{A}$ tensors of the species $\mathbf{1}\mathrm{A}_\alpha$, $\mathbf{1}\mathrm{A}_\beta$, $\mathbf{1}\mathrm{B}_\alpha$ and $\mathbf{1}\mathrm{B}_\beta$ as determined from the corresponding EPR powder spectra and the determined orientations α and β of the z principal axis directions of the magnetic tensors allow an assignment to defective PW units with one missing $\mathrm{Cu^{2+}}$ ion. Based on EPR intensities of powder materials and XRD studies of single crystals, it is possible that about 10 % of the PW units are defective in the MOF structure, which represents an important addition to the so-far known crystal structure.[153] Additionally, it is one of the few cases, where the nature of defects has been successfully identified in MOF materials.

4.2 Adsorption Characteristics of HKUST-1

Section 2.4.2 has shown that even for the well-studied MOF $\mathrm{Cu_3(btc)_2}$, there is a lack of information about the local structure of the material, especially for the gas adsorption processes it is aimed at, and this can only be resolved by single crystal studies. One possibility – that single crystal EPR investigations could reveal formerly unknown properties of the material – will be presented here.

4.2.1 Dehydration and Adsorption of Methanol on $\mathrm{Cu_3(btc)_2}$

It will be shown later that it is useful to address the pure MOF HKUST-1 ($\mathrm{Cu_3(btc)_2}$) by means of single crystal cw EPR. This may at first sight not seem reasonable since one does not expect to find the antiferromagnetically coupled $S = 1$ state of the Cu / Cu PW at low temperatures. Nevertheless, EPR spectra of $\mathbf{2}_{\mathrm{act}}$ and $\mathbf{2}_{\mathrm{MeOH}}$ are shown Fig. 4.4. Further information about the sample preparation and orientation is given in Fig. B.6 on page 102 of Section B.3 and again in Section A.1 and Section B.3.2 in the Appendix. While the spectra of $\mathbf{2}_{\mathrm{act}}$ can be explained with $\mathrm{Cu^{2+}}$ impurities in the cryostat interfering often at low signal intensities,[153]

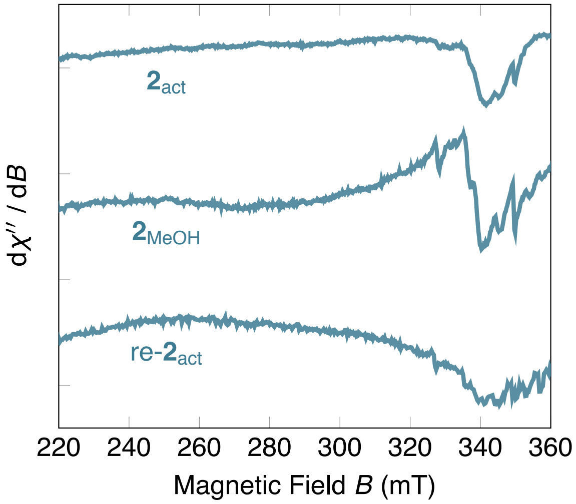

Fig. 4.4 EPR spectra of $\mathbf{2}_{act}$, $\mathbf{2}_{MeOH}$ and reactivated 2: Single crystal EPR spectra of $\mathbf{2}_{act}$, $\mathbf{2}_{MeOH}$ and reactivated **2** at 8 K sample temperature showing distinct reversible line shape modification upon gas adsorption. Individual resonance field lines are not resolved due to the dominant $S = 1$ spin state of the Cu / Cu PW units in $Cu_3(btc)_2$.

surprisingly the CH_3OH gas adsorption afterwards leads to a broad signal at 335 mT which has been assigned to Cu^{2+} in an unknown coordination.[163] It is neither possible to detect apparent HFS signals nor to find an evidence for an angular dependency of the signal. Moreover, and remarkably, it must be noted that after a reactivation the signal disappears on repeated occasions. At this point, an interpretation of the observations cannot be given, but for Fig. 4.11B a reference will be given to this observation to discuss a similar effect in $Cu_{2.965}Zn_{0.035}(btc)_2$.

4.2.2 Dehydration and Gas Adsorption on $Cu_{2.965}Zn_{0.035}(btc)_2$

Dehydrated $Cu_{2.965}Zn_{0.035}(btc)_2$ After dehydration of $\mathbf{3}_{AS}$, the single crystals of **3** have been measured and denoted as $\mathbf{3}_{act}$ according to the procedure given in Section B.3.2 in the Appendix. After this activation process, the EPR spectra show well-resolved, angular dependent resonance field lines of several paramagnetic Cu^{2+} ion species as depicted in Fig. 4.5A(a) in comparison to the same orientation of other gas loaded samples of **3** (Fig. 4.5A(b–d)). Fig. 4.5B shows four, individual single crystal spectra and simulations of $\mathbf{3}_{act}$. They will be explained in more detail later.

The complete experimental and simulated angular dependencies of the resonance fields of $\mathbf{3}_{act}$ for a rotation of the external magnetic field $\mathbf{B}_0$ about the crystallographic [1 1 1] axis of the crystal $\mathbf{3}_{act}$ are plotted in Fig. 4.6. First, they can be fitted using the Spin Hamiltonian terms for the electron Zeeman and hyperfine interactions, Eqn. 2.2 and 2.3 from Eqn. 2.1. The **g** and **A** tensors are axially symmetric with the principal axis values given in Tab. 4.2. The principal axis orientations of the respective **g** and **A** tensors of all species are found to be collinear.

Tab. 4.2 shows the principal axes values in columns 1–4 of the axially symmetric **g** and **A** tensors for all investigated samples of $Cu_{2.965}Zn_{0.035}(btc)_2$. At present, the reader may focus on the first line for the sample under discussion here ($\mathbf{3}_{act}$), and the fifth column may be consulted after further remarks in this Subsection. To simulate the resonance field positions presented above in Fig. 4.6, the **g** and **A** principal axis values from the respective powder samples have been used as initial values and optimized for the single crystals.[40]

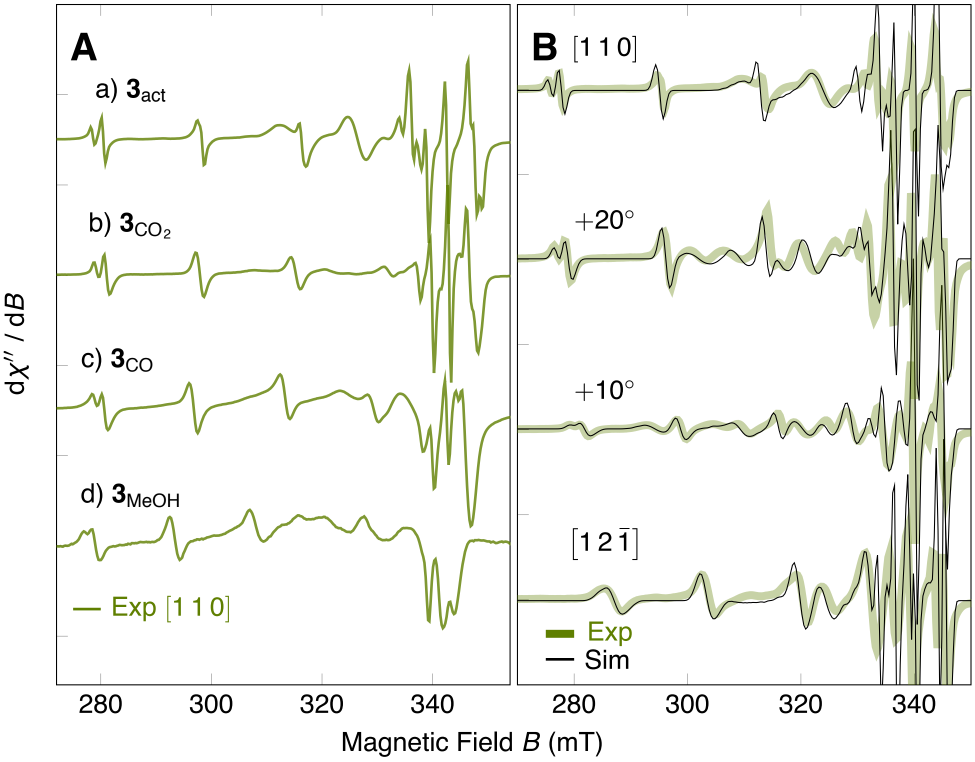

Fig. 4.5
Comparative EPR spectra of 3 and $\mathbf{3_{act}}$ in detail:
(A) Experimental EPR spectra of all single crystal samples of **3** at 8 K with $\mathbf{B}_0$ along the crystallographic [1 1 0] axis.
(B) Selected experimental and simulated Cu^{2+} EPR spectra for $\mathbf{3}_{act}$ at a rotation around the crystallographic [1 1 1] axis. Thick colored lines represent experimental spectra while the thin black lines are the simulations with details given in the text.

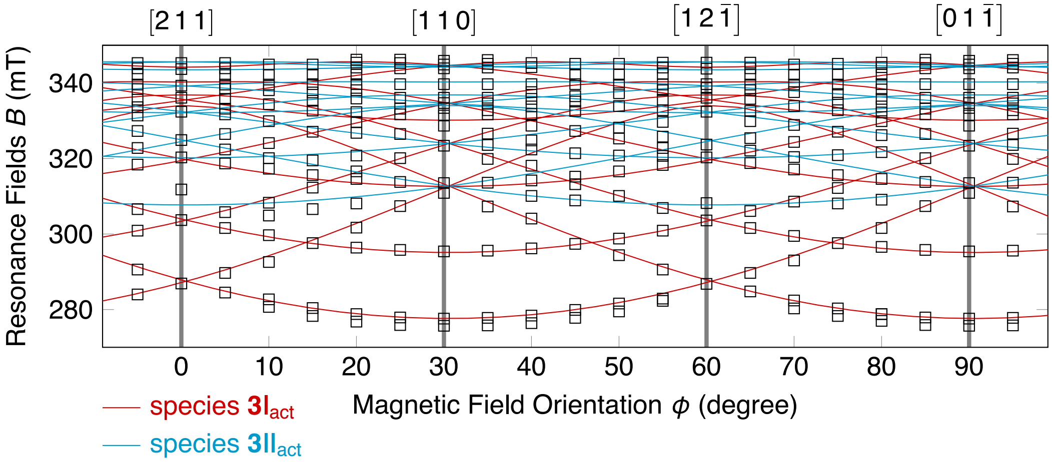

Fig. 4.6 Resonance field lines and simulations of $\mathbf{3_{act}}$: Angular dependent EPR resonance fields of Cu^{2+} species found for $\mathbf{3}_{act}$ at a quarter turn around the [1 1 1] axis (black squares). Solid lines represent simulated angular dependencies of the resonance fields using the parameters in Tab. 4.2 and 4.3 for $^{63}Cu^{2+}$, while $^{65}Cu^{2+}$ is manifested in the line splitting around directions marked [1 1 0]. EPR signals of six magnetically non-equivalent symmetry-related Cu^{2+} species are observed, which can be grouped in two classes labelled by species of group $\mathbf{3I}_{act}$ and $\mathbf{3II}_{act}$.

Tab. 4.2 EPR tensor principal axis values of $Cu_{2.965}Zn_{0.035}(btc)_2$: Principal axes values and angular distribution width $\Delta\alpha$ of the $\mathbf{g}$ and $\mathbf{A}$ tensors of the most abundant Cu^{2+} species $^{63}Cu^{2+}$ of groups **3**I and **3**II in various single crystals of $Cu_{2.965}Zn_{0.035}(btc)_2$.

Sample **3**	g_{zz}	$g_{xx,yy}$	A_{zz} / 10^{-4}/cm	$A_{xx,yy}$ / 10^{-4}/cm	$\Delta\alpha$ /°
$\mathbf{3}_{act}$	2.281(2)	2.046(1)	187(2)	32(2)	3.0(5)
$\mathbf{3}_{CO_2}$	2.293(2)	2.049(2)	182(2)	26(2)	5.0(5)
$\mathbf{3}_{CO}$	2.300(1)	2.051(2)	175(2)	23(2)	5.0(5)
$\mathbf{3}_{MeOH}$	2.336(2)	2.058(1)	158(2)	15(2)	6.0(5)

Tab. 4.3 EPR tensor principal axis orientations of $Cu_{2.965}Zn_{0.035}(btc)_2$: Principal axis orientations (Euler angles ϕ, θ) of the $\mathbf{g}$ and $\mathbf{A}$ tensors of the Cu^{2+} species of groups **3**I and **3**II in all single crystals of $Cu_{2.965}Zn_{0.035}(btc)_2$ with respect to crystal frame according to EasySpin convention,[42] errors $\Delta\phi = \Delta\theta = \pm 1°$, and deduced crystal axes as explained in Section 4.2.3.

Species	ϕ	θ	Group	Crystal Axis
31	45°	−90°	**3**I	[1 1 0]
32	0	−45°		[1 0 1]
33	90°	−45°		[0 1 1]
34	45°	90°	**3**II	$[\bar{1}\,1\,0]$
35	0	45°		$[\bar{1}\,0\,1]$
36	90°	45°		$[0\,\bar{1}\,1]$

Deviations from the powder values will be presented and discussed in Section 4.2.3. It is obvious, that the resonance fields shown in Fig. 4.6 originates from several different angular dependencies and in total six magnetically non-equivalent, symmetry related and distinct species with an equal, sixfold symmetry have been found. All six sets of resonance field lines have been fitted with the same **g** and **A** principal axis values, but different principal axis orientations. These can be found in Tab. 4.3.

The first three orientations belong to a group of species referred to as **3I** throughout this manuscript, while the remaining three are marked **3II**. The principal axis orientations of the **g** and **A** tensors are obtained by a rotation of their z principal axis in the $\mathbf{B}_0$-plane around the [1 1 1] axis (corresponding to the angle ϕ) to fit all resonance peaks. At first, three magnetically non-equivalent Cu^{2+} incorporation sites can be fitted (group $\mathbf{3I}_{\text{act}}$). They reach their largest effective HFS in a parallel orientation to the external magnetic field $\mathbf{B}_0$ one after another separated by 60°. This effective HFS corresponds to the maximum HFS based on former results on powder samples and the symmetry axes, denoted by z, of the **g** and **A** tensors of the three species of group $\mathbf{3I}_{\text{act}}$ are found to be embedded in the (1 1 1) plane.[163] The angular dependencies of the resonance fields of two of the three species of the group $\mathbf{3I}_{\text{act}}$ intersect every 30°. The low field HFS lines meet for one intersection at about 285 mT and for the subsequent intersection at about 310 mT. The latter intersection marks the orientation of the highest HFS of the third orientation of the species of group $\mathbf{3I}_{\text{act}}$. Secondly, three further species labelled as set of species $\mathbf{3II}_{\text{act}}$ are identified in the spectra mainly in the spectral region 305 mT – 340 mT. They follow the angular dependencies of species $\mathbf{3I}_{\text{act}}$ but are shifted to that by 30° such that they reach their orientation with the largest effective HFS in the considered (1 1 1) plane where the three species of group $\mathbf{3I}_{\text{act}}$ do not have their maximum HFS. Hereby the z principal axis directions of the **g** and **A** tensors of the group $\mathbf{3II}_{\text{act}}$ species are lifted by about 55(1)° with respect to $\mathbf{B}_0$ and hence the (1 1 1) plane, each. Altogether, the fitted single crystal angular dependencies for all six Cu^{2+} species of $\mathbf{3}_{\text{act}}$ displayed in Fig. 4.6 show a very good agreement for all identified resonance field positions. Due to the cubic symmetry of HKUST-1, no further rotations than those around [1 1 1] axes have been carried out as all other rotational planes would provide equal or less information.

To explore $\mathbf{3}_{\text{act}}$ in more detail, the reader's attention shall now be directed back to Fig. 4.5B. Those single crystal EPR spectra of $\mathbf{3}_{\text{act}}$ are measured for four distinct orientations of the magnetic field $\mathbf{B}_0$ within the (1 1 1) plane. The presented spectra show the typical patterns of mononuclear Cu^{2+} ions with $S = \frac{1}{2}$ electron spin interacting with nuclear magnetic moments of ^{63}Cu and ^{65}Cu isotopes. The resonance fields vary from 278 mT to 344 mT. Fig. 4.5B displays the maximum HFS in this plane for species of group $\mathbf{3I}_{\text{act}}$ in the spectrum recorded for $\mathbf{B}_0$ parallel to the crystallographic [1 1 0] axis which corresponds to $\mathbf{B}_0$ aligned along the symmetry axes of the **g** and **A** tensors. In case of the second species in group $\mathbf{3II}_{\text{act}}$ the maximum HFS in the (1 1 0) plane is obtained for $\mathbf{B}_0$ along the crystallographic [1 1 2] axis.

For the individual spectral simulations, the exact line shapes have been taken into consideration. For that purpose, a specific line broadening mechanism has been developed, which is adoptable to all investigated samples. The requirements on this line broadening model were as follows: As seen in Fig. 4.5B, the spectra with $\mathbf{B}_0$ along the crystallographic [1 1 0] axis suffers from almost no line broadening and the HFS lines of the ^{63}Cu and ^{65}Cu isotopes are well-resolved for the low field signals. From this spectrum, a minimal moderate line broadening of 1.3 mT peak-to-peak line width had been deduced for all resonance lines. Now,

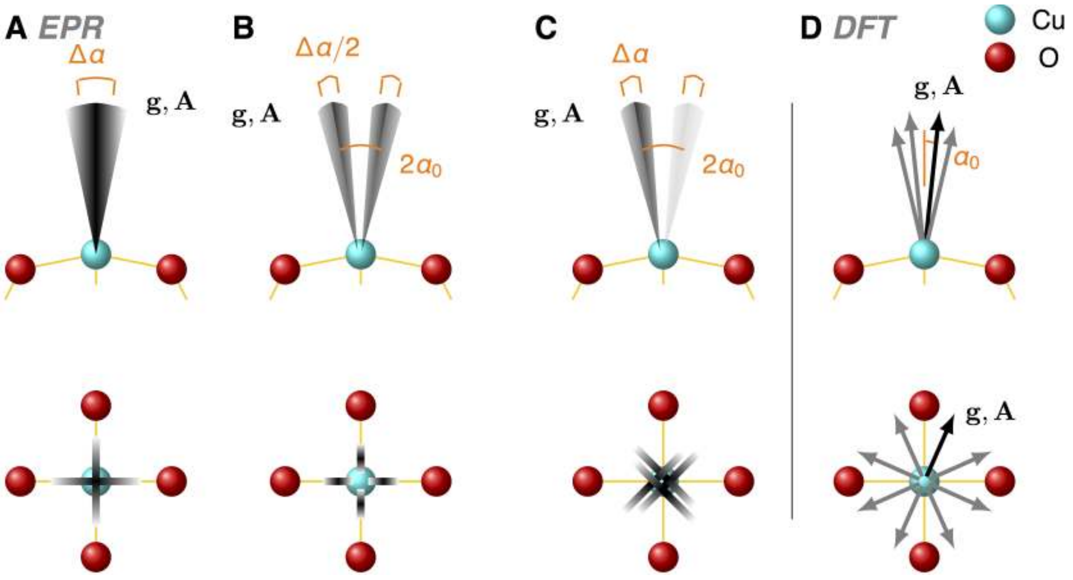

Fig. 4.7 Cu^{2+} $\mathbf{g}$ and $\mathbf{A}$ Tensor Principal Axis Orientations: Cu^{2+} $\mathbf{g}$ and $\mathbf{A}$ tensor principal axis orientations (black) as deduced by spectral simulations from EPR data (shades indicate Gaussian distribution). The tilting angle distribution $\Delta\alpha$ and static tilting angle α_0 are depicted in orange, respectively.
(A) Along the Cu – O$_P$ bond direction with single distribution $\Delta\alpha$ as given in Tab. 4.2 per orientation around $\alpha_0 = 0$.
(B) Along the Cu – O$_P$ bond direction with two distributions of width $\Delta\alpha/2$ per orientation around $\alpha_0 = \pm|\alpha_0|$ as given in Tab. 4.4.
(C) In the more complex model between two Cu – O$_P$ bonds with two distributions of width $\Delta\alpha$ around $\alpha_0 = \pm|\alpha_0|$.
(D) Static angle α_0 deduced from DFT (grey arrows show mirror vectors).

at only 30° of rotation further with $\mathbf{B}_0$ along a crystallographic [1 1 2] axis, the resonance lines have become significantly broader. From the comparison of the experimental and simulated powder spectra one possible reason for a line width broadening can be identified.[163]

Although it is showing well-resolved HFS signals in the g_{zz} part indicating only moderate strain and line broadening effects, not all the four HFS lines in the g_{zz} part fit equally well in their line width: resonance field lines for higher fields of $\mathbf{B}_0$ have slightly broader line widths as those for lower fields. Having aleady observed this increasing line width in the single crystals **1** of Section 4.1,[153] it was rated as a typical sign for correlated $\mathbf{g}$ and $\mathbf{A}$ strain distributions.[154] Consequently, such a correlated Gaussian $\mathbf{g}$ and $\mathbf{A}$ strain distribution has been considered in the simulations of all single crystal spectra of **3**.[163] The correlation approximation and parameters are given in Section B.5 in the Appendix.

However, this was not enough to explain all line widths of the tested samples of **3**, as all well-known, conventional line broadening mechanisms presented in Section 2.1.2 would allow for the specific effects observed in the powder materials but not in the single crystals. Instead, an additional distribution of the $\mathbf{g}$ and $\mathbf{A}$ tensors' principal axis orientations must be assumed to account for the observed line shapes of the Cu^{2+} EPR signals recorded in those spectra, where $\mathbf{B}_0$ is pointing along all non-canonical crystallographic axes orientations. This can be motivated by the assumption that ligands, which are known to coordinate in such a position with respect to the C_4 axis of the PW, might also be able to perturb the **g** and **A** tensor orientations of PWs in presence of adsorbents.[164] In fact, it was found useful to apply a similar mechanism also to $\mathbf{3}_{\mathrm{act}}$, although with less pronouncement in terms of that assumed distribution.[163] In the simulations, the **g** and **A** tensor principal axis orientations have been distributed over a small set of angles α and weighted them by a Gaussian distribution with width $\Delta\alpha$ around the respective equilibrium position $\alpha_0 = 0°$. This is the parameter given in the final, fifth column of Tab. 4.2.

In particular, for this modified simulation approach it was assumed that different models for the tilting of the **g** and **A** tensor principal axis orientations away from the C_4 axis of the PW could apply such that in the simplest approach a typical projection onto the plane perpendicular to the C_4 symmetry axis of the PW points towards the PW's oxygen atom along the existing $\mathrm{Cu-O_P}$ bond direction. The statistical average over a group of such tensors is distributed in a Gaussian fashion around the linear apical bond in each of the two $\mathrm{Cu-O_P}$ directions, as well as for every of the six orientations given in Tab. 4.3. This is shown in Fig. 4.7A for one of these six PWs. Considering a moderate value of $\Delta\alpha = 3.0°$, this broadening mechanism together with the correlated strain effects is sufficient to simulate all single crystal spectra in Fig. 4.5B including the $g_{xx,yy}$ part of the corresponding powder pattern.

At this point, one could argue that also other models could be possible and assume a somewhat more complex approach: a slightly bent adsorption complex structure with an angle α_0 as deviation from the linear average complex, and for each bent configuration a similar, but separate Gaussian distribution. This means, that every group of tensor orientations has a non-linear equilibrium position $\alpha_0 \neq 0°$, as for example two conformations with $\alpha_0 = \pm|\alpha_0|$ and two corresponding Gaussian distribution widths of $\Delta\alpha/2$ as depicted in Fig. 4.7B.

To offer even more choices for the best model, for symmetry reasons it is also possible to propose a rotated projection of these tilts in between two $\mathrm{Cu-O_P}$ bonds, which is shown in Fig. 4.7C. For this model, it was necessary to roughly double the Gaussian distribution width $\Delta\alpha$ with respect to the model in Fig. 4.7B to achieve an appropriate line width of the spectra. The three competing models are discussed later in Section 4.2.3. Then, they will be put into context with the DFT calculations presented in Section 2.4.2 and displayed here as Fig. 4.7D already.

Adsorption of Carbon Monoxide on $Cu_{2.965}Zn_{0.035}(btc)_2$ The spectra of $\mathbf{3}_{\mathrm{CO}}$ show besides the broader, but still well-resolved resonance field lines of Cu^{2+} species of groups $\mathbf{3I}_{\mathrm{CO}}$ and $\mathbf{3II}_{\mathrm{CO}}$ a broad spectrum which was assigned to a third Cu^{2+} species, species **3III**.[163] In the following, the relatively well-resolved resonance field lines are presented, and will be similarly treated as those of $\mathbf{3}_{\mathrm{act}}$. Following this, the very broad background spectrum will be discussed further.

Cu^{2+} Species of Group $3I_{CO}$ and $3II_{CO}$ EPR spectra of $\mathbf{3}_{\mathrm{CO}}$ show the relatively well-resolved resonance field lines which can be assigned to the previously described sixfold symmetric angular dependency of a repeated four-line pattern of anisotropic EPR single crystal spectra of the two respective mononuclear $^{63,65}Cu$ isotopes. These spectra are shown in Fig. 4.8 and can be fitted by the previously mentioned terms in Eqn. 2.1, yielding the values presented in the third line of Tab. 4.2 and directions of Tab. 4.3. With these values, the

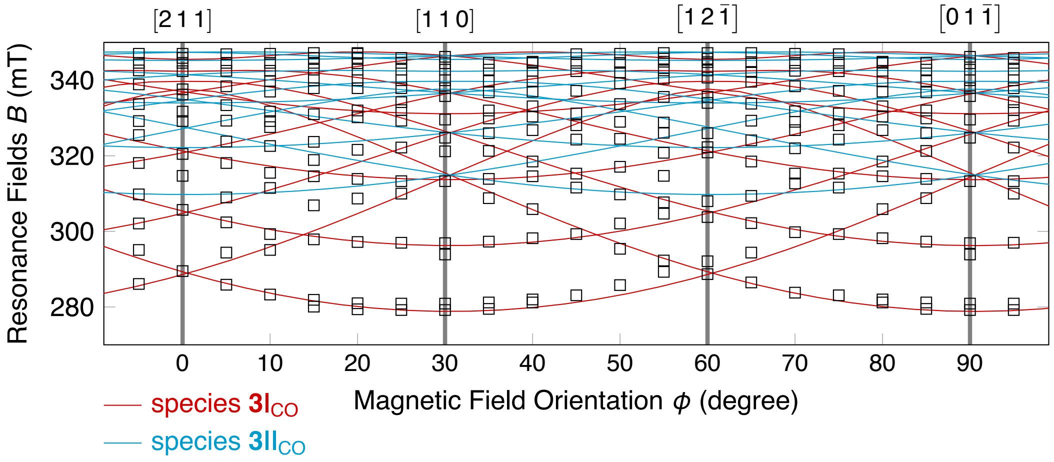

Fig. 4.8 Resonance field lines and simulations of $\mathbf{3}_{\mathrm{CO}}$: Angular dependent EPR resonance fields of Cu^{2+} species found for $\mathbf{3}_{\mathrm{CO}}$ at a quarter turn around the [1 1 1] axis (black squares). Solid lines represent simulated angular dependencies of the resonance fields using the parameters in Tab. 4.2 and 4.3. Again, EPR signals of six magnetically non-equivalent symmetry-related Cu^{2+} species are observed, which can be grouped in two classes labelled by species of groups $\mathbf{3I}_{\mathrm{CO}}$ and $\mathbf{3II}_{\mathrm{CO}}$.

single crystal angular dependence of $\mathbf{3}_{\mathrm{CO}}$ shows again a good agreement for all identified resonance fields. Again, the simulation has shown that the principal axes orientations of the **g** and **A** tensors are collinear with an uncertainty of 3°. The individual single crystal spectra and simulations of $\mathbf{3}_{\mathrm{CO}}$ are shown in Fig. 4.9A. Almost all the presented experiments show well-resolved single crystal anisotropic Cu^{2+} spectra with the resonance fields varying from approximately 279 mT to 346 mT, which is not so much different from $\mathbf{3}_{\mathrm{CO_2}}$. However, the spectral resolution of the lines is less due to an increased line width especially towards the crystallographic $\left[1\,1\,\bar{2}\right]$ axis orientation. In terms of the line broadening mechanism described above it was found that the increased line width could rather be simulated by increasing the correlation parameters given in Tab. B.4 on page 106 in the Appendix than the angular perturbation $\Delta\alpha$, which is up to half of a degree comparable to $\mathbf{3}_{\mathrm{CO_2}}$. For an exclusive fitting of the resolved angular peaks, no further adjustments are necessary when compared to the simulations described before.[163] Fig. 4.9B shows such an example, where all individual simulations are separated from each other to show all six Cu^{2+} incorporation sites for one random orientation, which is depicted below in Fig. 4.10 on page 78 to show the applied Euler angles. It was found that the spectral simulations for the resolved peaks of $\mathbf{3}_{\mathrm{CO}}$ correlate with the experimental spectra with almost no exception.

Cu^{2+} Species $\mathbf{3III}_{\mathrm{CO}}$ Besides the well-resolved single crystal EPR resonance lines, an underlying, broad and almost angular independent signal of a further Cu^{2+} species **3III** is present in the $g_{xx,yy}$ spectral range of the Cu^{2+} ion EPR spectra of $\mathbf{3}_{\mathrm{CO}}$. This very behavior has also been found for the sample $\mathbf{3}_{\mathrm{MeOH}}$,[163] and it is important to note that the signal disappears on repeated occasions for reactivated samples $\mathbf{3}_{\mathrm{act}}$. It can be seen in Fig. 4.9B and Fig. 4.11B as broad baseline modulation of the experimental spectra of $\mathbf{3}_{\mathrm{CO}}$ and

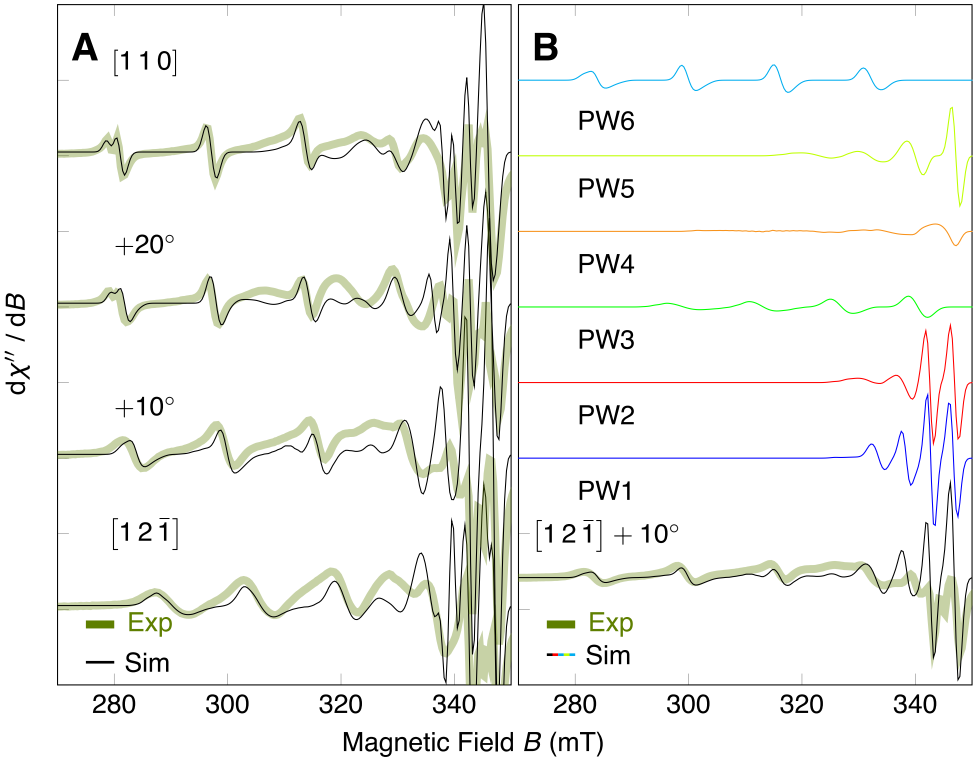

Fig. 4.9
EPR spectra of $\mathbf{3}_{\mathrm{CO}}$ in detail and the individual incorporation sites of Cu^{2+}:
(A) Selected experimental and simulated Cu^{2+} EPR spectra for $\mathbf{3}_{\mathrm{CO}}$ at a rotation around the crystallographic $[1\,1\,1]$ axis. For details of the simulation procedure see text.
(B) Experimental EPR spectrum of $\mathbf{1}_{\mathrm{CO}}$ (green, thick line) and the composition of the respective simulation of both Cu^{2+} isotopes in six incorporation sites with Spin Hamiltonian parameters for $\mathbf{1}_{\mathrm{CO}}$ and correlated $\mathbf{g}$ and $\mathbf{A}$ strains. The respective $\mathbf{g}$ and $\mathbf{A}$ principal axis orientations with the Euler angles from Tab. 4.3 used here are depicted in Fig. 4.10 on page 78.

$\mathbf{3}_{\mathrm{MeOH}}$ around 335 mT. In actual simulations, the signal could not be identified clearly by means of the given theoretical model with tested angular perturbations of up to $\Delta\alpha \leq 30°$. For this reason, **3III** is not considered in the spectral simulations anywhere in this manuscript.

Other Adsorbed Gases Other adsorbents have been tested for the single crystals of $\mathrm{Cu}_{2.965}\mathrm{Zn}_{0.035}(\mathrm{btc})_2$. $\mathbf{3}_{\mathrm{CO}_2}$ does not differ greatly from $\mathbf{3}_{\mathrm{act}}$ in terms of the general Cu^{2+} species found (no **3III**), while it is similar to $\mathbf{3}_{\mathrm{CO}}$ concerning the line broadening models shown in Fig. 4.7 and has similar $\mathbf{g}$ and $\mathbf{A}$ principal axis values as $\mathbf{3}_{\mathrm{CO}}$ with only slightly less correlated $\mathbf{g}$ and $\mathbf{A}$ strains.[163] Likewise, $\mathbf{3}_{\mathrm{MeOH}}$ shall only be introduced as that sample with most deviating $\mathbf{g}$ and $\mathbf{A}$ principal axis values compared to $\mathbf{3}_{\mathrm{act}}$ and even more pronounced line broadening effects and correlated strains than those of $\mathbf{3}_{\mathrm{CO}}$.[163] The interested reader is therefore guided to the original publication for more details than those found in Tab. 4.2, Tab. 4.4 and Fig. 4.5A.

4.2.3 Discussion of the Experimental and Calculated Tensor Values and Orientations

Review of DFT Results The optimized DFT calculations performed by P. Petkov initiated after the new single crystal EPR results revealed a distinct distortion of the isolated mixed Cu / Zn PW units in contrast to the idealized structure.[163] The principal axis orientations of the $\mathbf{g}$ and $\mathbf{A}$ tensors can be analyzed from the DFT data, and a schematic representation of the result is given in Fig. 4.7D for $\mathbf{3,DFT}_{\mathrm{MeOH}}$ as excerpt of

Tab. 4.4 DFT results for $Cu_{2.965}Zn_{0.035}(btc)_2$ under absorption: Principal axis orientations and angular tilting α_0 of the z principal axis directions of **g** and **A** tensors and binding energies of the ligand to the Cu^{2+} in the DFT computed PWs of $Cu_{2.965}Zn_{0.035}(btc)_2$.

Computed Structure	g_{zz}	g_{yy}	g_{xx}	A_{zz} / 10^{-4}/cm	A_{yy} / 10^{-4}/cm	A_{xx} / 10^{-4}/cm	α_0 /°	BE / eV
3,DFT$_{\mathrm{act}}$	2.179	2.045	2.044	−274	−32	−30	1.0	
3,DFT$_{CO_2}$	2.182	2.047	2.045	−273	−29	−23	0.4	-0.24
3,DFT$_{CO}$	2.195	2.050	2.050	−260	−14	−14	0.3	-0.60
3,DFT$_{MeOH}$	2.201	2.055	2.054	−270	−15	−15	2.0	-0.69

one PW from the periodic, unit cell cluster of $Cu_{2.965}Zn_{0.035}(btc)_2$ with about the same Zn^{2+} concentration as in the experimentally-studied **3**. The results presented in Tab. 4.4 show overall axially symmetric **g** and **A** tensors with principal axis values with a satisfying trend as known from powder EPR studies on the material.[40,149,151,163] Additionally, geometric optimization by DFT on the MOF $Cu_{2.965}Zn_{0.035}(btc)_2$ has revealed slightly perturbed but almost collinear **g** and **A** principal axis orientations not pointing along the C_4 axis of the PW for all adsorption states from the ideal structure assumed in Fig. 2.11A which has now to be discussed in context of the EPR results presented in the previous Subsection.

Overall, with an identical trend of increasing g factors with respect to an increasing magnitude of the binding energies of the adsorbed ligands and decreasing HFS, DFT indeed provides a reasonable correspondence to the experimental values. The binding energies of the axial ligand (if applicable) to the Cu^{2+} center of the PWs determined by DFT are also summarized in Tab. 4.4. In the original publication it was additionally introduced a hypothetical, isoelectronic but defective Cu / Cu PW containing one Cu^{+} which can be a possible modification in $Cu_{2.965}Zn_{0.035}(btc)_2$ with its major PW configuration of Cu / Cu PW metal centers.[163] It was found that the binding energies of ligand-Cu^{2+} (Cu / Zn PW) and ligand-Cu^{+} (Cu / Cu PW) are very similar and therefore the **g** and **A** tensors should not be very different.[163] Consequently, it suggests that in cw EPR Cu / Zn PW and Cu / Cu PW PWs might be difficult to distinguish. Thus, the ligand-Cu^{2+} coordination in Cu / Zn PW is primarily in this thesis. The previously mentioned rhombic deviation for **3,DFT**$_{CO_2}$ of $A_{yy} = -29 \times 10^{-4}/\mathrm{cm} \neq A_{xx} = -23 \times 10^{-4}/\mathrm{cm}$ can now, regarding the experimental findings given in Tab. 4.2 be compared with $\left|A_{xx,yy}\right| = 26(2) \times 10^{-4}/\mathrm{cm}$ right in between. This issue will also be discussed below.

A tilting angle of 1.0° was found for **3,DFT**$_{\mathrm{act}}$, 0.4° for **3,DFT**$_{CO_2}$, 0.2° for **3,DFT**$_{CO}$ and 2.0° for **3,DFT**$_{MeOH}$ of the z principal axis directions of the **g** tensors of Cu^{2+} in the static, optimized structures with respect to the Cu/Zn axis of the PW. Note that this axis does not coincide with the direction of the ligand-Cu^{2+} bond found in the optimized structure. The z principal axis directions of the **A** tensors correlate reasonably well with those of the **g** tensors (deviations of 0.1°, 0.2°, 0.0° and 0.3°, respectively) and can therefore be seen as collinear in accordance to the experimental results presented above. The projections of the **g** tensor z principal axis directions onto the plane spanned by the $Cu-O_P$ bonds in the PW are rotated by 37°, 40°, 24° and 38°, respectively, from a $Cu-O_P$ bond and therefore situated mostly in between two of the PWs' four oxygens O_P. The optimized structure itself resembles those angles by the finding, that for

3,DFT$_{\text{act}}$, **3,DFT**$_{\text{CO}}$ and **3,DFT**$_{\text{MeOH}}$ two adjacent Cu – O$_\text{P}$ bonds are about one percent longer than the two other Cu – O$_\text{P}$ bonds, forming themselves a tilted PW, while in the frozen structure of **3,DFT**$_{\text{CO}_2}$ only a single bond is shortened by that order of magnitude, leading to the rhombic **g** tensor pointed out in Tab. 4.4.

Principal Axis Values from EPR and XRD Regarding the results achieved from single crystal cw EPR and presented in Section 4.2.2, the rotations of the single crystals of **3** with respect to $\mathbf{B}_0$ in the (1 1 1) plane revealed the presence of six magnetically non-equivalent Cu^{2+} incorporation sites in the single crystal of $\text{Cu}_{2.965}\text{Zn}_{0.035}(\text{btc})_2$ with the same principal axis values of their **g** and **A** tensors. Therefore, the six distinct Cu^{2+} species are chemically equivalent but incorporated at different crystallographic lattice sites. Their Spin Hamiltonian parameters differ for each of the samples **3**$_{\text{act}}$, **3**$_{\text{CO}_2}$, **3**$_{\text{CO}}$, and **3**$_{\text{MeOH}}$ (Tab. 4.2) but coincide reasonably well given the mutual uncertainties with the findings for the powder samples, and indicate the influence of the adsorption process on the cupric ion coordination. In particular, it was found that only slight disagreements for $\Delta g_{zz} = -0.002$ and $\Delta A_{zz} = +3 \times 10^{-4}/\text{cm}$ for **3**$_{\text{act}}$ and $\Delta g_{xx,yy} = 0.002$ for **3**$_{\text{MeOH}}$ compared to publications of powder materials had to be taken into account.[40,163,164]

A variation of the principal axis values of the **g** and **A** tensors of the cupric ion indicates a change in the coordination geometry as outlined in Section 2.1.1.[193] The experimentally-obtained increase of g_{zz} and the decrease of A_{zz} correspond to a distortion of the square planar coordination geometry towards a square pyramidal coordination. Such an increase of g_{zz} is observed in combination with a decrease of the HFS upon adsorption of all tested and calculated adsorbent compared to the activated material as found for the powder materials before.[40,164] Furthermore, in the single crystals, the axial ligand field is found to be strongest for CH_3OH and decreases via CO and CO_2 to the activated sample **3**$_{\text{act}}$.[163]

The DFT calculations supported the observations by predicting a decreasing trend in the computed g_{zz} factors in an almost symmetric **g** tensor for the various PW configurations tested, **3,DFT**$_{\text{MeOH}}$, **3,DFT**$_{\text{CO}}$, **3,DFT**$_{\text{CO}_2}$ and **3,DFT**$_{\text{act}}$, and increasing A_{zz} principal axis values of the HFS tensor as shown in Tab. 4.4. This is correlated to the equally decreasing binding energies listed for the same computed models, except for **3,DFT**$_{\text{MeOH}}$ which shows slightly higher principal axis values for **A** than **3,DFT**$_{\text{CO}}$. One assumption is that the coordination of CH_3OH involves several orientations with similar binding energies that could lower especially the A_{zz} value with respect to A_{zz} of **3,DFT**$_{\text{CO}}$. Therefore, this deviation was attributed to a computational insufficiency.[163] The rhombic deviation in g_{xx} and g_{yy} of **3,DFT**$_{\text{CO}_2}$ can be explained by the expected averaging from the CO_2 ligand molecule: while the DFT calculation presents a static, frozen picture, it was shown earlier that the low energy required to rotate the CO_2 molecule at its bond to Cu^{2+} of 2 kJ/mol can lead to several frozen-molecule positions with equivalent energy but almost unchanged g_{zz} values, while the g_{xx} and g_{yy} average out over a rotated azimuthal angle.[164] The experimental finding for **3**$_{\text{CO}_2}$ of $A_{xx,yy} = 26(2) \times 10^{-4}/\text{cm}$, which is very well the mean value of **3,DFT**$_{\text{CO}_2}$ $A_{xx} = 23(2) \times 10^{-4}/\text{cm}$ and $A_{yy} = 29(2) \times 10^{-4}/\text{cm}$, is the distribution of this averaged value measured by EPR and it confirms therefore again the assumption of the averaged value.[163] Additionally, if such small deviations would really be present, they could hardly be observed with the given experimental, spectral resolution of X-band EPR spectroscopy.

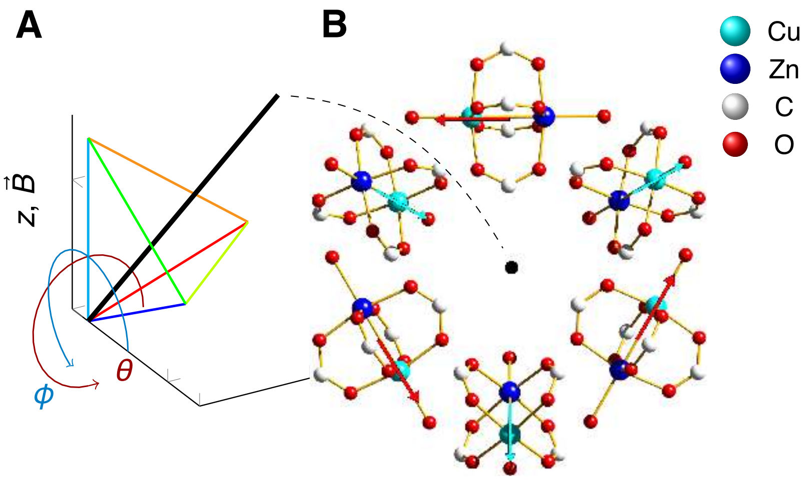

Fig. 4.10
Incorporation sites of Cu^{2+} in $Cu_{2.965}Zn_{0.035}(btc)_2$:
(A) The principal axis orientations with respect to the z axis of the simulated spectra in Fig. 4.9B with indication of the Euler angles ϕ, θ used for manipulation of the tensor system (Tab. 4.3) and a [1 1 1] axis (thick, black).
(B) Schematic representation of the structure of all PW orientations occurring in the hydrated MOF $Cu_{2.965}Zn_{0.035}(btc)_2$ viewed along a crystallographic [1 1 1] axis (black dot). All PWs show $\mathbf{g}$ and $\mathbf{A}$ tensors pointing from Zn^{2+} to Cu^{2+} along each PW's C_4 axis. Species of group **3**I (red) are incorporated in the $(1\,1\,1)$ plane, species of **3**II (cyan) are raised from it.

Deducing the Lattice Sites Geometrically, three species (group **3**I) were found to be incorporated with the z axes of their $\mathbf{g}$ and $\mathbf{A}$ tensors parallel to the crystallographic $(1\,1\,1)$ plane and each aligned along the crystallographic $\left[1\,\bar{1}\,0\right]$ axes, $\left[0\,1\,\bar{1}\right]$ axes or $\left[1\,0\,\bar{1}\right]$ axes. Additionally, three further species (group **3**II) are identified with z axes orientations along the crystallographic [1 1 0] axes, [0 1 1] axes and [1 0 1] axes of the cubic crystal lattice.

HKUST-1 with its $Fm3m$ space group has 36 Cu^{2+} pairs in the lattice cell that are forming six magnetically non-equivalent sites in accordance with the observed six magnetically non-equivalent Cu^{2+} species in the studied $Cu_{2.965}Zn_{0.035}(btc)_2$ crystals of $\mathbf{3}_{\text{act}}$, $\mathbf{3}_{CO_2}$, $\mathbf{3}_{CO}$ and $\mathbf{3}_{MeOH}$.[145] In a cubic lattice, the [1 1 1] axis corresponds to a threefold screw axis. Indeed, for the rotation of the magnetic field about the [1 1 1] axis two groups of angular dependencies (**3**I and **3**II) were observed and each consists out of four resonance lines belonging three species and showing a threefold symmetry. The PW units have a local C_4 rotational axis about the vector joining the two Cu^{2+} ions in the pair. The C_4 axes for the six magnetically non-equivalent sites of the PWs point along the six face diagonals of the cubic lattice cell, the crystallographic $\left[1\,\bar{1}\,0\right]$ axes, $\left[0\,1\,\bar{1}\right]$ axes, $\left[1\,0\,\bar{1}\right]$ axes, [1 1 0] axes, [0 1 1] axes and [1 0 1] axes. It is natural to assume that the symmetry axis (z axis) of the cupric ion $\mathbf{g}$ and $\mathbf{A}$ tensors in the mixed PWs in which one Cu^{2+} ion has been substituted by Zn^{2+} will also point along these local C_4 axes in perfect agreement with the six experimentally-found z axes orientations of these tensors (Tab. 4.3) and the DFT results. Fig. 4.10B illustrates a projection of the orientations of the six magnetically non-equivalent PWs units onto the $(1\,1\,1)$ plane together with experimentally-determined z axis orientations of the coaxial Cu^{2+} $\mathbf{g}$ and $\mathbf{A}$ tensors of the mixed Cu / Zn PW pairs. Consequently, one can conclude that the single crystal measurements further validate the powder measurements by finding the Cu^{2+} species in $Cu_{2.965}Zn_{0.035}(btc)_2$ at all crystallographically possible, former dinuclear Cu / Cu PW sites of $Cu_3(btc)_2$,[40] representing another method to verify a successful substitution of Cu^{2+} by Zn^{2+} ions in the PWs of this MOF.[163]

4.2.4 Discussion of the Experimental Tensor Orientation Distributions

Powder spectra of zinc doped $\mathrm{Cu_{2.965}Zn_{0.035}(btc)_2}$, both of activated materials and upon adsorption of $\mathrm{CO_2}$, CO and $\mathrm{CH_3OH}$, can be satisfactorily simulated using correlated **g** and **A** strain effects (Section B.5 in the Appendix). However, to explain the line shapes of the $\mathrm{Cu^{2+}}$ EPR signals in the recorded single crystal spectra of **3**, it was found that is not enough to apply just such correlated strain effects, while also unresolved ^{1}H hyperfine couplings can be excluded based on an earlier ENDOR study of the material.[40] Therefore, a simple model based on a tilt of the z symmetry axes of the $\mathrm{Cu^{2+}}$ ions' **g** and **A** tensors due to the adsorption process was also chosen. In a first approach of such a model, it was assumed that a perturbation of the local C_4 symmetry of the PW unit could be observed. The z axes of both tensors are oriented such their projections onto the plane perpendicular to the C_4 axis and spanned by the four carboxylate oxygen atoms $\mathrm{O_P}$ of the PW unit binding to the $\mathrm{Cu^{2+}}$ ion is along one of the four $\mathrm{Cu-O_P}$ bonds. It was expected that adsorbate molecules with a low symmetry such as $\mathrm{CH_3OH}$ but also various linear molecules such as $\mathrm{CO_2}$ would form a bent adsorption complex with the $\mathrm{Cu^{2+}}$ ions as is has been verified experimentally recently by pulsed EPR spectroscopy by Jee et al.[164] and would hereby destroy the local C_4 symmetry of the PW unit. Consequently, the z axes orientation of the **g** and **A** tensors might deflect from the former C_4 symmetry axes and can be described by this model (Fig. 4.7A). Otherwise, a small linear symmetric molecule such as CO or a highly symmetric one such as $\mathrm{H_2O}$ adsorbed at the host PW's $\mathrm{Cu^{2+}}$ binding site is expected to point straight along the C_4 axis as depicted in Fig. 4.10B for adsorbed water (represented by the ligand's central $\mathrm{O_L}$ atom for the hydrated structure).[164] Therefore, the z axes of the **g** and **A** tensors should also point along the local C_4 symmetry axis in such cases. Then, any distortion from this z axes' alignment would indicate deviations of the real structure from the ideal single crystal structure e.g. due to structural defects and should be significantly less than in the above case of bent adsorption complexes formed by molecules with lower symmetry.

The simulations implemented in the work involved a first, simple model from Fig. 4.7A. Here, it was assumed that all four possible orientations of the tensors z axes would occur with equal probability and that they could be distributed around the C_4 axis by $\Delta\alpha$ in a Gaussian fashion with an average position $\alpha_0 = 0°$. The conducted simulation can now be used to find a Gaussian distribution width that the spectral simulations would favor. After comparison of many spectra of **3**, it was found that the tilt of the z axes of the **g** and **A** tensors towards one of the $\mathrm{Cu-O_P}$ bonds provides a reasonably accurately-broadened line shapes of the $\mathrm{Cu^{2+}}$ EPR resonance lines with $\Delta\alpha = 3.0(5)°\ldots 6.0(5)°$ in comparison to further models tested, another model involves a bent adsorption structure with two equilibrium positions of the z principal axis orientations with an intermediate splitting of $2\alpha_0$, their projection at first along the $\mathrm{Cu-O_P}$ direction and a distribution of width $\Delta\alpha/2$ (Fig. 4.7B) and further with the projections exactly between two of the $\mathrm{Cu-O_P}$ bonds (45° from one $\mathrm{Cu-O_P}$ bond in the plane perpendicular to the C_4 axis) and a distribution of width back at the starting value of approximately $\Delta\alpha$ (Fig. 4.7C, $\Delta\alpha$ according to Tab. 4.2). However, upon further inspection of these two models, there was no evidence pointing to significant improvements in the line broadening of the spectral simulations. For the simulations with the model of Fig. 4.7B, the computational efforts doubled in favor of a decreasing distribution width. For the model described by Fig. 4.7C, the distribution width was

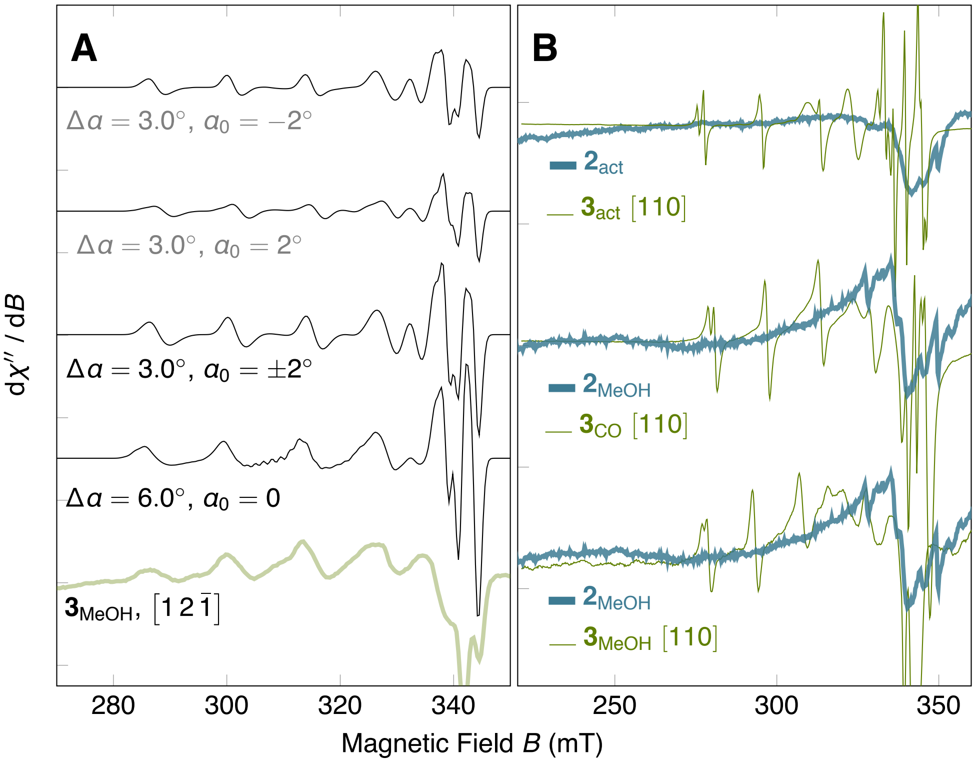

Fig. 4.11
Comparison of broadening models; $\mathbf{2}_{\mathrm{act}}$, $\mathbf{2}_{\mathrm{MeOH}}$ compared to $\mathbf{3}_{\mathrm{act}}$, $\mathbf{3}_{\mathrm{MeOH}}$ and $\mathbf{3}_{\mathrm{CO}}$.:
(A) Comparison of the line broadening models with static angles $\Delta\alpha$ delivered from DFT (see Section 2.4.2) and tilting angle distribution α_0 found by EPR.
(B) EPR spectra recorded for a larger magnetic field range of samples $\mathbf{2}_{\mathrm{act}}$ and $\mathbf{2}_{\mathrm{MeOH}}$ (cyan) in comparison to the spectra of $\mathbf{3}_{\mathrm{act}}$, $\mathbf{3}_{\mathrm{CO}}$ and $\mathbf{3}_{\mathrm{MeOH}}$ (lime).

also found to be $\Delta\alpha$ with still the twofold number of spectra, which must be computed for the fit. Naturally, even further amalgamations of these models and directions might occur.

Nevertheless, the experimentally-recorded EPR resonance lines did not allow for a more certain choice between these models, as they all provided reasonably well broadened spectral simulations. Therefore, all spectral simulations shown involved only the simplest model shown in Fig. 4.7A. Considering the unresolved background signal of Cu^{2+} species **3**III, even this simplest model provides sufficiently accurately-broadened resonance field lines. On the other hand, the more complex models tested for the spectral simulations (Fig. 4.7B–C) also lead to similarly broadened EPR resonance lines, as Fig. 4.11A shows for $\mathbf{3}_{\mathrm{MeOH}}$ as an example. Here, the equilibrium positions $\alpha_0 = \pm 2^\circ \neq 0^\circ$ were chosen and $\Delta\alpha$ was decreased to only half the value of the original spectral simulation of $\mathbf{3}_{\mathrm{MeOH}}$ for the two Gaussian curves, each. As one can see, such a small distribution of the tilting angle already leads to almost sufficiently broadened EPR lines. Therefore, from the spectral simulations alone, it is difficult to decide for an appropriate model, as both the perturbation direction and the distribution width can be chosen rather arbitrarily in the simulations.[163]

The remaining discussion joins the DFT calculations and the spectral simulations of the single crystal cw EPR spectra of **3**, as one now can decide that the most complex model presented in Fig. 4.7C meets the DFT results most accurately. It is therefore likely, that one can describe the changes of the Spin Hamiltonian **g** and **A** principal axis orientations to involve at least one main tilting direction between two of the $Cu-O_P$ bonds, each, leading to four possible tilting directions per PW. The equilibrium positions α_0 given in Tab. 4.4 as predicted by DFT can be a reasonable assumption also for the spectral simulations and, as the DFT data is derived from a single, perfect unit cell of $Cu_{2.965}Zn_{0.035}(btc)_2$, it is likely that unaccounted strain effects within the MOF framework, presumably caused by lattice defects, may lead to the deviations in the **g** and **A** tensor orientations observed by EPR and described by the Gaussian distributions in the spectral simulations with a distribution width amounted to $\Delta\alpha$ as given in Tab. 4.2. Therefore, it was assessed that the DFT data agrees sufficiently well to the model described in Fig. 4.7C for the experimental observations which because of the SNR of individual line shapes alone otherwise would not allow to confirm a specific model. Within the current scientific research in this area, such structural changes during activation and upon adsorption on Zn^{2+} substituted $Cu_{2.965}Zn_{0.035}(btc)_2$ single crystals have never been monitored with competing techniques to EPR that could give estimates about this kind of behavior.[163]

At this point, it is important to recall the results of a distinctively deformed baseline shown in Section 4.2.1. With the knowledge about species **3**III obtained for $\mathbf{3}_{CO}$ and $\mathbf{3}_{MeOH}$ of $Cu_{2.965}Zn_{0.035}(btc)_2$ it is reasonable to attribute the broad signal observed for the single crystal cw EPR spectra of $Cu_3(btc)_2$ (Fig. 4.4) to a similar species as the latter ones noted. For them as well, neither apparent HFS signals nor clear evidence for an angular dependency was found. It is remarkable to note that after a reactivation the signal disappears as described earlier. Simulations with the proposed simple models from above using even distribution widths up to $\Delta\alpha \approx 30°$ do not reproduce the signal shape, but it is very likely that the origin of species **3**III and the Cu^{2+} EPR signal of **2** are similar, as Fig. 4.11B shows. Here, the signal of $\mathbf{2}_{MeOH}$ represents an almost ideal baseline for $\mathbf{3}_{CO}$ and $\mathbf{3}_{MeOH}$.

As the Cu^{2+} species **3**III thus occurs in both materials **2** and **3**, it cannot be related to the Cu / Zn PW but seems to be a general feature of HKUST-1. Therefore, one has to conclude that whatever defect gives rise to the spectra of species **3**III is independent from the observations obtained for the species of group **3**I and **3**II in $Cu_{2.965}Zn_{0.035}(btc)_2$ upon adsorption. Other than that, it is not addressed in the scope of this work.

4.2.5 Conclusions for $Cu_{2.965}Zn_{0.035}(btc)_2$

While a former study addressed the HFS interaction to various ligands,[197] in the recently published work the influence of the adsorption of various gases on the Cu / Zn PW in **3** has been explored by DR aided single crystal cw EPR spectroscopy.[163] These measurements demonstrate likewise the versatility of the DRs for EPR measurements at non-ambient conditions, in this case again at low temperatures and now in the presence of various gas atmospheres. The adsorption of CO_2, CO and CH_3OH induces changes in the principal values of the **g** and **A** tensors of the Cu^{2+} ions as well as in the observed EPR line patterns both in the powder and single crystal spectra of **3**.[40] Otherwise, the single crystal EPR studies of **3** upon adsorption of various gases indicate that the overall orientations of the cupric ion **g** and **A** tensors of the mixed Cu / Zn PW is not significantly affected by the gas adsorption process.

In particular, nicely resolved, distinct, angular dependent EPR spectra of six mononuclear Cu^{2+} ion incorporation sites according to the crystal structure in the single crystals of the framework $Cu_{2.965}Zn_{0.035}(btc)_2$ were observed and their origin from mixed Cu / Zn PW units was confirmed.[163] Further, an important line broadening effect was monitored, which can reasonably well be explained by a tilting of the **g** and **A** z principal axis directions of the host Cu^{2+} ions in the PWs by a few degrees. Different models for this perturbation have been proposed and inspired by DFT calculations it was suggested that a probable tilting direction lays between two Cu–O bonds of the PW and an equilibrium tilting angle would be of the order of a few degrees. Moreover, a distribution in the real structure was postulated and small differences for the monitored adsorption of CO, CO_2 and CH_3OH with respect to each of these parameters have been described. It must be stressed that those minor changes in the z principal axis directions could never be observed by powder EPR before in MOFs.

4.3 Ferromagnetic Resonance in SURMOF-2 Thin Films

This Section will present an overview of the results obtained for two members of the SURMOF-2 family, (Cu,bdc) SURMOF-2 (**4**) and (Cu,bpdc) SURMOF-2 (**5**) (cf. Section 2.4.3). The content of this Section has been published recently in parts in Friedländer et al.[139] EPR measurements recorded for the SURMOF-2 **4** and **5** reveal rather unexpected properties. The data recorded for (Cu,bdc) SURMOF-2 with the $\mathbf{B}_0$ oriented in the film plane shows a very intense and relatively broad signal at a resonance field of 114 mT at 5.5 K. Both the resonance field and the linewidth of this signal display pronounced dependencies on temperature and film orientation. This signal disappears at temperatures $T \geq 28$ K and importantly it shows a characteristic variation of the resonance field with the angle θ_F between the substrate and the magnetic field.[139] Further measurement conditions are summarized in Section A.1 in the Appendix. In principle, such a signal could be explained by the presence of magnetic species with a high g-value of $g_j \approx 5.6$ or even greater, but such a species was not expected to be incorporated in the material from the fabrication conditions and the careful analysis carried out before by J. Liu, M. Addicoat, P. Petkov, N. Vankova, R. Rüger, A. Kuc, W. Guo, W. Zhou, B. Lukose, Z. Wang, P. Weidler, T. Heine and C. Wöll, who investigated and analyzed the sample by XRD, infrared reflection absorption spectroscopy (IRRAS) and Raman spectroscopy.[139] At this point, the EPR measurements presented below in Section 4.3.1 and further magnetic characterization by M. Ziese with the help of a SQUID have been performed.[1] In Section 4.3.2, the conclusions drawn from all observations and the DFT calculations performed by the group of T. Heine are discussed.

4.3.1 The Unusual g Factor and Exploration of the Magnetic Anisotropy

Images of the films and their treatment is given in Section B.3.3 of the Appendix. Preliminary tests with SURMOF-2 on other substrates, SURMOF-2 powders and Q-band cw EPR measurements supported the drawn conclusions presented below but did not reveal any further insights, especially regarding particular $S = 1$ or other EPR signals of the Cu^{2+} pairs that were expected but could not be resolved due to an insufficient SNR. Of all tested sample configurations, thin films of SURMOF-2 frameworks show the most well-reproducible EPR spectra with highest SNR in X-band. Therefore, these thin film measurements are selected for the results given in the following.[139]

Fig. 4.12A shows the EPR spectra of (Cu,bdc) SURMOF-2 and (Cu,bpdc) SURMOF-2 at similar temperatures and film orientations ($\mathbf{B}_0$ perpendicular to film normal). The signal with $g_j \approx 5.6$ and $g_j \approx 7.8$,

---

[1] see also Sect. 1.2.4 in supporting information of [139]: `http://dx.doi.org/10.1002/anie.201606016`

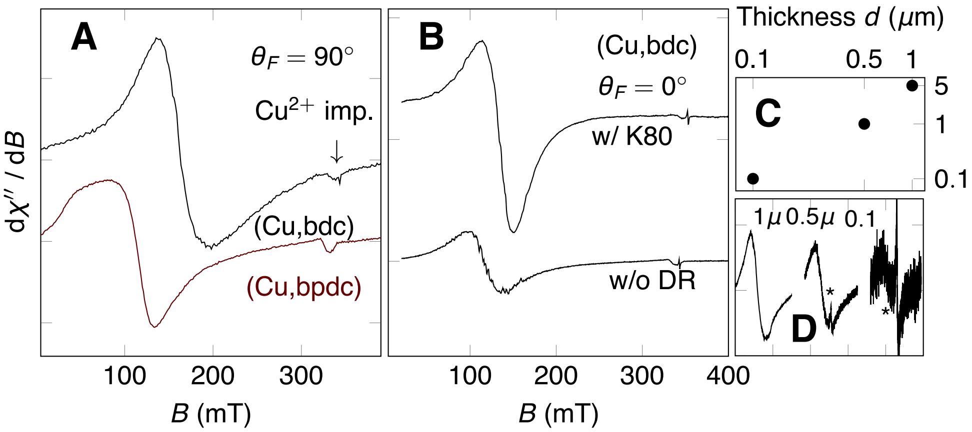

Fig. 4.12

FMR spectra of 4 and 5: Thin films measured with cw EPR
(A) Comparative spectra at 9 K, $\mathbf{B}_0 \perp$ film normal ($\theta_F = 90°$), the arrows mark cryostat Cu^{2+} signal.
(B) Signals with $\mathbf{B}_0 \parallel$ film normal can be enhanced by DRs.
(C) FMR signal in dependence of film thickness (double log. axes).
(D) Shows the three signals with linear intensity axis but shifted resonance fields for presentation, asterisks mark Cu^{2+} impurity.

respectively, does not show any microwave power saturation at low temperatures. It disappears at temperatures $T \geq 28$ K, where only a broad signal of the conduction electrons from gold layer coated MHDA substrate is detected (see Fig. B.8 on page 105 in the Appendix). Though such high g values can be observed for magnetic $4f$ and $3d$ ions with electron spins $S \geq 5/2$ and rare earth ions with $J = \frac{1}{2}$,[198] the characteristic features of this signal are rather uncommon for EPR spectra of isolated paramagnetic species but typical for FMR signals of two-dimensional structures.[80,82,199,200] Fig. 4.12B shows that the SNR can be increased again by the help of DRs which was necessary to obtain the spectra of a 0.1 μm thin film of **4** displayed in Fig. 4.12C and D, where the dependence of the double integrated FMR signal on the film thickness is shown. The experiment shows that the film thickness results in different intense FMR signals and magnetic moments. The experiments are depicted in Fig. B.8 on page 105 in the Appendix.

Fig. 4.13A shows the dependence of the FMR signal of (Cu,bdc) SURMOF-2 on the temperature, while Fig. 4.13B summarizes the apparent g factor and $\mathbf{B}_0$ resonance fields for (Cu,bdc) SURMOF-2 and (Cu,bpdc) SURMOF-2. The labels in Fig. 4.13A mark impurities from the resonator (Fe) and the MHDA substrate. Below 20 K the linewidth decreases linearly with temperature until it saturates below about 8 K. For (Cu,bpdc) SURMOF-2 the linewidth decreases linearly below a higher temperature of about 25 K. As outlined in Section 2.1.5, the Curie temperature might be determined from the linewidth as the onset of the linewidth decrease.[89] In agreement with the T_C determined from the susceptibility,[139] this yields $T_C = 18(1)$ K for (Cu,bdc) SURMOF-2 and $T_C = 22(2)$ K for (Cu,bpdc) SURMOF-2, as indicated by the opaque line construction in Fig. 4.13B. The g factor of the FMR signal of (Cu,bdc) SURMOF-2 decreases continuously from $g_J = 5.6(1)$ at 5.5 K to $g_J = 2.1(1)$ at 28 K in the paramagnetic phase and from $g_J = 8.2(2)$ at 5.5 K to $g_J = 2.3(2)$ at 32 K for (Cu,bpdc) SURMOF-2. There the internal fields due to the magnetic ordering have vanished and the g value approaches those of the now magnetically uncoupled paramagnetic species. The observed value $g_J = 2.1(1)$ for the (Cu,bdc) SURMOF-2 film at 28 K ($T \geq T_C$) is typical for isolated cupric ions and antiferromagnetically coupled cupric ion pairs in solids where the angular momentum is quenched.[152,193,201] Indeed, it is in agreement with literature values of the mean g factor of the spin triplet state of Cu(II) dimers measured for other MOFs.[40,152] In the ferromagnetic phase the resonance field decreases considerably (increase of g_J) which might, at first glance, be related to the ferromagnetic

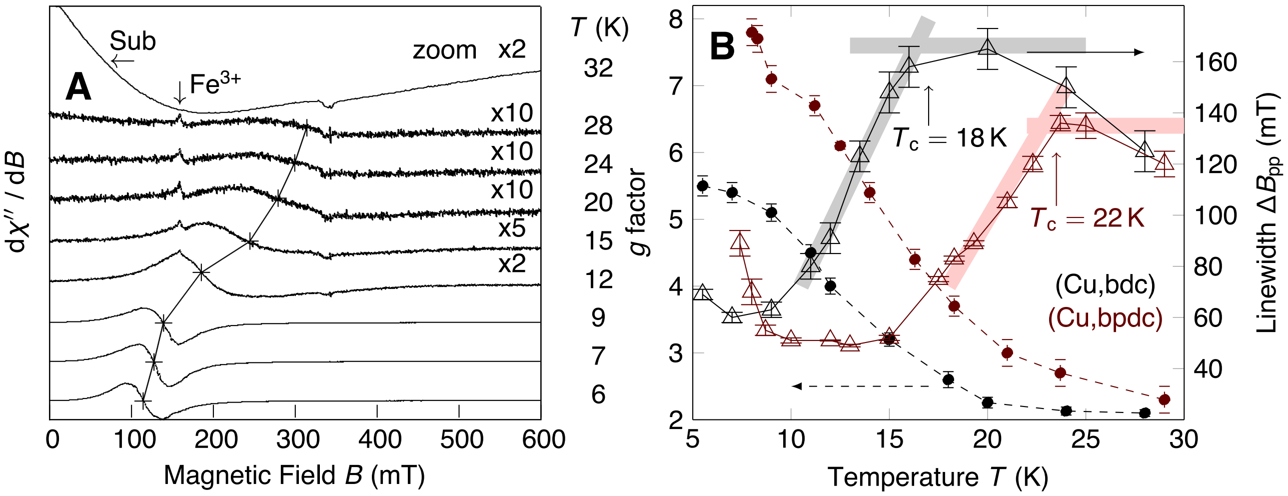

Fig. 4.13 Temperature dependent FMR spectra of 4 and 5:

(A) Thin film FMR spectra at different temperatures of (Cu,bdc) SURMOF-2 with the FMR signal indicated by +. The connecting lines are guides for the eye. The arrows mark the substrate (Sub) visible at temperatures above 30 K and the Fe^{3+}-impurity signal of the resonator.

(B) Temperature dependence of the g factor (dots, dashed lines) and the peak-to-peak linewidth (triangles) of the FMR signal measured for $\theta_F = 90°$ for (Cu,bdc) SURMOF-2 (black) and (Cu,bpdc) SURMOF-2 (red). The lines are guides for the eye. Above 28 K the g factor is about 2.1(1) The opaque lines illustrate the determination of T_C from the linewidth.

ordering. An important difference in the EPR results of (Cu,bdc) SURMOF-2 is manifested in a different Curie temperature as presented in Fig. 4.13B.

Fig. 4.14A shows the dependence of the FMR signal of (Cu,bdc) SURMOF-2 on the thin film orientation and Fig. 4.14B compares the resonance fields of (Cu,bdc) SURMOF-2 with the fitted behavior yielding the magnetic anisotropy parameters indicated below. Both the resonance field and the line width change periodically with the angle θ_F which is characteristic for FMR signals of thin films.[14] The resonance field for parallel configuration $\mathbf{B}_0 \parallel$ film normal ($\theta_F = 0°$) approaches the resonance field at temperatures above the ferromagnetic phase. It was observed that the extent of this anisotropy may vary for different films and may also become smaller for prolonged storage times of a film sample. To understand the angular dependence of the FMR signal, a magnetocrystalline anisotropy energy containing uniaxial second and fourth order anisotropy terms as outlined in Section 2.1.5 and Eqn. 2.69 was assumed. The solid line in Fig. 4.14B was obtained with anisotropy fields $\mu_0 H_{2\perp} = 2K_{2\perp}/M_S = 8\,\mathrm{mT}$ and $\mu_0 H_{4\perp} = 2K_{4\perp}/M_S = 45\,\mathrm{mT}$ as well as a g factor of $g^{\mathrm{fm}} = 4.3$ and is in good agreement with the data. The total anisotropy field $\mu_0 H_A = \mu_0 H_{2\perp} + \mu_0 H_{4\perp} = 53\,\mathrm{mT}$ is considerably smaller than the estimate above obtained from the magnetization curves;[139] in view of the large uncertainty of the magnetization curve approach this might be regarded as satisfactory. As it was already indicated by the temperature dependence of the resonance field in Fig. 4.13B, the g factor strongly increases in the ferromagnetic phase. In the perpendicular field orientation ($\theta_F = 0°$) Eqn. 2.69 yields the resonance field Eqn. 2.71. Since the resonance fields in the paramagnetic phase and in the ferromagnetic phase at $T = 7\,\mathrm{K}$ for $\theta_F = 0°$ are almost identical and $B_{0\perp} + M_{\mathrm{eff}}$

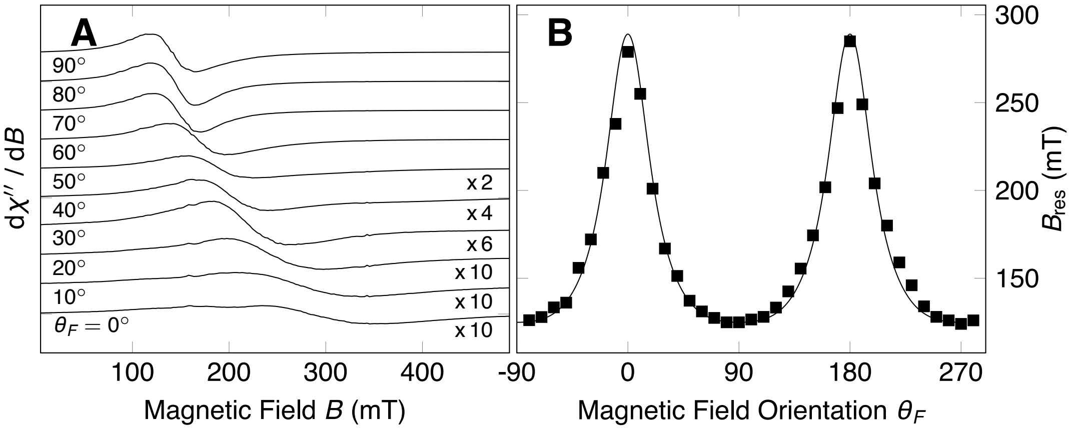

Fig. 4.14 Angular dependent FMR spectra of (Cu,bdc) SURMOF-2: Angular dependent FMR spectra of **4**:
(A) comparative spectra at 7 K measured at different angles θ_F between the applied magnetic field and the film normal.
(B) The resonance fields of (Cu,bdc) SURMOF-2 measured at 7 K as a function of the angle θ_F between the applied magnetic field and the film normal (filled squares). The solid black line is a fit to Eqn. 2.69.

steadily increases with decreasing temperature up to 114 mT at 5.5 K (Fig. 4.13B), the gyromagnetic ratio must increase with decreasing temperature. Such a strong g factor increase is unconventional and points towards the unconventional coupling mechanism in this compound. Finally, for all studied SURMOF-2 thin film samples the obtained angular dependence of the FMR signal indicates an alignment of the magnetic easy axis parallel to the film plane.

Total magnetization measurements by M. Ziese using a SQUID setup provided independent evidence for the presence of ferromagnetism in the SURMOF-2 samples.[139] The magnetization curves of the (Cu,bdc) SURMOF-2 are also very similar from those of the (Cu,bpdc) SURMOF-2 and yield a comparable Curie temperature of 18.0(5) K and 22.0(5) K, respectively,[139] in accordance to the FMR data. Similarly, these experimental results clearly indicate the presence of intrinsic ferromagnetism which is not induced by high magnetic fields, in contrast to the previously studied MOF systems.[139,181] One can deduce also from the magnetization hysteresis measured with $\mathbf{B}_0$ applied parallel and perpendicular to the film that the film normal is a magnetic hard axis.

4.3.2 Discussion of the Spin-Canting Model

Under the assumption that all specimen had about the same sample sizes of about $3 \times 3\,\mathrm{mm}^2$ resulting in about 10^{16} unit cells for the 1 μm thick (Cu,bdc) SURMOF-2 film, it can be estimated by the DR aided SNR enhancements shown in Fig. 4.12B-D that the FMR signal intensity relates to the film thickness by a power law. This shows that the observed ferromagnetic phase is indeed originating from the bulk sample of the thin film instead of being a surface effect. Further it was confirmed that for $T \geq T_C$, g_J approaches the g value found for square planar coordinated Cu^{2+} in MOFs.[40]

These magnetic properties exhibited by the (Cu,bdc) SURMOF-2 system cannot be understood based on the previously published structure by Liu et al.[174] The proposed, intact, non-deformed PW units of Cu^{2+} pairs herein are characterized by an antiferromagnetic singlet ground state as stated in the previous two Sections, where the two spins of the adjacent metal ions couple antiferromagnetically with a coupling strength of 38 meV or more.[202,203] On the basis of new powder-diffraction Rietveld XRD (PXRD) data obtained by coauthors,[139] the structural model proposed in this earlier work must be rejected.[174] Instead, the Rietveld refinement yielded an unexpected strong deviation of Cu^{2+} atoms aligned along a straight line (Fig. 2.12). Since the quality of the PXRD-data is not sufficient for a determination of the O and C atoms in the (Cu,bdc) SURMOF-2 compound, it was carried out a systematic theoretical re-investigation of the structure starting from the new experimental data.[139] Hereby T. Heine and co-workers were able to obtain from ab initio Born–Oppenheimer molecular dynamics (MD) and associated simulated annealing calculations the structure shown in Fig. 2.12.[139] While the position of the Cu^{2+} atoms is essentially the same as that determined by the Rietveld refinement of the PXRD data, this structure also shows violations of the intact PW units and – unlike the defect PW units found in ${}^{3}_{\infty}[Cu^{I}_{2}Cu^{II}_{2}(H_2O)_2L_2Cl_2]$– consists of semi-PWs forming slightly deformed 1D chains of Cu^{2+} ions linked together in a zipper-like fashion. This novel Cu^{2+}–acetate structure motive has two Cu – Cu distances, a short one of 2.47 Å and a longer one of 3.85 Å. This is a very unusual arrangement and has not yet been observed or considered in other Cu^{2+}–carboxylate based MOF type. A motif with remote similarity has been found in copper phosphonates, where a weak ferromagnetism arising from spin canting was observed.[204] In contrast to previous reports,[136] a clear orientation dependence of the FMR signal on the direction of $\mathbf{B}_0$ is observed. Such an orientation dependence of the FMR signal, a crucial signature for a FM ordering in a thin film, is thus reported for a MOF sample for the first time.[139]

4.3.3 Conclusions for (Cu,bdc) SURMOF-2 and (Cu,bpdc) SURMOF-2

The quasi-1D Cu^{2+} chain is almost perfectly positioned in a plane and as the investigated specimen are members of an isoreticular series of MOFs, the lattice-constant of these molecular solids can be changed easily by using organic struts of different lengths like for example the bdc and bpdc linkers without changing the Cu – Cu distances in the chain.[174] The EPR measurements have shown that via this method the Curie temperature can easily be scaled. FMR was observed for the first time in this kind of thin film MOF materials in absence of strong external magnetic fields and the T_C is remarkably high in comparison to similar materials.[139]

5 Summary, Conclusion and Outlook

5.1 High Sensitivity EPR with Dielectric Resonators and Planar Microresonators

In recent years, several new techniques have been applied in EPR spectroscopy. Ultra high field EPR is available via different projects,[205–207] and highly advanced, ultra-short and arbitrarily shaped pulses known from NMR can now be generated for pulsed EPR spectroscopy by a growing scientific community.[208–210] These technological progresses have enhanced EPR sensitivity by orders of magnitude and allowed previously unknown insights in matters of various kind.[211,212] Besides the fact that these important improvements require expensive instrumentation, the scientific community needs widely applicable solutions that can satisfy the necessity for an increased sensitivity for all contributors. Among those which could soon be realized, single chip solutions may play the most radical role as low-cost resonators with high sensitivity in the future.[120,213] As seen also in the context of this work, they even appear to be a promising alternative to entire, current spectrometer designs, given their all-in-one chip approach.[68]

One of these more established, high-sensitivity EPR spectroscopy methods based on PCB-like miniature resonators is the PMR with typical sub-wavelength dimensions. Those lumped circuit resonators known for their high filling factors have achieved outstanding performance in spin sensitivity,[16,128] but while integrated spectrometer ASICs including the resonator and all mw parts on one PCB try to become substitutes for whole spectrometers, PMRs, which are cheap in fabrication, could possibly serve as an alternative to expensive, high quality traditional resonators for measurements in which superior sensitivity for ultra-small samples plays a key role. In the same way, in recent years DRs have gone from niche applications for a limited set of radical samples and ambient measurement conditions to versatile, easy and cheap upgrades for existing spectrometer setups at various temperatures and atmospheres.[186]

In the present work the latter two techniques have been presented and compared to other EPR resonators in terms of pure sensitivity as SNR, but also normalized SNR gain with respect to the mw $\mathbf{B}_1$ field. While for PMRs the main focus was the implementation of an actual setup for cw and pulsed EPR at room temperature, DRs have successfully been applied to various porous MOF samples with low spin density to obtain new insights in the structures.[139,153,163] In particular, as shown in Section 3.1, it was possible to evaluate a new series of effective EPR silent DRs based on barium lanthanide titanates solid solutions (BLTss) with the general formula $\mathrm{Ba}_{6-x}\mathrm{Ln}_{8+2x/3}\mathrm{Ti}_{18}\mathrm{O}_{54}$ ($\mathrm{Ln} = \mathrm{Sm}, \mathrm{Nd}$) with small dielectric losses and dielectric constants of about 80.[186] The DRs can easily be used in combination with cavity resonators and flow cryostats for experiments in room temperature and down to 4.2 K. The sample can be kept in quartz glass tubes for measurements of dehydrated or gas-loaded samples. Disk-shaped DRs can be employed to tune stacked, double DRs or for measurements of thin film samples, and ring DRs are especially suited for low volume samples such as tiny single crystals. The developed DRs have shown their experimental reliability and proved to be applicable in various MOF material studies published recently and summarized below.[153,163] As shown in Section 3.1.2, the impurity content has been optimized within the collaboration project, yielding very low contents such that intrinsic EPR signals from the DRs are acceptable. Relatively thin, ring shaped DRs perform best at all investigated temperatures with respect to both the relative conversion factors of the mw $\mathbf{B}_1$ field and normalized SNR gain. The highest normalized SNR gain achieved was an enhancement of 19 at normalized mw power-$\mathbf{B}_1$ conversion and room temperature, and up to 15 at low temperatures of 8 K. The additional $\mathbf{B}_1$ field enhancements only near the sample of a factor of maximally 4.8 at all temperatures helps additionally to suppress impurity signals from the cryostat interfering with the specimen under study as outlined in Section 3.1.3. Hence, although the latter $\mathbf{B}_1$ field enhancements must be regarded separately for most cw EPR applications, the combined SNR enhancement of a factor of 80 (see Tab. 3.2 for all results) can be deemed the highest repeatedly achieved total SNR gain in the scope of this work.

In Section 3.2.2, the SNR enhancement efficiency of PMRs with home-build setups has been analyzed and compared to high sensitivity cavity resonator combinations. With the most advanced probehead setup R2.1 and sapphire PMRs T2, a spin sensitivity of about $10^9\,\mathrm{spins}/(\mathrm{G} \times \mathrm{Hz}^{1/2})$ has been estimated. This value represents at least a reproduction of the previously reported value in Narkowicz et al.[128] The achieved PMR setup allows for a stable PMR mode ready for room temperature cw EPR measurements involving multiple sample exchanges. Various tests with variations in the sample geometry have shown SNR gains of 51 or more for very small, planar samples with diameters below 50 μm in comparison to conventional cavity resonators. It was shown that this SNR gain has not yet reached its maximum and holds an inverse relationship to the sample size. For very small samples, the SNR enhancement can even outreach the correction for the $\mathbf{B}_1$ field enhancement, which at present tests was at least 25 times larger than a BRUKER MD5 resonator. Due to this property, it could be shown in Section 3.2.3 that the PMR setup can be excellently altered for pulsed EPR measurements requiring significantly lower mw pulse powers by two orders of magnitudes, and can be used to achieve higher bandwidths due to the low quality factor. Altogether, these results demonstrate the significant potential of the PMR approach not only for pulse, but also for cw EPR.

The work has shown possibilities to increase the sensitivity with respect to cavity resonators alone by a factor of 19, which has proven to save a factor in the order of several hundred over time for the acquisition of cw EPR spectra of small, porous crystalline MOF samples. The spin sensitivity for ultra-small and flat samples in the most advanced PMR setup built for this work was $1 \times 10^9\,\mathrm{spins}/\mathrm{G}\sqrt{\mathrm{Hz}}$, which can potentially be decreased further for appropriate samples. This, however, may not compare to the spin sensitivity in high field EPR, where for example a spin sensitivity of $4 \times 10^8\,\mathrm{spins}/\mathrm{mT}$ was reported already decades ago.[214] Nevertheless, this is a remarkable result for X-band EPR spectroscopy. Tab. 5.1 summarizes the obtained SNR enhancements and $\mathbf{B}_0$ amplifications.

Finally, a comparison between the DRs and PMRs can only be discussed with respect to cw EPR as the developed DRs are not suitable for pulsed EPR measurements. At present, the DR wins in the short-run, but over time, it falters as the sample dimensions decrease. It is clear that the PMR represents the cheaper setup,

Tab. 5.1 Summary – Comparison of DR and PMR: Achieved SNR enhancements and power conversion factors C_i/C_{ref} (Eqn. 2.75) for the DRs in combination with cavity resonators (comparable results for BRUKER ER 4102ST and 4119HS) and best PMR in comparison to the respective standard BRUKER resonators ([1] MD5 used with pulse EPR for determination of C_{PMR}).

Resonator	DR K80-H'	PMR T2
C_i/C_{ref}	4.2	25[1]
normalized SNR gain	cavity×19	
absolute SNR enhancement	cavity×80	≥ 51

both in terms of the price tag on the PMR itself as well as with regards to the fact that the required host cavity resonator for the DR will always be more expensive than the PMRs alone. However, both DRs and PMRs could be produced in larger scales and therefore more cheaply. With respect to cw EPR in particular, the $\mathbf{B}_1$ field enhancement must be considered as well. Here, the approximate $\mathbf{B}_1$ enhancement of 25 might be crucial if power saturation plays a role, hence if the sample size is measured in μm rather than nm length scales, the PMR may be regarded as too advanced and overly complex in application. On the other hand, for ultra-small samples, the option to decrease the Ω-loop diameter and the dual-use capability for pulsed EPR measurements allow the PMR to be considered as advantageous in many cases, possibly winning the high-sensitivity competition in the long term.

Concerning the MOF material studies conducted for this work, the decision made in favor of DRs or PMRs therefore was a pragmatic outcome. Firstly, growing large single crystals from $Cu_{2.965}Zn_{0.035}(btc)_2$ or $Cu_3(btc)_2$ and even more for ${}^3_\infty[Cu^I{}_2Cu^{II}{}_2(H_2O)_2L_2Cl_2]$ is a difficult task, while another issue was that the film thickness of (Cu,bdc) SURMOF-2 and (Cu,bpdc) SURMOF-2 could not be extended as desired. However, the total spin number in the different single crystal or thin film specimens did not fall below 10^{13} spins on average, and the smallest sample size was well above 10 μm. As such, there was no need to optimize resonators for ultra-small samples, and a higher prioritization could be afforded to the experimental handling itself. This involved a relatively simple sample exchange with multiple measurements at low temperature. Moreover, some sample preparations involved non-ambient atmospheres which would be difficult to achieve in the case of PMRs. For this reason, the SNR gain of about 8.5 delivered for most applications by the frequently applied DRs of type K80-H was substantial enough (cf. Tab. 3.2), instead of the hypothetical orders of magnitudes in SNR, which are possible with small loop-diameter PMRs. The focus of the PMR research during the majority of the project work was therefore attributed to the implementation of the PMR in a working setup for the associated experimental situations.

5.2 New Insights in Porous Metal-Organic Frameworks by EPR

The novel insights gained by DR-aided high sensitivity cw EPR at low temperatures and non-ambient conditions about ${}^3_\infty[Cu^I{}_2Cu^{II}{}_2(H_2O)_2L_2Cl_2]$, $Cu_{2.965}Zn_{0.035}(btc)_2$, $Cu_3(btc)_2$ and (Cu,bdc) SURMOF-2/ (Cu,bpdc) SURMOF-2 will now be summarized. Firstly, although nearly all EPR measurements involved single crystals of only a few hundred micrometers sample size with as few as 10^{13} spins and thin films of only a few micrometers thickness have been performed in a conventional X-band EPR spectrometer, reasonable angular dependent single crystal EPR spectra and thin film FMR signals could be obtained in almost every experiment. The measurements have been performed frequently at 8 K sample temperature and below, demonstrating the successful detection of signals originating from ferromagnetically coupled chains and paramagnetic mononuclear $\mathrm{Cu^{2+}}$ ions around $g = 2$ with almost no interfering signals from the sensitivity enhancing DR. This demonstrates the feasibility and potential of the applied DR-aided cw EPR spectroscopy at conventional X-band spectrometers for the study of small single crystals, even in the case of porous, low-density materials like MOFs. Multiple results confirmed that the sensitivity enhancement is at least one order of magnitude,[186] saving hundreds of accumulations for the angular resolved single crystal cw EPR measurements.

The work described here revealed relatively well identifiable, distinct, angular dependent EPR spectra of mononuclear $\mathrm{Cu^{2+}}$ ion species in single crystals of the frameworks ${}^3_\infty[\mathrm{Cu^I_2Cu^{II}_2(H_2O)_2L_2Cl_2}]$ (**1**) and very well resolved spectra of $\mathrm{Cu_{2.965}Zn_{0.035}(btc)_2}$ (**3**). Additionally, similarities found between $\mathrm{Cu_3(btc)_2}$ (**2**) and **3** helped to interpret the data. In particular, the spectra of ${}^3_\infty[\mathrm{Cu^I_2Cu^{II}_2(H_2O)_2L_2Cl_2}]$ were sufficient to identify two different species of mononuclear $\mathrm{Cu^{2+}}$ ions which could be identified as magnetically nonequivalent crystallographic lattice sites in the MOF network.[153] This allowed the detection and determination as $\mathrm{Cu^{2+}}$ defect species for the first time by single crystal EPR. The verification of the defect species could only be obtained from the angular dependent spectra, allowing the information to be related to the crystallographic axes of ${}^3_\infty[\mathrm{Cu^I_2Cu^{II}_2(H_2O)_2L_2Cl_2}]$. In the case of the studied MOF network $\mathrm{Cu_{2.965}Zn_{0.035}(btc)_2}$ it was possible to classify six different species of the mononuclear $\mathrm{Cu^{2+}}$ ions which can be identified as magnetically nonequivalent crystallographic lattice sites in the framework.[163] From these angular dependent EPR spectra, the formation of substituted Cu / Zn PW pairs could be confirmed. The principal axis orientations of the **g** and **A** tensors of $\mathrm{Cu^{2+}}$ in Cu / Zn PW pairs have been obtained for numerous crystal specimen at different adsorption states, and could be compared to results from DFT structural information. In this way, minor changes in the cw EPR spectra could be tracked and interpreted as a slightly conformed network, and it was possible to map the small distortions for the different adsorbents with high accuracy. These measurements completed earlier powder EPR investigations and XRD studies and verified that the **g** and **A** tensors of the $\mathrm{Cu^{2+}}$ species in the compounds are very sensitive to minor structural changes in the framework. The minor changes have never been observed by powder EPR or XRD before in MOFs. Furthermore, it was possible to analyze an angular dependent FMR signal in (Cu,bdc) SURMOF-2 (**4**) and (Cu,bpdc) SURMOF-2 (**5**). As a result, it was possible to prove signatures of ferromagnetic behavior and determine the Curie temperature in accordance with SQUID measurements.[139] In contrast to previous reports, a clear orientation dependence of the FMR signal on the direction of the externally-applied magnetic field was observed, which helped to develop an improved structural model of cupric metal ion chains with ferromagnetic coupling in the ground state in the SURMOF-2 class.

Most importantly, the results of this work demonstrate that conventional cw X-band EPR, with the help of inexpensive, new high-sensitivity enhancements, can aid in the exploration of defects and adsorption sites in MOF compounds, suggesting an interesting field for new MOF studies using conventional EPR spectrometers.

A Devices and Experimental Conditions

A.1 CW EPR Experiments at the BRUKER EMX Micro X-Band Spectrometer

The cw EPR measurements at X-band frequencies were carried out using a BRUKER EMX Micro X-band spectrometer equipped with various cavity resonators, optionally a flow cryostat and goniometer. Powder cw EPR measurements at a frequency of 9.41 GHz were carried out using a BRUKER ER 4119HS cylindrical cavity resonator. Typically, five accumulations were taken per spectrum with a conversion time of 20.48 ms and a time constant of 10.24 ms with a resolution of 2 data points per 0.1 mT for a sweep width of 200 mT. The spectra were recorded with moderate mw powers of 2 mW for $^3_\infty[\mathrm{Cu^I{}_2Cu^{II}{}_2(H_2O)_2L_2Cl_2}]$ powders and very low powers of 2 μW for $\mathrm{Cu_{2.965}Zn_{0.035}(btc)_2}$ powders to minimize poorly resolved signals of other paramagnetic centers such as $\mathrm{Cu^{2+}}$ impurities in the cryostat or the identified $\mathrm{Cu^{2+}}$ species **3**III.

Single crystal cw EPR measurements at a frequency of 9.78 GHz were carried out using a BRUKER ER 4119HS cylindrical cavity resonator coupled with the DR (see Section B.1.1). Often, only two scans were enough to resolve all resonance lines as for example of $\mathrm{Cu_{2.965}Zn_{0.035}(btc)_2}$, while especially for $^3_\infty[\mathrm{Cu^I{}_2Cu^{II}{}_2(H_2O)_2L_2Cl_2}]$ and $\mathrm{Cu_3(btc)_2}$ in orientations with low intensity up to 40 accumulations were executed to ensure a better signal detection. The single crystal spectra were recorded with very low powers of about 60 μW to make use of the DR $\mathbf{B}_1$ enhancement suppressing the non-enhanced impurities in the cryostat.

The thin film EPR measurements did not lead to saturation effects of the FMR signals even at low temperatures, such that a mw power of 5 mW has been used for **4** and **5**. Typically, $\mathrm{Cu^{2+}}$ powder and single crystal cw EPR spectra were recorded with a $\mathbf{B}_0$ modulation field strength of 0.5 mT and a modulation frequency of 100 kHz. FMR signals have been recorded with a modulation amplitude of 0.5 mT, too.

Low temperature EPR experiments at the BRUKER EMX Micro spectrometer for samples **1**, **2** and **3** (cf. list of samples, p. XI) were typically recorded at 8 K sample temperature achieved by a moderate He-gas flow in the cryostat, while several temperature dependencies naturally required a heating of the cooling agent. Room temperature experiments have been performed mostly without cryostat unless this was needed to ensure comparability with respect to the $\mathbf{B}_1$ field conversion for SNR determinations.

Other resonators have been employed to adopt to non-standard experimental needs including dual insert methods for stacked DR tests (illustration in Fig. B.1C). Quantification powder cw EPR measurements for the determination of spin numbers have been carried out on the same spectrometer with a BRUKER ER 4105DR dual cavity resonator. SNR comparison tests at room temperature have been carried out with various cavity resonators, ranging from rectangular standard single cavities (BRUKER ER 4102ST) to ultra-high quality cavities (BRUKER ER 4122SHQ).[103]

Continuous Flow Cryostat: OXFORD ESR 900 Series The OXFORD ESR 900 flow cryostat was used to regulate the temperature in the cavity resonators at the X-band EMX Micro spectrometer. The cryogen used in the laboratory is gaseous helium which can cool down a sample in a low pressure evacuated sample tube to minimal 5.5 K according to various commonly applied calibrations procedures. It is however hard to achieve this temperature in a reproducible way such that 8 K was the most common low temperature employed for the single crystal EPR measurements, limiting the He consumption reasonably. The cryostats inner support quartz safely supports cylindrical EPR sample tubes of up to 5 mm outer diameter.[185] Because the ESR 900 is frequently applied in X-band cw EPR, it was used as dimension reference for the development of the DRs.

A.2 CW EPR Experiments at the VARIAN E-112 X-Band Spectrometer

The experimental PMR setups for cw EPR have been prepared at the legacy VARIAN Century E-Line E112 spectrometer and optional immersion cryostat (Section A.2). Different PMRs from batch T1 and T2 were ordered from the SPP collaborator group of D. Suter et al. (see Section B.1.4) to match the klystron frequency tunable between $8.6 \cdots 9.6\,\mathrm{GHz}$. The DPPH spectra were recorded with uncalibrated mw output powers of $0.5 \cdots 2\,\mathrm{mW}$, unless saturation experiments required more $\mathbf{B}_1$ field strengths. DPPH EPR spectra were recorded with a calibrated $\mathbf{B}_0$ modulation field strength of 0.19 mT and a modulation frequency of 100 kHz. The home-written Hewlett Packard HP VEE digitizer uses a Meilhaus ME-300 10 bit analog-to-digital converter (ADC), limiting the EPR signal detection to only $2^{10} = 1024$ voltage step divisions. To overcome this limitation, it is crucial that SNR tests are recorded for two different receiver gains using the largest setting possible at the spectrometer for the noise detection. Here, it may be helpful to record two different spectral ranges to avoid the signal while detecting the noise figure.

The spectra taken for the calibration curve of the PMR probehead R2.1 with narrow modulation coils designed to reach high modulation magnetic field strengths (inset of Fig. 3.9) are depicted in Fig. A.1A. The spectra have been compared to the simulated linewidth of a $S = \frac{1}{2}$ DPPH radical species with 0.19 mT Gaussian linewidth derived by EasySpin (not shown).[28,42] The modulation coils have been prepared to reach the inductance of the VARIAN standard cavities, which at are about $L = 0.2 \cdots 0.4\,\mathrm{mH}$.

Among DPPH presented in Section 3.2.2 other samples have been tested to explore the usability for single crystal EPR and prepare pulsed EPR measurements. As the cw EPR setup only supported room temperature measurements, none of the samples **1** – **5** presented in this thesis were considered. However, several other standard EPR samples such as BDPA and other single crystals like of a $\underline{5}-\mathrm{Ni/Cu}-11.6$ complex provided by the group of R. Kirmse, Leipzig, with a similar structure as described by Gruschinski and Rodenstein[215] were tested in an angular dependent cw EPR measurement with excellent SNR as seen in Fig. A.1B.

Immersion Cryostat: OXFORD CF935 Series The VARIAN E-112 and BRUKER EELEXSYS (Section A.3) spectrometers are equipped with cryostats of the OXFORD CF935 Series.[185] It immerses the entire probehead in the cryogen flow and was chosen for the PMR development because it is compatible with

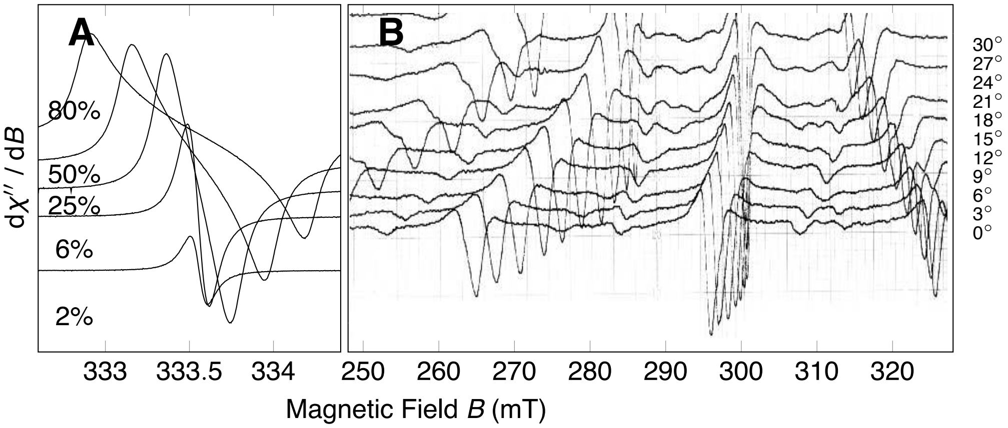

Fig. A.1 Planar microresonator modulation coil calibration and sample measurement:
(A) Experimental EPR spectra of $S = \frac{1}{2}$ free radical DPPH with different modulation voltages applied to the modulation coils of setup R2.1. The tuning caps were adjusted similarly for all measurements to achieve an optimal response.
(B) Angular dependent single crystal room temperature cw EPR spectra of an non-oriented Cu^{2+} species obtained from $\underline{5}$ – Ni/Cu – 11.6 with R2.1 and T2 by turning the external magnets and the modulation coils. Spectra show 3° increments.

many different cavities with diameters smaller than 43.7 mm including modulation coils. The CF-cryostats are used with liquid helium.

A.3 Pulsed EPR measurements at the BRUKER ELEXSYS E580 X-Band Spectrometer

The shown 2-pulse 2-phase cycling field sweep (FS ESE), 2-pulse $\frac{\pi}{2} - \tau - \pi - \tau$ 2-phase / 3-pulse $\frac{\pi}{2} - \tau - \frac{\pi}{2} - T - \frac{\pi}{2} - \tau$ 4-phase cycling electron spin echo envelope modulation (ESEEM) spectra have been recorded on the BRUKER ELEXSYS E580 spectrometer as illustrated for the $\frac{\pi}{2} - \tau - \pi - \tau$ pulse sequence in Fig. A.2A using non-selective mw pulses of $p_{\frac{\pi}{2}} = 30\,\text{ns}$ and $p_{\pi} = 60\,\text{ns}$ and a 2- and 4-step, respectively, phase cycle to cancel out unwanted echoes,[216] and a mw power at 34 dB attenuation of the output travelling wave tube amplifier (TWT/A) power, a mw frequency of 9.618 GHz and 39 dB video gain. The first sample tested was the micro crystalline single crystal diamond described in Section 3.2.3 and shown in Fig. A.2B,C.

A.4 The Network Analyzer HP 8510B

The Hewlett Packard HP 8510B network analyzer is a wide dynamic range reflection and transmission spectrometer for RF frequencies. The system contains a cw source and transmitter HP 83621A to cover the range from 45 MHz · · · 20 GHz, a receiver unit (referred to as scattering "S" parameter test set) and data manipulation and display unit. It may be used among others to record the S_{11} input reflection, S_{12} forward

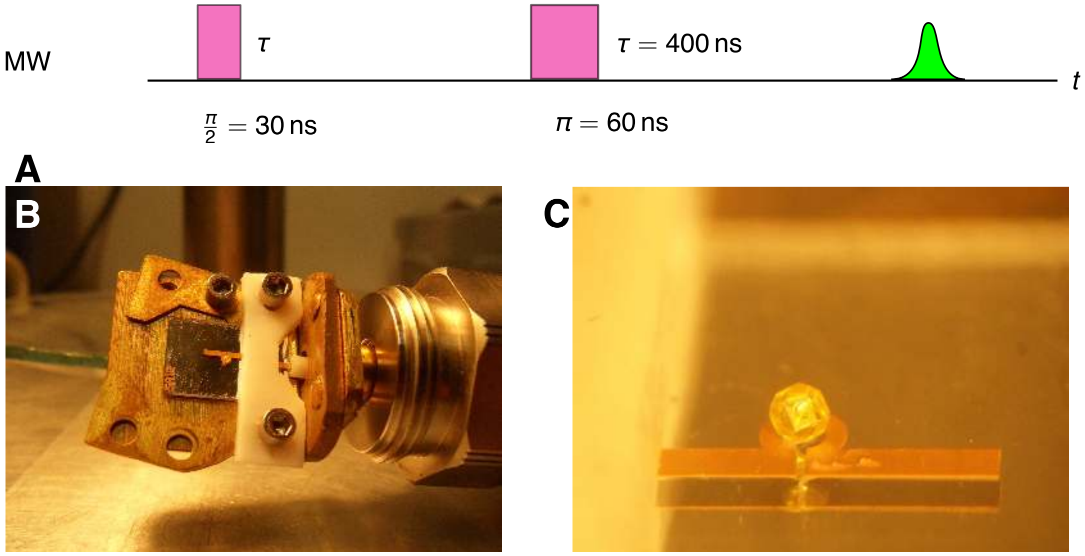

Fig. A.2 Prototype pulse setup for planar microresonators: The setup was only used for prototype testing in this work.
(A) Illustration of standard pulsed $\frac{\pi}{2} - \tau - \pi - \tau$ EPR scheme with pulse positions, durations (p_{π}, $p_{\frac{\pi}{2}}$).
(B) The prototype PMR setup combining PMR T2 with an earlier setup R1 attached to the network analyzer. The PMR is loaded by a micro crystalline diamond sample.
(C) The micro crystalline diamond single crystal sample with P1 centers in the PMR Ω-loop.[190–192]

transmission, (voltage) standing wave ratio VSWR (often shortened to SWR only), signal phase and Smith diagram.[28,217] The digital data can be exported to a home-written LabVIEW interface. In contrast to EPR X-band spectrometers, the network analyzer is not using WG15 waveguides but PC-7 and 3.5 mm connectors, which may be adapted to the widely-used N-type / SMA system.[218]

B Investigation Procedures

B.1 Auxiliary Microwave Techniques

The preparation for all customized resonator implementations involved resonance frequency and -quality checks of the DRs and PMRs, coupling of the latter two to cavity resonators and microstrip plugs as well as tests of self-customized cables and transducers. These tests have been performed with the network analyzer introduced in Section A.4. The most important parameter is the scattering S_{11} input reflection coefficient, which allows to evaluate the quality factor Q of a mw resonator system and the signal damping.[217] The S_{11} parameter characterizes the quality of the impedance matching of the mw component in the network to the $50\,\Omega$ standard used. A small value describes the absence of reflected signals and thus a good matching. It is frequently measured in the logarithmic unit dB, such that $S_{11} = -3\,\mathrm{dB}$ describes that about $\frac{1}{2}$ of the incident power is lost. The width at this power loss defines Q,

$$Q = \frac{\Delta f_{3\,\mathrm{dB}}}{f_0}, \tag{B.1}$$

where f_0 is the frequency of the minimum of a resonance. Typically, $S_{11} < -50\,\mathrm{dB}$ for high quality, critically coupled cw EPR cavity resonators and $Q > 3000$ for them. S_{11} can be directly related to the VSWR, which is 1 for a perfectly matched resonator ($S_{11} = -\infty\,\mathrm{dB}$).[217] Again, critical couplings of cavity resonators typically are below VSWR < 1.001.

B.1.1 Dielectric Resonator Microwave Characterization

The main preparation task of the DR mw characterization consisted of the determination of the coupled resonance frequency for the DR cylinder height reduction. Apart from that, the DR-cavity resonator combinations have been checked for among others the coupled Q factors of all appearing DR modes and possible applications of stacked DRs (illustration in Fig. B.1C) according to the procedures given above in Section B.1. Those results have been summarized in Section 3.1 and Fig. 3.1. Also, the temperature dependent EPR experiments for the DR characterization have been monitored as shown in Tab. 3.1.[186] To explore the possibilities of utilizing DRs coupled to antennae and find the frequencies shown in Fig. 3.1C(2,5,8) and other properties of the DRs without coupling to a cavity resonator, small shields as those depicted in Fig. B.1A,B with cavity dimensions $\varnothing_{\mathrm{ID}} \leq \frac{\lambda}{2}$ have been constructed and the DRs measured therein have been coupled with semi rigid waveguides used as antennae to acquire the S_{11} reflection and S_{12} forward transmission damping.[95] Due to the small shield boxing of the DR, this configuration is referred to as 'boxed DR' in

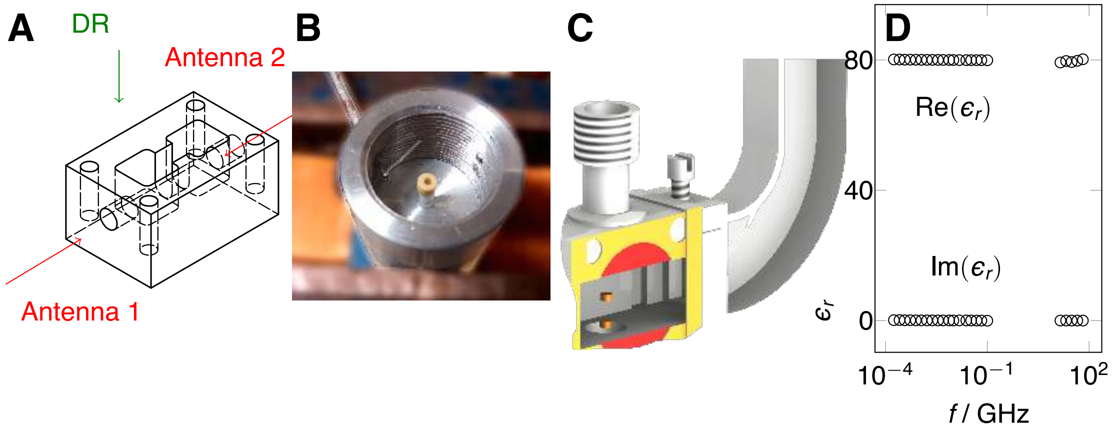

Fig. B.1 Dielectric resonator characterization and configuration:
(A) Rectangular small shield for up to two DRs and two antennae allowing reflection S_{11} and transmission S_{12} scattering measurements.
(B) Cylindrical shield used for antennae orientation dependent tests for DR couplings.
(C) Illustration of stacked, dual DR in cavity resonator.
(D) Real and imaginary part of dielectric permittivity versus RF frequency f of DR K80-H measured by M. Šimėnas, Vilnius.

Fig. 3.1. Fig. B.1C,D show a sketch of a dual DR application and the relative dielectric permittivity of the final DR material.

The unmatched frequencies f_{boxed} in Fig. 3.1C(2,5,8) of the $\text{TE}_{10\delta}$-mode weakly coupled to the semi rigid waveguide cable core antenna has been measured in a cylindrical shield of sub-wavelength dimensions while the frequencies f_{coupled} of the coupled DRs and quality factors Q in Tab. 3.1 were acquired using the network analyzer at the regular EPR setup, replacing the usual mw bridge. Usual values for the VSWR of the coupled DRs in the cavity are between $1.05 \cdots 1.3$ and hence close to, but larger than those of empty cavity resonators. Therefore, coupling can be limited to match only over three to four orders of magnitude of mw power, especially at very low temperatures. S_{11} at critical coupling in a DR/ cavity resonator system is typically around -45 dB.

At optimal coupling obtained for the DR being centered in the vertical sample axis of the cavity resonator, the coupled mode manifests in a united DR and cavity resonator frequency, which has a maximum. Off center positions of the DR result in a lower-frequency, primary mode which still can be used for cw EPR (e.g. in case of too high center-matched frequencies) but loses in SNR both due to non-optimal mw couplings but also decreasing $\mathbf{B}_0$ modulation field strength with is typically only obtained around the center of the cavity resonator. Additionally, the uncoupled DR mode emerges and increases in frequency for off center DR positions, but the SNR is typically not sufficient for usage in EPR if it is frequency wise in reach at all. After all, this phenomenon allows to find the optimal DR position in the cavity resonator by monitoring the mode preview of the tuning and matching process.

Tab. B.1 Coupled and boxed dielectric resonator modes microwaves properties: Cavity resonator coupled DRs' Q_{DR} factor (Eqn. B.2) and standalone resonance frequency, scattering parameter, quality factor and voltage standing wave ratio in antennae coupled boxed configuration. Errors in f, S_{11} and VSWR in last digit given, $\Delta Q = \pm 10$. The last line shows the properties of the DR without hole, K80, listed in Tab. 3.1. Those modes could be identified as $\text{TE}_{01\delta}$ and $\text{HE}_{01\delta}$ modes according to Fig. 3.1C.

DR height /	in cavity	$\text{TE}_{01\delta}$				$\text{HE}_{01\delta}$			
mm	Q	f / GHz	$-S_{11}$ / dB	Q	VSWR	f / GHz	$-S_{11}$ / dB	Q	VSWR
1.96	2100	9.68	10	450	1.5	11.38	25	120	1.11
2.12	2820	9.64	16	240	1.3	11.10	26	110	1.10
2.25	3540	9.45	17	160	1.3	10.62	23	110	1.15
2.46	5210	9.19	9	230	1.9	10.10	29	70	1.06
2.57	5950	9.28	22	150	1.15	9.96	36	70	1.03
2.93 (K80)	8170	9.01	19	400	1.22	9.42	36	100	1.02

B.1.2 Dielectric Resonators in Use

The DRs obtained from A. Belous et al., Kyiv,[100] were further customized for the needs in our spectrometers by reducing the cylinder height L to match the coupled DR–cavity frequency to the respective cavity resonators in use (9.4 ⋯ 9.7 GHz). The final DRs are provided with a 1.2 mm hole for sample insertion as shown in Fig. 3.1A and the DR radius finally was settled as $a = 1.8$ mm. Different cylinder heights in the range $L = 1.7 \cdots 2.9$ mm have been achieved by the grinding process. The EPR sample tubes applied are 4.4 mm × 0.3 mm, which in turn safely fit into the support quartz of the available cryostat (Section A.1). The initial values for a, L and the dielectric constant $\varepsilon_r = 75 \cdots 85$ of the DRs have been adopted to meet those geometrical requirements by Eqn. 2.74 and tested to ensure the quality of the materials (Fig. B.1D). This has been possible due to the excellent materials with desired properties available now (Section 2.2.1).[100]

The DRs have been tested with several cavity resonators available, without obtaining different results within the uncertainties. This applies both for rectangular cavity types such as the BRUKER ER 4102st and ER 4105DR dual cavity used in the publication,[186] but also high-sensitivity cylindrical cavities such as ER 4119hs. The measured overall quality factor Q of the coupled DR–cavity system is always lower than the quality factor of the unloaded cavity resonator, and from Eqn. 2.39 it can be derived

$$\frac{1}{Q_{\text{DR}}} = \frac{1}{Q_{\text{DR+Cav.}}} - \frac{1}{Q_{\text{Cav.}}}. \tag{B.2}$$

Tab. B.1 lists the Q factors and other mw parameters for the two lowest frequency DR modes determined for the boxed DR in the rectangular dual shield shown in Fig. B.1A and included in the plot of Fig. 3.1C(2,5). The relatively large tolerance in Q is mostly due to the difficulty to separate the DR mode from reflections in the microwave network. From all these modes, some few seem usable, but the majority has either a relatively high VSWR, or the Q factor is rather small such that an actual usage for EPR would probably require much more investigation which has been beyond the scope of this work.

DRs are in use in many fields of mw engineering. The selected DR material has been chosen after several iterations of the manufacturing process by A. Belous et al. and variation in the material suppliers. Fig. B.2

Fig. B.2 Alternative DR materials tested: EPR spectra of approximately equal amounts of earlier DR materials,[187] and materials with higher $\varepsilon_r = 160$ have been tested (K160) as well as the PCB material of PMR T1, Rogers Corp. Ro3(010), here at room temperature.[119] C1 and C2 mark dielectric capacitor materials showing large amounts of paramagnetic impurities visible already at room temperature and demonstrating the purity of the K80 material used for the DRs K80-H.

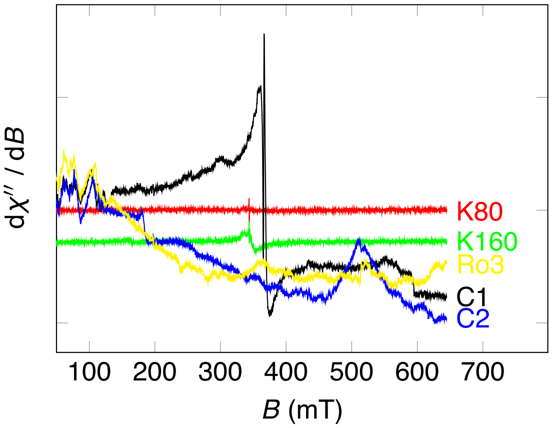

shows earlier DR materials and other DRs used in electronics tested by EPR and shows the high content of paramagnetic impurities in contrast to the material finally selected for the DRs K80-H.

B.1.3 Planar Microresonator Microwave Network Tests

The network analyzer is the most important tool to implement a PMR in a mw network, because the PMR mode is typically so broad that it cannot be detected in an EPR spectrometer during the tuning and matching routine. During the evolution of the PMR setups it turned out, that it is moreover not always easy with all PMRs to find the mode with many other reflections being present in the systems. Then, it can be identified more easily by tuning the PMR frequency with the help of dielectric materials near the Ω-loop to see the frequency dependence of the modes of interest in the S_{11} scattering plot. Fine tuning of the scattering characteristics included improvements of cable junctions and plugs to cancel unwanted cable reflections, match impedances for the PMR coupling and detect frequency shifts upon sample uptakes or temperature changes. These characteristics have to be known to perform cw and pulsed EPR experiments.

B.1.4 Planar Microresonators in Use

Tab. B.2 shows the PMRs used for the various experiments. They were supplied by D. Suter et al. within the SPP project. The large tolerances especially for T1 are attributed to the bad coupling in setup R1 leading to a strong influence on the mw properties. Obviously, not the most suitable PMRs of T1 were used in the final setups. This was due to the fast degeneration of the contacts on the Ro3010 PCB material. Batch T2 is the new PMR type fabricated on sapphire single crystal substrate without hole in the Ω-loop shown in Fig. B.3A and C.

Fig. 3.8A shows the S_{11} reflection parameters with all mw wiring necessary (cyan and green curve). It has been stated on page 55 that the implementations in the spectrometer lead to various mw reflections in the cables and plugs, imitating high-quality resonant structures and that tuning the spectrometer on such a peak does not enhance the sensitivity of the cw EPR measurement. Instead, the SNR is governed by the underlying Q of the PMR. This is shown in Tab. B.3, comparing the SNR of various, narrow S_{11} reflections

Tab. B.2 Planar microresonator mode microwaves properties: Resonance frequency, scattering parameter and quality factor of all 500 μm Ω-loop PMRs. $\Delta f = \pm 0.1$ GHz, $\Delta S_{11} = \mp 5$ dB, $\Delta Q = \pm 2$

PMR	PMR	mw properties			notes
batch	label	f / GHz	$-S_{11}$ / dB	Q	
#1	A12	9.3	19	26	hole, used as T1
	A21	9.3	28	25	no hole
	A41	9.1	9	18	hole, used as T1
	A43	9.2	18	30	no hole
#2	5A12	9.61	14	65	T2-pulsed
	5A25	9.35	16	55	cw-T2

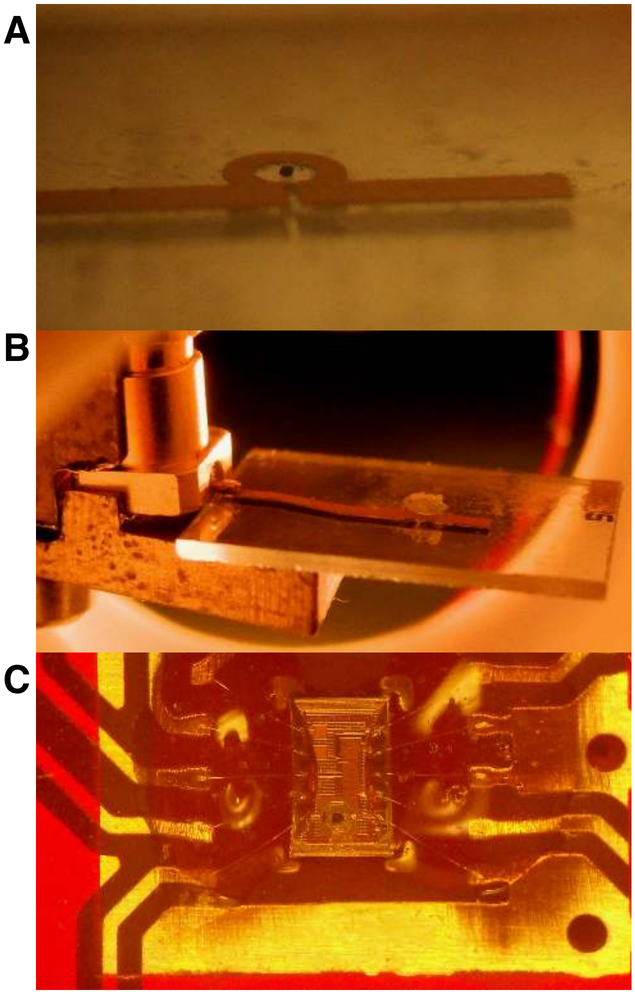

Fig. B.3 Planar microresonator and chip spectrometer with samples: Close-up views of high sensitivity chips.

(A) PMR T2 with small DPPH sample (10^{15} spins), showing the transparent sapphire single crystal substrate. The inner Ω-loop diameter is 500 μm, the overall structure length shown here 4 mm.

(B) Side view of the PMR in cw EPR setup R2.1 with a larger Cu^{2+} MOF crystal which is not further discussed here. The viewing direction through the modulation coil axis shows the mSMP coupling to the microstrip line of the PMR.

(C) Integrated chip spectrometer ASIC by J. Anders, Ulm, with the same DPPH sample in the single loop octagonal mw $\mathbf{B}_1$ coil with about the same diameter as that of the PMR.

Tab. B.3 PMR probe head quasi-resonances: Related to Fig. 3.8A this table lists probable reflections in the waveguides and transducers of R1 with high apparent Q factors tested with EPR revealing non-superior SNR at quasi-resonance frequencies $f_{R1,i}$ with $\Delta f = f_{R1,i} - f_{T1}$ versus PMR resonance frequency f_{T1}.

Δf / MHz	Q	SNR
0 (f_{T1})	24	
−255	128	657
−188	320	867
−119	202	970
−51	301	1152
≈0	454	1246
12	304	1297
91	320	1224
162	308	981

around the actual mode frequency. As it can be seen, the SNR is not correlated to the quasi-quality factors of the reflections, but instead resembles the inherit S_{11} curve of the PMR.

B.2 EPR Microwave Power Calibration

B.2.1 Saturation Power for Dielectric Resonators with cw EPR

To test the relative conversion factors C_i/C_{ref} of all DR resonators coupled to the cavity resonator versus the conversion factor of the unloaded cavity as reference C_{ref}, a homogeneously saturating sample such as a solid BDPA radical sample can be used.[28] Fig. B.4 shows the typical saturation behavior known for such samples, but a more accurate procedure is shown by Nesmelov et al., who relate the rollover saturation curves to the square root incident mw power.[189] In the latter the resonators are compared by the point with half rollover saturation. The method is in particularly advantageous for small saturation powers since it does not rely on identifying a maximum in a saturation curve at powers as low as a few hundred nW. With the help of this information the sensitivity enhancement due to a change in η and Q can be separated from the signal enhancement due to the increasing $\mathbf{B}_1$ mw power as shown in Fig. 3.3.

B.3 Sample Preparation

B.3.1 Single Crystal Preparation

${}^3_\infty[\mathrm{Cu^I_2Cu^{II}_2(H_2O)_2L_2Cl_2}]$ (**1**) was prepared by solvothermal synthesis with H_2O/MeCN (water / acetonitrile, volume ratio 1 : 1) as a solvent.[149] The obtained crystals have a maximum length of about 200 μm along the crystallographic b axis and up to 50 μm in a and c direction (Fig. B.5A). The latter two are well distinguishable due to the typical rooftop tails of the short needles as shown in Fig. B.5B. Crystal axis assignment for single crystals of **1** was performed using a STOE IPDS-2T image plate detector system with laboratory Mo-Kα

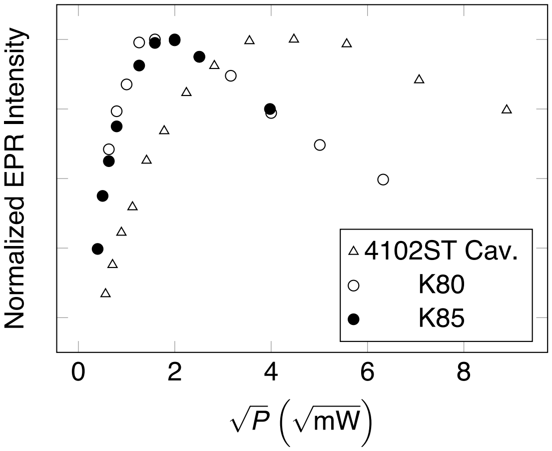

Fig. B.4 Normal saturation curve of BDPA used for DR $\mathbf{B}_1$ calibration: Normalized cw EPR intensity magnitudes of homogeneously saturating $S = \frac{1}{2}$ signal of free radical in BDPA. The disk DR materials can be shown in that way, while the ring DRs saturate at such small powers that the rollover saturation curves as shown in Fig. 3.3 are more suited for evaluation.

radiation (λ = 71.073 pm) and the data was processed with the STOE X-AREA software by P. Eckold et al..[219]

HKUST-1 (**2**) and the Zn^{2+} doped material $Cu_{2.965}Zn_{0.035}(btc)_2$ (**3**) were prepared by a slightly modified solvothermal synthesis established in literature and used earlier both for the pure and Zn-substituted HKUST-1.[40,134] In a typical setup, 2.4 mmol of $Cu(NO_3)_2 \cdot 3\,H_2O$ (0.5394 g) and 0.36 mmol of $Zn(NO_3)_2 \cdot 6\,H_2O$ (0.108 g) were dissolved in 10 mL of a 1 : 1 volume mixture of water and ethanol in a 15 mL Pyrex vessel, closed and placed in an autoclave. The autoclave was heated by 10 K/min in an oven to 398 K for 12 h. The subsequent cooling was done with a rate of −5 K/min. The turquoise-blue product was filtered and washed with 10 mL of ethanol three times, once per day. The resulting crystals are described below in Fig. B.6. S. Kaskel et al. applied single crystal XRD to ensure a successful crystal growth and ICP-OES to detect the Zn concentration in the crystals.[220]

B.3.2 Single Crystal Handling and EPR

Alignment The investigated single crystals of **1**, **2** and **3** are shown in Fig. B.5A and Fig. B.6. For **1**, the green specimen is placed with its flat *ab* face on a quartz glass fiber end with 200 μm diameter such that the *c* axis is pointing along the axis of the wire. All single crystals are fixed, and **1** is additionally covered with two component epoxy which neither has a measurable effect on the crystal lattice according to XRD nor it gives any detectable EPR resonances. The coverage of ${}^{3}_{\infty}[Cu^{I}{}_2Cu^{II}{}_2(H_2O)_2L_2Cl_2]$ is crucial as it maintains the crystal's stability under multiple cooling and warming processes. However, it also prevents studies under gas adsorption and leads to the blurred photo. It was learned later with **2** and **3** that very low cooling rates (see B.3.2) can preserve the crystals' structure even under gas adsorption, which allowed the careful fixing of **2** / **3** only at one face, leaving the others open for gas transfer. Fig. B.5B shows the **1** crystal shape with the corresponding crystal axes assignment. The alignment of the small crystal **1** can be altered both with respect to the DR and the external magnetic field $\mathbf{B}_0$ in the cryostat by inserting the thin quartz glass fiber in an impurity free quartz glass rod of 1 mm diameter beveled to house the fiber as shown in Fig. B.5C. This rod fits in the hole of the DR as described later and places the crystal almost exactly in the radial and lateral

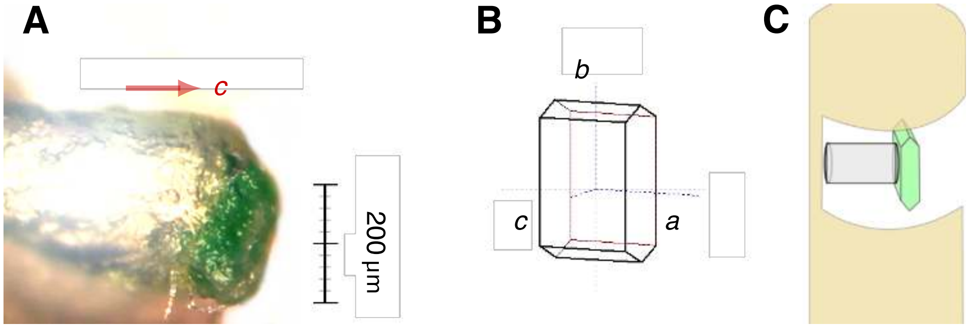

Fig. B.5 **$^{3}_{\infty}[\mathrm{Cu^{I}_{2}Cu^{II}_{2}(H_2O)_2L_2Cl_2}]$ crystal axis assignment:** Optical light microscopy image as published earlier.[153]

(A) The single crystal of **1** taken for all experiments containing about 10^{13} spins of mononuclear Cu^{2+} ions. It is glued on a 200 μm glass fiber such that the crystals' c axis is pointing along the axis of the wire. The glue encloses the sample completely.

(B) Depicted crystal dual-rooftop needle outline with crystallographic axes indicated.

(C) Sketch of the beveled quartz glass rod with 1 mm diameter housing the crystal glued to the fiber. In that way, the tiny crystal can be statically adjusted in one plane inside the DR, while the DR is rotated in the second plane.

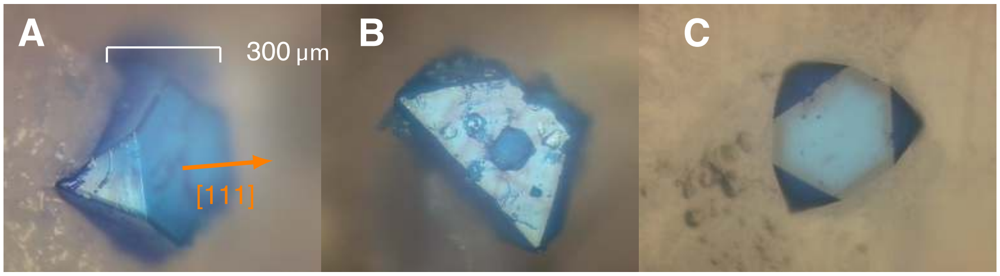

Fig. B.6 **$\mathrm{Cu_{2.965}Zn_{0.035}(btc)_2}$ single crystals:** Optical light microscopy images. All faces are normal to crystallographic $[1\,1\,1]$ axes.

(A) Single crystal of $\mathbf{3}_{\mathrm{AS}}$ containing about 10^{14} spins of mononuclear Cu^{2+} ions stuck in grease which was only used for this image.

(B) Additional residual solvent liquid is present on another sample of $\mathbf{3}_{\mathrm{AS}}$.

(C) Almost perfect tetrahedral shape of this specimen.

middle of the DR. The larger crystals of **2** and **3** have a side length of around 400 μm. As the crystals result into a typical tetrahedral shape as shown in Fig. B.6, every face is a (1 1 1) plane such that a simple crystal orientation can be performed by face alignment as shown in Fig. B.6A.

De-/ Adsorption After synthesis the crystal $\mathbf{2}_{\mathrm{AS}}$ / $\mathbf{3}_{\mathrm{AS}}$ contain about 50% ethanol and have a light blue color as seen in Fig. B.6. The activated samples $\mathbf{2}_{\mathrm{act}}$ / $\mathbf{3}_{\mathrm{act}}$ were dried under vacuum at 393 K for 24 h to obtain dehydrated materials with removed axial ligand molecules. The dehydration was performed while having the crystal fixed in the EPR sample tube as ready-to-measure setup including the DR. The crystals of $\mathbf{2}_{\mathrm{act}}$ / $\mathbf{3}_{\mathrm{act}}$ then get a dark blue color; the final vacuum after evacuation was 3×10^{-2} mbar. Subsequently, the sample tubes as depicted later in Fig. B.7 on page 104 with the dehydrated materials were closed and cooled to room temperature without further air contact. In the following, EPR measurements and gas adsorption was performed at the same crystals and in the same setups: carbon dioxide adsorbed samples $\mathbf{3}_{\mathrm{CO_2}}$ were prepared from dehydrated samples $\mathbf{3}_{\mathrm{act}}$ by adsorbing CO_2 and carbon monoxide adsorbed samples $\mathbf{3}_{\mathrm{CO}}$ by adsorbing CO at 10 mbar at room temperature and methanol adsorbed samples $\mathbf{2}_{\mathrm{MeOH}}$ / $\mathbf{3}_{\mathrm{MeOH}}$ were prepared by adsorbing CH_3OH at its vapor pressure at room temperature for 1 h, respectively. EPR measurements were performed after very slow cooling in the EPR spectrometer to 8 K and a subsequent warming and reactivation led to samples like $\mathbf{2}_{\mathrm{act}}$ / $\mathbf{3}_{\mathrm{act}}$ and could be reused again for gas adsorption. For that purpose, the evacuation valve has been maintained during all EPR measurements. Fast cool-down and warm-up cycles during the EPR measurements limited the reusability of the crystals. Best results have been achieved for slow cooling and heating rates of about ∓500 K/h.

Low temperature cw EPR The DRs were placed at the lower end of a standard EPR quartz glass sample tube with an inner diameter of 4 mm. For **1** one and the same single crystal was used to investigate the angular dependence of the EPR spectra for rotations about three distinct axes. These axes were chosen to be preferably parallel to the crystal axes a, b and c. Due to the distinct needle shaped crystal **1** it was possible to specifically select the intended orientations, yet with a systematic error of at least ±5° for various reasons. Firstly, the crystals faces are not perfectly aligned with the glass fiber. Secondly, the glass fiber has not been oriented ideally in the beveled glass rod. Moreover, the glass rod is not fully erected along the DRs symmetry axis and the DR is not entirely correctly aligned in the resonator, a compromise devoted to the easy setup allowing for fast sample changes. Then the crystal was rotated by the angle φ about one of the chosen axes, each in steps of $\Delta\varphi = 5°$. This angle may have a systematic error of up to $\Delta_{\mathrm{err}}\varphi = 5°$, too. The rotations were followed up for at least 220° to meet all signals occurring for a C_2 rotational symmetry of **1**. The single crystals of **2** and **3** were glued with a (1 1 1) plane crystal face on the quartz glass fiber such that a [1 1 1] axis is pointing along the axis of the EPR sample tube. The crystal is fixed but not covered with two component epoxy which has no detectable EPR resonances to allow a dehydration of the crystal and gas adsorption. Fig. B.7A shows an illustration and Fig. B.7B a photo of the actual crystal mounted on the fiber and the fiber itself placed in a PTFE holder to align it in the EPR sample tube. The whole setup including EPR sample tube, vacuum valve, DR and single crystal mounted in the latter has been rotated around one of the crystals' [1 1 1] axes (named z in Fig. B.7B) with a conventional goniometer inside the cryostat in the

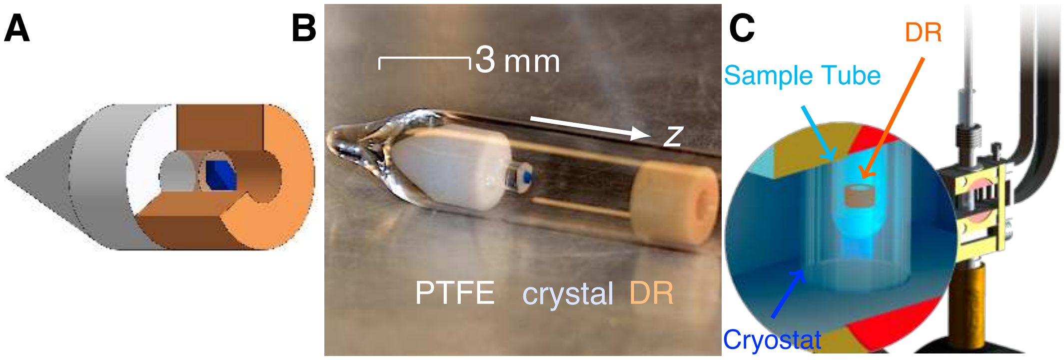

Fig. B.7 Single crystal handling in dielectric resonators: Addition of the DR to a regular EPR sample tube allowing for all gas adsorption experiments.
(A) Sketch of the PTFE holder (white) holding the transparent quartz glass fiber which positions the specimen right in the middle of the DR (orange, opened for display here only).
(B) Photo of this setup in regular EPR sample tube with sample of **3** mounted. The DR is not slid fully down. The external magnetic field $\mathbf{B}_0$ is rotated perpendicular to the indicated z-axis.
(C) Sketch of a sample tube inserted in a regular cavity resonator with flow cryostat.

cavity resonator (Fig. B.7C).

B.3.3 Thin Film Treatment

For (Cu,bdc) SURMOF-2 (**4**) and (Cu,bpdc) SURMOF-2 (**5**), a clean gold substrate (100 nm Au / 5 nm TiO_2 deposited on Si wafers) was immersed into the ethanolic solutions of 16-ercaptohexadecanoic acid (MHDA) with a concentration of 20 μM for about 2 days to obtain a carboxylic groups-terminated self-assembled monolayers (SAMs) substrate and then rinsed with the pure ethanol and gently dried under nitrogen flux before use. The procedure for the preparation of the SURMOFs investigated in this work was done using an established high throughput spray system described in detail elsewhere.[221] The SAMs substrates were sprayed with a 1 mM of $Cu_2(CH_3COO)_4 \cdot H_2O$ ethanol solution for 10 seconds and then with a 0.2 mM of 1,4-benzendicarboxylic acid (BDC) or 0.1 mM of 4,4′-biphenyl dicarboxylic acid (BPDC) ethanol solution for 20 seconds at room temperature. In between, pure ethanol was used for rinsing to remove the unreacted ligands (BDC or BPDC) or metal connectors (Cu acetates). The above steps were repeated to grow thicker layers. An example of the thin film is shown in Fig. B.8.

Prior to the measurements, different Au layer thicknesses of the substrate have been tested to reduce effects from conduction electrons on the cw EPR spectra, which finally could be carried out at relative high mw power of 5 mW and $\mathbf{B}_0$ modulation amplitudes of 0.5 mT as stated above. Separate spectra for the substrate have been acquired as presented in Fig. B.8A for all recorded temperatures and film orientations to exclude that the observed effects originate from it. The SURMOF-2 films on their substrate with film thickness of about 1 μm and film area of about 0.1 cm^2 were mounted on a 3 mm quartz rod as shown in Fig. B.8B and their orientation with respect to the external magnetic field $\mathbf{B}_0$ in the spectrometer was controlled by a goniometer. Ultra-thin films have been placed on a DR as shown in Fig. B.8C.

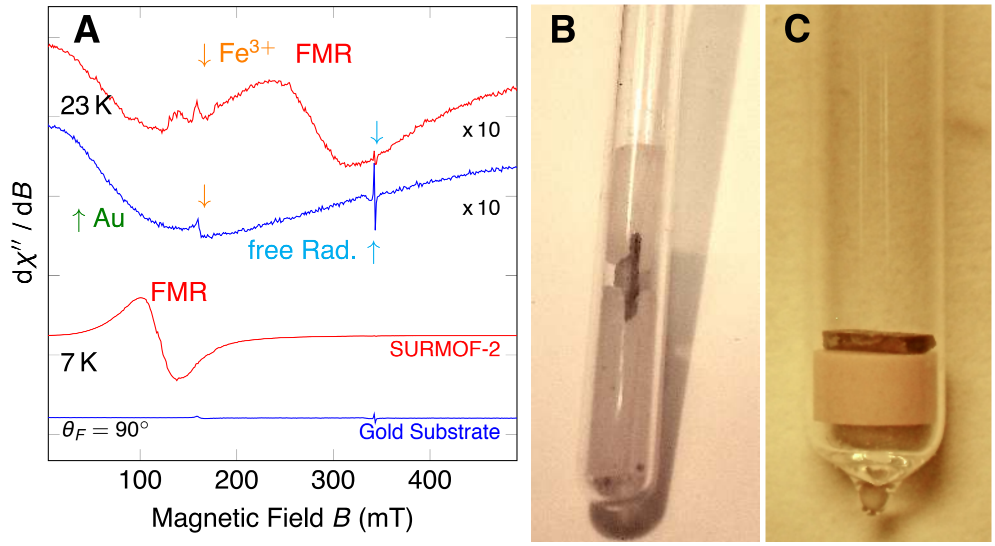

Fig. B.8 SURMOF-2 thin film substrate and sample handling: To prevent fast degeneration, thin films were sealed in EPR sample tubes.

(A) EPR spectra of the substrate, which does not have EPR signals to confuse with FMR signals or other signals from the perpendicularly oriented (Cu,bdc) SURMOF-2 thin films. Au marks the common gold substrate signal in both upper curves appearing above 20 K. Fe^{3+} marks an iron impurity in the used ESR900 cryostat, the free radical is inherit in the substrate material. The broad FMR signal is marked as such.

(B) The thin film is hold between to pieces of glass to orient it in the sample tube.

(C) (Cu,bdc) SURMOF-2 with very thin film thickness can be measured by placing it on a DR.

Tab. B.4 Strain correlation parameters of ^{63}Cu in various adsorption states of 3: Spin Hamiltonian principal axis values and correlation of the mononuclear ^{63}Cu species in single crystals of $Cu_{2.965}Zn_{0.035}(btc)_2$. The ^{65}Cu isotope's values are derived directly from the given values.

Sample	$g_{\|\|}$	$g_{\perp}$	$A_{\|\|}$ / 10^{-4}/cm	$A_{\perp}$ / 10^{-4}/cm	$\Delta g_{\|\|}$	m / 10^{-4}/cm	k / 10^{-4}/cm
$\mathbf{1}_{\mathrm{act}}$	2.281(2)	2.046(1)	187(2)	32(1)	< 0.001	262	785
$\mathbf{1}_{\mathrm{CO_2}}$	2.293(2)	2.049(2)	182(1)	26(1)	0.007	300	870
$\mathbf{1}_{\mathrm{CO}}$	2.300(1)	2.051(2)	175(2)	23(1)	0.005	350	980
$\mathbf{1}_{\mathrm{MeOH}}$	2.336(2)	2.058(1)	158(2)	15(1)	0.007	420	1170

B.4 Crystal Structure Visualizations

Diamond 3.2f with POV-Ray and Avogadro were used to visualize the structures.[222–224]

B.5 Spectral CW EPR Simulations

Analysis of the EPR spectra are based on the EasySpin numerical simulation package,[42] installed in MATLAB.

In the samples of **3** (Section 4.2.2) only moderate strain effects have been encountered, yet an increasing line widths of the HFS signals in the $g_{||}$ part with increasing $\mathbf{B}_0$ field for the Cu^{2+} species points to slightly correlated **g** and **A** strain distributions.[154] Consequently, such a correlated Gaussian **g** and **A** strain distribution has been considered in the simulation of all spectral EPR simulations.

For the simulation of the single crystal spectra of **3** a Gaussian distribution of the $g_{||}$ values with a center at the given $g_{||}$ value in Tab. B.4 and the width of $\Delta g_{||}$ therein was applied. The HFS parameters $A_{||}$ are as well assumed to be correlated with the Gaussian distributed values $g_{||}(i)$ by Eqn. 2.78, where m and k are fitted using the respective EPR spectra. These values are given in Tab. B.4 as well.

B.6 Computer Aided Construction

For this work many parts of the probehead and spectrometer / cryostat mountings have been constructed, customized and improved. They were built by the faculty machinery shop according to construction blueprints generated by a student's version of Autodesk Inventor Professional software, which allowed precise design plans involving 3D models of the produced parts. By this, design fails due to mismatches of the constructed parts could be excluded and an efficient adoption to new ideas have been facilitated. On the following two pages blueprints of the most important parts of the PMR probehead R2.1 are presented.

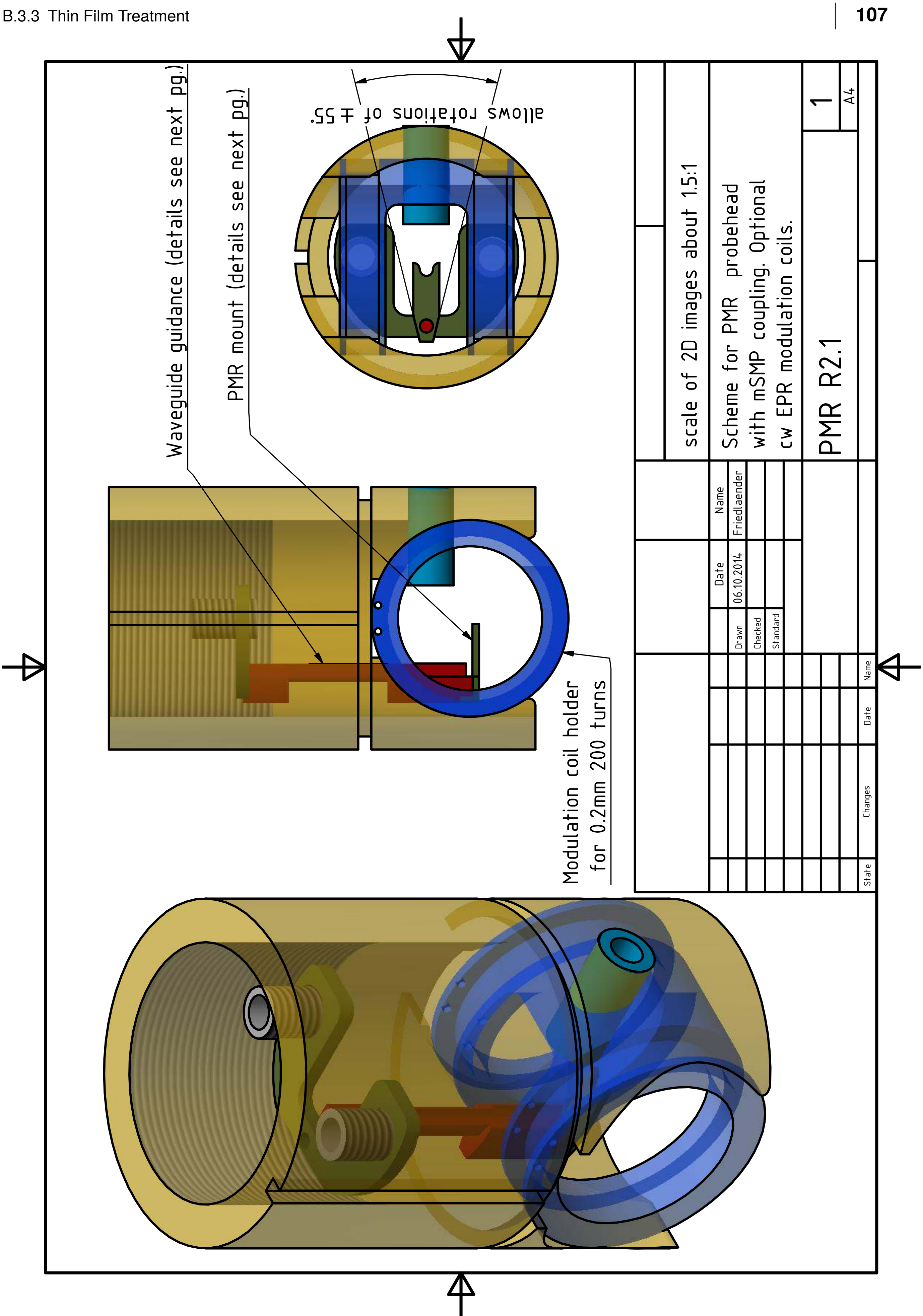
Waveguide guidance (details see next pg.)
PMR mount (details see next pg.)
allows rotations of ± 55°
Modulation coil holder for 0.2mm 200 turns
scale of 2D images about 1.5:1
Scheme for PMR probehead with mSMP coupling. Optional cw EPR modulation coils.
PMR R2.1
1
A4
Date
Name
Drawn
06.10.2014
Friedlaender
Checked
Standard
State
Changes
Date
Name

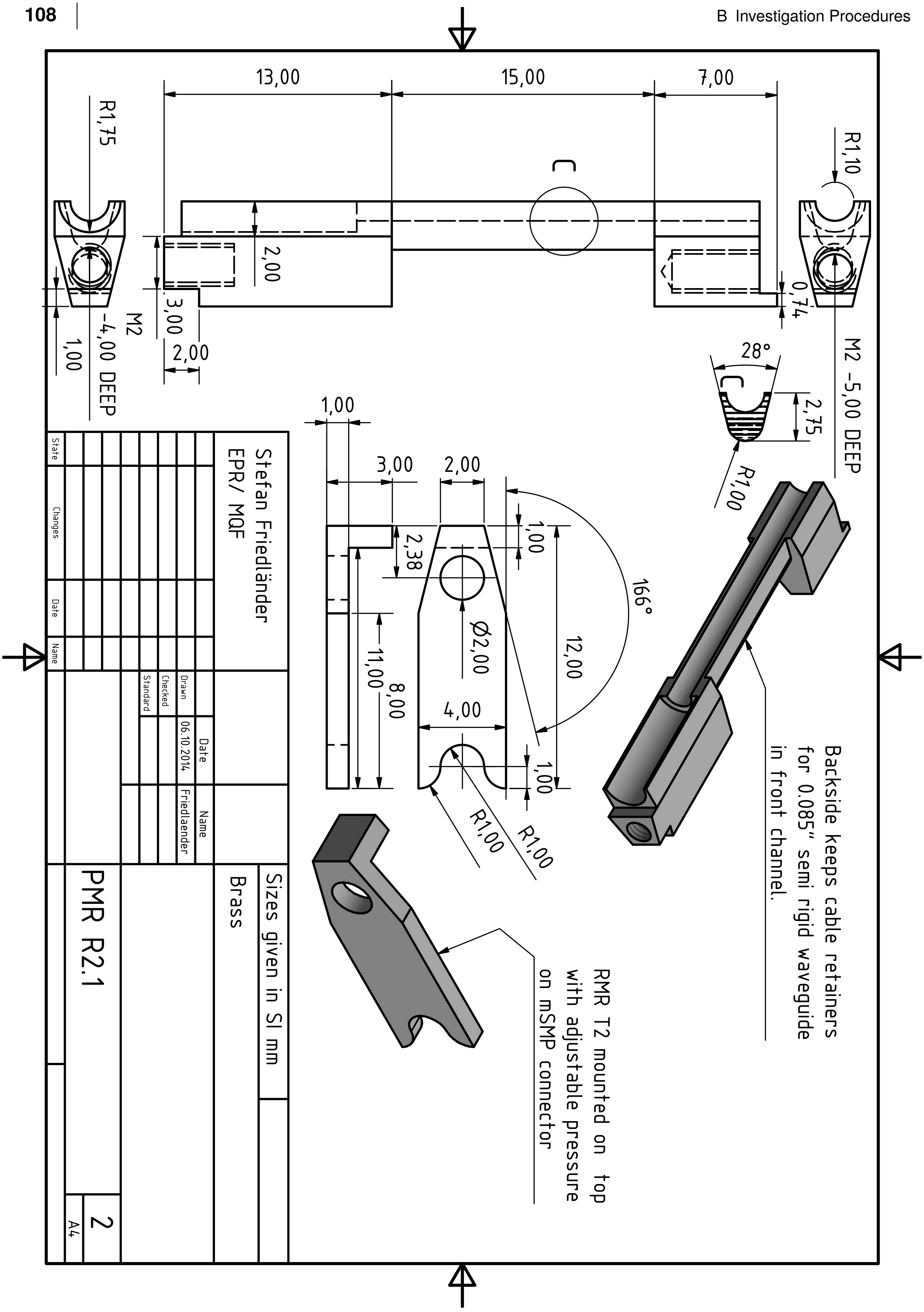

Backside keeps cable retainers for 0.085" semi rigid waveguide in front channel.

RMR T2 mounted on top with adjustable pressure on mSMP connector

Bibliography

[1] Zavoisky, E., ‘Об Оцуцтвии Анизотропии дљa Магнитоспинпвого Резонанса’, *J. Phys. USSR* **1945**, *9*, 447.

[2] Nehrkorn, J., Martins, B. M., Holldack, K., Stoll, S., Dobbek, H., Bittl, R., Schnegg, A., ‘Zero-Field Splittings in metHb and metMb with Aquo and Fluoro Ligands: a FD-FT THz-EPR Study’, *Mol. Phys.* **2013**, *111*, 18-19, 2696.

[3] Blume, R. J., ‘Electron Spin Relaxation Times in Sodium-Ammonia Solutions’, *Phys. Rev.* **1958**, *109*, 6, 1867.

[4] Gordon, J., Bowers, K., ‘Microwave Spin Echoes from Donor Electrons in Silicon’, *Phys. Rev. Lett.* **1958**, *1*, 10, 368.

[5] Schweiger, A., Jeschke, G., *Principles of Pulse Electron Paramagnetic Resonance*, Oxford University Press on Demand **2001**.

[6] Kirmse, R., Stach, J., ‘ESR-Spektroskopie: Anwendungen in der Chemie’, *Wiss. Taschenbücher* **1985**.

[7] Beckert, D., Mehler, K., ‘Investigation of Hydrogen Atom Addition to Vinyl Monomers by Time Resolved ESR Spectroscopy’, *Berichte der Bunsengesellschaft für physikalische Chemie* **1983**, *87*, 7, 587.

[8] Gielen, M., Willem, R., Wrackmeyer, B., *Fluxional Organometallic and Coordination Compounds*, John Wiley & Sons **2005**.

[9] Atherton, N., *Principles of Electron Paramagnetic Resonance*, Ellis Horwood Limited, Chichester, England **1993**.

[10] Weil, J. A., Bolton, J. R., *Electron Paramagnetic Resonance*, Wiley-Interscience, 2nd edition **2007**.

[11] Savchenko, D., Pöppl, A., Kalabukhova, E. N., Greulich-Weber, S., Rauls, E., Schmidt, W. G., Gerstmann, U., ‘Materials Science Forum – Spin-Coupling in Heavily Nitrogen-Doped 4H-SiC’, *Trans. Tech. Publ.* **2009**, *615*, 343.

[12] Jakes, P., Kungl, H., Schierholz, R., Eichel, R.-A., ‘Analyzing the Defect Structure of CuO-Doped PZT and KNN Piezoelectrics from Electron Paramagnetic Resonance’, *IEEE transactions on ultrasonics, ferroelectrics, and frequency control* **2014**, *61*, 9, 1447.

[13] Jeschke, G., ‘DEER Distance Measurements on Proteins’, *Annu. Rev. Phys. Chem.* **2012**, *63*, 419.

[14] Gerhardter, F., Li, Y., Baberschke, K., ‘Temperature-Dependent Ferromagnetic-Resonance Study in Ultrahigh Vacuum: Magnetic Anisotropies of Thin Iron Films’, *Phys. Rev. B* **1993**, *47*, 17, 11204.

[15] Stach, J., Böttcher, R., Kirmse, R., ‘ENDOR-Untersuchungen an Übergangsmetallkomplexen mit organischen Liganden’, *Zeitschrift für Chemie* **1985**, *25*, 1, 1.

[16] Schoeppner, C., Wagner, K., Stienen, S., Meckenstock, R., Farle, M., Narkowicz, R., Suter, D., Lindner, J., 'Angular Dependent Ferromagnetic Resonance Analysis in a Single Micron Sized Cobalt Stripe', *J. Appl. Phys.* **2014**, *116*, 3, 033913.

[17] Köhler, K., Kirmse, R., Böttcher, R., Abram, U., Gribnau, M., Keijzers, C., Boer, E. D., 'Single-Crystal EPR, 35,37Cl and 14,15N ENDOR and ESEEM Studies on (Ph4As)[TcVINCl4/TcVOCl4]. II. Determination of the 35,37Cl and 14,15N Hyperfine and Quadrupole Tensors by ENDOR and ESEEM', *Chemical Physics* **1990**, *143*, 1, 83 .

[18] Kevan, L., 'Catalytically Important Metal Ion Intermediates on Zeolites and Silica Surfaces', *Res. Chem. Intermed.* **1987**, *8*, 1, 53.

[19] Haberlandt, R., Michel, D., Pöppl, A., Stannarius, R., *Molecules in Interaction with Surfaces and Interfaces*, volume 634, Springer Science & Business Media **2004**.

[20] Pöppl, A., Hartmann, M., Kevan, L., 'Electron Spin Resonance and Electron Spin Echo Modulation Studies of Cu(II) Ion Coordination and Adsorbate Interaction in Ion-Exchanged AlMCM-41 Mesoporous Materials', *J. Phys. Chem.* **1995**, *99*, 47, 17251.

[21] Hartmann, M., Kunz, S., Himsl, D., Tangermann, O., Ernst, S., Wagener, A., 'Adsorptive Separation of Isobutene and Isobutane on Cu_3 $(BTC)_2$', *Langmuir* **2008**, *24*, 16, 8634.

[22] Jee, B., Koch, K., Moschkowitz, L., Himsl, D., Hartman, M., Pöppl, A., 'Electron Spin Resonance Study of Nitroxide Radical Adsorption at Cupric Ions in the Metal-Organic Framework Compound $Cu_3(btc)_2$', *J. Phys. Chem. Lett.* **2011**, *2*, 357.

[23] Mendt, M., Jee, B., Himsl, D., Moschkowitz, L., Ahnfeldt, T., Stock, N., Hartmann, M., Pöppl, A., 'A Continuous-Wave Electron Paramagnetic Resonance Study of Carbon Dioxide Adsorption on the Metal-Organic Frame-Work MIL-53', *Appl. Magn. Reson.* **2014**, *45*, 3, 269.

[24] Allendorf, M., Bauer, C., Bhakta, R., Houk, R., 'Luminescent Metal–Organic Frameworks', *Chem. Soc. Rev.* **2009**, *38*, 5, 1330.

[25] Kurmoo, M., 'Magnetic Metal–Organic Frameworks', *Chem. Soc. Rev.* **2009**, *38*, 5, 1353.

[26] Jain, P., Dalal, N. S., Toby, B. H., Kroto, H. W., Cheetham, A. K., 'Order–Disorder Antiferroelectric Phase Transition in a Hybrid Inorganic–Organic Framework with the Perovskite Architecture', *J. Am. Chem. Soc.* **2008**, *130*, 32, 10450.

[27] Prestipino, C., Regli, L., Vitillo, J., Bonino, F., Damin, A., Lamberti, C., Zecchina, A., Solari, P., Kongshaug, K., Bordiga, S., 'Local Structure of Framework Cu(II) in HKUST-1 Metallorganic Framework: Spectroscopic Characterization upon Activation and Interaction with Adsorbates', *Chem. Mater.* **2006**, *18*, 5, 1337.

[28] Poole, Jr., C. P., *Electron Spin Resonance*, Interscience Publishers, New York **1967**.

[29] Zeeman, P., 'Ueber einen Einfluss der Magnetisirung auf die Natur des von einer Substanz emittirten Lichtes', *Verhandlungen der Physikalischen Gesellschaft zu Berlin* **1882**, 127.

[30] Gerlach, W., Stern, O., 'Der experimentelle Nachweis der Richtungsquantelung im Magnetfeld', *Zeitschrift für Physik* **1922**, *9*, 1, 349.

[31] Uhlenbeck, G. E., Goudsmit, S., ‘Spinning Electrons and the Structure of Spectra’, *Nature* **1926**, *117*, 264.

[32] Abragam, A., Pryce, M.-H. L., *Theory of the Nuclear Hyperfine Structure of Paramagnetic Resonance Spectra in Crystals – In: Proceedings of the Royal Society of London A: Mathematical, Physical and Engineering Sciences*, volume 205 of *1080*, The Royal Society **1951**.

[33] Larmor, J., ‘LXIII. On the Intensity of the Natural Radiation from Moving Bodies and its Mechanical Reaction’, *The London, Edinburgh, and Dublin Philosophical Magazine and Journal of Science* **1904**, *7*, 41, 578.

[34] Landé, A., ‘Termstruktur und Zeemaneffekt der Multipletts’, *Zeitschrift für Physik* **1923**, *19*, 1, 112.

[35] Pryce, M., ‘Spin-Spin Interaction within Paramagnetic Ions’, *Phys. Rev.* **1950**, *80*, 6, 1107.

[36] Lorenz, M., Böttcher, R., Friedländer, S., Pöppl, A., Spemann, D., Grundmann, M., ‘Local Lattice Distortions in Oxygen Deficient Mn-Doped ZnO Thin Films, Probed by Electron Paramagnetic Resonance’, *J. Mater. Chem. C* **2014**, *2*, 25, 4947.

[37] Böttcher, R., Pöppl, A., Lorenz, M., Friedländer, S., Spemann, D., Grundmann, M., ‘^{55}Mn Pulsed ENDOR Spectroscopy of Mn^{2+} Ions in ZnO Thin Films and Single Crystal’, *J. Magn. Reson.* **2014**, *245*, 0, 79 .

[38] Heisenberg, W., Jordan, P., ‘Anwendung der Quantenmechanik auf das Problem der anomalen Zeemaneffekte’, *Zeitschrift für Physik* **1926**, *37*, 4, 263.

[39] Schweiger, A., ‘Puls-Elektronenspinresonanz-Spektroskopie: Grundlagen, Verfahren und Anwendungsbeispiele’, *Angew. Chem., Int. Ed.* **1991**, *103*, 3, 223.

[40] Jee, B., Eisinger, K., Gul-E-Noor, F., Bertmer, M., Hartmann, M., Himsl, D., Pöppl, A., ‘Continuous Wave and Pulsed Electron Spin Resonance Spectroscopy of Paramagnetic Framework Cupric Ions in the Zn(II) Doped Porous Coordination Polymer $\mathrm{Cu}_{3-x}\mathrm{Zn}_x(\mathrm{btc})_2$’, *J. Phys. Chem. C* **2010**, *114*, 39, 16630.

[41] Coulomb, C., ‘Premier Mémoire sur l’Électricité et le Magnétisme’, *Histoire de l’Académie Royale des Sciences* **1785**, 569.

[42] Stoll, S., Schweiger, A., ‘EasySpin, a Comprehensive Software Package for Spectral Simulation and Analysis in EPR’, *J. Magn. Reson.* **2006**, *178*, 42.

[43] Weber, R. T., Jiang, J., Barr, D. P., *EMX User’s Manual*, Bruker Instruments, Inc., Billerica, MA USA, 2.3 edition **1998**.

[44] Bloch, F., ‘Nuclear Induction’, *Phys. Rev.* **1946**, *70*, 7-8, 460.

[45] Heisenberg, W., ‘Über den anschaulichen Inhalt der quantentheoretischen Kinematik und Mechanik’, *Zeitschrift für Physik* **1927**, *43*, 3, 172.

[46] Schneider, F., Plato, M., *Experimental Techniques in Electron Spin Resonance*, Verlag Karl Thiemig KG, Munich **1971**.

[47] Hecht, E., *Optik*, Studium, De Gruyter, München **2014**.

[48] Maxwell, J. C., ‘A Dynamical Theory of the Electromagnetic Field’, *Phil. Trans. R. Soc. Lond.* **1865**,

155, 459-512.

[49] Hertz, H., ‘Ueber sehr schnelle electrische Schwingungen’, *Annalen der Physik* **1887**, *267*, 7, 421.

[50] Freudenberg, H., ‘Das erste Klystron schwingt bei 13 cm Wellenlänge’, *Funkgeschichte* **1997**, *113*.

[51] Jackson, J. D., *Classical Electrodynamics*, Wiley, New York, 3. edition **1999**.

[52] Burghaus, O., Rohrer, M., Gotzinger, T., Plato, M., Möbius, K., ‘A Novel High-Field/High-Frequency EPR and ENDOR Spectrometer Operating at 3 mm Wavelength’, *Meas. Sci. Technol.* **1992**, *3*, 8, 765.

[53] Sturgeon, B. E., Britt, R. D., ‘Sensitive Pulsed EPR Spectrometer with an 8–18 GHz Frequency Range’, *Rev. Sci. Instrum.* **1992**, *63*, 4, 2187.

[54] Hankiewicz, J. H., Stenland, C., Kevan, L., ‘Pulsed S-Band Electron Spin Resonance Spectrometer’, *Rev. Sci. Instrum.* **1993**, *64*, 10, 2850.

[55] Willer, M., Forrer, J., Keller, J., Van Doorslaer, S., Schweiger, A., Schuhmann, R., Weiland, T., ‘S-Band (2–4 GHz) Pulse Electron Paramagnetic Resonance Spectrometer: Construction, Probe Head Design, and Performance’, *Rev. Sci. Instrum.* **2000**, *71*, 7, 2807.

[56] Astashkin, A., Enemark, J., Raitsimring, A., ‘26.5–40 GHz Ka-Band Pulsed EPR Spectrometer’, *Concepts Magn. Reson., Part B* **2006**, *29*, 3, 125.

[57] Newman, D., Urban, W., ‘Interpretation of S-State Ion EPR Spectra’, *Adv. Phys.* **1975**, *24*, 6, 793.

[58] Koß, G. and Reinhold, W. and Hoppe, F., *Lehr- und Übungsbuch Elektronik*, Hanser **2005**.

[59] Schirm, L., ‘Halbleiterdioden zur Mikrowellenerzeugung’, *Physik in unserer Zeit* **1975**, *6. Jhrg.*, 3.

[60] Windsch, H., *Einführung in die Methode und die Anwendungsmöglichkeiten der paramagnetischen Elektronenresonanz*, Sekt. Phys. d. KMU Leipzig, Abt. Strukt. d. Mat., EPR-Gr. and Sekt. HF-Spektr. d. Phys. Ges. d. DDR **1968**.

[61] Pike, K. J., Kemp, T. F., Takahashi, H., Day, R., Howes, A. P., Kryukov, E. V., MacDonald, J. F., Collis, A. E., Bolton, D. R., Wylde, R. J., Orwick, M., Kosuga, K., Clark, A. J., Idehara, T., Watts, A., Smith, G. M., Newton, M. E., Dupree, R., Smith, M. E., ‘A Spectrometer Designed for 6.7 and 14.1 T–DNP-Enhanced Solid-State MAS NMR Using Quasi-Optical Microwave Transmission’, *J. Magn. Reson.* **2012**, *215*, 0, 1 .

[62] Mahdjour, H., Clark, W. G., Baberschke, K., ‘High-Sensitivity Broadband Microwave Spectroscopy with Small Nonresonant Coils’, *Rev. Sci. Instrum.* **1986**, *57*, 6, 1100.

[63] Meier, T., Reichardt, S., Haase, J., ‘High-Sensitivity NMR Beyond 200,000 Atmospheres of Pressure’, *J. Magn. Reson.* **2015**, *257*, 39.

[64] Abragam, A., Goldman, M., ‘Principles of Dynamic Nuclear Polarisation’, *Rep. Prog. Phys.* **1978**, *41*, 3, 395.

[65] Blank, A., Levanon, H., ‘Filling Factor of a Paramagnetic Sample in a Rectangular Cavity: Theory and Application’, *Spectrochim. Acta, Part A* **2000**, *56*, 2, 363 .

[66] Blank, A., Levanon, H., ‘Filling Factor in a Pulsed Electron Paramagnetic Resonance Experiment’, *Spectrochim. Acta, Part A* **2002**, *58*, 6, 1329 .

[67] Arieli, D., Vaughan, D. E. W., Strohmaier, K. G., Thomann, H., Bernardo, M., Goldfarb, D., ‘Studies

of Fe(III) Incorporated into AlPO4-20 by X- and W-Band EPR Spectroscopies', *Magn. Reson. Chem.* **1999**, *37*, 13, S43.

[68] Boero, G., Bouterfas, M., Massin, C., Vincent, F., Besse, P.-A., Popovic, R. S., Schweiger, A., 'Electron-Spin Resonance Probe Based on a 100 μm Planar Microcoil', *Rev. Sci. Instrum.* **2003**, *74*, 11, 4794.

[69] Jeschke, G., *Einführung in die ESR-Spektroskopie*, Universität Konstanz **2006**.

[70] Kittel, C., Gress, J. M., Lessard, A., *Einführung in die Festkörperphysik*, volume 14, Oldenbourg München **1969**.

[71] Curie, P., *Propriétés Magnétiques des Corps a Diverses Températures*, 4, Gauthier-Villars et fils **1895**.

[72] Néel, L., 'Propriétés Magnétiques de l'État Magnétique et Énergie d'Interaction entre Atomes Magnétiques', *Ann. de Phys.* **1936**, *5*, 232.

[73] McElfresh, M., 'Fundamentals of Magnetism and Magnetic Measurements', *Quantum Design* **1994**.

[74] Arkadiew, W., 'Über die Absorption elektromagnetischer Wellen an zwei parallelen Drähten', *Annalen der Physik* **1919**, *363*, 2, 105.

[75] Landau, L. D., Lifshitz, E., 'On the Theory of the Dispersion of Magnetic Permeability in Ferromagnetic Bodies', *Phys. Z. Sowjetunion* **1935**, *8*, 153, 101.

[76] Kittel, C., 'Interpretation of Anomalous Larmor Frequencies in Ferromagnetic Resonance Experiment', *Phys. Rev.* **1947**, *71*, 4, 270.

[77] Kittel, C., 'On the Theory of Ferromagnetic Resonance Absorption', *Phys. Rev.* **1948**, *73*, 155.

[78] Kittel, C., 'On the Gyromagnetic Ratio and Spectroscopic Splitting Factor of Ferromagnetic Substances', *Phys. Rev.* **1949**, *76*, 743.

[79] Kittel, C., 'Excitation of Spin Waves in a Ferromagnet by a Uniform RF Field', *Phys. Rev.* **1958**, *110*, 1295.

[80] Farle, M., 'Ferromagnetic Resonance of Ultrathin Metallic Layers', *Rep. Prog. Phys.* **1998**, *61*, 7, 755.

[81] Lindner, J., *Ferromagnetische Resonanz an ultradünnen magnetischen Einfach- und Mehrfachlagen der 3d-Übergangsmetalle – Statik und Dynamik*, Ph.D. thesis, Freie Universität Berlin **2002**.

[82] Gerhardter, F., Li, Y., Baberschke, K., 'Temperature-Dependent Ferromagnetic-Resonance Study in Ultrahigh Vacuum: Magnetic Anisotropies of Thin Iron Films', *Phys. Rev. B* **1993**, *47*, 11204.

[83] Van Vleck, J. H., 'Concerning the Theory of Ferromagnetic Resonance Absorption', *Phys. Rev.* **1950**, *78*, 3, 266.

[84] Smit, J., Beljers, H., 'Ferromagnetic Resonance Absorption in $BaFe_{12}O_{19}$, a Highly Anisotropic Crystal', *Philips J. Res.* **1955**, *10*, 2, 113.

[85] Baselgia, L., Warden, M., Waldner, F., Hutton, S. L., Drumheller, J. E., He, Y. Q., Wigen, P. E., Maryško, M., 'Derivation of the Resonance Frequency from the Free Energy of Ferromagnets', *Phys. Rev. B* **1988**, *38*, 2237.

[86] Valstyn, E., Hanton, J., Morrish, A., 'Ferromagnetic Resonance of Single-Domain Particles', *Phys. Rev.* **1962**, *128*, 5, 2078.

[87] Gilbert, T. L., ‘A Phenomenological Theory of Damping in Ferromagnetic Materials’, *IEEE Trans. Magn.* **2004**, *40*, 6, 3443.

[88] Platow, W., Anisimov, A., Dunifer, G., Farle, M., Baberschke, K., ‘Higher-Order Magnetic Anisotropies and the Nature of the Spin-Reorientation Transition in Face-Centered-Tetragonal Ni(001)/Cu(001)’, *Phys. Rev. B* **1997**, *55*, 3708.

[89] Schulz, B., Schwarzwald, R., Baberschke, K., ‘Magnetic Properties of Ultrathin Ni/Cu(100) Films Determined by a UHV-FMR Study’, *Surf. Sci.* **1994**, *307–309, Part B*, 0, 1102 .

[90] Richtmyer, R. D., ‘Dielectric Resonators’, *J. Appl. Phys.* **1939**, *10*, 6, 391.

[91] Okaya, A., Barash, L. F., ‘The Dielectric Microwave Resonator’, *Proc. IRE* **1962**, *50*, 10, 2081.

[92] Rosenbaum, F. J., ‘Dielectric Cavity Resonator for ESR Experiments’, *Rev. Sci. Instrum.* **1964**, *35*, 11, 1550.

[93] Cohn, S. B., ‘Microwave Bandpass Filters Containing High-Q Dielectric Resonators’, *IEEE Trans. Microwave Theory Tech.* **1968**, *16*, 4, 218.

[94] Kajfez, D., Guillon, P., eds., *Dielectric Resonators*, Artech House, Dedham, MA **1986**.

[95] Kishk, A. A., Antar, Y. M. M., eds., *Antenna Engineering Handbook*, chapter 17: Dielectric Resonator Antennas, McGraw-Hill **2007**, 51 – 68.

[96] Labbe, P., ‘Tungsten Oxides, Tungsten Bronzes and Tungsten Bronze-Type Structures’, in ‘Key Engeneering Materials’, volume 68, Trans. Tech. Publ., 293.

[97] Blank, A., Stavitski, E., Levanon, H., Gubaydullin, F., ‘Transparent Miniature Dielectric Resonator for Electron Paramagnetic Resonance Experiments’, *Rev. Sci. Instrum.* **2003**, *74*, 5, 2853.

[98] Geifman, I., Golovina, I., Kofman, V., Zusmanov, E., ‘The Use of Ferroelectric Material for Increasing the Sensitivity of EPR Spectrometers’, *Ferroelectrics* **1999**, *234*, 1, 81.

[99] Geifman, I., Golovina, I., ‘Optimization of Ferroelectric Resonators for Enhanced EPR Sensitivity’, *Concepts Magn. Reson.* **2005**, *26B*, 1, 46.

[100] Belous, A., Ovchar, O., Valant, M., Suvorov, D., ‘Abnormal Behavior of the Dielectric Parameters of $\mathrm{Ba}_{6-x}\mathrm{Ln}_{8+2x/3}\mathrm{Ti}_{18}\mathrm{O}_{54}$ (Ln= La–Gd) Solid Solutions’, *J. Appl. Phys.* **2002**, *92*, 7, 3917.

[101] Golovina, I., Geifman, I., Belous, A., ‘New Ceramic EPR Resonators with High Dielectric Permittivity’, *J. Magn. Reson.* **2008**, *195*, 52.

[102] Froncisz, W., Hyde, J. S., ‘The Loop-Gap Resonator: a New Microwave Lumped Circuit ESR Sample Structure’, *J. Magn. Reson. (1969)* **1982**, *47*, 3, 515 .

[103] *User Service Training Course – Chapter 5: EPR Resonators*, Bruker Biospin **2012**.

[104] Sienkiewicz, A., Vileno, B., Garaj, S., Jaworski, M., Forro, L., ‘Dielectric Resonator-Based Resonant Structure for Sensitive ESR Measurements at High-Hydrostatic Pressures’, *J. Magn. Reson.* **2005**, *177*, 2, 261.

[105] Jaworski, M., Sienkiewicz, A., Scholes, C. P., ‘Double-Stacked Dielectric Resonator for Sensitive EPR Measurements’, *J. Magn. Reson.* **1997**, *124*, 87.

[106] Mattar, S. M., Emwas, A. H., ‘A Tuneable Doubly Stacked Dielectric Resonator Housed in an Intact

TE102 Cavity for Electron Paramagnetic Resonance Spectroscopy', *Chem. Phys. Lett.* **2003**, *368*, 724.

[107] Sienkiewicz, A., Qu, K., Scholes, C. P., 'Dielectric Resonator-Based Stopped-Flow Electron Paramagnetic Resonance', *Rev. Sci. Instrum.* **1994**, *65*, 1, 68.

[108] Lassmann, G., Schmidt, P. P., Lubitz, W., 'An Advanced EPR Stopped-Flow Apparatus Based on a Dielectric Ring Resonator', *J. Magn. Reson.* **2005**, *172*, 312.

[109] Pospieszalski, M. W., 'Cylindrical Dielectric Resonators and Their Applications in TEM Line Microwave Circuits', *IEEE Trans. Microwave Theory Tech.* **1979**, *27*, 3, 233.

[110] del Monaco, S., Brivati, J., Gualtieri, G., Sotgiu, A., 'Dielectric Resonators in a TE102 X-Band Rectangular Cavity', *Rev. Sci. Instrum.* **1995**, *66*, 10, 5104.

[111] Mattar, S. M., ElNaggar, S. Y., 'Analysis of Two Stacked Cylindrical Dielectric Resonators in a TE102 Microwave Cavity for Magnetic Resonance Spectroscopy', *J. Magn. Reson.* **2011**, *209*, 174.

[112] Golovina, I. S., Kolesnik, S. P., Geifman, I. N., Belous, A. G., 'Novel Multisample Dielectric Resonators for Electron Paramagnetic Resonance Spectroscopy', *Rev. Sci. Instrum.* **2010**, *81*, 4, 044702.

[113] Yi, H. R., Klein, N., 'High-Q Cryogenic Dielectric Resonator Filters for C-band and Ku-band Frequencies', *IEEE Trans. Appl. Supercond.* **2001**, *11*, 1, 489.

[114] Blank, A., Suhovoy, E., Halevy, R., Shtirberg, L., Harneit, W., 'ESR Imaging in Solid Phase Down to Sub-Micron Resolution: Methodology and Applications', *Phys. Chem. Chem. Phys.* **2009**, *11*, 31, 6689.

[115] Mett, R. R., Sidabras, J. W., Golovina, I. S., Hyde, J. S., 'Dielectric Microwave Resonators in TE011 Cavities for Electron Paramagnetic Resonance Spectroscopy', *Rev. Sci. Instrum.* **2008**, *79*, 9.

[116] Elnaggar, S. Y., Tervo, R., Mattar, S. M., 'Optimal Dielectric and Cavity Configurations for Improving the Efficiency of Electron Paramagnetic Resonance Probes', *J. Magn. Reson.* **2014**, *245*, 0, 50 .

[117] Elnaggar, S. Y., Tervo, R., Mattar, S. M., 'Coupled Modes, Frequencies and Fields of a Dielectric Resonator and a Cavity Using Coupled Mode Theory', *J. Magn. Reson.* **2014**, *238*, 0, 1 .

[118] Dietz, B., Iachello, F., Miski-Oglu, M., Pietralla, N., Richter, A., von Smekal, L., Wambach, J., 'Lifshitz and Excited-State Quantum Phase Transitions in Microwave Dirac Billiards', *Phys. Rev. B* **2013**, *88*, 104101.

[119] Rogers Corporation, 'High Frequency Circuit Materials Product Selector Guide', *Technical report* **1999**.

[120] Narkowicz, R., Suter, D., 'Tuner and Radiation Shield for Planar Electron Paramagnetic Resonance Microresonators', *Rev. Sci. Instrum.* **2015**, *86*, 2.

[121] Johansson, B., Haraldson, S., Petterson, L., Beckman, O., 'A Stripline Resonator for ESR', *Rev. Sci. Instrum.* **1974**, *45*, 11, 1445.

[122] Boehme, C., Lips, K., 'A Pulsed EDMR Study of Hydrogenated Microcrystalline Silicon at Low Temperatures', *Phys. Status Solidi C* **2004**, *1*, 5, 1255.

[123] Boero, G., Gualco, G., Lisowski, R., Anders, J., Suter, D., Brugger, J., 'Room Temperature Strong

Coupling Between a Microwave Oscillator and an Ensemble of Electron Spins', *J. Magn. Reson.* **2013**, *231*, 0, 133 .

[124] Morita, Y., Ohno, K., 'EPR of Submicroliter Aqueous Samples Using a Microcoil', *J. Magn. Reson.* **1993**, *A 102*, 344.

[125] 'CST - Computer Simulation Technology, www.cst.com', **2016**.

[126] 'COMSOL Multiphysics, www.comsol.com', **2016**.

[127] Wallace, W. J., Silsbee, R. H., 'Microstrip Resonators for Electron-Spin Resonance', *Rev. Sci. Instrum.* **1991**, *62*, 7, 1754.

[128] Narkowicz, R., Suter, D., Stonies, R., 'Planar Microresonators for EPR Experiments', *J. Magn. Reson.* **2005**, *175*, 275.

[129] Narkowicz, R., Suter, D., Niemeyer, I., 'Scaling of Sensitivity and Efficiency in Planar Microresonators for Electron Spin Resonance', *Rev. Sci. Instrum.* **2008**, *79*, 084702.

[130] Twig, Y., Suhovoy, E., Blank, A., 'Sensitive Surface Loop-Gap Microresonators for Electron Spin Resonance', *Rev. Sci. Instrum.* **2010**, *81*, 104703.

[131] Banholzer, A., Narkowicz, R., Hassel, C., Meckenstock, R., Stienen, S., Posth, O., Suter, D., Farle, M., Lindner, J., 'Visualization of Spin Dynamics in Single Nanosized Magnetic Elements', *Nanotechnology* **2011**, *22*, 29, 295713.

[132] Janiak, C., Vieth, J. K., 'MOFs, MILs and More: Concepts, Properties and Applications for Porous Coordination Networks (PCNs)', *New J. Chem.* **2010**, *34*, 11, 2366.

[133] Corma, A., Garcia, H., Llabrés i Xamena, F., 'Engineering Metal Organic Frameworks for Heterogeneous Catalysis', *Chem. Rev.* **2010**, *110*, 8, 4606.

[134] Schlichte, K., Kratzke, T., Kaskel, S., 'Improved Synthesis, Thermal Stability and Catalytic Properties of the Metal-Organic Framework Compound $Cu_3(BTC)_2$', *Microporous Mesoporous Mater.* **2004**, *73*, 1, 81.

[135] Zhang, X. X., Chui, S. S.-Y., Williams, I. D., 'Cooperative Magnetic Behavior in the Coordination Polymers $[Cu_3\ (TMA)_2L_3](L= H_2O$, Pyridine)', *J. Appl. Phys.* **2000**, *87*, 9, 6007.

[136] Shen, L., Yang, S.-W., Xiang, S., Liu, T., Zhao, B., Ng, M.-F., Göettlicher, J., Yi, J., Li, S., Wang, L., Ding, J., Chen, B., Wei, S.-H., Feng, Y. P., 'Origin of Long-Range Ferromagnetic Ordering in Metal–Organic Frameworks with Antiferromagnetic Dimeric-Cu(II) Building Units', *J. Am. Chem. Soc.* **2012**, *134*, 17286.

[137] Doorslaer, S. V., Caretti, I., Fallis, I., Murphy, D., 'The Power of Electron Paramagnetic Resonance to Study Asymmetric Homogeneous Catalysts Based on Transition-Metal Complexes', *Coordination Chemistry Reviews* **2009**, *253*, 15–16, 2116 .

[138] Mavrandonakis, A., Vogiatzis, K. D., Boese, A. D., Fink, K., Heine, T., Klopper, W., 'Ab Initio Study of the Adsorption of Small Molecules on Metal–Organic Frameworks with Oxo-Centered Trimetallic Building Units: The Role of the Undercoordinated Metal Ion', *Inorg. Chem.* **2015**, *54*, 17, 8251.

[139] Friedländer, S., Liu, J., Addicoat, M., Petkov, P., Vankova, N., Rüger, R., Kuc, A., Guo, W., Zhou,

W., Lukose, B., Wang, Z., Weidler, P. G., Pöppl, A., Ziese, M., Heine, T., Wöll, C., 'Linear Chains of Magnetic Ions Stacked with Variable Distance: Ferromagnetic Ordering with a Curie Temperature above 20 K', *Angew. Chem., Int. Ed.* **2016**, *55*, 41, 12683.

[140] Goldfarb, D., Bernardo, M., Strohmaier, K., Vaughan, D., Thomann, H., 'Characterization of Iron in Zeolites by X-Band and Q-Band ESR, Pulsed ESR, and UV-Visible Spectroscopies', *J. Am. Chem. Soc.* **1994**, *116*, 14, 6344.

[141] Hartmann, M., Kevan, L., 'Generation of Ion-Exchange Capacity by Silicon Incorporation into the Aluminophosphate VPI-5/AIPO 4-8 Molecular Sieve System', *J. Chem. Soc., Faraday Trans.* **1996**, *92*, 19, 3661.

[142] Hartmann, M., Kevan, L., 'Transition-Metal Ions in Aluminophosphate and Silicoaluminophosphate Molecular Sieves: Location, Interaction with Adsorbates and Catalytic Properties', *Chem. Rev. (Washington, DC, U. S.)* **1999**, *99*, 3, 635.

[143] Maurelli, S., Vishnuvarthan, M., Chiesa, M., Berlier, G., Van Doorslaer, S., 'Elucidating the Nature and Reactivity of Ti Ions Incorporated in the Framework of AlPO-5 Molecular Sieves. New Evidence from 31P HYSCORE Spectroscopy', *Journal of the American Chemical Society* **2011**, *133*, 19, 7340.

[144] Arieli, D., Prisner, T., Hertel, M., Goldfarb, D., 'Resolving Mn Framework Sites in Large Cage Aluminophosphate Zeotypes by High Field EPR and ENDOR Spectroscopy', *Phys. Chem. Chem. Phys.* **2004**, *6*, 1, 172.

[145] Chui, S. S.-Y., Lo, S. M.-F., Charmant, J. P., Orpen, A. G., Williams, I. D., 'A Chemically Functionalizable Nanoporous Material $[Cu_3 (TMA)_2 (H_2O)_3]_n$', *Science* **1999**, *283*, 5405, 1148.

[146] Chowdhury, P., Mekala, S., Dreisbach, F., Gumma, S., 'Adsorption of CO, CO_2 and CH_4 on Cu-BTC and MIL-101 Metal Organic Frameworks: Effect of Open Metal Sites and Adsorbate Polarity', *Microporous Mesoporous Mater.* **2012**, *152*, 246.

[147] Ferreira, A. F., Santos, J. C., Plaza, M. G., Lamia, N., Loureiro, J. M., Rodrigues, A. E., 'Suitability of Cu-BTC Extrudates For Propane–Propylene Separation by Adsorption Processes', *Chem. Eng. J.* **2011**, *167*, 1, 1.

[148] Eckold, P., *Kupferhaltige Koordinationspoymere basierend auf thiophenverbrückten 1,2,4-Triazolylbenzoesäuren zur Anwedung in der heterogenen Katalyse*, Master's thesis, Universität Leipzig **2012**.

[149] Šimėnas, M., Kobalz, M., Mendt, M., Eckold, P., Krautscheid, H., Banys, J., Pöppl, A., 'Synthesis, Structure, and Electron Paramagnetic Resonance Study of a Mixed Valent Metal–Organic Framework Containing Cu_2 Paddle-Wheel Units', *J. Phys. Chem. C* **2015**, *119*, 4898.

[150] Pöppl, A., Kunz, S., Himsl, D., Hartmann, M., 'CW and Pulsed ESR Spectroscopy of Cupric Ions in the Metal-Organic Framework Compound Cu_3 (BTC) $_2$', *J. Phys. Chem. C* **2008**, *112*, 7, 2678.

[151] Kozachuk, O., Khaletskaya, K., Halbherr, M., Bétard, A., Meilikhov, M., Seidel, R. W., Jee, B., Pöppl, A., Fischer, R. A., 'Microporous Mixed-Metal Layer-Pillared $[Zn_{1-x}Cu_x(bdc)(dabco)_{0.5}]$ MOFs: Preparation and Characterization', *Eur. J. Inorg. Chem.* **2012**, 1688.

[152] El Mkami, H., Mohideen, M. I. H., Pal, C., McKinlay, A., Scheimann, O., Morris, R. E., 'EPR and

Magnetic Studies of a Novel Copper Metal Organic framework (STAM-I).', *Chem. Phys. Lett.* **2012**, *544*, 17.

[153] Friedländer, S., Šimėnas, M., Kobalz, M., Eckold, P., Ovchar, O., Belous, A. G., Banys, J., Krautscheid, H., Pöppl, A., 'Single Crystal Electron Paramagnetic Resonance with Dielectric Resonators of Mononuclear Cu^{2+} Ions in a Metal–Organic Framework Containing Cu_2 Paddle Wheel Units', *J. Phys. Chem. C* **2015**, *119*, 33, 19171.

[154] Carl, P. J., Larsen, S. C., 'EPR Study of Copper-Exchanged Zeolites: Effects of Correlated g- and A-Strain, Si/Al Ratio, and Parent Zeolite', *J. Phys. Chem. B* **2000**, *104*, 28, 6568.

[155] Eaton, G. R., Eaton, S. S., Barr, D. P., Weber, R. T., *Quantitative EPR*, Springer Science & Business Media Amsterdam **2010**.

[156] Kahn, O., 'Dinuclear Complexes with Predictable Magnetic Properties', *Angew. Chem., Int. Ed.* **1985**, *24*, 10, 834.

[157] Kozlevčar, B., Šegedin, P., 'Structural Analysis of a Series of Copper (II) Coordination Compounds and Correlation with their Magnetic Properties', *Croat. Chem. Acta* **2008**, *81*, 369.

[158] Perec, M., Baggio, R., Sartoris, R. P., Santana, R. C., Peñna, O., Calvo, R., 'Magnetism and Structure in Chains of Copper Dinuclear Paddlewheel Units', *Inorg. Chem.* **2010**, *49*, 695.

[159] Li, H., Eddaoudi, M., O'Keeffe, M., Yaghi, O. M., 'Design and Synthesis of an Exceptionally Stable and Highly Porous Metal-Organic Framework', *Nature* **1999**, *402*, 6759, 276.

[160] Wang, Z., Cohen, S. M., 'Postsynthetic Modification of Metal–Organic Frameworks', *Chem. Soc. Rev.* **2009**, *38*, 5, 1315.

[161] Zeng, M.-H., Wang, B., Wang, X.-Y., Zhang, W.-X., Chen, X.-M., Gao, S., 'Chiral Magnetic Metal-Organic Frameworks of Dimetal Subunits: Magnetism Tuning by Mixed-Metal Compositions of the Solid Solutions', *Inorg. Chem.* **2006**, *45*, 18, 7069.

[162] Nevjestić, I., Depauw, H., Leus, K., Kalendra, V., Caretti, I., Jeschke, G., Van Doorslaer, S., Callens, F., Van Der Voort, P., Vrielinck, H., 'Multi-Frequency (S, X, Q and W-band) EPR and ENDOR Study of Vanadium (IV) Incorporation in the Aluminium Metal–Organic Framework MIL-53', *Chem. Phys. Chem.* **2015**, *16*, 14, 2968.

[163] Friedländer, S., Petkov, P. S., Bolling, F., Kultaeva, A., Böhlmann, W., Ovchar, O., Belous, A. G., Heine, T., Pöppl, A., 'Continuous-Wave Single-Crystal Electron Paramagnetic Resonance of Adsorption of Gases to Cupric Ions in the Zn(II)-Doped Porous Coordination Polymer $Cu_{2.965}Zn_{0.035}(btc)_2$', *J. Phys. Chem. C* **2016**, *120*, 48, 27399.

[164] Jee, B., St. Petkov, P., Vayssilov, G. N., Heine, T., Hartmann, M., Pöppl, A., 'A Combined Pulsed Electron Paramagnetic Resonance Spectroscopic and DFT Analysis of the $^{13}CO_2$ and ^{13}CO Adsorption on the Metal–Organic Framework $Cu_{2.97}Zn_{0.03}(btc)_2$', *J. Phys. Chem. C* **2013**, *117*, 16, 8231.

[165] Kahn, O., *Molecular Magnetism*, Wiley-VCH, Weinheim **1993**.

[166] Bleaney, B., Bowers, K. D., 'The Bleaney-Bowers Effect', *Proc. R. Soc.* **1952**, *Series A*, 214, 451.

[167] Hyde, K., Gordon, G., Kokoszka, G. F., 'Magnetic Properties of Some Binuclear Copper (II) Com-

plexes', *J. Inorg. Nucl. Chem.* **1968**, *30*, 2155.

[168] Melník, M., 'Study of the Relation between the Structural Data and Magnetic Interaction in Oxo-Bridged Binuclear Copper (II) Compounds', *Coord. Chem. Rev.* **1982**, *42*, 259.

[169] Kato, M., Muto, Y., 'Factors Affecting the Magnetic Properties of Dimeric Copper (II) Complexes', *Coord. Chem. Rev.* **1988**, *92*, 45.

[170] Li, J.-R., Yu, Q., Sañudo, E. C., Tao, Y., Bu, X.-H., 'An Azido-Cu(II)-Triazolate Complex with utp-Type Topological Network, Showing Spin-Canted Antiferromagnetism', *Chem. Commun.* **2007**, 2602.

[171] Zhu, M., Su, S.-Q., Hao, X.-Z. S. Z.-M., Song, S.-Y., Zhang, H.-J., 'Spin Canting Magnetization in a 3D Cu (II) Complex Based on Molybdate Oxide Cluster and 5-Triazole Isophthalic Acid', *Dalton Trans.* **2012**, *41*, 13267.

[172] Moulton, B., Lu, J., Hajndl, R., Hariharan, S., Zaworotko, M. J., 'Crystal Engineering of a Nanoscale Kagomé Lattice', *Angew. Chem., Int. Ed.* **2002**, *41*, 2821.

[173] Shekhah, O., Wang, H., Kowarik, S., Schreiber, F., Paulus, M., Tolan, M., Sternemann, C., Evers, F., Zacher, D., Fischer, R. A., et al., 'Step-by-Step Route for the Synthesis of Metal-Organic Frameworks', *J. Am. Chem. Soc.* **2007**, *129*, 49, 15118.

[174] Liu, J., Lukose, B., Shekhah, O., Arslan, H. K., Weidler, P., Gliemann, H., Bräse, S., Grosjean, S., Godt, A., Feng, X., Müllen, K., Magdau, I.-B., Heine, T., Wöll, C., 'A Novel Series of Isoreticular Metal Organic Frameworks: Realizing Metastable Structures by Liquid Phase Epitaxy', *Sci. Rep.* **2012**, *2*, 921.

[175] Wolf, S. A., Awschalom, D. D., Buhrman, R. A., Daughton, J. M., von Molnár, S., Roukes, M. L., Chtchelkanova, A. Y., Treger, D. M., 'Spintronics: A Spin-Based Electronics Vision for the Future', *Science* **2001**, *294*, 5546, 1488.

[176] Ising, E., 'Beitrag zur Theorie des Ferromagnetismus', *Zeitschrift für Physik* **1925**, *31*, 1, 253.

[177] Johannes, M., Richter, J., Drechsler, S.-L., Rosner, H., '$Sr_2Cu(PO_4)_2$: A Real Material Realization of the One-Dimensional Nearest Neighbor Heisenberg Chain', *Phys. Rev. B* **2006**, *74*, 17, 174435.

[178] Kawasaki, Y., Gavilano, J. L., Keller, L., Schefer, J., Christensen, N. B., Amato, A., Ohno, T., Kishimoto, Y., He, Z., Ueda, Y., et al., 'Magnetic Structure and Spin Dynamics of the Quasi-One-Dimensional Spin-Chain Antiferromagnet $BaCo_2V_2O_8$', *Phys. Rev. B* **2011**, *83*, 6, 064421.

[179] Stone, M. B., Lumsden, M. D., Nagler, S. E., Singh, D. J., He, J., Sales, B., Mandrus, D., 'Quasi-One-Dimensional Magnons in an Intermetallic Marcasite', *Phys. Rev. Lett.* **2012**, *108*, 16, 167202.

[180] Gambardella, P., Dallmeyer, A., Maiti, K., Malagoli, M., Eberhardt, W., Kern, K., Carbone, C., 'Ferromagnetism in One-Dimensional Monatomic Metal Chains', *Nature* **2002**, *416*, 6878, 301.

[181] Bloch, E. D., Queen, W. L., Krishna, R., Zadrozny, J. M., Brown, C. M., Long, J. R., 'Hydrocarbon Separations in a Metal-Organic Framework with Open Iron(II) Coordination Sites', *Science* **2012**, *335*, 6076, 1606.

[182] Shekhah, O., Liu, J., Fischer, R. A., Woll, C., 'MOF Thin Films: Existing and Future Applications',

Chem. Soc. Rev. **2011**, *40*, 1081.

[183] Shekhah, O., Wang, H., Zacher, D., Fischer, R., Wöll, C., 'Growth Mechanism of Metal–Organic Frameworks: Insights into the Nucleation by Employing a Step-by-Step Route', *Angew. Chem., Int. Ed.* **2009**, *48*, 27, 5038.

[184] Arslan, H. K., Shekhah, O., Wieland, D. F., Paulus, M., Sternemann, C., Schroer, M. A., Tiemeyer, S., Tolan, M., Fischer, R. A., Wöll, C., 'Intercalation in Layered Metal–Organic Frameworks: Reversible Inclusion of an Extended π-System', *J. Am. Chem. Soc.* **2011**, *133*, 21, 8158.

[185] Oxford Instruments, *Cryostats for Electron Spin Resonance Spectroscopy*, www.oxford-instruments.com **2004**.

[186] Friedländer, S., Ovchar, O., Voigt, H., Böttcher, R., Belous, A., Pöppl, A., 'Dielectric Ceramic EPR Resonators for Low Temperature Spectroscopy at X-Band Frequencies', *Appl. Magn. Reson.* **2015**, *46*, 1, 33.

[187] Friedländer, S., *Increasing Sensitivity in EPR – Approaches for Spectroscopy of Single Crystals and Thin Films*, Master's thesis, University of Leipzig **2013**.

[188] Fricke, R., Jerschkewitz, H.-G., Öhlmann, G., 'Electron Spin Resonance Studies of Free and Supported 12-Heteropoly Acids. Part 3.—The Stability of Unsupported $H_{3+n}(PV_nMo_{12-n}O_{40})\cdot xH_2O$ in Air and in a Vacuum', *J. Chem. Soc., Faraday Trans. 1* **1986**, *82*, 11, 3479.

[189] Nesmelov, Y. E., Surek, J. T., Thomas, D. D., 'Enhanced EPR Sensitivity from a Ferroelectric Cavity Insert', *J. Magn. Reson.* **2001**, *153*, 7.

[190] Shames, A. I., Osipov, V. Y., Boudou, J. P., Panich, A. M., von Bardeleben, H. J., Treussart, F., Vul', A. Y., 'Magnetic Resonance Tracking of Fluorescent Nanodiamond Fabrication', *J. Phys. D: Appl. Phys.* **2015**, *48*, 15, 155302.

[191] Orlinskii, S., Bogomolov, R., Kiyamova, A., Yavkin, B., Mamin, G., Turner, S., Van Tendeloo, G., Shiryaev, A., Vlasov, I., Shenderova, O., 'Identification of Substitutional Nitrogen and Surface Paramagnetic Centers in Nanodiamond of Dynamic Synthesis by Electron Paramagnetic Resonance', *Nanosci. Nanotechnol. Lett.* **2011**, *3*, 1, 63.

[192] Smith, W., Sorokin, P., Gelles, I., Lasher, G., 'Electron-Spin Resonance of Nitrogen Donors in Diamond', *Phys. Rev.* **1959**, *115*, 6, 1546.

[193] Hathaway, B., Billing, D., 'The Electronic Properties and Stereochemistry of Mono-Nuclear Complexes of the Copper (II) Ion', *Coord. Chem. Rev.* **1970**, *5*, 2, 143.

[194] Tominaga, H., Ono, Y., Keii, T., 'Spectroscopic Study of Cu (II) Ions Supported on Silica Gel by Cation Exchange Method', *J. Catal.* **1975**, *40*, 2, 197.

[195] Kevan, L., 'Electron Spin Echo Studies of the Location and Coordination of Metal Species on Oxide Surfaces', *Acc. Chem. Res.* **1987**, *20*, 1, 1.

[196] Sakaguchi, U., Addison, A. W., 'Spectroscopic and Redox Studies of Some Copper (II) Complexes with Biomimetic Donor Atoms: Implications for Protein Copper Centres', *J. Chem. Soc., Dalton Trans. 1* **1979**, *4*, 600.

[197] Gul-E-Noor, F., Jee, B., Mendt, M., Himsl, D., Pöppl, A., Hartmann, M., Haase, J., Krautscheid, H., Bertmer, M., 'Formation of Mixed Metal $Cu_{3-x}Zn_x(btc)_2$ Frameworks with Different Zinc Contents: Incorporation of Zn^{2+} into the Metal–Organic Framework Structure as Studied by Solid-State NMR', *J. Phys. Chem. C* **2012**, *116*, 39, 20866.

[198] Ivanshin, V. A., Litvinova, T. O., Ivanshin, N. A., Pöppl, A., Sokolov, D. A., Aronson, M. C., 'Evolution of the 4f Electron Localization from YbRh2Si2 to YbRh2Pb Studied by Electron Spin Resonance', *J. Exp. Theor. Phys.* **2014**, *118*, 5, 760.

[199] Rubinstein, M., Lubitz, P., Wang, H., Li, Q., 'Ferromagnetic Resonance in an Ultrathin Manganate Film', *Solid State Commun.* **1999**, *109*, 12, 745 .

[200] Yoshitomi, H., Vidyasagar, R., Kitayama, S., Kita, T., Ohta, H., Okubo, S., Fukuoka, Y., Sakurai, T., 'Ferromagnetic Properties of GdN Thin Films Studied by Temperature Dependent Circular Polarized Spectroscopy', *Appl. Phys. Lett.* **2012**, *101*, 7, 072403.

[201] Pöppl, A., Hartmann, M., Böhlmann, W., Böttcher, R., 'Coordination Geometry of the Copper−Pyridine Complex in Frozen Solution As Studied by Proton and Deuterium Two-Dimensional Hyperfine Sublevel Correlation Electron Spin Resonance Spectroscopy', *J. Phys. Chem. A* **1998**, *102*, 20, 3599.

[202] Hay, P. J., Thibeault, J. C., Hoffmann, R., 'Orbital Interactions in Metal Dimer Complexes', *J. Am. Chem. Soc.* **1975**, *97*, 17, 4884.

[203] St Petkov, P., Vayssilov, G. N., Liu, J., Shekhah, O., Wang, Y., Wöll, C., Heine, T., 'Defects in MOFs: A Thorough Characterization', *Chem. Phys. Chem.* **2012**, *13*, 8, 2025.

[204] Guo, L.-R., Zhu, F., Chen, Y., Li, Y.-Z., Zheng, L.-M., 'Layered Copper Compounds Based on 4-(3-Bromothienyl) Phosphonate (BTP): Weak Ferromagnetism Observed in $(Cu_2(4,4'\text{-}bpy)_{0.5}(BTP)_2)\cdot H_2O$', *Dalton Trans.* **2009**, *40*, 8548.

[205] Nehrkorn, J., Schnegg, A., Holldack, K., Stoll, S., 'General Magnetic Transition Dipole Moments for Electron Paramagnetic Resonance', *Phys. Rev. Lett.* **2015**, *114*, 010801.

[206] Akhtar, W., Schnegg, A., Veber, S., Meier, C., Fehr, M., Lips, K., 'CW and Pulsed Electrically Detected Magnetic Resonance Spectroscopy at 263GHz/12T on Operating Amorphous Silicon Solar Cells', *J. Magn. Reson.* **2015**, *257*, 94.

[207] Gysler, M., El Hallak, F., Ungur, L., Marx, R., Hakl, M., Neugebauer, P., Rechkemmer, Y., Lan, Y., Sheikin, I., Orlita, M., Anson, C. E., Powell, A. K., Sessoli, R., Chibotaru, L. F., van Slageren, J., 'Multitechnique Investigation of Dy3 - Implications for Coupled Lanthanide Clusters', *Chem. Sci.* **2016**, *7*, 4347.

[208] Pribitzer, S., Doll, A., Jeschke, G., 'SPIDYAN, a MATLAB Library for Simulating Pulse EPR Experiments with Arbitrary Waveform Excitation', *J. Magn. Reson.* **2016**, *263*, 45.

[209] Doll, A., Qi, M., Wili, N., Pribitzer, S., Godt, A., Jeschke, G., 'Gd (III)–Gd (III) Distance Measurements with Chirp Pump Pulses', *J. Magn. Reson.* **2015**, *259*, 153.

[210] Spindler, P. E., Waclawska, I., Endeward, B., Plackmeyer, J., Ziegler, C., Prisner, T. F., 'Carr–Purcell Pulsed Electron Double Resonance with Shaped Inversion Pulses', *J. Phys. Chem. Lett.* **2015**, *6*, 21,

4331.

[211] Katz, I., Fehr, M., Schnegg, A., Lips, K., Blank, A., 'High Resolution In-Operando Microimaging of Solar Cells with Pulsed Electrically-Detected Magnetic Pesonance', *J. Magn. Reson.* **2015**, *251*, 26.

[212] Kraffert, F., Steyrleuthner, R., Meier, C., Bittl, R., Behrends, J., 'Transient Electrically Detected Magnetic Resonance Spectroscopy Applied to Organic Solar Cells', *Appl. Phys. Lett.* **2015**, *107*, 4, 043302.

[213] Kiss, S., Rostas, A., Heidinger, L., Spengler, N., Meissner, M., MacKinnon, N., Schleicher, E., Weber, S., Korvink, J., 'A Microwave Resonator Integrated on a Polymer Microfluidic Chip', *J. Magn. Reson.* **2016**, *270*, 169 .

[214] Prisner, T. F., Rohrer, M., Möbius, K., 'Pulsed 95 GHz High-Field EPR Heterodyne Spectrometer with High Spectral and Time Resolution', *Appl. Magn. Reson.* **1994**, *7*, 2, 167.

[215] Gruschinski, S., Rodenstein, A., 'Ligand Exchange Reactions of Copper (II) Complexes of Urea Type Ligands: Syntheses, Structures, EPR Spectroscopy', *Zeitschr. f. org. und anorg. Chem.* **2012**, *638*, 7-8, 1179.

[216] Gemperle, C., Aebli, G., Schweiger, A., Ernst, R., 'Phase Cycling in Pulse EPR', *J. Magn. Reson. (1969)* **1990**, *88*, 2, 241 .

[217] Kummer, M., *Grundlagen der Mikrowellentechnik*, VEB Verlag Technik Berlin **1989**.

[218] *Microwaves101.com* **2016**.

[219] Stoe & Cie GmbH, X-Area Darmstadt **2006**.

[220] Hausdorf, S., 'Materials Center at TU Dresden, Einwaagen für CuBTC- und CuBTC(Zn)-Einkristalle', **2016**, unpublished lab report.

[221] Arslan, H. K., Shekhah, O., Wohlgemuth, J., Franzreb, M., Fischer, R. A., Wöll, C., 'High-Throughput Fabrication of Uniform and Homogenous MOF Coatings', *Adv. Funct. Mater.* **2011**, *21*, 22, 4228.

[222] Brandenburg, K., *Diamond 3.0*, Crystal Impact GbR, Bonn **2004**.

[223] Persistence of Vision Pty. Ltd., Williamstown, Victoria, Australia, *Persistence of Vision Raytracer, V. 3.7* **2016**.

[224] Hanwell, M. D., Curtis, D. E., Lonie, D. C., Vandermeersch, T., Zurek, E., Hutchison, G. R., 'Avogadro: An Advanced Semantic Chemical Editor, Visualization, and Analysis Platform', *J. Cheminf.* **2012**, *4*, 17.

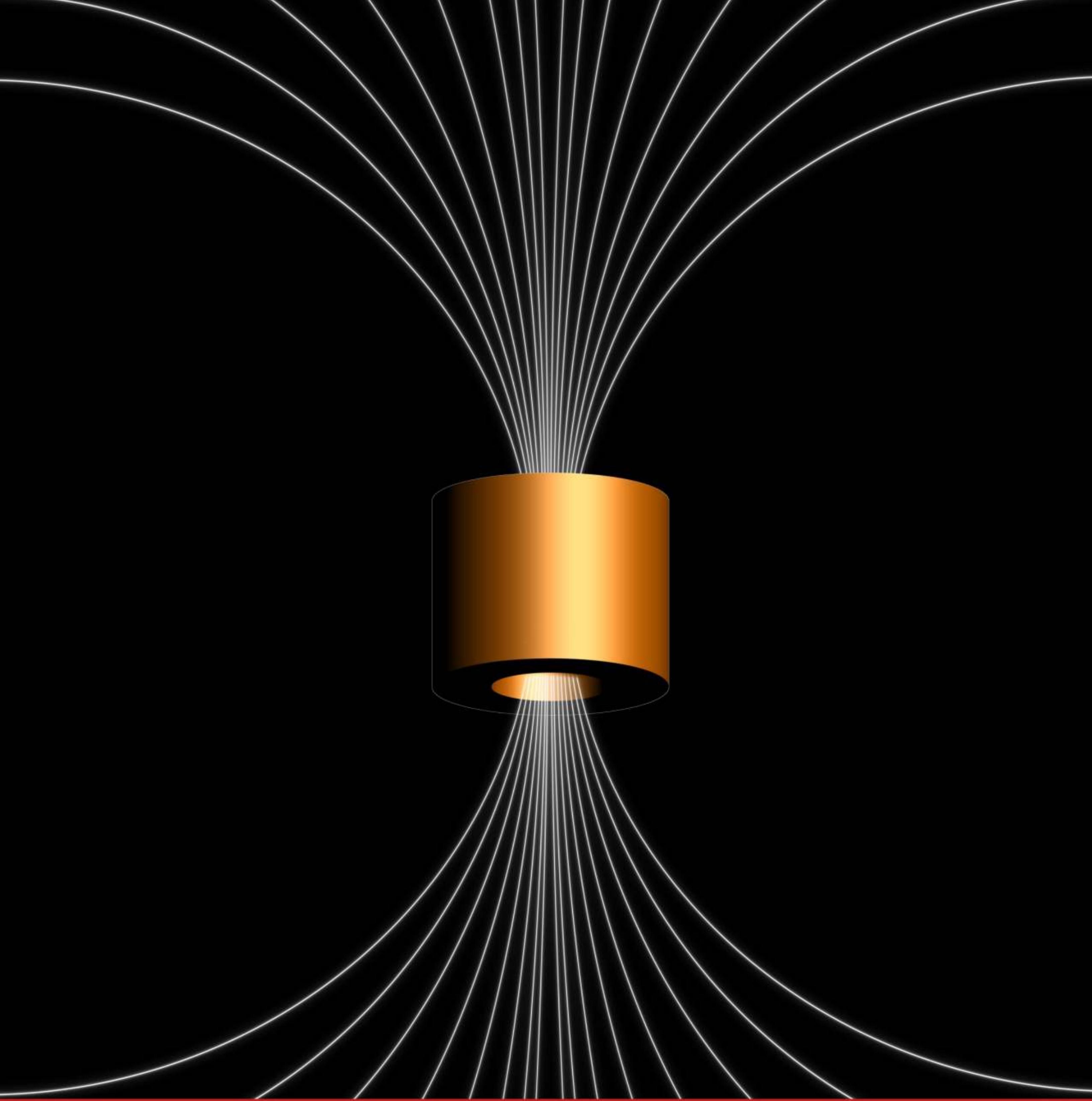

Dissertation

Stefan Friedländer

Universität Leipzig

2017